

Aerodynamics and Aeroacoustics of Propeller Operation at Negative Thrust A Computational Study

Goyal, J.

DOI

[10.4233/uuid:0cf573ad-f7ca-41d6-8b43-342359f50db6](https://doi.org/10.4233/uuid:0cf573ad-f7ca-41d6-8b43-342359f50db6)

Publication date

2025

Document Version

Final published version

Citation (APA)

Goyal, J. (2025). *Aerodynamics and Aeroacoustics of Propeller Operation at Negative Thrust: A Computational Study* (1 ed.). [Dissertation (TU Delft), Delft University of Technology].
<https://doi.org/10.4233/uuid:0cf573ad-f7ca-41d6-8b43-342359f50db6>

Important note

To cite this publication, please use the final published version (if applicable).
Please check the document version above.

Copyright

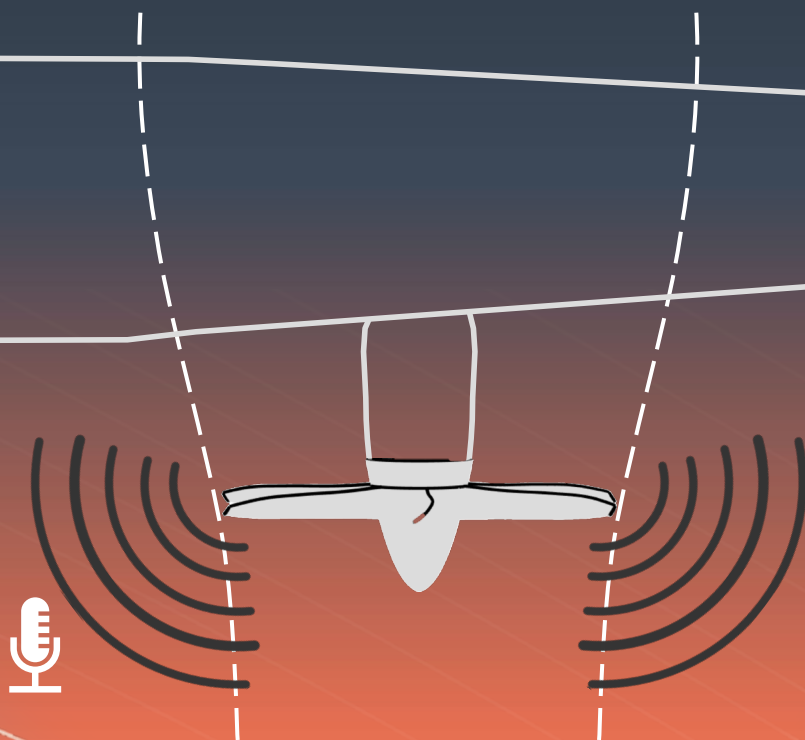
Other than for strictly personal use, it is not permitted to download, forward or distribute the text or part of it, without the consent of the author(s) and/or copyright holder(s), unless the work is under an open content license such as Creative Commons.

Takedown policy

Please contact us and provide details if you believe this document breaches copyrights.
We will remove access to the work immediately and investigate your claim.

Aerodynamics and Aeroacoustics of Propeller Operation at Negative Thrust

A Computational Study



Jatinder Goyal

AERODYNAMICS AND AEROACOUSTICS OF PROPELLER OPERATION AT NEGATIVE THRUST

A COMPUTATIONAL STUDY

**AERODYNAMICS AND AEROACOUSTICS OF
PROPELLER OPERATION AT NEGATIVE THRUST**
A COMPUTATIONAL STUDY

Dissertation

for the purpose of obtaining the degree of doctor
at Delft University of Technology,
by the authority of the Rector Magnificus prof. dr. ir. T.H.J.J. van der Hagen,
Chair of the Board for Doctorates,
to be defended publicly on
Friday 20 June 2025 at 12:30 o' clock

by

Jatinder GOYAL

Master of Science in Aerospace Engineering,
Delft University of Technology, the Netherlands

born in Mandi Kalan, India.

This dissertation has been approved by the promotor.

Composition of the doctoral committee:

Rector Magnificus,	chairperson
Prof. dr. ir. C.J. Simão Ferreira	Delft University of Technology, <i>promotor</i>
Prof. dr. F. Avallone	Politecnico di Torino, Italy, <i>promotor</i>
Prof. dr. D. Ragni	Delft University of Technology, <i>promotor</i>
Dr. ir. T. Sinnige	Delft University of Technology, <i>copromotor</i>

Independent members:

Prof. dr. D. Casalino	Delft University of Technology
Prof. dr. A.M.A. Guardone	Politecnico di Milano, Italy
Dr. B. Ortun	ONERA, France
Prof. dr. M. Roger	École Centrale de Lyon, France
Prof. dr. F. Scarano	Delft University of Technology, <i>reserve member</i>



This research was funded by the European Union's Horizon 2020 Research and Innovation programme under grant agreement number 875551.

Keywords: Propeller aeroacoustics, propeller aerodynamics, propeller slipstream characteristics, energy-harvesting, CFD

Printed by: Haveka

Cover: Illustration of propeller operation at negative thrust mounted on an ATR-72 aircraft. Designed by Jatinder Goyal, edited by Rashika Jain.

Copyright © 2025 by J. Goyal

ISBN 978-94-6518-071-7

An electronic version of this dissertation is available at
<http://repository.tudelft.nl/>.

It's going to be legen—wait for it

SUMMARY

Future regional and short to medium-range aircraft are expected to use propellers for sustainable aviation, possibly with (hybrid-)electric propulsion systems. This will enable innovative integration of aero-propulsive systems, potentially increasing the overall aerodynamic efficiency of the airframe and propellers, resulting in a lighter airframe and increased passenger comfort. The presence of electric motors and propellers in such configurations, in addition, offers a unique opportunity to leverage propellers as airbrakes by operating them at negative thrust. This approach offers multiple potential advantages, including shorter landing runs, enhanced landing manoeuvrability, energy harvesting during braking operations, faster aircraft turnaround times, and reduced community noise exposure. Despite these potential advantages, the aerodynamic and aeroacoustic characteristics of propellers operating in negative thrust mode remain largely unexplored. This thesis addresses this knowledge gap through computational analysis, comparing the performance of isolated propeller configurations in negative thrust mode with the well-understood positive thrust mode.

A computational approach was chosen for its ability to provide pressure and velocity fields throughout the entire domain of interest, including detailed data on blade surfaces. High-fidelity simulations (lattice-Boltzmann very large-eddy simulations) were conducted for a previous-generation turboprop aircraft propeller in an isolated configuration, analysing multiple blade pitch settings. Due to the availability of reference experimental data, the simulations were performed at relatively low Reynolds and Mach numbers compared to typical cruise flight conditions of propeller aircraft. Acknowledging the importance of the tip Mach number as a critical similarity parameter for aeroacoustics, some of the analyses were conducted at higher tip Mach numbers to ensure a more robust assessment of the aeroacoustic characteristics.

Operating a conventional propeller in negative thrust mode results in the operation of the positively cambered blade sections at negative angles of attack, which results in flow separation starting from the blade tip. A detailed analysis of the isolated propeller at 0° angle of attack (AoA) and a constant helicoidal tip Mach number showed that flow separation around the blades in negative thrust conditions led to 2 to 6 times higher fluctuations in integrated thrust compared to positive thrust conditions. This flow separation induces substantial broadband fluctuations in blade loading, 18% for inboard sections and 30% for the blade tip, relative to the time-averaged loading under negative thrust conditions. In contrast, such fluctuations are negligible at positive thrust conditions. Additionally, flow separation in negative thrust mode results in significantly higher broadband noise levels, about 15–20 dB higher along the propeller axis compared to positive thrust conditions. However, within the propeller plane, noise levels were observed to be 10 dB higher in the positive thrust regime than in the negative thrust regime at a given absolute thrust level of $|T_C = 0.08|$. The lower noise levels when operating at negative thrust conditions are attributed to two factors: the lower magnitude of the negative

torque compared to the positive torque at a given thrust level and the inboard shift of the blade loading in negative thrust conditions due to the stall of the blade tip. These findings suggest that a steeper and quieter descent compared to conventional approaches could be achieved using negative thrust, provided that the negative torque generated is equal to or less than the torque required for conventional propeller operation during landing (without considering the effect of inflow angle on propeller noise).

Operating a propeller at a non-zero angle of attack introduces a periodic variation in the geometric angle of attack of the blade sections over the azimuth, leading to a dynamic stall of propeller blade sections when operating under negative thrust conditions, with flow attaching on the advancing side and separating on the retreating side. This results in increased broadband fluctuations in blade loading on the retreating side. Near the blade tip ($r/R = 0.90$), the periodic fluctuations deviate from a sinusoidal pattern due to the operation of blade sections in a deep stall region, where broadband fluctuations in the local thrust coefficient ($\pm 7\%$ of the mean thrust level) become comparable in magnitude to the periodic variations (-10% to $+7\%$ of the mean thrust level). The periodic variations in blade loading over the azimuth at non-zero AoA lead to a significant change in noise directivity compared to the 0° AoA case. When operating at positive thrust, noise levels significantly increase in regions opposite the tilt direction and decrease significantly towards the tilt direction. Conversely, noise increases toward the tilt direction under negative thrust conditions and decreases away from it. This pattern is beneficial for community noise reduction, as the community lies below the aircraft, away from the tilt direction.

While this thesis focuses on isolated propeller configurations, insights can be derived for a potential wing immersed in a propeller slipstream by considering the dynamic pressure and swirl angle within the slipstream. For a propeller operating at 0° AoA under negative thrust conditions, the slipstream is expected to cause a more significant reduction in the lift on the upgoing blade side compared to the downgoing blade side due to the direction of the swirl. Conversely, under positive thrust conditions, the impingement of the propeller slipstream on the potential wing is likely to result in a more significant lift increase on the upgoing blade side than on the downgoing blade side. When operating at a non-zero angle of attack, the dynamic pressure within the slipstream is higher on the downgoing blade side than on the upgoing blade side for both positive and negative thrust conditions. Consequently, these slipstream characteristics tend to reduce the lift disparities between the upgoing and downgoing blade sides under positive thrust at a non-zero AoA, compared to the 0° AoA case. However, under negative thrust conditions, a non-zero AoA further amplifies the differences in lift generation between the upgoing and downgoing blade sides compared to the 0° AoA scenario.

While high-fidelity simulations provide deeper insights into various physical phenomena, they are not always practical due to their significant computational costs. A systematic evaluation of different numerical tools with varying levels of fidelity against experimental data revealed that low-fidelity methods, such as Blade Element Momentum (BEM) theory and Lifting Line (LL) theory, are suitable for predicting propeller performance and general trends as long as the flow remains attached, i.e., under positive thrust conditions up to moderate thrust levels. However, their applicability in negative thrust mode is limited due to the breakdown of inherent assumptions caused by flow

separation. On the other hand, wall-resolved ($y^+ < 1$) Reynolds-Averaged Navier-Stokes (RANS) simulations, both steady and unsteady, performed well across both positive and negative thrust conditions, with errors below 2% for both thrust and power magnitudes near the maximum power output point in the negative thrust regime. Lattice-Boltzmann very-large-eddy simulations (LB-VLESs) with $y^+ \leq 10$ showed excellent agreement with experimental data, with less than 1% error near the maximum power output point, though at a significant computational cost. In contrast, LB-VLESs with $y^+ \geq 15$ could reasonably predict propeller performance in cases without flow separation, with computational costs comparable to unsteady RANS. However, the wall model used in these simulations introduces errors in modelling flow separation, leading to a 16% overestimation of power magnitude near the maximum power output point. The advantage of using LB-VLESs with $y^+ \geq 15$ lies in better preservation of propeller wake structures due to lower numerical diffusion and a lower computational cost per mesh element than RANS, making them valuable for studying propeller-wing interactions. These findings highlighted that the choice of method should be informed by the desired accuracy and computational resources available, balancing the trade-offs between detailed resolution and overall cost.

The absence of the blade loading distributions from the experiments often hinders the comparison of different numerical methods against experimental data. Obtaining experimental blade loading distributions accurately often poses a challenge owing to the limitations of conventional measurement techniques. A potential alternative is the "wake-informed lifting line model," which estimates blade loading distributions using phase-locked slipstream velocity data. The evaluation of the efficacy of this method using steady RANS data demonstrated that the model reasonably predicts the radial thrust distribution, with a 2% overprediction of the peak value under attached flow conditions. In the case of flow separation, the model captures the radial gradients and overall shape of the thrust distribution but exhibits discrepancies in absolute values. Incorporating profile drag contributions through external polar data improves the predictions, resulting in a 1.9% overprediction of the peak thrust value and a slight outboard shift in the thrust distribution compared to the steady RANS data. When applied to experimental phase-locked slipstream data, the model exhibited performance similar to that observed in the validation case. Thus, the wake-informed LL model shows promise as a tool for obtaining experimental blade loading distributions and enhancing experimental analysis.

The findings of this thesis demonstrate that propellers operating in negative thrust conditions exhibit distinct aerodynamic and aeroacoustic characteristics compared to positive thrust conditions. These altered characteristics present a promising avenue for reducing community noise not only through the possibility of steeper descents but also through changes in the noise emissions from the propeller itself. This research lays the groundwork for future research and development, paving the way for the successful integration of negative thrust operation into (hybrid-)electric aircraft and, therefore, contributing to more sustainable and quieter aviation solutions.

SAMENVATTING

Voor duurzame luchtvaart, zullen toekomstige vliegtuigen voor korte tot middellange regionale vluchten naar verwachting gebruik maken van propellers, mogelijk met (hybride) elektrische aandrijfsystemen. Dit zal een innovatieve integratie van de aerodynamische en de aandrijvingssystemen mogelijk maken, wat mogelijk het gehele aerodynamische rendement van zowel het vliegtuig als de propellers kan verhogen, wat resulteert in een lichter toestel en meer comfort voor de passagiers. Propellers met elektromotoren dergelijke configuraties bieden bovendien een unieke kans om propellers als luchtremmen te gebruiken door ze met negatieve stuwkracht te laten werken. Deze benadering biedt meerdere potentiële voordelen, waaronder kortere landingstrajecten, verbeterde wendbaarheid tijdens het landen, energierterugwinning tijdens het remmen, snellere omlooptijden van vliegtuigen en minder geluidsoverlast voor omwonenden. Ondanks deze potentiële voordelen is er echter nog maar weinig onderzoek gedaan zijn de aerodynamische en aeroakoestische eigenschappen van propellers die gebruikt worden in een negatieve stuwkrachtmodus. Dit proefschrift beoogt deze ontbrekende kennis aan te vullen door middel van numerieke simulaties, waarbij de prestaties van geïsoleerde propellerconfiguraties in negatieve stuwkrachtmodus worden vergeleken met de bekende eigenschappen positieve stuwkrachtmodus.

Er is gekozen voor een numerieke aanpak omdat dit het mogelijk maakt de druk- en snelheidsvelden in het volledige domein weer te geven, inclusief gedetailleerde resultaten aan de bladoppervlakken. Er zijn high-fidelity simulaties (lattice-Boltzmann very large-eddy simulations) uitgevoerd voor een propeller van een vorige generatie turbo-prop vliegtuig in een geïsoleerde configuratie, waarbij meerdere invalshoeken zijn geanalyseerd. Vanwege de beschikbaarheid van experimentele referentiegegevens zijn de simulaties uitgevoerd bij relatief lage Reynolds- en Machgetallen in vergelijking met typische kruissnelheden van propellervliegtuigen. Gezien het belang van het tip-Machgetal als een kritieke vergelijkingsparameter voor aero-akoestiek, zijn enkele analyses ook uitgevoerd bij hogere tip-Machgetallen om een robuustere beoordeling van de aero-akoestische eigenschappen mogelijk te maken.

Het gebruik van een conventionele propeller in negatieve stuwkrachtmodus resulteert erin at de positief gebogen bladsecties bij negatieve invalshoeken werken, waardoor beginnend bij de bladuiteinde loslating plaatsvindt. Een gedetailleerde analyse van de geïsoleerde propeller bij een instroming met een invalshoek van 0° en een constant tip-Machgetal, toonde aan dat loslating van de stroming in negatieve stuwkrachtmodus leidde tot 2 tot 6 keer hogere fluctuaties in geïntegreerde stuwkracht vergeleken met positieve stuwkrachtmodus. Deze loslating veroorzaakt aanzienlijke fluctuaties in de bladbelasting in een breed frequentiespectrum, 18% voor de binnenste delen en 30% bij de bladtip, vergeleken met de gemiddelde belasting bij negatieve stuwkracht. Bij positieve stuwkracht zijn dergelijke fluctuaties daarentegen verwaarloosbaar. Bovendien resulteert de loslating bij negatieve stuwkracht in significant hogere niveaus van het geluid

in een breed frequentiespectrum, langs de as van de propeller ongeveer 15–20 dB hoger vergeleken met positieve stuwkrachtcondities. In het vlak van de propeller werden echter juist in het positieve stuwkrachtregime geluidsniveaus waargenomen die ongeveer 10 dB hoger waren dan in het negatieve stuwkrachtregime bij dezelfde absolute stuwkracht van $|T_C| = 0.08$. Deze lagere geluidsniveaus bij negatieve stuwkracht worden toegeschreven aan twee factoren: de lagere grootte van het negatieve koppel vergeleken met het positieve koppel bij dezelfde stuwkracht en de inwaartse radiale verschuiving van de bladbelasting bij negatieve stuwkracht als gevolg van de stall (overtrek) bij de bladtip. Deze bevindingen suggereren dat, in vergelijking met conventionele benaderingen, een steilere en stillere daling kan worden bereikt door gebruik te maken van negatieve stuwkracht, op voorwaarde dat het gegenereerde negatieve koppel gelijk is aan of minder is dan het koppel dat nodig is voor conventionele propellerwerking tijdens de landing (zonder rekening te houden met het effect van de instroomhoek op het propellergeluid).

Een instroomhoek ongelijk aan nul veroorzaakt een periodieke variatie in de geometrische invalshoek van de bladsecties langs de azimuth, wat leidt tot een dynamische stall (overtrek) van propellerbladsecties in negatieve stuwkrachtcondities, waarbij de stroming aan de oprukkende zijde het blad volgt en loslaat van het blad aan de terugtrekkende zijde. Dit resulteert in grotere fluctuaties in bladbelasting in een breed frequentiespectrum aan de terugtrekkende zijde. Nabij de bladtip ($r/R = 0.90$) wijken de periodieke schommelingen af van een sinusvorming patroon door de deep stall in deze bladsecties, waarbij schommelingen in de lokale stuwkrachtcoëfficiënt met een breed frequentiespectrum ($\pm 7\%$ van het gemiddelde stuwkrachtniveau) in grootte vergelijkbaar worden met de periodieke variaties (-10% tot $+7\%$ van het gemiddelde stuwkrachtniveau). De periodieke variaties in belasting over het azimuth bij een instroomhoek ongelijk aan nul leiden tot een significante verandering in de richtingsafhankelijkheid van het geluid vergeleken met een instroomhoek van 0° . Bij een positieve stuwkracht nemen de geluidsniveaus significant toe in gebieden tegenover de kantelhoek en nemen ze significant af in de richting van de kantelhoek. Omgekeerd, neemt bij een negatieve stuwkracht het geluid toe in de richting van de kantelhoek en neemt het af weg van de kantelhoek. Dit patroon is gunstig voor geluidsreductie in de gemeenschap, omdat de gemeenschap onder het vliegtuig ligt, weg van de kantelhoek.

Hoewel dit proefschrift zich richt op geïsoleerde propellerconfiguraties, kunnen inzichten worden afgeleid voor een potentiële vleugel gehuld in een propellerslipstroom door rekening te houden met de dynamische druk en wervelhoek binnen de slipstroom. Voor een propeller met negatieve stuwkracht en een invalshoek van 0° , wordt verwacht dat de slipstroom een grotere reductie in lift zal veroorzaken aan de opgaande bladzijde vergeleken met de neergaande bladzijde vanwege de richting van de werveling. Omgekeerd, zal bij positieve stuwkracht het botsen van de propellerslipstroom op de potentiële vleugel waarschijnlijk resulteren in een grotere liftoename aan de opgaande bladzijde dan aan de neergaande bladzijde. Bij een invalshoek groter of kleiner dan 0° (niet-nul), is de dynamische druk binnen de slipstroom hoger aan de neergaande bladzijde dan aan de opgaande bladzijde bij zowel positieve als negatieve stuwkracht. Dit effect van een niet-nul invalshoek werkt de liftverschillen tussen de opgaande en neergaande bladzijde tegen (ten opzichte van een invalshoek van 0°) bij positieve stuwkracht, terwijl de liftverschillen juist worden vergroot bij negatieve stuwkracht.

Hoewel simulaties met een hoog betrouwbaarheidsniveau een dieper inzicht geven in verschillende fysische verschijnselen, zijn ze niet altijd praktisch vanwege de aanzienlijke rekenkosten. Een systematisch vergelijk van meerdere numerieke methodes met experimentele data, toonde aan dat methodes met een lager betrouwbaarheidsniveau, zoals Blade Element Momentum (BEM) theorie en Lifting Line (LL) theorie, ook geschikt zijn voor het voorspellen van propellerprestaties en algemene trends. Dit onder voorwaarde dat de stroming aangesloten blijft, en dus bij positieve stuwkrachtcondities tot matige stuwkrachtniveaus. Hun toepasbaarheid in negatieve stuwkrachtmodus is beperkt vanwege het optreden van loslating. Wall-resolved ($y^+ < 1$) Reynolds-Averaged Navier Stokes (RANS)-simulaties (zowel tijdsafhankelijk als tijdsafhankelijk) daarentegen, presteerden goed onder zowel positieve als negatieve stuwkrachtcondities. Zowel stuwkracht, als vermogensgrootten in de buurt van het punt van maximaal geproduceerd vermogen in het negatieve stuwkrachtregime, kwamen overeen met afwijkingen van minder dan 2%. Lattice-Boltzmann simulaties met zeer grote wervelingen (LB-VLEs) met $y^+ \leq 10$ toonden een uitstekende overeenkomst met experimentele gegevens, met minder dan 1% afwijking in de buurt van het punt van maximaal geproduceerd vermogen, maar tegen aanzienlijke rekenkosten. LB-VLEs met $y^+ \geq 15$, in tegenstelling, konden de propellerprestaties ook redelijk voorspellen in gevallen zonder loslating, maar met rekenkosten vergelijkbaar met tijdsafhankelijke RANS. Het wandmodel dat in deze LB-VLEs simulaties wordt gebruikt introduceert echter fouten in de modellering van loslating, wat leidt tot een overschatting van de vermogensgrootte in de buurt van het punt van maximaal geproduceerd vermogen van 16%. Het voordeel van het gebruik van LB-VLEs met $y^+ \geq 15$ ligt in het beter behouden van wervelstructuren in de propeller slipstroom door lagere numerieke diffusie, en lagere rekenkosten per mesh-element dan RANS. Dit maakt LB-VLEs waardevol voor het bestuderen van propeller-vleugel interacties. Deze bevindingen benadrukken dat de keuze van de methode moet worden bepaald door de gewenste nauwkeurigheid en de beschikbare rekenkracht, waarbij de afweging moet worden gemaakt tussen gedetailleerde resolutie en totale kosten.

Het ontbreken van experimentele meetdata van bladbelastingsverdelingen bemoeilijkt vaak de vergelijking van verschillende numerieke methoden met experimentele metingen. Het nauwkeurig bepalen van bladbelastingsverdelingen in experimenten vormt doorgaans een uitdaging vanwege de beperkingen van conventionele meettechnieken. Een mogelijk alternatief is het “zog-geïnformeerde lifting line-model”, dat bladbelastingsverdelingen schat op basis van fasevergrendelde snelheidsmetingen in de slipstroom. De evaluatie van de effectiviteit van deze methode, met behulp van tijdsafhankelijke RANS-simulaties, toonde aan dat het model de radiale stuwkrachtverdeling redelijk goed voorspelt, met een overschatting van 2% van de piekwaarde onder aanliggende stromingscondities. In het geval van loslating weet het model de radiale gradiënten en de algemene vorm van de stuwkrachtverdeling te reproduceren, maar vertoont het afwijkingen in de absolute waarden. Het opnemen van profielweerstand door middel van externe polaire gegevens verbetert de voorspellingen, wat resulteert in een overschatting van 1.9% van de maximale stuwkracht en een lichte verschuiving naar buiten in de stuwkrachtverdeling ten opzichte van de tijdsafhankelijke RANS simulaties. Bij toepassing op experimentele fasevergrendelde slipstroombetingen vertoonde het model vergelijkbare prestaties als in de validatiecasus. Het zog-geïnformeerde LL-model

blijkt dus veelbelovend als hulpmiddel voor het verkrijgen van experimentele bladbelastingsverdelingen en het versterken van experimentele analyses.

De bevindingen van dit proefschrift tonen aan dat propellers die onder negatieve stuwkrachtcondities opereren, duidelijk andere aerodynamische en aero-akoestische eigenschappen vertonen dan bij positieve stuwkracht. Deze gewijzigde eigenschappen bieden een veelbelovende mogelijkheid om het omgevingsgeluid te verminderen – niet alleen dankzij de mogelijkheid tot steilere dalingen, maar ook door veranderingen in de geluidsemissie van de propeller zelf. Dit onderzoek legt de basis voor toekomstig onderzoek en ontwikkeling, en baant de weg voor een succesvolle integratie van negatieve stuwkracht in (hybride-)elektrische vliegtuigen. Daarmee levert het een bijdrage aan duurzamere en stillere luchtvaartoplossingen.

CONTENTS

Summary	vii
Samenvatting	xi
Nomenclature	xix
I Background and Methods	1
1 Introduction	3
1.1 Propeller Operation at Negative Thrust	4
1.1.1 Mechanism of Using Propellers for Aerodynamic Braking	5
1.1.2 State of the art	6
1.2 Objective of the Dissertation	8
1.3 Scope and Research Approach	9
1.4 Dissertation Outline	11
2 Numerical Methods and Setup	13
2.1 Propeller Geometry	14
2.2 Reference Experimental Setup	14
2.3 Numerical Methods Used in the Thesis	15
2.4 Description of Numerical Methods	16
2.4.1 Blade-element-momentum Theory	16
2.4.2 Lifting Line Theory.	17
2.4.3 Steady RANS Simulations	17
2.4.4 Unsteady RANS Simulations	19
2.4.5 Lattice-Boltzmann Very Large Eddy Simulations.	19
2.4.6 Hanson's Frequency Domain Model	22
2.5 Operating Conditions.	22
2.6 Comparison of Grid Specifications and Computational Costs.	22
3 Assessment and Validation of CFD Methods	25
3.1 Grid Convergence Study for SRANS Simulations	26
3.2 LB-VLESS _{$\gamma^+ \geq 15$} : Zero Angle of Attack	27
3.2.1 Convergence and Validation Study of Integral Performance Param- eters	28
3.2.2 Convergence and Validation Study of Slipstream Parameters	30
3.2.3 Convergence Study of Far-field Aeroacoustics	33
3.3 LB-VLESS _{$\gamma^+ \geq 15$} : Non-zero Angle of Attack.	36
3.3.1 Positive Thrust Condition ($J = 0.60$)	36
3.3.2 Negative Thrust Condition ($J = 1.10$)	37

II	Aerodynamic and Aeroacoustic Phenomena	39
4	Propeller Aerodynamics and Aeroacoustics at Zero Angle of Attack	41
4.1	Introduction	42
4.2	Aerodynamic Performance	42
4.2.1	Time-Averaged Performance Analysis	43
4.2.2	Unsteady Aerodynamic Performance Analysis	46
4.2.3	Slipstream	47
4.3	Far-field Acoustic Characteristics	50
4.3.1	Far-field Noise Directivity and Power Spectrum Density	51
4.3.2	Noise Source Map	52
4.3.3	Effect of Thrust Coefficient on OSPL	55
4.3.4	Main Inferences for Landing Using Negative Thrust Settings.	57
4.4	Key Findings	58
5	Propeller Aerodynamics and Aeroacoustics at Non-zero Angle of Attack	61
5.1	Physical Mechanisms and Reference Frames for Operation of a Propeller at a Non-zero Angle of Attack	62
5.1.1	Azimuthal Position.	62
5.1.2	Local Advance Ratio	62
5.1.3	In-Plane Force and Delayed Aerodynamic Response.	62
5.1.4	Freestream-Aligned Performance Parameters	63
5.2	Aerodynamic Results	63
5.2.1	Integrated Performance	64
5.2.2	Propeller Blade Loading	65
5.2.3	Flow around the Blade Sections	68
5.2.4	Broadband Fluctuations	70
5.2.5	Propeller Slipstream	73
5.3	Far-field Aeroacoustic Results.	77
5.3.1	Noise Directivity in the Plane of Propeller Rotation	78
5.3.2	Noise Directivity in the Plane along the Propeller Axis	83
5.4	Key Findings	87
III	Assessment of Aerodynamic Models	89
6	Benchmarking of Aerodynamic Models for Propellers	91
6.1	Overview of Operating Conditions	92
6.2	Time-Averaged Integrated Performance.	92
6.3	Flow Around the Propeller Blades.	96
6.3.1	Positive Thrust Condition ($J = 0.60$)	97
6.3.2	Negative Thrust Condition ($J = 1.10$)	100
6.4	Total Pressure Coefficient and Blade Loading	102
6.4.1	Positive Thrust Condition ($J = 0.60$)	103
6.4.2	Negative Thrust Conditions ($J = 1.10, 1.48$).	105
6.5	Phase-Locked Flowfield in the Propeller Slipstream.	107
6.5.1	Positive Thrust Condition ($J = 0.60$)	107
6.5.2	Negative Thrust Condition ($J = 1.10$)	108

6.6	Key Findings	109
6.6.1	BEM and LL Theories	109
6.6.2	RANS Simulations	110
6.6.3	LB-VLES Simulations	111
6.6.4	Choosing the Optimal Method	111
7	Propeller Blade Loading from Experimental Slipstream Data	113
7.1	Introduction	114
7.2	Lifting Line Models	115
7.2.1	Conventional Lifting Line Model	115
7.2.2	Wake-informed Lifting Line Model	115
7.2.3	Load-informed Lifting Line Model	117
7.3	Setup of the Wake-informed Lifting Line Model	117
7.3.1	Slipstream data	118
7.3.2	Identifying Shape and Location of Blade Wake and Tip Vortex	118
7.3.3	Setup of Helical Wake System	120
7.3.4	Setup of Control Points	122
7.3.5	Objective Function and Solution Algorithm	127
7.3.6	Post-processing	127
7.4	Validation of Wake-informed Lifting Line Model	128
7.4.1	Axial Induction.	128
7.4.2	Blade Loading Distributions	131
7.4.3	Integrated Thrust and Power.	134
7.5	Experimental Test Case	135
7.5.1	Axial Induction.	136
7.5.2	Integrated Thrust and Power.	138
7.5.3	Blade Loading Distributions	139
7.6	Key Findings	142
IV	Conclusion	143
8	Conclusions and Recommendations	145
8.1	Conclusions.	145
8.1.1	Aerodynamic and Aeroacoustic Characteristic Analysis	145
8.1.2	Aerodynamic Modelling	150
8.1.3	Blade Loading Distributions from Wake Measurements	152
8.2	Recommendations	154
V	Appendices	157
A	Importance of Rotational Effects for Aerodynamic Performance Predictions	159
A.1	Effect of Rotation on Sectional Characteristics	159
A.2	Effect of Rotation on Integrated Performance Predictions.	160
B	Influence of Spinner and Nacelle on Propeller Performance	163
B.1	Integrated Performance.	163
B.2	Blade Loading Distributions	165

C Validation of Momentum and Lifting Line Wake Modelling	167
C.1 Load-informed BEM and Lifting Line	167
C.2 Axial Induction based on 3D Biot-Savart's Law	168
C.3 Results	168
Bibliography	171
Acknowledgments	183
Curriculum Vitae	185
List of Publications	187

NOMENCLATURE

VARIABLES

α	=	angle of attack, °
$\beta_{0.7R}$	=	blade pitch angle at 70% of the radius, °
$\Delta\phi$	=	$\tan^{-1}\left(\frac{Y_C}{N_C}\right)$, phase delay, °
$\Delta J'$	=	$\frac{V_\infty \cos \alpha_\infty}{\left(n + \frac{V_\infty \sin \alpha_\infty \sin \phi}{2\pi r}\right) D} - J$, change in local advance ratio due to in-plane velocity component
δP	=	pressure jump over given annulus, N/m ²
δr	=	radial width of given annulus, m
Δt	=	time step, s
δT	=	thrust over given annulus, N
$\Delta\alpha_{gr}$	=	change in local geometric angle of attack due to in-plane velocity component at the blade section located at r
$\Delta\alpha_\infty$	=	relative change in performance parameter at non-zero α_∞ compared to $\alpha_\infty = 0^\circ$
ϵ	=	rate of dissipation of turbulent kinetic energy, m ² /s ³
η_p	=	$\frac{TV_\infty}{P}$, propeller efficiency
η_t	=	$\frac{P}{TV_\infty}$, turbine efficiency
η_{eh}	=	$-\frac{8P}{\pi\rho_\infty V_\infty^3 D^2}$, energy-harvesting efficiency
Γ	=	bound circulation, m ² /s
Γ^*	=	$\frac{\Gamma}{V_\infty D}$, non-dimensional bound circulation
Ω	=	$2\pi n$, rotational speed, rad/s
ϕ	=	azimuthal position, °

ρ	=	air density, kg/m ³
σ	=	standard deviation
τ_w	=	wall shear stress, Pa
θ	=	axial directivity angle, °
θ_{swirl}	=	$\tan^{-1} \left(\frac{V_t - V_\infty \sin \alpha_\infty \sin \phi}{V_x} \right)$, swirl angle, °
ϕ	=	inflow angle at a given blade section, °
ζ	=	chordwise coordinate, m
a_x	=	$\frac{V_x - V_\infty}{V_\infty}$, axial induction
B	=	number of propeller blades
c	=	section chord, m
c_o	=	speed of sound at freestream condition, m/s
C_n	=	$\int_0^1 C_{p_s} d\zeta / c$, normal-force coefficient
c_d	=	sectional drag coefficient
C_f	=	$\frac{\tau_w}{q_\infty}$, skin-friction coefficient
c_l	=	sectional lift coefficient
C_P	=	$\frac{P}{\rho_\infty n^3 D^5}$, propeller power coefficient
c_p	=	$\frac{P'}{\rho_\infty n^3 D^4}$, sectional power coefficient
C_T	=	$\frac{T}{\rho_\infty n^2 D^4}$, propeller thrust coefficient
c_t	=	$\frac{T'}{\rho_\infty n^2 D^3}$, sectional thrust coefficient
C_{p_s}, c_p	=	$\frac{p - p_\infty}{0.5 \rho_\infty ((V_\infty \cos \alpha_\infty)^2 + (\Omega r + V_\infty \sin \alpha_\infty \sin \phi)^2)}$, sectional pressure coefficient
C_{P_t}, C_{p_t}	=	$\frac{p_t - p_{t_\infty}}{q_\infty}$, total pressure coefficient
D	=	propeller diameter, m
D'	=	drag force per unit span, N/m

f	=	frequency, Hz
F_N	=	Force in the normal direction (Z-Axis), N
F_Y	=	Force in the side direction (Y-Axis), N
h_i	=	average cell size of grid i , m
J	=	$\frac{V_\infty}{nD}$, propeller advance ratio
k	=	turbulent kinetic energy, m^2/s^2
L	=	lift force, N
M	=	$\frac{V}{c_0}$, Mach number
M_{ht}	=	$\sqrt{M_\infty^2 + M_{tip}^2}$, helicoidal tip rotational Mach number
M_{rot}	=	$\frac{\Omega r}{c_0}$, local radial rotational Mach number
M_{tip}	=	$\frac{\Omega R}{c_0}$, tip rotational Mach number
n	=	propeller rotation speed, Hz
N	=	number of elements on a VR level
N_C	=	$\frac{F_N}{\rho_\infty V_\infty^2 D^2}$, normal force coefficient based on freestream dynamic pressure
P	=	propeller power, W
p	=	static pressure, Pa
P'_c	=	$\frac{P'}{\rho_\infty V_\infty^3 D}$, sectional power coefficient based on freestream dynamic pressure
p_{ref}	=	2×10^{-5} , reference sound pressure, Pa
p_t	=	total pressure, Pa
P_C	=	$\frac{P}{\rho_\infty V_\infty^3 D^2}$, propeller power coefficient based on freestream dynamic pressure
Q	=	torque, N·m
q	=	$p \left(1 + \frac{\gamma - 1}{2} M^2 \right)^{\frac{\gamma}{\gamma - 1}} - p$, dynamic pressure, Pa
R	=	propeller radius, m

r	=	radial coordinate, m
r_x	=	radius of the annulus at the axial distance x in the slipstream which emanated from the radial coordinate r at the propeller blade, m
Re_c	=	Reynolds number based on chord of the propeller blade
T	=	propeller thrust, N
t	=	section thickness, m
T'_c	=	$\frac{T'}{\rho_\infty V_\infty^2 D'}$, sectional thrust coefficient based on freestream dynamic pressure
t_{sim}	=	simulation time for instantaneous measurements, s
T_C	=	$\frac{T}{\rho_\infty V_\infty^2 D^2}$, propeller thrust coefficient based on freestream dynamic pressure
U_ϕ	=	estimated discretization uncertainty
V	=	velocity, m/s
x	=	axial coordinate, m
Y, Z	=	Axes in the plane of propeller rotation, m
y^+	=	dimensionless wall distance
Y_C	=	$\frac{F_Y}{\rho_\infty V_\infty^2 D^2}$, side force coefficient based on freestream dynamic pressure
$\vec{\omega}_t^*$	=	$\frac{\vec{\omega}_t D}{V_\infty}$, non-dimensional out-of-plane vorticity
$\vec{\omega}_t$	=	out-of-plane vorticity, 1/s

SUB- AND SUPERSCRIPTS

'	=	per unit span
∞	=	freestream
a	=	axial
eff	=	combination of axial and rotational components
t	=	tangential
D	=	drag force contribution
L	=	lift force contribution

$T < 0$	=	negative thrust condition
$T > 0$	=	positive thrust condition
x	=	along the axial direction
$y^+ \geq 15$	=	simulations with $y^+ \geq 15$
$y^+ \leq 10$	=	simulations with $y^+ \leq 10$
FWH	=	calculated by propagating the pressure-time signal to far-field using FWH analogy
HM	=	calculated using Hanson's model
mic	=	virtual microphone location
NR	=	without rotational effects

ABBREVIATIONS

2D	=	two-dimensional
3D	=	three-dimensional
AoA	=	angle of attack, °
BEM	=	blade element momentum
BPF	=	Bn , blade passing frequency, Hz
CAA	=	computational aeroacoustics
CFD	=	computational fluid dynamics
CPU	=	central processing unit
FWH	=	Ffowcs Williams–Hawkings
LB-VLEs	=	lattice-Boltzmann very large-eddy simulations
LL	=	lifting line
NACA	=	National Advisory Committee for Aeronautics
NASA	=	National Aeronautics and Space Administration
OSPL	=	overall sound pressure level, dB
PIV	=	particle image velocimetry
PSD	=	power spectrum density, dB/Hz

RMS	=	root mean square
RMSE	=	root mean square error
RPKs	=	revenue passenger kilometres, km
SAFs	=	sustainable aviation fuels
SPL	=	sound pressure level, dB
SRANS	=	steady Reynolds-averaged Navier-Stokes
URANS	=	unsteady Reynolds-averaged Navier-Stokes
VR	=	variable resolution
w/o	=	without

PART I

BACKGROUND AND METHODS

1

INTRODUCTION

The undeniable and concerning impacts of global warming are becoming increasingly evident. In 2023, the global mean temperature increased by $(1.40 \pm 0.12)^\circ\text{C}$ compared to the pre-industrial average of 1850–1900, making it the hottest year in 174 years of recorded history [1]. The rate of global mean sea level rise has more than doubled since the last decade of the 20th century, reaching an alarming high in 2023 [1].

Transportation is currently the second-largest contributor to global CO₂ emissions [2], with the aviation sector alone responsible for approximately 2.5% of the global CO₂ emissions in 2018 [3]. When non-CO₂ emissions such as contrail formation and NO_x emissions are included, aviation's contribution to global warming increases to an estimated 3.5% [4]. This impact is projected to grow significantly in the future as demand for air travel continues to outpace improvements in system efficiency [5, 6]. For instance, from 2013 to 2019, passenger air traffic increased at a rate four times faster than the improvements in aircraft fuel efficiency [7]. These trends highlight the urgent need for a comprehensive, multi-pronged strategy to achieve sustainable aviation, encompassing policy reforms, the promotion of greener travel alternatives, and strategic fleet planning [8].

Technological advancements are key to achieving sustainable aviation. Airbus forecasts that alternative energy sources, next-generation aircraft, and disruptive technologies will contribute to approximately 89% of the reduction in CO₂ emissions of aviation by 2050 [9]. Sustainable aviation fuels (SAFs), hydrogen, and batteries are some of the promising alternative energy sources [10, 11]. Regardless of the chosen energy source, electric motors are being explored to either assist combustion engines or fully replace them in future aircraft designs. Electric motors offer two significant advantages in improving system efficiency[12]. Firstly, they enhance powertrain efficiency by improving the transmission efficiency from energy sources to propulsive devices, with electric motors achieving efficiencies of around 90%, compared to the 30%–40% efficiency of conventional turbine engines. Secondly, the scalability of the electric motors expands the design space, enabling disruptive concepts such as boundary-layer ingestion, distributed propulsion, wing-tip mounted propellers, etc., which can significantly improve

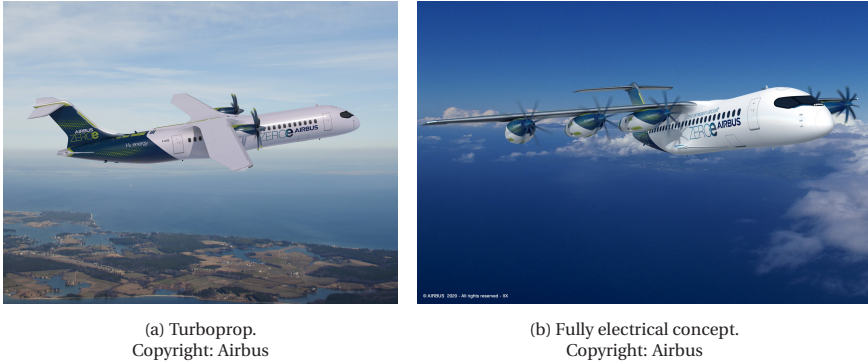


Figure 1.1: Airbus ZEROe concepts for short-haul flights¹ (1000 nmi)

the aero-propulsive efficiency of the aircraft [13–16].

While all-electric configurations with batteries are not yet feasible for short-haul flights (up to 1500 km) due to battery energy limitations [17], they can be a viable solution for ultra-short-range flights (up to 500 km) that account for 5% of commercial aviation emissions [7]. For longer ranges, hybrid-electric aircraft offer a promising alternative.

Propeller-driven aircraft remain an environment-friendly option for ranges up to 1500 km that account for 33% of commercial aviation emissions [7]. Studies by NASA showed that propellers can offer up to 18% lower fuel consumption compared to turbofans without significantly increasing travel time [18]. Recent research has also highlighted the benefits of flying at lower altitudes and slower speeds to significantly reduce aviation's climate impact, further supporting the case for propellers [19, 20]. Despite potential economic advantages due to lower fuel consumption, turboprops have a limited market share, less than 12% revenue passenger kilometres (RPKs), for flights under 1500 km [7]. Research suggests that higher operating costs, lower cruise speeds, and historically low fuel prices are the primary reasons and not passenger comfort, safety, noise, or vibration concerns, which are often mistakenly cited [21, 22]. Increasing fuel prices and the implementation of carbon taxes could incentivise airlines to reconsider turboprops, both for their environmental benefits and potential economic savings [21]. Moreover, the lower cruise speeds associated with turboprops are less problematic for flight ranges up to 1500 km, especially with advancements in turboprop design.

The introduction of hybrid-electric turboprop using hydrogen combustion and fuel cell-powered fully electric ZEROe concepts by Airbus¹ for 1852 km (1000 nmi) are examples where the combination of electric motors and propellers are planned to be used to reduce the carbon emissions of short-haul flights.

1.1. PROPELLER OPERATION AT NEGATIVE THRUST

The combination of electric motors and propellers in future aircraft designs presents an exciting opportunity to utilise propellers for braking during descent and landing phases.

¹<https://www.airbus.com/en/innovation/low-carbon-aviation/hydrogen/zeroe#concepts>

Compared to conventional braking devices, such as dive flaps, propellers can achieve significantly higher average deceleration [23, 24]. The increased drag from propellers enables steeper descents, allowing aircraft to cruise at higher altitudes for longer periods and thus reducing community noise exposure during the approach [25]. Additionally, propellers used as airbrakes can shorten the landing roll and potentially improve aircraft manoeuvrability during landing. Besides, electric motors have a possibility of reversibility, meaning they can be used as generators. When combined with propellers, this capability enables the propellers to act as airborne wind turbines during braking operations. The regenerated energy can be used to charge the batteries, reducing the time needed to charge them on the ground. Finally, reduced descent times contribute to faster turnaround times for aircraft, enhancing overall operational efficiency.

The following section delves deeper into the working principle of using propellers as braking devices. Following this, a summary of the existing literature is presented, highlighting the research gaps that need to be addressed to successfully integrate the braking function of propellers into future (hybrid-)electric aircraft.

1.1.1. MECHANISM OF USING PROPELLERS FOR AERODYNAMIC BRAKING

This section explains the operational principle of using propellers as airbrakes, illustrated through velocity triangles at a propeller blade section shown in Fig. 1.2. In a conventional propulsive condition, the effective velocity, which is a combination of freestream velocity and the rotational speed of the propeller, acts at an angle greater than the zero-lift angle of the blade section. This generates a positive lift force at the blade section, leading to positive thrust and torque, as depicted in Fig. 1.2a.

To utilise a propeller as an airbrake, lift must be generated in the opposite direction as compared to the conventional propulsive operation, resulting in negative thrust and negative torque (assuming the lift component in the torque direction exceeds that of the drag component). There are two methods to achieve negative lift. The first approach involves operating blade sections at an angle of attack lower than its zero-lift angle so that the direction of the lift is reversed, resulting in thrust and torque being inverted. This can be accomplished by either lowering the rotational speed of the propeller, or decreasing the pitch angle of the blades, or a combination of both. Figure 1.2b illustrates this approach with a lowered pitch angle while maintaining constant rotational speed. In this approach, the positively cambered airfoils operate at negative angles of attack, resulting in flow separation around the blades. The flow separation increases sectional drag, which in turn reduces the amount of power regenerated (P) and consequently decreases the energy-harvesting efficiency (η_{eh}) defined as:

$$\eta_{eh} = \frac{-8P}{\rho_{\infty} D^2 V_{\infty}^3} \quad (1.1)$$

The second approach involves pitching the blades beyond 90° , essentially flipping them so the camber of the blade section is downstream and rotating the propeller blades in the opposite direction, as illustrated in Fig. 1.2c. While this approach creates a blade camber favourable for energy harvesting, it also results in an undesired reverse twist along the blade span. Consequently, the outboard part of the blade generates negative thrust, while the inboard part produces positive thrust.

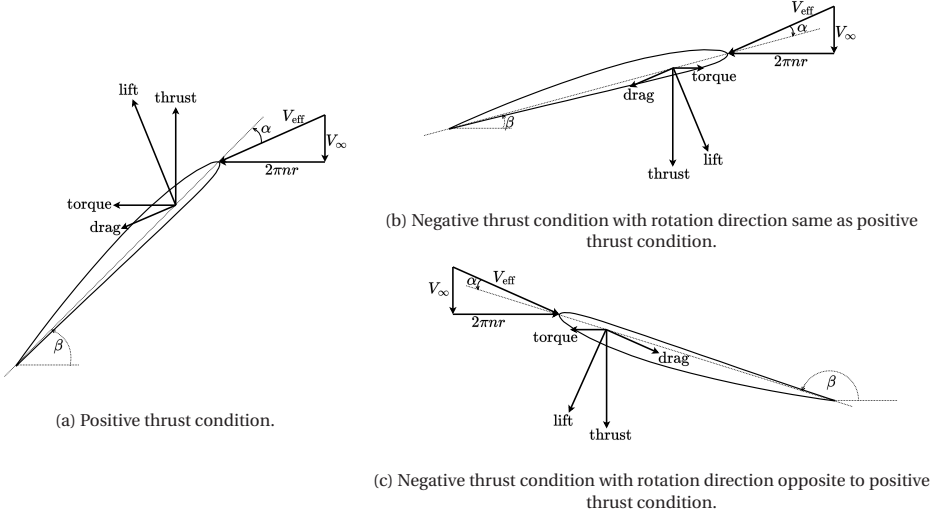


Figure 1.2: Velocity triangles at propeller blade section for different operational modes (ignoring inductions).

Both approaches for aerodynamic braking using propellers have their limitations. While the second approach offers a more favourable airfoil camber, it requires a complex manoeuvre (flipping and rotating propeller blades in the opposite direction), which is considered impractical for real-world applications. Therefore, this dissertation focuses solely on the first approach.

1.1.2. STATE OF THE ART

The effectiveness of the propellers as aerodynamic brakes was first investigated by NACA in 1933 and 1944 [23, 24]. Experimental studies at the time demonstrated that propellers could achieve significantly higher average deceleration and lower terminal velocities compared to conventional dive flaps, making them effective aerodynamic brakes. The ability of the propellers to produce high negative thrust even at low airspeeds makes them particularly good for reducing the landing run. Despite these findings, the concept did not gain widespread attention for many years.

The interest in the negative thrust operation of propellers emerged in 1998 as a way to harvest energy during atmospheric updrafts, which could be used to extend the flight time of the gliders [26]. A subsequent study by Barnes derived an expression for the aerodynamic design and performance of the glider using symmetrical airfoils for regeneration [27]. In another study, he also provided insight into the required electrical architecture in addition to aerodynamics [28]. A theoretical analysis was carried out in 2012 to evaluate the performance of gliders using regenerative capabilities of propeller operation at negative thrust while accounting for the weight of the added systems. It was concluded that a standard class glider could be used for cross-country flight training using energy harvesting to extend the flight range [29]. Despite these promising results, the applicability of these findings to commercial aviation is limited due to the significant

differences in aircraft weight, operational altitudes, and mission profiles.

The use of propeller operation at negative thrust for energy regeneration has been applied successfully to marine propellers [30]. In this project, a highly efficient hybrid-electric propulsion system was designed and installed on a whale-watching boat, resulting in a regeneration of 4–5 kW when sailing at 5 kn. Pipistrel, a general aviation manufacturer, has also proven the potential of using unducted propellers at negative thrust for energy regeneration in their electric trainer aircraft, achieving 19% energy savings through propeller design optimisation [31]. The Japanese project FEATHER further demonstrated the feasibility of using negative thrust produced by propellers for control of descent rate without conventional airbrakes [32].

Besides, the negative thrust mode for energy regeneration has been studied in detail for turbofans using analytical, numerical, and experimental methods [33–37]. Courty-Audren et al. analysed the negative thrust mode for an axial fan numerically and experimentally for direct and reverse flow (with opposite rotation) directions. The reverse flow direction was found to have more potential due to the reduced relative Mach number than the direct mode [33]. Garcia Rosa et al. showed that a high-bypass turbofan operating in negative thrust mode leads to the outer 60% part of the blade extracting energy from the flow and creating pressure loss, whereas the internal 40% part of the blade adds work to the flow. Overall, this results in a net extraction of work from the airflow [35]. Despite the detailed research on the operation of turbofans in turbine mode, the results are not directly applicable to propellers. The presence of the duct modifies the blade tip effects along with the distortion of the inflow due to viscous effects. The presence of the stator further influences the rotor performance. During the negative thrust operation, the stator vanes experience large negative angles of attack, leading to stall [34]. This affects the overall mass flow rate through the engine and has an adverse effect on the system performance. These effects are not relevant for unducted single-blade-row propellers.

For a typical aircraft configuration, the propeller design is expected to be dominated by the propulsive phases, i.e., climb and cruise, rather than the descent phase. Therefore, operation in the negative thrust mode will represent an off-design condition. Different investigations of conventional propellers in the negative thrust regime have reported an energy-harvesting efficiency of about 10% without any optimisation for this mode [38, 39]. These low efficiencies result from the contrasting nature of positive and negative thrust operations, with conventional propellers optimised for positive thrust having positively cambered blade sections that are prone to flow separation at negative thrust conditions [39].

Using propellers as aerodynamic brakes in configurations where the performance of the airframe heavily depends on the characteristics of the propeller slipstream may reduce overall system efficiency. This is because the slipstream generated by a propeller operating in negative thrust mode is expected to differ markedly from the well-understood propulsive slipstream, particularly in terms of velocity gradients, pressure gradients, and vorticity. In tractor configurations, while increased dynamic pressure and swirl in the propeller slipstream improve aerodynamic performance in propulsive mode [40, 41], reduced dynamic pressure and reversed swirl in negative thrust conditions can lead to a loss of lift on the wing, thereby adversely affecting the system performance [39].

This underscores the need for further research to comprehend the specific characteristics of blade loading, slipstream behaviour, and the interactions between the propeller and the airframe under negative thrust conditions.

Besides no research (to the best of the author's knowledge) has studied the noise sources of unducted propellers operating at negative thrust. While a recent study [25] numerically investigated the effect of windmilling rotors on community noise, it did not focus on noise generation at the source. Understanding noise generation at the source is crucial, especially since negative thrust operations are likely to occur close to the ground without acoustic linings around the propellers. Propellers operating in stall or near-stall conditions at negative thrust could exhibit changes in noise directivity and levels compared to their propulsive operation characteristics. Furthermore, flow separation on the blades in negative thrust conditions may lead to increased broadband noise and potentially induce structural vibrations, which could contribute to additional structure-borne noise.

1.2. OBJECTIVE OF THE DISSERTATION

The extensive literature available on propellers is primarily focused on the conventional propulsive mode [40–45]. In contrast, research on the operation of unducted propellers in the negative thrust mode is almost non-existent. The limited literature that is available for the latter is mainly focused on aerodynamics and based on assumptions that are not representative of commercial aviation. Besides, the aeroacoustics of such an operation has, to the author's best knowledge, never been studied. A detailed understanding of the aerodynamics and aeroacoustic characteristics of the propellers in the negative thrust mode is crucial for their successful implementation in future (hybrid-)electric aircraft. This understanding will allow aircraft designers to maximise the potential benefits of negative thrust mode while making informed decisions on design trade-offs, ultimately leading to the development of quieter and more energy-efficient (hybrid-)electric aircraft. The objective of this thesis is to provide this crucial missing information, as summarised in the central research question:

How do the aerodynamic and aeroacoustic characteristics of an unducted propeller change when operated in negative thrust mode compared to conventional propulsive mode?

To answer the research question, investigations have been carried out analysing both positive and negative thrust modes to explain and quantify the differences in blade loading, slipstream characteristics, and far-field noise emissions, focusing on the following sub-questions:

- RQ1. What physical mechanisms drive the low regenerative efficiency observed for conventional propellers operating in the negative thrust mode, and how do these mechanisms influence the resulting blade loading, slipstream, and far-field noise characteristics when compared to the conventional positive thrust mode?
- RQ2. How do the key physical phenomena that drive the aerodynamic and aeroacoustic performance of a propeller in positive and negative thrust mode change when

operating at non-zero angles of attack?

Having understood the mechanisms driving the aerodynamic and aeroacoustic performance of the propellers in positive and negative thrust conditions, the suitability of different numerical tools to model these mechanisms was investigated based on the following sub-questions:

RQ3. How do various numerical models compare against experimental data in their ability to predict the aerodynamic performance of propellers in both positive and negative thrust conditions?

The comparison of different numerical methods against experimental data was hindered by the absence of the blade loading distributions from the experiments. To address this gap, the following subquestion was investigated:

RQ4. How accurately can the blade loading distributions be extracted a posteriori from wake measurements using potential flow methods in both positive and negative thrust conditions?

1.3. SCOPE AND RESEARCH APPROACH

This thesis focuses on understanding the fundamental physical phenomena that govern the aerodynamic and aeroacoustic performance of propellers operating under negative thrust conditions while comparing these with well-established propulsive conditions. To this end, the thesis utilises a scaled-down model of a previous-generation turboprop aircraft propeller with unswept blades, conducting multi-fidelity numerical simulations focused solely on isolated propeller configurations. The selection of this specific propeller is based on the availability of experimental validation data to ensure the reliability of simulation results.

The choice of numerical simulations as the primary research tool in this thesis is motivated by several key factors. Firstly, the computational approach provides detailed pressure and velocity fields across the entire domain, including blade surfaces. This allows for a comprehensive analysis of the underlying physical phenomena, which might be challenging in experimental setups that are typically optimised to capture specific, anticipated effects. Secondly, simulations enable straightforward bookkeeping of contributions from different components, facilitating a better understanding of different physical phenomena. Additionally, acquiring reliable aeroacoustic data from wind tunnel tests is often hindered by challenges such as the need for expensive equipment (microphones and other acquisition hardware), background noise, and reflections from the walls and support structures. Numerical simulations circumvent these challenges and enable precise control over physical parameters, ensuring accurate matching of desired variables, such as the absolute thrust coefficient, thereby enabling fair comparisons. However, accurately modelling complex flow physics, such as flow separation, remains a challenge in numerical simulations, potentially limiting the insights derived from these methods. To mitigate these limitations, the numerical setups employed in this thesis have been extensively validated against experimental data.

The available experimental data for validation was limited to model-scale tests conducted in low-speed, unpressurised wind tunnels [46]. Consequently, the simulated Mach and Reynolds numbers were also relatively low compared to real-world flight conditions. Hence, the data obtained from the simulations have been affected by the presence of laminar separation bubbles, a thicker boundary layer, and the absence of compressibility effects as compared to full-scale conditions [47, 48]. This might lead to an overestimation of flow separation in the negative thrust mode when compared to real flight conditions where the Reynolds number is typically an order of magnitude higher. Nevertheless, flow separation is still expected in real-scale flights due to the operation of positively cambered airfoils at negative angles of attack. Therefore, the primary physical phenomena affecting aerodynamic propeller performance in negative thrust conditions are expected to be consistent between scaled model simulations and real-flight scenarios.

The freestream Mach number considered in the available experimental data was also considerably low ($M_\infty < 0.12$), with the helicoidal tip Mach number below 0.60. This is deemed acceptable, as the negative thrust conditions are expected to be relevant in the approach phase of the flight, for which the freestream Mach number is relatively low. Consequently, the analyses focused exclusively on subsonic conditions without considering the transonic or supersonic effects that might occur in the propeller blade-tip region, such as shock wave formation and other associated phenomena. Given that the tonal and broadband noise do not scale equally with the helicoidal tip Mach number of the propeller, some of the analyses were performed at relatively higher freestream Mach number ($M_\infty = 0.29$) with a corresponding higher helicoidal tip Mach number ($M_\infty = 0.74$). This scenario was selected to better represent the approach phase of flight, where negative thrust operations are expected to be relevant. This study only considered the noise generated by the blade loading (dipole) and blade thickness (monopole) sources. Contributions from propeller wake and other non-linear noise mechanisms (quadrupole sources), which can become significant under transonic and supersonic conditions, were not considered.

The propeller used in this study was a conventional propeller and, therefore, not specifically optimised for negative thrust operation. Typically, the propeller design is dominated by cruise phase requirements to minimise energy consumption, as the descent phase generally represents a small portion of the overall mission profile. Hence, the analyses presented in this thesis using a conventional propeller design are expected to be equally relevant for cases where the propeller is specifically optimised to minimise energy consumption while also considering negative thrust operation during descent. Additionally, the propeller used in this thesis has unswept blades, which is not representative of modern propeller designs. Despite this, the physical mechanisms affecting the performance in positive and negative thrust are expected to be similar for both unswept and swept blades. Therefore, the insights gained here can be applied to the analysis and design of swept propellers as well.

All analyses presented in this thesis have been conducted using isolated propeller configurations. This approach was chosen to focus on the changes in propeller aerodynamics and acoustics between positive and negative thrust modes at the blade level without the influence of the wing or other airframe components. However, for real-life

applications, the study needs to be extended further to installed configurations. This work is intended to serve as the foundation for such efforts in the future.

1.4. DISSERTATION OUTLINE

This dissertation is organised into four main parts, as illustrated schematically in Fig. 1.3. **Part I** lays the groundwork for the research. Following the introduction presented in this chapter, Chapter 2 details the various numerical methods employed in the study, including a description of the chosen propeller geometry and the operating conditions used for the analyses. Chapter 3 provides the grid dependence study and comparison against experimental data for computational fluid dynamics (CFD) simulations.

Part II focuses on analysing aerodynamic and aeroacoustic characteristics of conventional propellers operating in both positive and negative thrust conditions. This section leverages high-fidelity simulations to gain a comprehensive understanding of these characteristics. Chapter 4 investigates the changes in blade loading, slipstream characteristics, and far-field noise emissions between positive and negative thrust conditions at a zero-degree angle of attack and, therefore, addresses the first sub-question outlined earlier. Chapter 5 builds upon the findings of Chapter 4 and expands the analysis to non-zero angles of attack, addressing the second sub-question.

Having established an understanding of the key mechanisms influencing propeller performance in negative thrust conditions, **Part III** explores the capabilities of different tools for modelling these aerodynamic phenomena. Chapter 6 presents a comparative analysis of the capabilities of various numerical tools, ranging from low-fidelity methods like blade-element-momentum (BEM) theory to high-fidelity lattice-Boltzmann very large eddy simulations (LB-VLEs) to predict the aerodynamic performance of the propellers. The models are compared against the available experimental data for both positive and negative thrust conditions, addressing the third sub-question.

One significant challenge encountered when comparing numerical data with experimental data is the unavailability of the blade loading from experiments. To address this challenge, a method based on potential flow theory has been assessed. This method enables the estimation of blade loading from wake measurements. Chapter 7 details and validates this method, further evaluating its performance in both positive and negative thrust conditions.

Finally, **Part IV** presents the conclusions of the research (Chapter 8). Apart from the summary of the key observations drawn from the work in this dissertation, recommendations for future work are also given.

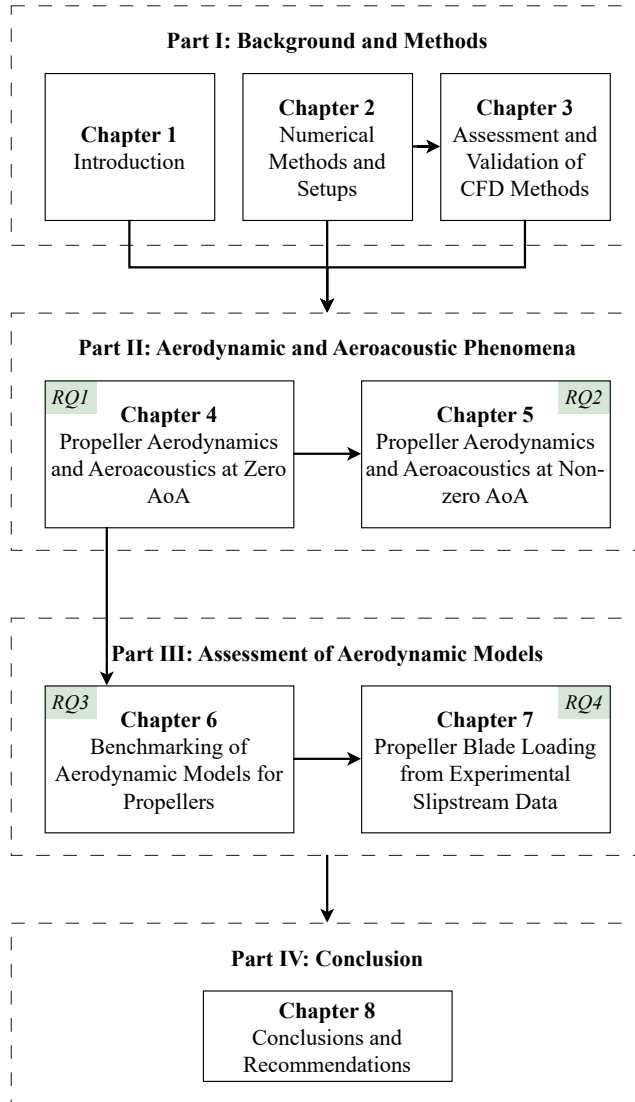


Figure 1.3: Dissertation Outline

2

NUMERICAL METHODS AND SETUP

Chapter 1 outlined the societal and scientific context of this thesis, from which the research objectives were derived. A variety of multi-fidelity numerical methods have been used to achieve these objectives. This chapter delves into the specifics of these methods, detailing their computational setups and the experimental data used for the validation. The chapter begins with a description of the reference propeller geometry in Section 2.1, followed by a brief description of the reference experimental setup in Section 2.2. Subsequently, Section 2.3 presents an overview of the different numerical tools and their linkage to meet various research objectives. Then, the numerical methods and their computational setups are described one by one in Section 2.4, after which Section 2.5 lists the operating conditions used for the grid dependence studies and extensive validation against experimental data. Finally, Section 2.6 offers a comparison of the computational costs associated with the different numerical methods.

The contents of this chapter have been adapted from Refs. [49], [50], and [51].

2.1. PROPELLER GEOMETRY

The propeller used in this entire thesis is the TUD-XPROP, a scaled version of a propeller for a previous-generation regional turboprop aircraft. The propeller has a diameter of 0.4064 m and a hub diameter of 0.092 m. The nacelle of the propeller extended up to approximately $1.6D$ downstream. Originally, the propeller had six blades; however, only three blades were used in the reference experiment due to limitations of the power dissipation system when operating at negative thrust [46]. Therefore, only the three-bladed variant of the propeller has been used in this thesis. The propeller can be seen in Fig. 2.1a along with its geometry parameters in Fig. 2.1b.

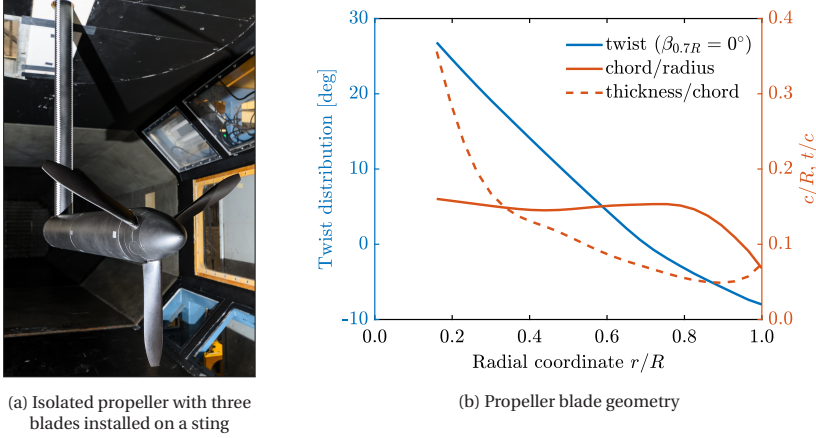


Figure 2.1: Propeller setup in the wind tunnel and geometry

2.2. REFERENCE EXPERIMENTAL SETUP

The numerical methods used in this thesis have been validated against experimental data from Nederlof et al. [46]. For this purpose, comparisons are made with experimental load cell data, 5-hole pressure probe data, and phase-locked particle image velocimetry (PIV) data at a pitch setting of 15° at $0.7R$ ($\beta_{0.7R} = 15^\circ$). The experiments were conducted at a freestream Mach number of 0.09, with the helicoidal tip Mach number ranging from 0.21 to 0.51. The Mach numbers at the propeller blades are considered representative of subsonic conditions. As the TUD-XPROP is a scaled-down model, the Reynolds number, based on the chord of the blade sections in experiments, is an order of magnitude lower than in full-scale flights. Operating the propeller at these lower Reynolds numbers in the experiments led to an increased susceptibility to flow separation and the presence of separation bubbles on the propeller blades. Consequently, matching numerical results with experimental data at these lower Reynolds numbers is more challenging than for full-scale flight conditions.

The uncorrected experimental data from Nederlof et al. [46] were corrected for wind-tunnel boundary interference. Three different corrections were applied to correct the freestream velocity based on Barlow et al. [52]: 1) solid blockage due to the nacelle, 2) solid and wake blockage due to the support structure, and 3) propeller slipstream block-

age. For the 0° AoA case, response models for C_T and C_P as a function of the J were determined using polynomial fits based on corrected data. The initial polynomial orders were determined by minimising the root mean square errors (RMSE). Subsequently, terms with a greater than 5% probability of having a non-zero coefficient due to random error were removed to obtain a reduced-order response model [53]. The uncertainties of the response models were based on the 95% confidence interval. This approach resulted in a 4th-order polynomial fit for C_T vs J and a 3rd-order polynomial fit for C_P vs J . The results for other parameters (η_p , η_t and η_{eh}) were calculated from the results obtained from the response models for C_T and C_P .

Similarly, for non-zero AoA cases, symmetric polynomial fits centred around the 0° AoA were employed to develop reduced-order response models for thrust, power, side force, and normal force coefficients (T_C , P_C , Y_C , and N_C , respectively). These models are based on corrected experimental data and express the coefficients as functions of AoA. This fitting process utilised data relative to the 0° AoA results, ensuring consistency between the zero and non-zero AoA reduced-order models at 0° AoA.

2.3. NUMERICAL METHODS USED IN THE THESIS

In this thesis, various methods ranging from low-fidelity to high-fidelity were used to address the main research question and its associated subquestions previously described in Section 1.2. The numerical methods used are shown in Fig. 2.2, and their application to the various subquestions is summarised in Table 2.1.

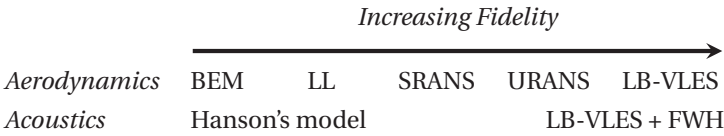


Figure 2.2: Numerical methods used for simulating the aerodynamic and acoustic performance of the propeller

Table 2.1: Overview of the numerical methods used for different research objectives

Method	RQ1 (Chapter 4)	RQ2 (Chapter 5)	RQ3 (Chapter 6)	RQ4 (Chapter 7)
BEM			✓	
LL			✓	✓
SRANS			✓	✓
URANS			✓	
LB-VLES _{$y^+ \geq 15$}	✓	✓	✓	
LB-VLES _{$y^+ \leq 10$}			✓	
Hanson's model	✓			

To address sub-questions RQ1 and RQ2, which explored the physical mechanisms influencing the aerodynamic and aeroacoustic performance of propellers under positive and negative thrust conditions at zero and non-zero AoA, LB-VLES $_{y^+ \geq 15}$ combined with the Ffowcs Williams and Hawkins (FWH) analogy were utilised. The corresponding analyses are detailed in Chapters 4 and 5 respectively. The choice of these simulations was driven by the limitations of RANS simulations, which fully rely on turbulence modelling and are, therefore, not suitable for capturing broadband noise sources. On the other hand, LB-VLES $_{y^+ \leq 10}$ would offer higher accuracy, however their excessive computational cost (discussed in Section 2.6, Tables 2.3 and 2.4) limited their extensive use. Consequently, LB-VLES $_{y^+ \geq 15}$ simulations were adopted as a compromise between accuracy and computational cost [49]. Although the FWH analogy allows for the separation of thickness and loading noise based on monopole and dipole terms, it does not enable further decomposition of loading noise into contributions from torque and thrust. To overcome this constraint, Hanson's model [54] was employed in combination with LB-VLES $_{y^+ \geq 15}$, facilitating a more detailed analysis of tonal noise sources (Chapter 4).

To answer sub-question RQ3, a comparative assessment of the capabilities of BEM, LL, SRANS, URANS, LB-VLES $_{y^+ \geq 15}$ and LB-VLES $_{y^+ \leq 10}$ in modelling the aerodynamic performance of the propeller was carried out. The corresponding findings are presented in Chapter 6. Lastly, the LL model used in Chapter 6 forms the basis of the “wake-informed LL” model described in Chapter 7. This modified LL model utilises phase-locked slipstream velocity data to estimate blade loading distributions and addresses sub-question RQ4.

2.4. DESCRIPTION OF NUMERICAL METHODS

This section provides a brief description of the various numerical methods employed in this thesis, including their computational setups. The section begins with an overview of the aerodynamic models, progressing from low-fidelity to high-fidelity models and concludes with a description of Hanson's frequency domain model, which is used for analysing tonal noise sources.

2.4.1. BLADE-ELEMENT-MOMENTUM THEORY

A classic blade-element-momentum (BEM) model was implemented based on Rwigema [55] and Burton et al. [56]. The blade section properties (lift and drag polar data) were calculated using RFOIL [57], which is a modification of the well-known 2D-panel method XFOIL [58]. RFOIL was selected for its ability to account for the influence of Coriolis and centrifugal forces on the boundary-layer characteristics of rotating airfoils through a quasi-3D model [59, 60], refer to Appendix A for more details. Moreover, RFOIL can predict lift and drag coefficients better in the post-stall region compared to XFOIL [61]. The source code¹ of the BEM model used in this thesis can be found on the 4TU.ResearchData repository [62].

The BEM calculations used 50 radial stations with cosine distribution along the blade span to achieve higher resolution in the root and tip regions of the blade, where the gradients in loading are highest. To account for compressibility and Reynolds number ef-

¹The code was not optimised for speed.

fects, polar data were collected at different Mach and Reynolds numbers at 24 radial stations using RFOIL. Subsequently, the data were interpolated to local Mach and Reynolds numbers based on the local effective velocity and chord of the airfoil sections along the blade span. This interpolation occurred in two steps. Firstly, the polar data were interpolated using Delaunay triangulation of the sample points. In this step, the polar data were obtained for the given radial location at a given angle of attack, and the local Reynolds number for all the input Mach numbers. In the subsequent step, the acquired polar data were linearly interpolated to obtain the values at the specified local effective Mach number. To account for hub and tip loss, Prandtl tip correction [63] was implemented. Additionally, Glauert's correction [56] was implemented for highly loaded propellers in the negative thrust regime; however, this correction never became active for the operating conditions considered in this thesis.

2.4.2. LIFTING LINE THEORY

This research used the semi-free-wake lifting-line (LL) theory as described by Katz and Plotkin [64]. Although a free-wake lifting-line theory would provide higher accuracy, its substantial computational resource requirements generally make it impractical for low-fidelity analysis. The same polar data and interpolation scheme were used for the lifting line as for BEM theory in the preceding section. Also, the compressibility and Reynolds number effects were taken into account in the same manner as in the BEM theory.

The LL calculations were performed using 50 radial stations uniformly distributed along the blade span (unlike BEM theory) to avoid numerical instability caused by small elements at the root and tip. The pitch of the wake was defined based on the solution as per the so-called 'semi-free' wake approach [65]. An initial helical wake was defined with an arbitrary pitch based on the initial guess of the average axial induction (a_x) at the rotor. Based on this wake, the converged circulation distribution (change in circulation $\leq 10^{-6}$ per section) and induction were calculated at the propeller blades. The pitch of the helical wake was redefined based on this converged average axial induction at the rotor until the change in the newly calculated average axial induction was within the tolerance level (10^{-3}).

To account for the contraction of the helical wake, Eq. (2.1) derived by Veldhuis [40] was used. Though this wake model does not account for vortex roll-up, it does account for the influence of the axial velocity increment and contraction within the slipstream.

$$\frac{r_x}{r} = \sqrt{\frac{1 + a_x}{1 + a_x \left(1 + \frac{x}{\sqrt{r^2 + x^2}}\right)}} \quad (2.1)$$

where r_x is the contracted radius of the annulus at an axial distance of x downstream of the propeller, r is the radius of the annulus at the propeller disk, and a is the average axial induction of the given annulus at the rotor disk.

2.4.3. STEADY RANS SIMULATIONS

The RANS equations for compressible flow were solved using ANSYS®Fluent 2019 R3 [66], which is a commercial, unstructured, finite-volume, cell-centred solver. The simulations were solved for a single-blade wedge domain in a steady manner using a multi-

Following the CFD setup of previous research efforts for similar problems [39, 67, 68], total-pressure inlet, pressure outlet, and pressure far-field boundary conditions were used in combination with a conformal periodic boundary condition for the side boundaries to avoid interpolation errors. The propeller blade and spinner were modeled as no-slip stationary walls in the moving reference frame, and the nacelle was modeled as a no-slip stationary wall in the absolute reference frame. The air density was calculated using the ideal gas assumption, and the dynamic viscosity was computed using Sutherland’s law. The turbulence modelling was based on the Spalart-Allmaras method with a modification proposed by Dacles-Mariani et al. [69, 70]



18

ments. The first-layer thickness of inflation layers was tuned to keep the $y^+ \leq 1$ as per the requirement of the Spalart-Allmaras turbulence model. The grid density in the whole domain was controlled by wall refinement of no-slip walls and volume refinement of the domains. The grid density was kept similar over the propeller blade and nacelle, i.e., the zoomed part of the domain shown in the bottom part of the Fig. 2.3. Upstream and downstream of the blade and nacelle, the grid density was reduced to optimise the computational cost.

2.4.4. UNSTEADY RANS SIMULATIONS

Assuming the unsteady RANS (uRANS) solution will behave in a similar way as the SRANS solution, the grid used for SRANS simulations was copied and rotated to generate the remaining two blades of the propeller geometry, resulting in a cylindrical domain. The sliding mesh approach was used to solve the URANS equations with a time step equivalent to a 2° rotation for all the advance ratios. The time step was chosen based on the recommendation by Stokkermans et al. [67] The second-order backward Euler scheme was used with the implicit formulation for the time-stepping. The URANS simulation was initialised with the converged solution from the SRANS solution of the cylindrical domain. The simulation was run for two rotations, from which the last rotation was used for the analysis. It was ensured that the results from the last rotation were converged by monitoring the integrated forces and checking the variation in blade loading over the rotation.

2.4.5. LATTICE-BOLTZMANN VERY LARGE EDDY SIMULATIONS

The LB-VLESs represent the highest-fidelity numerical approach employed in this thesis. For a comprehensive understanding of the lattice-Boltzmann method (LBM), readers can refer to the detailed descriptions available in Succi [71] and Shan et al. [72] The LB-VLES equations were solved using SIMULIA@PowerFLOW 6-2021-R6, a commercially available solver. The LB-VLES solver implemented in PowerFLOW uses a wall model approach. As per Romani et al. [73], in order to well predict boundary layer separation and start resolving turbulence features, near-wall grid refinement is needed with $y^+ \leq 10$.

Unlike traditional RANS simulations, where stretched cells can be used to achieve low y^+ values, the LB-VLES solver implemented in PowerFLOW requires an octree mesh with cells having a strict aspect ratio of 1 and a Courant number of 1. These requirements result in a significant computational cost increase when attempting to reach $y^+ \leq 10$ over the propeller blade surface. This cost increase is attributed to the need for both an increase in mesh size (number of cells) and a decrease in the time step with the decrease in y^+ at the blade surface. Consequently, though LB-VLESs with $y^+ \leq 10$ can be instrumental in obtaining the detailed flow features around the propeller blades and understanding the propeller aerodynamics and aeroacoustics (especially in the presence of flow separation), this great detail comes at an equally great computational cost.

Therefore, most practical studies use $y^+ \geq 15$ to reduce the computational cost. However, it is essential to remember that higher y^+ values can delay the transition to resolved turbulence, potentially leading to inaccuracies in predicting features like flow separation and reattachment. Considering these advantages and drawbacks, this thesis employed

two types of LB-VLESs:

1. $LB-VLESs_{y^+ \geq 15}$: These LB-VLESs were run with $y^+ \geq 15$. Each simulation ran for ten propeller revolutions, with the final eight used for analysis. Although only four revolutions were required to obtain the aerodynamic solution, with the first two revolutions being the transient and the next two used for analysis, the simulation duration was extended to ten revolutions due to the interest in aeroacoustics. Convergence was assessed by monitoring the moving mean of the integrated forces over a revolution and ensuring that its variation remained below 1%.
2. $LB-VLESs_{y^+ \leq 10}$: These LB-VLESs were run with $y^+ \leq 10$. These simulations were initialised using the solution of $LB-VLESs_{y^+ \geq 15}$. The $LB-VLESs_{y^+ \leq 10}$ were run in total for four propeller rotations, out of which the last three were used for the analysis. Although only two revolutions were necessary to achieve a converged aerodynamic solution, comprising one transient and one revolution for the analysis, the simulation was extended to four revolutions due to the interest in aeroacoustics.

SOLVER DESCRIPTION AND NUMERICAL SETUP

The computational domain was a cube with a domain size of $128D$; see Fig. 2.4a. Such a large domain size was motivated by the interest in aeroacoustics, specifically to minimise acoustic reflections from the domain boundaries. The computational domain was discretized using a Cartesian mesh, employing 19 discrete velocities in three dimensions (D3Q19), including a third-order truncation of the Chapman-Enskog expansion. An explicit time integration approach was applied to solve the equations with a Courant number of 1 to maintain numerical stability. The particle distribution within the domain was determined using a collision term based on a unique Galilean invariant [74], and the equilibrium distribution followed the Maxwell-Boltzmann distribution [75]. PowerFLOW utilises a very-large eddy simulation (VLES) model to account for the effects of subgrid unresolved turbulence scales. This model relies on the $k-\epsilon$ renormalisation equations [76] to predict the turbulent relaxation time, a crucial parameter in turbulence modelling.

The boundaries of the domain were specified as a velocity inlet, a pressure outlet, and slip walls. The angle of attack was varied by rotating the inlet velocity around the Y-axis. The large domain size ensured a uniform total pressure profile at the inlet and minimised the influence of boundary conditions on the simulation results. No-slip conditions were applied to the propeller blades, spinner, and nacelle. The treatment of no-slip boundary conditions on walls in PowerFLOW is approximated using a pressure-gradient extended wall model [77, 78]. This model extends the generalised law-of-the-wall model [79] to consider the impact of pressure gradients on boundary layer development.

For the sliding mesh, a volume of revolution was defined around the propeller blades and spinner; see Fig. 2.4b. In the radial direction, a clearance of $0.1R$ was defined between the blade tip and the outer edge of the rotating domain. Similarly, in the axial direction, a clearance of $0.05R$ was defined between the spinner edge and the edge of the rotating domain.

In total, thirteen variable resolution (VR) regions were employed for $LB-VLESs_{y^+ \geq 15}$, based on the work of Avallone et al. [80]. The $LB-VLESs_{y^+ \leq 10}$ included two additional

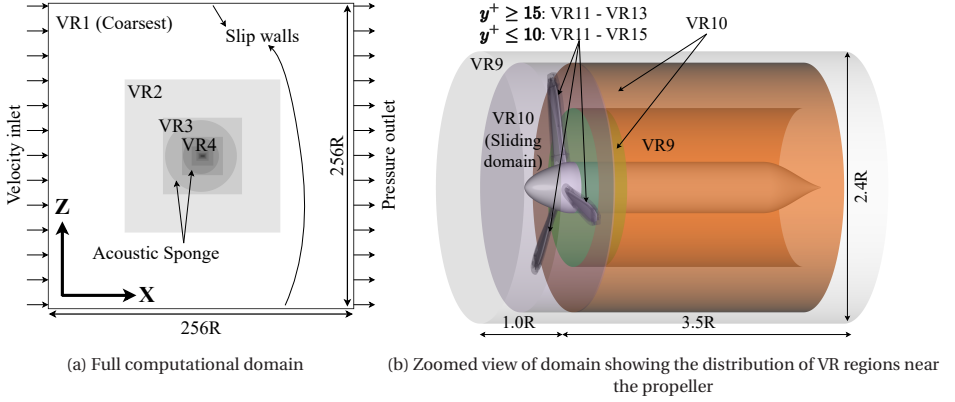


Figure 2.4: Computational domain and boundary conditions along with the VR regions for LB-VLES simulations

VR regions within VR13. Therefore, only the voxels surrounding the propeller blades were modified in LB-VLES $_{y^+ \leq 10}$. The cell volume changes by a factor of 8 between different VR regions. The finest three VR regions (VR13-11) in LB-VLES $_{y^+ \geq 15}$ are marked in Fig. 2.4b. VR10 was used in the sliding domain and downstream up to a distance of $0.5R$ from the propeller. Further downstream, a hollow cylinder with VR10 resolution was used to capture the strong gradients associated with tip vortices. Finally, VR9 was used in a cylinder with a radius of $1.2R$ encompassing the propeller blades, spinner, and blade, extending $1R$ upstream and $3.5R$ downstream of the propeller.

Beyond the primary VR regions, VR regions 4-8 were required to ensure domain size sufficiency to minimise the impact of boundary conditions on the aerodynamic solution. Further, three additional VR regions (VR1-3) were used to minimise acoustic reflections resulting in such a large domain size ($128D$). An acoustic sponge was also used between VR3 and VR4 to absorb any remaining acoustic reflections coming from the boundaries by exponentially varying the kinematic viscosity per unit temperature from $0.005 \text{ m}^2/(\text{s}\cdot\text{K})$ at $15R$ up to $0.5 \text{ m}^2/(\text{s}\cdot\text{K})$ at $30R$ as shown in Fig. 2.4a. The acoustic sponge started at a distance of $15R$ from the propeller centre, ensuring minimal impact on the aerodynamic results.

It is important to note that, in PowerFLOW, the computational cost of cells within a coarser VR region decreases by a factor of $2^{N_{\text{VR}}-1}$, where N_{VR} is the number of VR regions finer than the considered VR region. This means that despite expanding the domain to $128D$ compared to the conventional domain size of $15D-20D$ for aerodynamic simulations, the increase in the computational cost due to the additional VR regions (VR1-3) was negligible. The details of the computational cost can be found in Tables 2.3 and 2.4.

FAR-FIELD NOISE COMPUTATION

The thesis used FWH analogy to compute far-field noise to save computational costs associated with acoustic wave propagation to the far field. The FWH analogy was solved based on the forward-time solution [81] of Farassat's formulation 1A [82] using the post-processing software SIMULIA® PowerACOUSTIC. This formulation includes surface in-

tegral terms, i.e., acoustic monopoles (thickness noise) and dipoles (loading noise). The volume integral, i.e., quadrupole term, is neglected in this formulation, which accounts for the non-linear effects in the volume surrounding the integration surface. The quadrupole term was assumed to be negligible for the operating conditions considered in this thesis as the convective Mach number of the propeller wake is less than 0.30 [83].

2.4.6. HANSON'S FREQUENCY DOMAIN MODEL

Various analytical and numerical models based on the FWH formulation are available in the literature for predicting rotor tonal noise. Among the most commonly used are the models developed by Gutin [84], Deming [85], Barry et al. [86], Hanson [54], and Farassat [87]. All these models require blade loading data as input, necessitating coupling with aerodynamic simulations to predict propeller tonal noise. The accuracy of tonal noise predictions improves with the precision of the blade loading data. Based on the recommendations of Kotwicz et al. [88], Hanson's frequency domain model was selected for this research due to its ability to handle complex geometries. The equations relevant to Hanson's model are clearly presented in the original reference [54], so they are not repeated here. The source code of Hanson's model used in this thesis can be found on the 4TU.ResearchData repository [89].

The tonal noise calculations using Hanson's model were performed using 100 radial stations with cosine distribution along the blade span to achieve higher resolution in the root and tip regions of the blade, where the gradients in the input loading are highest. For the predictions, blade loading was assumed to be parabolically distributed along the chord, while the actual thickness distribution of the blade sections was used.

2.5. OPERATING CONDITIONS

Two operating conditions, detailed in Table 2.2, were extensively used for validating the numerical methods throughout this thesis. These conditions were selected due to the availability of comprehensive experimental data from Nederlof et al. [46]

The first operating condition, with an advance ratio (J) of 0.60 and a pitch angle ($\beta_{0.7R}$) of 15° , represents a positive thrust condition with moderate thrust. The given pitch angle is not optimal for propulsive operation and leads to flow separation near the trailing edge, as discussed in Chapter 4. Consequently, if grid convergence is achieved under this condition, it can be reasonably assumed to be converged for other positive thrust conditions with fully attached flow. However, the grid convergence in the positive thrust regime does not ensure the convergence in the negative thrust regime due to pronounced flow separation under such conditions [39]. Therefore, the second operating condition with $J = 1.10$ and $\beta_{0.7R} = 15^\circ$, representing a negative thrust condition near maximum power output, was included.

2.6. COMPARISON OF GRID SPECIFICATIONS AND COMPUTATIONAL COSTS

Tables 2.3 and 2.4 present a comprehensive overview of the distinctions in grid specifications, time step settings, and the resultant computational expenses for achieving a

Table 2.2: Operating conditions used for the validation of numerical methods

Case	T_C^*	J	$\beta_{0.7R}$ [°]	V_∞ [m/s]	n [Hz]	M_{ht}	max Re_c
$T > 0$	+0.1176	0.60	15°	30	123.03	0.47	3.5×10^5
$T < 0$	-0.1073	1.10	15°	30	67.11	0.27	2.0×10^5

* Measured in experiments [46] and corrected for wind-tunnel boundary interference.

converged aerodynamic solution across different numerical tools, categorised by positive thrust condition ($J = 0.60$) and negative thrust condition ($J = 1.10$), respectively. It is imperative to acknowledge that the CPU hours listed in Tables 2.3 and 2.4 offer a rough estimation of the computational cost associated with these methods. The actual computational expenses may vary depending on factors such as the number of CPUs utilised and the underlying CPU architecture.

For SRANS and URANS simulations, the grid remains consistent across different advance ratios. However, LB-VLESs require a new grid for each change in advance ratio. URANS simulations have precisely three times the number of cells as SRANS simulations, obtained by copying and rotating the grid from SRANS simulations to obtain the entire propeller geometry.

The CPU hours required for the SRANS simulations depend on the grid and the number of iterations needed to achieve convergence, which did not change significantly with the advance ratio. In this thesis, the SRANS simulations were run for 10,000 iterations to obtain the converged aerodynamic solution, resulting in the computational cost of 780 and 800 hours for $J = 0.60$ and 1.10, respectively. This cost is significantly higher (approximately 40,000-50,000 times) than the low-fidelity tools BEM and LL, with a computational cost of less than 1 minute.

Table 2.3: Grid specifications and computational cost of different numerical methods for the positive thrust condition ($J = 0.60$)

Method	y^+	No. of cells	Δt [s]	Rotation per time step [°]	Average CPU hours per revolution	Total CPU hours for converged aerodynamic solution	No. of iterations or revolutions required for converged aerodynamic solution
BEM	--	50	--	--	--	< 1 min	≈ 100
LL	--	50	--	--	--	< 1 min	≈ 30
SRANS	< 1	9,620,832	--	--	78 h per 1,000 iters	780	10,000 iters
URANS	< 1	28,862,496	4.516e-05	2°	2,232	5,634	2 revs + initialisation
LB-VLES $_{y^+ \geq 15}$	≥ 15	62,314,804	1.654e-07	7.324e-03°	1,572	6,288	4 revs
LB-VLES $_{y^+ \leq 10}$	≤ 10	235,590,308	4.134e-08	1.831e-03°	49,766	105,820	2 revs + initialisation

The URANS simulations were initialised using the SRANS solution of the entire propeller geometry obtained after 5000 iterations to reduce the total number of revolutions required to obtain the converged solution. The CPU hours per revolution for URANS

Table 2.4: Grid specifications and computational cost of different numerical methods for the negative thrust condition ($J = 1.10$)

Method	y^+	No. of cells	Δt [s]	Rotation per time step [°]	Average CPU hours per revolution	Total CPU hours for converged aerodynamic solution	No. of iterations or revolutions required for converged aerodynamic solution
BEM	--	50	--	--	--	< 1 min	≈ 100
LL	--	50	--	--	--	< 1 min	≈ 30
SRANS	< 1	9,620,832	--	--	80 h per 1,000 iters	800	10,000 iters
URANS	< 1	28,862,496	8.279e-05	2°	810	2,820	2 revs + initialisation
LB-VLESS $_{y^+ \geq 15}$	≥ 15	62,029,252	1.732e-07	4.185e-03°	2,461	9,844	4 revs
LB-VLESS $_{y^+ \leq 10}$	≤ 10	234,454,461	4.331e-08	1.046e-03°	83,945	177,734	2 revs + initialisation

simulations depend on the number of iterations required for each time step to reach convergence. Achieving convergence criteria of residuals lower than 10^{-5} required 20 inner iterations for $J = 1.10$, while $J = 0.60$ required over 50 iterations, substantially increasing CPU hours per rotation for the latter condition.

The LB-VLESS $_{y^+ \geq 15}$ have a time step of two orders of magnitude smaller than URANS and almost three times as many cells. Nevertheless, for $J = 0.60$, LB-VLESS $_{y^+ \geq 15}$ exhibits lower computational costs per revolution (1,572 hrs) than URANS simulation (2,232 hrs), primarily due to the high number of inner iterations required for URANS. Conversely, at $J = 1.10$, the computational cost per revolution for LB-VLESS $_{y^+ \geq 15}$ (2,461 hrs) is almost three times higher than URANS simulations (810 hrs). This disparity arises from the lower number of inner iterations required to meet the convergence criteria in the URANS simulation and a higher number of time steps per revolution in the LB-VLESS $_{y^+ \geq 15}$. The LB-VLESS $_{y^+ \geq 15}$ needed to be run longer (4 revolutions) compared to URANS simulations (2 revolutions) to achieve convergence of the aerodynamic solution due to the lack of a good initialisation for the former. This resulted in a higher total computational cost for LB-VLESS $_{y^+ \geq 15}$ compared to URANS simulations, regardless of the advance ratios.

To reduce the total number of revolutions required to obtain the converged solution, the LB-VLESS $_{y^+ \leq 10}$ were initialised using the solution of LB-VLESS $_{y^+ \geq 15}$. As a result, only two revolutions were required to achieve the converged aerodynamic solution. In LB-VLESS $_{y^+ \leq 10}$, the mesh size increases by almost a factor of 4, and the time step decreases precisely by a factor of 4 compared to LB-VLESS $_{y^+ \geq 15}$. Theoretically, the computational cost (per revolution) of LB-VLESS $_{y^+ \leq 10}$ should increase by a factor of 16 compared to LB-VLESS $_{y^+ \geq 15}$. However, the increase in computational cost per revolution surpasses the factor of 16 for both advance ratios due to the increase in simulation data saving time and due to the non-linear scalability of the simulations with increasing CPUs. The increased computational cost for the $J = 1.10$ operating condition in both types of LB-VLESSs is attributed to the lower rotation per time step compared to the $J = 0.60$ condition.

3

ASSESSMENT AND VALIDATION OF CFD METHODS

In Part II of this thesis, LB-VLES simulations with $y^+ \geq 15$ have been extensively used to investigate aerodynamic and aeroacoustic phenomena. To ensure the reliability of the numerical results, a grid dependence study was conducted, with outcomes compared against experimental data. This study specifically examines the integrated performance, time-averaged total pressure coefficient behind the propeller plane, phase-locked slipstream velocity data, and far-field noise characteristics for the 0° AoA case. The non-zero AoA setups were subsequently derived from the 0° AoA case and validated primarily based on the relative changes in integrated performance due to the limited availability of experimental data. Additionally, as described in Chapter 2, RANS simulations were utilised as part of the benchmarking of aerodynamic models in Chapter 6. The grid dependence study used to select the appropriate mesh for RANS simulations is presented in this chapter. The assessment of numerical methods is presented in increasing order of complexity, starting with SRANS simulations in Section 3.1, followed by the evaluation of LB-VLES $_{y^+ \geq 15}$ for the 0° case in Section 3.2. Finally, Section 3.3 presents the validation of LB-VLES $_{y^+ \geq 15}$ at non-zero AoA.

3.1. GRID CONVERGENCE STUDY FOR SRANS SIMULATIONS

The grid was refined systematically for the grid convergence study, except for the inflation layer, as per the recommendation of starting the grid convergence study from the edge of the wall layer out by Roache [90]. Following the methodology used by Stokkermans et al. [67], the least-squares version of the grid convergence index proposed by Eça and Hoekstra [91] was used to estimate discretization error. Table 3.1 lists the grid size and refinement ratios h_i/h_1 for the studied configurations, where h_i is the average cell size of the grid i and h_1 represents the average cell size of the finest grid. Four different grids were used for the grid convergence study, where Grid 4 is the coarsest, and Grid 1 is the finest.

Table 3.1: Grid size of the SRANS simulations

Grid	4	3	2	1
Number of cells	2,909,433	6,097,112	9,620,832	19,130,159
h_i/h_1	1.87	1.46	1.26	1.00

The systematic grid convergence analysis was performed based on the integrated thrust and power coefficients for two operating conditions. Additionally, a qualitative assessment was made of the convergence in terms of the radial distributions of thrust and power along the blade span. The two conditions were chosen as the most challenging ones to reproduce numerically. The first condition is a positive thrust condition with a moderate thrust at $J = 0.61$ with $\beta_{0.7R} = 15^\circ$, which slightly differs from the one previously mentioned in Table 2.2. The second condition is the same negative thrust condition as listed in Table 2.2, i.e., $J = 1.10$ with $\beta_{0.7R} = 15^\circ$, close to the maximum power output point.

The results from the grid convergence study are given in Table 3.2, where U_ϕ represents the estimated discretization error based on the solution of the chosen grid (Grid 2). Due to the onset of separation near the tip of the blade (discussed later in Chapter 6), an oscillatory convergence was observed for both operating points. Due to the oscillatory convergence, the discretization error was determined using $U_\phi = 3\Delta_M$, where Δ_M represents the maximum difference between all the available solutions [91]. The propulsive condition ($J = 0.61$) has a maximum estimated discretization error of less than 1% for both C_T and C_P . However, the maximum estimated discretization error for the negative thrust condition ($J = 1.10$) is 3.37% and 6.40% for C_T and C_P , respectively. The increased discretization error results from significant flow separation on the propeller blades.

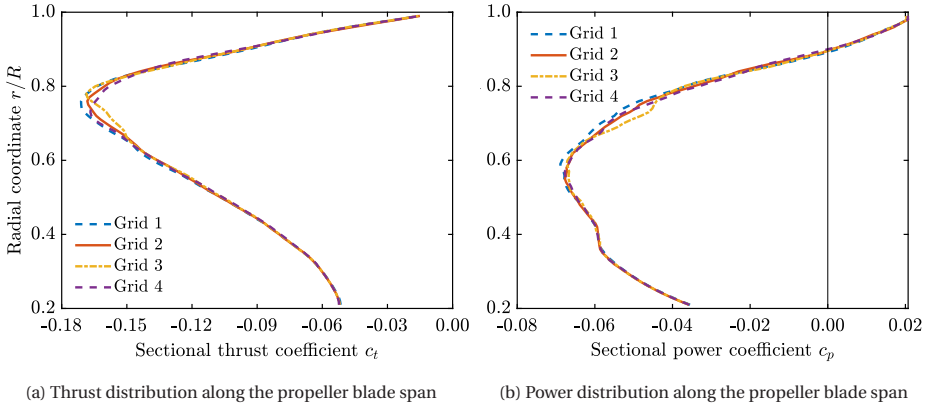
To further check the discrepancies between solutions obtained for different grids, radial distributions of thrust and power are compared in Fig. 3.1 for the operating point corresponding to the maximum uncertainty, i.e., $J = 1.10$. It can be observed that except for some minor differences in the outer region of the blade due to the onset of separation, the solutions for all the grids are in reasonable agreement. Assuming Grid 1 (the finest grid) as the reference, Grid 2 provides a better match of radial distributions of both thrust and power compared to the other grids. Therefore, Grid 2 was determined to be the most suitable in terms of the trade-off between computational cost and solution refinement and, therefore, was used to generate the results for other operating conditions, described

Table 3.2: Grid convergence study of SRANS simulations

Grid	$J = 0.61 (T > 0)$		$J = 1.10 (T < 0)$	
	C_T	C_P	C_T	C_P
4	0.03917	0.03785	-0.12713	-0.05458
3	0.03907	0.03776	-0.12660	-0.05420
2	0.03909	0.03778	-0.12724	-0.05480
1	0.03915	0.03779	-0.12803	-0.05537
Discretization error $ U_\phi $ (Based on Grid 2)	0.78%	0.74%	3.37%	6.40%

3

in Chapter 6.


Figure 3.1: Effect of grid refinement on the thrust and power distribution along the propeller blade in SRANS simulations for the negative thrust condition ($J = 1.10$)

3.2. LB-VLESS $_{y^+ \geq 15}$: ZERO ANGLE OF ATTACK

The operating conditions listed in Table 2.2 have been used for the grid dependence study and validation of LB-VLESS $_{y^+ \geq 15}$. Five different grids were compared for the grid dependence study with fine equivalent voxels varying from 1 million to 100 million, based on the previous study by Avallone et al. [80]. The fine equivalent elements represent the number of elements (N) weighted by the time stepping rate, which is proportional to the mesh resolution level (VR level) and is calculated as follows:

$$\text{Fine equivalent} = \frac{N(\text{finest scale})}{2^0} + \frac{N(\text{2nd finest scale})}{2^1} + \frac{N(\text{3rd finest scale})}{2^2} + \dots + \frac{N(\text{coarsest})}{2^{(n \text{ grid levels}-1)}} \quad (3.1)$$

The details of the grids can be found in Tables 3.3 and 3.4, where resolution is defined as the number of fine equivalent voxels per characteristic length. The characteristic length is chosen to be chord at $0.7R$ blade span, which is approximately 31 mm.

Table 3.3: Grids used for the grid dependence study of LB-VLESS _{$y^+ \geq 15$} - Positive thrust condition ($J = 0.60$)

Grid name	Grid label	Fine equivalent voxels	Resolution	$y^+_{0.7R,0.5c}$ (Front side)
very coarse	5	1,231,315	76	108
coarse	4	8,229,841	152	55
medium	3	26,780,737	228	34
fine	2	62,314,804	304	24
very fine	1	120,353,406	380	16

Table 3.4: Grids used for the grid dependence study of LB-VLESS _{$y^+ \geq 15$} - Negative thrust condition ($J = 1.10$)

Grid name	Grid label	Fine equivalent voxels	Resolution	$y^+_{0.7R,0.5c}$ (Front side)
very coarse	5	1,694,093	87	54
coarse	4	5,244,431	130	37
medium	3	23,134,459	217	22
fine	2	62,029,252	304	15
very fine	1	92,072,521	347	12

The setup was defined such that the blade-passing period of the propeller was an integral multiple of the time-step, which helps to avoid interpolation error in phase-locked and per-rotation averaged measurements. As the rotational speeds of the propeller are different at the chosen operating conditions, the chosen time-step is also different, resulting in a different resolution and mesh sizes. The flow was simulated for twelve revolutions for the medium grid (Grid 3) and used for seeding all the other resolutions. All the other resolutions were simulated for ten revolutions. After ensuring that the transient period was already over, the last eight revolutions were used for the post-processing for all the considered grids.

In the next sections, the integrated performance parameters, thrust coefficient C_T and power coefficient C_P , have been used to verify the convergence of the integrated performance of the propeller and are compared with the experimental values. Further, the radial distributions of the time-averaged total pressure coefficient have been used to verify the convergence of the slipstream flowfield. Additional validation of the setup has been performed by comparing the phase-locked axial and tangential velocity fields in the slipstream with the experimental data. Lastly, the convergence of the far-field acoustics is determined by comparing the noise directivity from different grids.

3.2.1. CONVERGENCE AND VALIDATION STUDY OF INTEGRAL PERFORMANCE PARAMETERS

Figure 3.2 shows the C_T and C_P time-averaged over the last eight revolutions for the different grids compared to the experimental value. The uncertainty of the experimental data is indicated using the shaded areas around the mean results. The standard deviation of the simulated thrust values is also shown using the shaded areas with an aver-

aging period of eight revolutions to provide a measure of the load fluctuations over the averaged rotations. The trends of the grid-dependence study have been supported with the help of skin friction contours and shearlines along the blade surface shown in Fig. 3.3 for the fine grid (Grid 2). The streamlines are also shown around three blade sections at radial coordinates of $0.3R$, $0.6R$, and $0.9R$, respectively.

In the positive thrust condition shown in Fig. 3.2a, the experimental thrust coefficient has an uncertainty of 2.4%, and the power coefficient has an uncertainty of 1.3%. The standard deviation of the simulated values is almost negligible, indicating the steadiness of the loads on the propeller blades. It is observed that C_T stays almost constant for Grid 4, Grid 3, and Grid 2 (coarse, medium, and fine, respectively). However, for Grid 1 (very fine), the thrust coefficient is increased by approximately 4% compared to Grid 2, 3, and 4. This trend can be explained as follows. As the propeller is operating at a comparatively low Reynolds number (3.5×10^5 based on the propeller chord at $0.7R$), a leading-edge separation bubble exists on both sides of the propeller blade as can be seen in Fig. 3.3a. The blade sections between $0.4R$ - $0.7R$ radial coordinate are on the verge of the trailing-edge separation on the pressure side, as indicated by the outward motion of shearlines at these locations. However, the prediction of the location of the separation bubble along the chord is very sensitive to the resolution of the boundary layer (y^+) besides the other parameters, such as incoming turbulence, surface roughness, and subgrid-scale modelling [92–95]. For such cases, having $y^+ \leq 1$ would be the ideal solution. However, as octree meshes are used in PowerFLOW, it becomes practically challenging to reach such y^+ values. Upto Grid 2, the y^+ values are greater than 20 on almost the whole blade surface on the suction side (front), see Table 3.1. However, the y^+ values are below 20 for Grid 1, which improves the prediction of laminar to turbulence transition [73], leading to a better thrust match with the experimental value for Grid 1 (very fine). The differences in the predicted trailing and leading edge separations along the blade span between different grids result in fluctuations in power coefficient (C_P) values between Grid 3, 2, and 1. The C_T predictions by LB-VLESS $_{y^+ \geq 15}$ are in good agreement with the experimental thrust for all the grids except Grid 5. However, the prediction of C_P is off by 14-15%, indicating that the drag is underpredicted by the LB-VLESS $_{y^+ \geq 15}$ leading to a low power value.

For the negative thrust condition shown in Fig. 3.2b, the uncertainty in experimental measurements and the standard deviation of simulation values are less than 1%. The convergence of thrust and power is achieved for the fine grid (Grid 2) with 8% underprediction in thrust and 16% overprediction in power compared to the experiment. The significant difference in the simulated integrated performance compared to the experimental data comes from the fact that there is a leading-edge separation bubble on the suction side (back) around the blade sections starting from the root until the radial coordinate of $0.85R$, see Fig. 3.3b. Further outboard, the blade sections are fully separated. It is known from literature [92–95] that even the separation-bubble length is very sensitive to subgrid-scale modelling and grid quality, making it extremely difficult to capture this condition accurately in the numerical simulation. Moreover, the low Reynolds number in this operating condition (2.0×10^5 based on the propeller chord at $0.7R$) promotes a trailing-edge separation on the pressure side (front) of the propeller blade. As there is a significant difference in the extent of flow separation between the two regimes (Fig. 3.3),

Grid 2 was considered good enough to understand the relative change in aerodynamic and aeroacoustic characteristics between the positive and negative thrust regimes.

The slipstream characteristics have been compared with the experimental data in the next subsection to scrutinise the results obtained from LB-VLESS _{$y^+ \geq 15$} further. The very coarse grid (Grid 5) has been omitted in further comparisons to keep the discussion clear and concise.

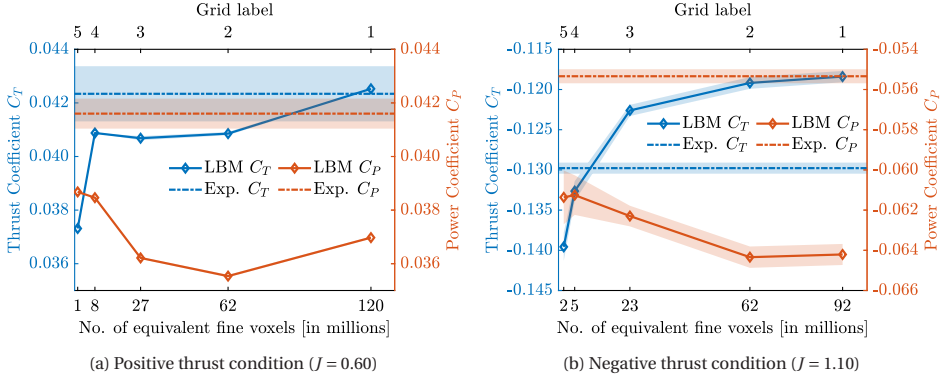


Figure 3.2: Effect of mesh refinement on the predicted integrated thrust and power

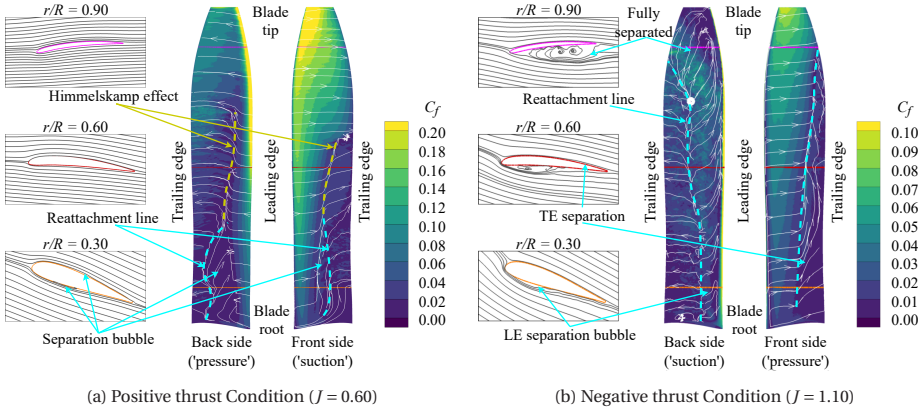


Figure 3.3: Visualisation of flow around the propeller blade using skin friction coefficient and shear lines (fine grid)

3.2.2. CONVERGENCE AND VALIDATION STUDY OF SLIPSTREAM PARAMETERS

The radial distributions of the time-averaged total pressure coefficient obtained from LB-VLESS _{$y^+ \geq 15$} in the slipstream at $0.15R$ downstream of the propeller (Fig. 3.4) have been compared with the experimental data [46] to evaluate the validity of

LB-VLESS _{$y^+ \geq 15$} . For $J = 0.60$ in Fig. 3.4a, The total pressure coefficient profile is similar for different grids except between the radial coordinate of $0.5R - 0.7R$. Besides the fluctuating peak values at the radial coordinate of $0.6R$ between different grids, the medium grid shows different radial gradients between $0.5R$ to $0.6R$. This is expected to be a consequence of the presence of a leading-edge separation bubble along with the trailing-edge separation onset as shown in Fig. 3.3a. At this operating condition, the blade tip is negatively loaded due to local negative angles of attack (Fig. 3.4a), as explained by ref. [46]. The experimental data shows a negative total pressure coefficient for $0.92 \leq r/R \leq 1$. However, in the simulations, the total pressure coefficient is negative only between $0.98 \leq r/R \leq 1$, resulting in a lower power requirement for a given thrust. The simulations underestimate the maximum value of the total pressure distribution, which is offset by overestimation in the outboard sections, resulting in a thrust value close to the experimental value. Thus, the blade loading distribution obtained from the simulations is expected to differ from that obtained in the experiments.

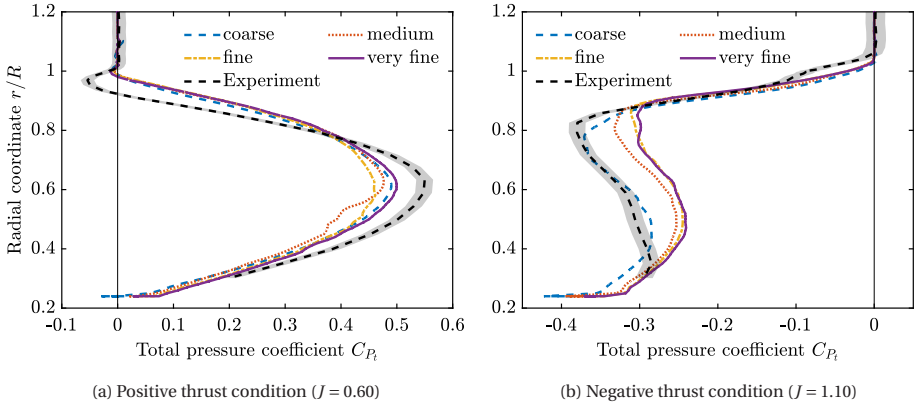


Figure 3.4: Radial distributions of time-averaged total pressure coefficient at $0.15R$ downstream of the propeller centre

Figure 3.4b shows the time-averaged total pressure profile for the negative thrust condition ($J = 1.10$). Looking at the convergence behavior, it is evident that the slipstream converges to a similar profile for fine and very fine grids. Except near the root (below the radial coordinate of $0.4R$), the total pressure distributions are similar in terms of gradients in the radial direction between simulations and experiments. Quantitatively, the total pressure distribution over the 10% most outboard blade radius matches with the experiment. At 40%-90% of blade radius, there is an overprediction of the total pressure, which agrees with the underprediction of the negative thrust observed in Fig. 3.2b. As the blade tip is completely separated (Fig. 3.3b), it is comparatively easier to predict in numerical simulations than a separated region with reattachment. This results in a good agreement for the outboard blade span for all the grids. However, the blade span between the root and the radial coordinate of $0.85R$ has separation at the leading edge with reattachment near the trailing edge. As the reattachment location is sensitive to the grid, it results in differences between the simulation and the experiment [92–95]. The

gradients of total pressure coefficient profiles in the radial direction are almost insensitive to the choice of the considered grids for both positive and negative thrust regimes, except for the medium grid between $0.5R$ - $0.6R$ for the positive thrust condition. Based on these comparisons, the fine grid was considered a good choice for the analyses and has been used for further comparison with the phase-locked PIV data [46].

The simulated phase-locked axial and tangential velocity fields have been compared with PIV data at 0° phase angle (ϕ) with respect to the propeller blade. The definition of the phase angle is shown in Fig. 3.5. Figures 3.6 and 3.7 show the comparison of phase-locked axial and tangential velocities for the positive ($J = 0.60$) and negative thrust condition ($J = 1.10$), respectively. In these figures, the contours of axial and tangential velocity components in the slipstream of the propeller are shown on the right part of the figure, along with the radial line plots at three different axial locations shown on the left. The contours on the top are obtained from PIV data, while those on the bottom are obtained from the current numerical simulations. The first radial line is close to the propeller blades ($x/R = 0.10$) for both operating conditions. The remaining two axial positions have been chosen such that one cuts the tip vortex, and the other is between two tip vortices. These radial lines are located at $x/R = 0.37$ and 0.60 for positive thrust and at $x/R = 0.40$ and 0.70 for negative thrust. The chosen axial positions are different between the two operating conditions due to their different advance ratios, leading to a different pitch between the tip vortices (i.e., different helix angles of the slipstream).

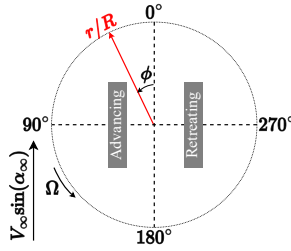


Figure 3.5: Definition of phase angle (ϕ)

In Figs. 3.6a and 3.6b, the velocity gradients near the tip vortices are larger in LB-VLESS $_{y^+ \geq 15}$ (referred as 'LBM' in the figure) compared to the PIV data, and the tip vortices are shifted slightly outwards in the LB-VLES results compared to the PIV data. These differences could originate from the slightly different blade loading. Such differences would lead to a difference in the local velocity in the slipstream, which means that the flow structures would also convect downstream at different velocities. Since the contours are shown at a fixed streamwise position in Figs. 3.6a and 3.6b, their position relative to the flow structures would differ, resulting in a relatively large offset in induced velocities. Other reasons could be an uncertainty in the blade position or minor inaccuracies in the calibration of the PIV setup, leading to a slight displacement of the data with respect to the actual physical coordinates. The line plots show that the gradients in the radial direction are adequately captured by LB-VLESS $_{y^+ \geq 15}$, though the peak is slightly underpredicted, which is consistent with observations from Fig. 3.4.

Figure 3.7 shows the same comparison for the negative thrust condition. The edge

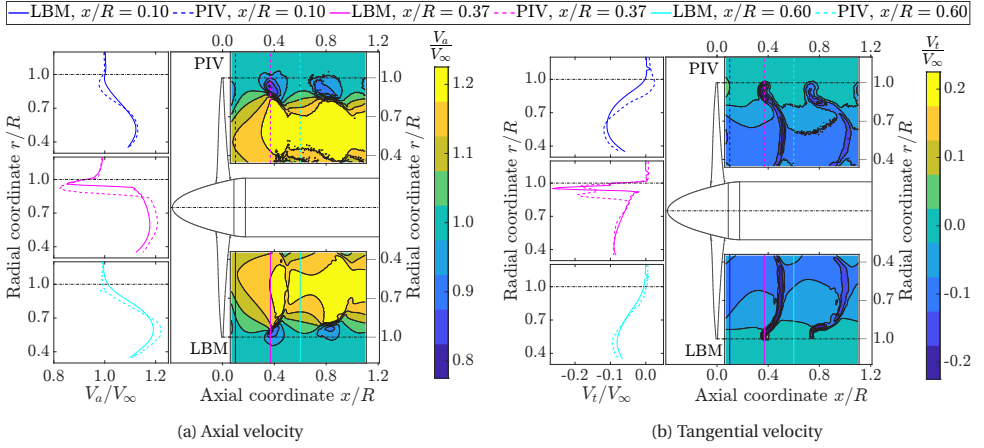


Figure 3.6: Comparison of the phase-locked slipstream from PIV data and LB-VLESS $_{y^+ \geq 15}$ for the positive thrust condition at $\phi = 0^\circ$ ($J = 0.60$, fine grid)

of the slipstream is at a higher radial coordinate in the LB-VLES results compared to the PIV data, as seen in the contours and the left-down corner line plot ($x/R = 0.7$). Again, the gradients in the radial direction from the LB-VLES data are in agreement with the PIV data. LB-VLESS $_{y^+ \geq 15}$ overpredict the peak of phase-locked axial velocity compared to experiments at $x/R = 0.1$ (Fig. 3.7a), which contradicts the time-averaged total pressure profile seen in Fig. 3.4b and the time-averaged axial velocity results shown in Fig. 3.8a. This apparent inconsistency is suspected to be a consequence of uncertainty in the phase-locked blade position in the experiment. To validate this hypothesis, a new comparison with the phase-locked PIV data at $x/R = 0.1$ is shown with arbitrary phase angles of 1° , 2° , and 5° in Fig. 3.8b. The LB-VLES $_{y^+ \geq 15}$ no longer overpredicts the peak at $x/R = 0.1$; instead, there is an underprediction that agrees with Fig. 3.8a, supporting the validity of the hypothesis.

Based on the comparison of the total pressure coefficient and axial and tangential velocities in the propeller slipstream, it has been proven that the fine grid (Grid 2) is able to predict the slipstream characteristics in terms of gradients in the radial and axial direction. Thus, the fine grid is deemed suitable for the further comparison of the aerodynamic characteristics of the positive and negative thrust regimes.

3.2.3. CONVERGENCE STUDY OF FAR-FIELD AEROACOUSTICS

As the dominant noise sources are anticipated to be within the first 10 BPFs [96], the aeroacoustic convergence has been determined by comparing the directivity patterns of overall sound pressure level (OSPL) for the range of 0.5 - 10 BPF. As LB-VLESS $_{y^+ \geq 15}$ work with a cartesian mesh, the three blades of the propeller have different discretization, resulting in different blade loadings. This difference was up to $\pm 4\%$ for the positive thrust condition ($J = 0.60$) compared to the blade-averaged loading and up to $\pm 1\%$ for the negative thrust condition ($J = 1.10$). This difference in the blade loading leads to tonal noise at a frequency of $(1/3)$ times the BPF in the power spectrum density (Fig. 3.10b); there-

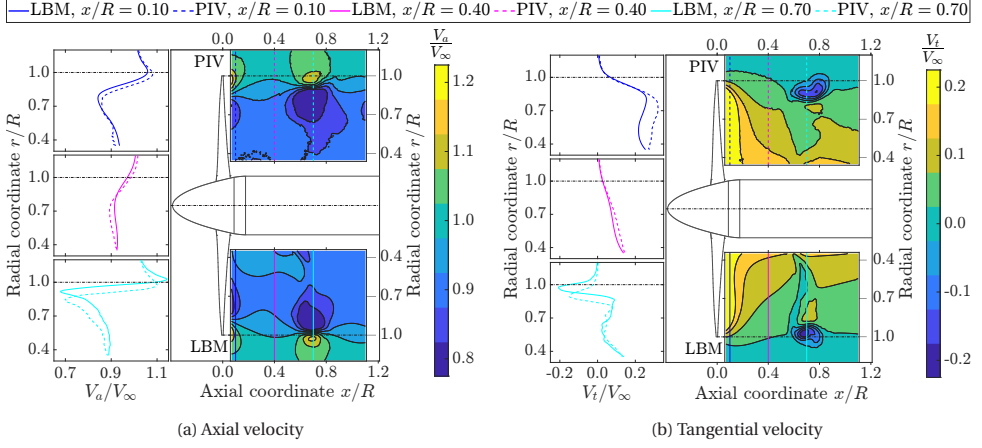


Figure 3.7: Comparison of the phase-locked slipstream from PIV data and LB-VLESs _{$y^+ \geq 15$} for the negative thrust condition at $\phi = 0^\circ$ ($J = 1.10$, fine grid)

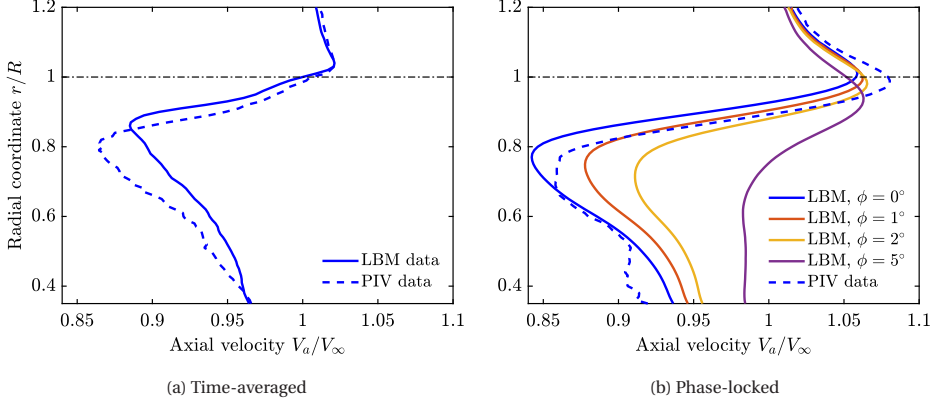


Figure 3.8: Time-averaged and phase-locked axial velocity profile at $x/R = 0.10$ for the negative thrust condition ($J = 1.10$, fine grid)

fore, the lowest frequency is chosen to be 0.5 BPF to eliminate the contribution from this numerical noise source. The OSPL was calculated using the FWH analogy on a ring with a radius of $20R$, with the axis aligned with the propeller plane and the center coinciding with the propeller center to ensure that the observer is in the far field. The OSPL directivity patterns for both configurations are shown in Fig. 3.9. The trends are shown for half of the ring ($\theta = 0^\circ - 180^\circ$) because of the axisymmetric inflow condition, where $\theta = 0^\circ$ lies along the propeller axis in front of the propeller and $\theta = 90^\circ$ lies in the propeller plane. Additionally, the power spectrum density (PSD) is shown for the fine grid (Grid 2) in Fig. 3.10 for two locations - propeller plane ($\theta = 90^\circ$) and propeller axis ($\theta = 0^\circ$).

For the positive thrust condition (Fig. 3.9a), the OSPL between 45° and 150° is almost identical between the different grids with differences below 1 dB as a consequence of

similar blade loading along the blade span. For the negative thrust condition (Fig. 3.9b), the difference in OSPL for different grids is below 1 dB at all the directivity angles except the coarse grid. In the propeller plane, tonal noise is the most dominant noise source, as seen in Fig. 3.10b. Since there are minute differences in blade loading between different grids, as previously shown in Fig. 3.4, the match of OSPL levels in the propeller plane between different grids is an expected trend. In the propeller plane, the first three BPFs are dominant for the positive thrust condition compared to only the first BPF in the negative thrust condition; see Fig. 3.10b. The 1/3 BPF caused by the different meshing of the three blades of the propeller is about 25-30 dB lower than the first BPF and thus did not affect the interpretation of the aeroacoustic results.

The broadband noise is expected to be the most dominant source along the propeller axis [96], which is indeed the case (Fig. 3.10a) for the given operating conditions. In the positive thrust condition, the main sources of broadband noise are expected to be trailing-edge noise and vortex shedding due to flow separation (Fig. 3.3a). The prediction of broadband noise levels is sensitive to the resolution of the relevant turbulent scales. The coarse grid does not sufficiently resolve these turbulent scales, resulting in low (broadband) noise along the propeller axis. However, the medium and the other grids are fine enough to capture these effects, as visible in OSPL levels. The OSPL increases from the medium to the fine grid due to the better resolution of the turbulence on the latter. A further refinement in the grid results in a decrease of 3 dB along the propeller axis from the fine grid to the very fine grid. Therefore, there is an oscillatory convergence. For noise along the propeller axis, prediction within 3 dB is considered enough for the analyses. Flow separation is the main source of broadband noise for the negative thrust condition. Due to strong flow separation in this condition (Fig. 3.3b), the turbulent scales are expected to be larger than for the positive thrust case. The medium and finer grids predict similar noise levels along the propeller axis with differences below 1 dB.

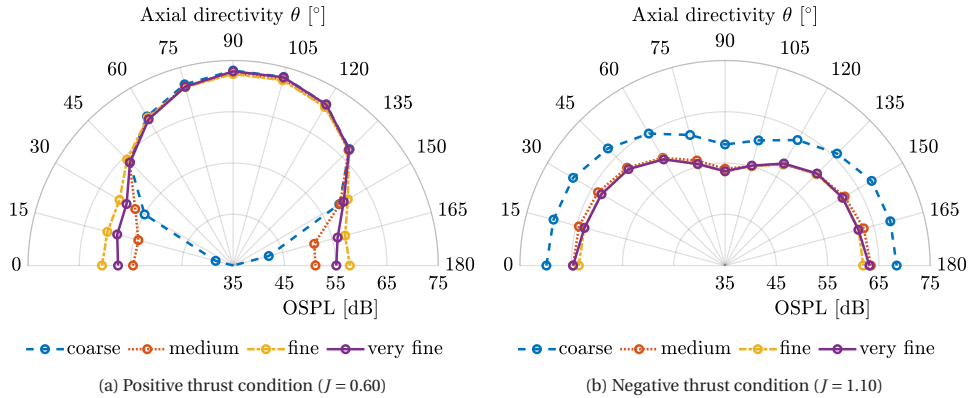


Figure 3.9: Effect of different grids on the OSPL directivity patterns

In the positive thrust condition, the noise in the propeller plane is about 12 dB higher than the noise along the propeller axis, which is an expected trend for conventional op-

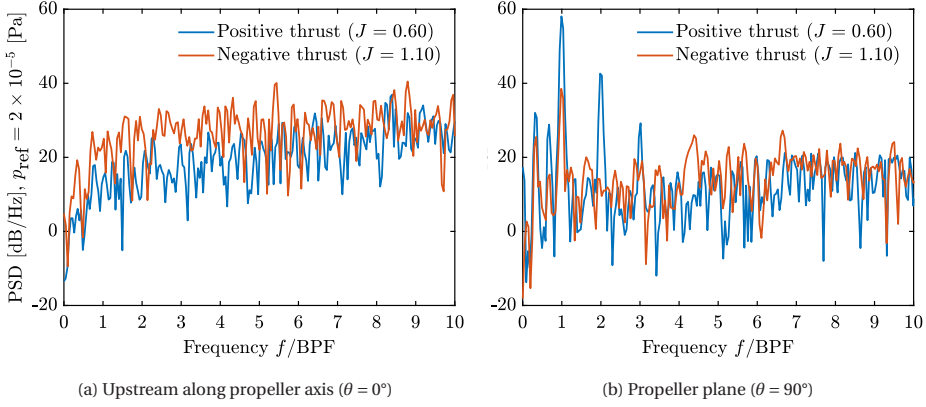


Figure 3.10: Power spectrum density at $\theta = 0^\circ$ and 90° for positive thrust and negative thrust conditions (fine grid)

eration. However, the trend is reversed for the negative thrust condition, i.e., the noise along the propeller axis is 11-12 dB higher than the noise in the propeller plane. This change in directivity is because of two reasons: a) the flow separation in the negative thrust condition significantly increases the broadband noise compared to the positive thrust condition (4-7 dB along the propeller axis); b) lower tonal noise in the negative thrust condition compared to the positive thrust condition (20 dB in the propeller plane), because of the lower blade-tip rotational Mach number and the lower absolute blade loading.

From the above comparisons, it is observed that the fine grid (Grid 2) is able to determine the changes in the noise source characteristics between the positive and negative thrust regimes. Hence, it is considered good enough for further analysis described in Chapter 4.

3.3. LB-VLESS _{$y^+ \geq 15$} : NON-ZERO ANGLE OF ATTACK

To ensure consistency, the setup validated for LB-VLESS _{$y^+ \geq 15$} at 0° AoA (Grid 2) was also used for the non-zero AoA simulations. The AoA was varied by rotating the inlet velocity around the Y-axis (refer to Fig. 2.4a). The validity of the setup for non-zero AoA was assessed by comparing the numerical results with experimental data.

Tables 3.5 and 3.6 present a comparison of simulated and measured (experimental) propeller performance parameters for both positive ($J = 0.60$) and negative thrust conditions ($J = 1.10$). These tables also report the experimental uncertainties calculated for a 95% confidence interval. Moreover, they present the key performance parameters at both 0° and 10° angles of attack, along with the relative change in performance at 10° AoA compared to 0° AoA.

3.3.1. POSITIVE THRUST CONDITION ($J = 0.60$)

For the positive thrust condition, the simulations underpredicted thrust (T_C) by 3% and power (P_C) by 15% at 0° AoA compared to experiments; see Table 3.5. This underpredic-

tion of thrust and power in simulations leads to a 13% higher propeller efficiency (η_p). Similar trends are observed at the 10° AoA, with underpredictions of 4% and 14% for thrust and power, respectively, resulting in a 12% overprediction of η_p . The side force (Y_C) from the simulation is 5% higher, while the normal force is 4% lower compared to the experiments at the 10° AoA. This leads to approximately 1° higher phase delay ($\Delta\phi$) in the simulation than in the experiment. Therefore, except for the power, various performance parameters obtained from simulations reasonably agree with the experiment at both angles of attack. The underprediction of power in simulations is likely caused by the underprediction of the drag in the simulations due to the inaccurate prediction of separation bubble length and reattachment location (Section 3.2).

Table 3.5: Propeller performance in the positive thrust condition ($J = 0.60$) at 0° and 10° angles of attack

Method	α_∞ [°]	T_C	P_C	η_p	T_{C_∞}	η_{p_∞}	Y_C	N_C	N_{C_∞}	$\Delta\phi$ [°]
Experiment	0°	0.1176	0.1926	0.6107	0.1176	0.6107	0	0.0003	0.0003	0°
		± 0.0029	± 0.0026	± 0.0171	± 0.0029	± 0.0171		± 0.0001	± 0.0001	
	10°	0.1274	0.1989	0.6374	0.1227	0.6170	0.0042	0.0158	0.0377	14.83°
		± 0.0030	± 0.0026	± 0.0177	± 0.0030	± 0.0170	± 0.0001	± 0.0002	± 0.0006	$\pm 0.01^\circ$
	$\Delta\alpha_\infty$ %	8.31%	3.26%	4.38%	4.33%	1.04%	--	--	--	--
		$\pm 3.69\%$	$\pm 1.95\%$	$\pm 4.11\%$	$\pm 3.59\%$	$\pm 3.97\%$				
LB-VLES	0°	0.1135	0.1645	0.6898	0.1135	0.6898	0	0	0	--
	10°	0.1219	0.1710	0.7131	0.1174	0.6868	0.0044	0.0152	0.0362	16.08°
	$\Delta\alpha_\infty$ %	7.42%	3.91%	3.38%	3.46%	-0.43%	--	--	--	--

To assess the validity of the simulations for studying the impact of a non-zero AoA on propeller performance, comparing the predicted relative change in performance ($\Delta\alpha_\infty$) at 10° AoA compared to the 0° AoA case is more informative than comparing absolute performance values. As per the experiments, increasing the AoA from 0° to 10° increases the thrust by $8\% \pm 4\%$, power by $3\% \pm 2\%$, and propeller efficiency by $4\% \pm 4\%$. The simulations show a similar trend with a 7% increase in thrust and a 4% increase in power, leading to a 3% increase in propeller efficiency. The experiments also show a $1\% \pm 4\%$ increase in propeller efficiency along the freestream direction (η_{p_∞}), while the simulations predict a small decrease. Despite the overprediction of absolute power, the simulated changes in performance with the increasing AoA lie within the experimental uncertainty, demonstrating the suitability of the simulations for studying AoA-induced effects on propeller performance when operating at positive thrust.

3.3.2. NEGATIVE THRUST CONDITION ($J = 1.10$)

Table 3.6 presents the simulated and measured propeller performance at 0° and 10° AoA at negative thrust ($J = 1.10$). The experimental data show a $6\% \pm 1\%$ decrease in thrust and $10\% \pm 1\%$ decrease in power at 10° AoA compared to the 0° AoA case, leading to a $4\% \pm 1\%$ decrease in turbine efficiency (η_t). The simulations capture these trends well, with a 7% decrease in thrust and a 10% decrease in power, resulting in a 3% decrease in turbine efficiency. This consistent relative change in propeller performance validates the suitability of simulations for studying AoA-induced effects on propeller performance

at negative thrust conditions.

Table 3.6: Propeller performance in the negative thrust condition ($J = 1.10$) at 0° and 10° angles of attack

Method	$\alpha_\infty [^\circ]$	T_C	P_C	η_t	T_{C_∞}	η_{t_∞}	Y_C	N_C	N_{C_∞}	$\Delta\phi [^\circ]$
Experiment	0°	-0.1073	-0.0416	0.3877	-0.1073	0.3877	0.0002	-0.0006	-0.0006	163°
		± 0.0006	± 0.0003	± 0.0032	± 0.0006	± 0.0032	± 0.0001	± 0.0001	± 0.0001	$\pm 0.10^\circ$
	10°	-0.1005	-0.0374	0.3727	-0.1007	0.3715	0.0038	0.0102	-0.0074	20.55°
		± 0.0008	± 0.0003	± 0.0042	± 0.0008	± 0.0042	± 0.0001	± 0.0001	± 0.0002	$\pm 0.01^\circ$
	$\Delta\alpha_\infty \%$	-6.31%	-9.99%	-3.87%	-6.09%	-4.16%	--	--	--	--
		$\pm 0.88\%$	$\pm 0.96\%$	$\pm 1.33\%$	$\pm 0.87\%$	$\pm 1.35\%$				
LB-VLES	0°	-0.0985	-0.0483	0.4908	-0.0985	0.4908	0	0	0	--
	10°	-0.0914	-0.0433	0.4741	-0.0920	0.4712	0.0030	0.0113	-0.0047	14.99°
	$\Delta\alpha_\infty \%$	-7.18%	-10.33%	-3.39%	-6.60%	-3.99%	--	--	--	--

While the simulations captured the relative change in propeller performance well, differences can be observed in the absolute performance prediction compared to experiments. Specifically, the simulations underpredict thrust magnitude by 8%-9% and overpredict power magnitude by 16%, resulting in a 27% higher turbine efficiency for both 0° and 10° AoA cases. At 10° AoA, the simulation underpredicts the side force by 21% and overpredicts the normal force by 11%, resulting in approximately 6° lower phase delay compared to experiments. These disparities in absolute values likely stem from limitations in modelling complex flow phenomena like separation and reattachment, as detailed in Chapter 6. Consequently, the numerical simulations predict a delayed onset of separation (vs. J) compared to experiments, leading to higher predicted thrust (and power) at the specified operating condition ($J = 1.10$). However, the performance predicted by simulations might still be representative of that obtained at a slightly lower J in the experiment.

Therefore, despite the overprediction of absolute propeller performance by simulations, the good agreement in relative changes validates their suitability for further analysis of AoA-induced effects on propeller performance in Chapter 5.

PART II

AERODYNAMIC AND AEROACOUSTIC PHENOMENA

4

PROPELLER AERODYNAMICS AND AEROACOUSTICS AT ZERO ANGLE OF ATTACK

Building on the validation of LB-VLESS $_{y^+ \geq 15}$ in Chapter 3, this chapter delves into the physical phenomena that govern the aerodynamic and aeroacoustic performance of the propeller in negative thrust mode at 0° compared to the positive thrust mode. As the propeller operates in the stall or near stall conditions in the negative thrust regime, the relative importance of the tonal and broadband noise is expected to change along with noise directivity and noise level compared to the propulsive regime. To ensure a fair comparison, the analysis has been conducted at a constant advance ratio, with variations in thrust achieved by adjusting the blade pitch angle.

The chapter begins with an overview of the operating conditions analysed and the rationale for their selection in Section 4.1. Next, the aerodynamic performance is examined in detail in Section 4.2, focusing on integrated performance metrics, blade loading distributions, and slipstream characteristics in both time-averaged and unsteady manner. Following this, the far-field aeroacoustics are analysed in Section 4.3, assessing noise directivity, power spectral density, and noise source maps at the propeller blades. Additionally, Hanson's model is used in combination with LB-VLESS $_{y^+ \geq 15}$ to gain further insights into the contribution of thrust and torque to the loading noise. Finally, the key findings are summarised in Section 4.4.

The contents of this chapter have been adapted from Ref. [50].

4.1. INTRODUCTION

A propeller operating at a constant speed was used to study the far-field aeroacoustics of the negative thrust regime compared to the conventional positive thrust regime. Given the constant helical tip Mach number, the thickness noise can be assumed to remain unchanged between the operational modes; therefore, it is easier to identify the changes in various noise sources due to the change in thrust and power (both direction and magnitude). The operational conditions were chosen based on a preliminary mission analysis of an ATR-42 aircraft with a relatively steep descent (5.5°). The resulting freestream Mach number was 0.29. The helicoidal tip Mach number was set to 0.74 to achieve reasonable similarity with a full-scale turboprop propeller. For this study, the simulations were performed at 0° angle of attack with respect to the propeller so that there was no periodic unsteady loading on the blades. In a realistic configuration, this would be an additional noise source. However, it was decided to eliminate this noise source in this study for ease of interpretation of the results. The pitch angle of the blade was changed from 10° to 45° with a step of 5° to vary the propeller loading. Although variations in blade pitch and loading can influence the boundary layer thickness, and consequently, the thickness noise, these changes are expected to be minor compared to the variations in loading noise.

As the propeller was operated at a fixed advance ratio, there was only a single operating point at which the propeller operated at its peak efficiency for the selected advance ratio. However, this was deemed acceptable because a difference in tip Mach number would affect the comparison more significantly than the obtained differences in propeller efficiency. An additional pitch setting with $\beta_{0.7R} = 37.57^\circ$ was evaluated to match the absolute thrust obtained at $\beta_{0.7R} = 20^\circ$, which has been used to evaluate the changes in noise sources due to the change in the operating regime (negative to positive thrust condition). The choice of $\beta_{0.7R} = 20^\circ$ as the reference for comparing the two regimes at an absolute thrust level was based on the earlier-mentioned preliminary mission analysis of an ATR-42 aircraft.

4.2. AERODYNAMIC PERFORMANCE

Figure 4.1 shows the differences in the instantaneous flow features around the propeller blades between the positive and negative thrust regimes for $T_C = \pm 0.08$ at 37.57° and 20° pitch settings, respectively. These figures show the contours of the skin friction coefficient and shearlines at the blade surface for the two conditions. In addition, streamlines are shown around three blade sections located at $0.3R$, $0.6R$, and $0.9R$. Figure 4.1a shows that the flow is attached along the whole blade span on the back side of the propeller for $T_C = +0.08$, except for the inboard sections that exhibit the presence of a separation bubble. The front side of the propeller shows a separation bubble at the mid-chord position, which can also be seen in the streamlines around the $0.3R$ blade section. This separation bubble is present from the root until around $0.35R$ and moves towards the trailing edge with increasing radial coordinate. For the blade sections present outboard of $0.35R$, the separation bubble extends up to the trailing edge, resulting in trailing-edge separation as seen in the streamlines around the blade sections at $0.6R$ and $0.9R$.

For the negative thrust condition ($T_C = -0.08$), the flow is attached on the front (pres-

sure) side of the propeller, except near the trailing edge on the inboard sections (around $0.5R$ - $0.8R$), see Fig. 4.1b. There is a trailing edge separation at these blade sections, as also indicated by the streamlines around the $0.6R$ blade section. On the back side of the propeller, the flow is attached only for a small portion of the chord near the leading edge, as indicated by the separation line. This leading-edge separation is a consequence of the operation of the blade sections at high negative angles of attack (as shown using streamlines around $0.3R$, $0.6R$ and 0.9). This trend is consistent with previous studies [39].

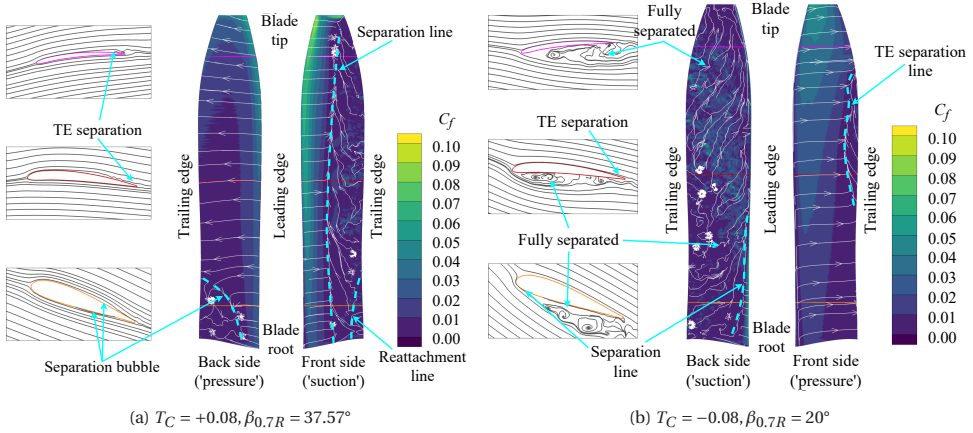


Figure 4.1: Visualisation of instantaneous flow around the propeller blade using skin friction coefficient and shear lines for $T_C = \pm 0.08$

4.2.1. TIME-AVERAGED PERFORMANCE ANALYSIS

Figure 4.2 shows the effect of the varying pitch on the propeller performance. As the advance ratio and freestream Mach number are constant for the analysis, the inflow angle is also constant (31.4° at $r/R = 0.7$, ignoring induction), see Fig. 4.3. Therefore, the lower the pitch angle, the more negative the angle of attack (AoA). Similarly, the higher the pitch angle, the higher the AoA. For the pitch angles up to 30° , the blade section at $r/R = 0.7$ operates at negative angles of attack. As the pitch angle is increased from 10° to 30° , the negative angles of attack at blade sections are reduced, which in turn reduces drag and negative lift. As both lift and drag contribute to the negative thrust, a monotonic trend of T_C is seen in Fig. 4.2a. On the other hand, the negative power magnitude is reduced by reducing the negative lift and increased by reducing the drag. The opposite nature of these effects results in a maximum power obtainable at a certain pitch for a given operating condition, around 15° in this case, as shown in Fig. 4.2a. The transition from negative to positive power occurs around 27.5° (Fig. 4.2a). In the positive thrust regime, the drag component opposes the lift component in the thrust direction, whereas both components contribute positively to the power. As the pitch is increased from 30° to 45° , the positive angles of attack increase at the blade sections, increasing lift and drag. Therefore, a monotonic trend is obtained for power in the positive thrust regime. As the

flow is still attached around most of the blade for the considered operating conditions (Fig. 4.1a), the increase in lift is more than the increase in drag, resulting in an increase of T_C with the increase in pitch angle. Figure 4.2b shows the variation in the efficiency

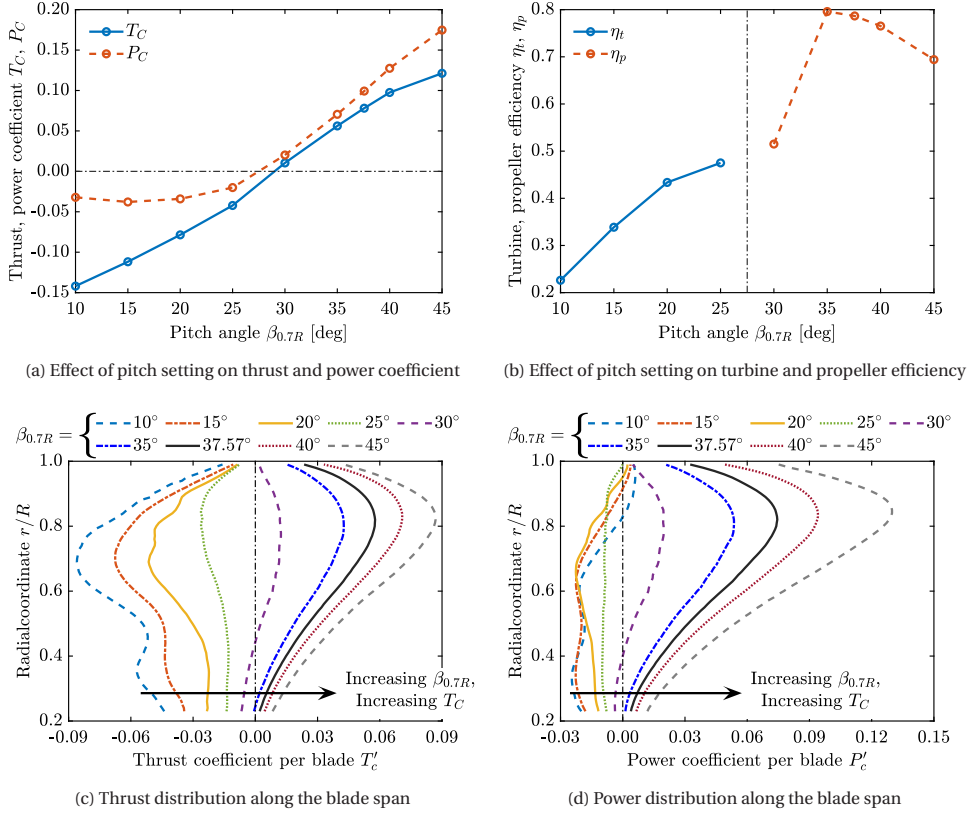


Figure 4.2: Effect of pitch change on propeller performance at $M_\infty = 0.29$, $M_{ht} = 0.74$ (Time-averaged)

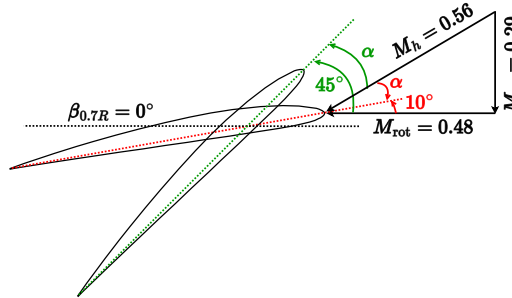


Figure 4.3: Velocity triangle for the constant operating condition at different pitch settings at $r/R = 0.7$ (ignoring induction)

of the propeller as a function of the pitch setting. Different definitions of efficiency are used for the positive and negative power regimes. The turbine efficiency (η_t), the inverse of the propeller efficiency, has been used for the negative thrust regime. It relates to the shaft power regenerated per unit of negative-propulsive power (TV_∞) produced, while the propeller efficiency (η_p) relates to the propulsive power (TV_∞) produced per unit of shaft power consumed. A higher turbine efficiency does not necessarily mean higher absolute power regeneration, which can be observed in the current case. The 25° pitch setting gives the highest turbine efficiency (Fig. 4.2b), while the 15° pitch setting results in maximum negative power magnitude (Fig. 4.2a). At the 25° pitch setting, the flow is still attached on the inboard part of the blade and is separated only on the outboard part. However, as the pitch angle is reduced to 20°, the flow is separated around a larger part of the blade span, resulting in a larger drag increase compared to the lift increase. This results in a larger increase in the negative thrust magnitude compared to the increase in the negative power magnitude, resulting in reduced turbine efficiency. As the pitch angle is reduced even further, there is no increase in the regenerated power; however, there is a significant increase in the negative thrust, further steepening the turbine efficiency slope. At 30° pitch, the propeller operates at a very inefficient positive thrust condition due to inboard sections operating in the negative thrust regime (Fig. 4.2c). As the pitch angle is increased to 35°, the propeller efficiency increases significantly (80%). With the further increase of pitch angle, the blade sections operate at higher loading and a sub-optimal lift-to-drag ratio, especially at 45° pitch, where the efficiency drops to 69%.

The thrust distribution along the blade span in Fig. 4.2c shows that the inboard part of the blade has a higher loading in the negative thrust regime than the positive thrust regime. The higher loading near the root is a consequence of higher absolute AoA at negative thrust conditions, leading to higher lift and drag. The loading peak is around a radial coordinate of $0.7R$ in the negative thrust operations, in contrast to the positive thrust regime, where the maximum is around $0.85R$. The flow separation around the blade tip shifts the peak inwards in the negative thrust regime; that is why the loading peak is located around $0.8R$ at 25° pitch, which shifts to $0.7R$ at 10° with the increase in flow separation. A local maximum is observed in the thrust distribution around $0.45R$ for the 10° and 15° pitch settings. The local lift magnitude in the negative thrust cases is negatively influenced by the flow separation (reduced c_l) and positively influenced by the increasing dynamic pressure with the increasing radial coordinate. Around $0.45R$, the decrease in the lift due to the flow separation is more than the corresponding increase in dynamic pressure due to the increasing rotational speed with the increasing radial coordinate. Though the drag also adds to the negative thrust magnitude, the major contribution comes from the lift (around 80%). Therefore, the local decrease in the lift magnitude results in a local maximum in the thrust distribution at the radial coordinate of $0.45R$ for 10° and 15° deg pitch settings seen in the Fig. 4.2c. The loading distribution for the 30° pitch setting shows that the inboard part of the blade operates in the negative thrust regime with AoA lower than the zero lift AoA. In contrast, the outboard part of the blade operates in the positive thrust regime with AoA higher than the zero lift AoA, resulting in a small positive thrust and power overall.

Figure 4.2d shows the power distribution along the blade span for different pitch settings. For the positive thrust conditions, the radial loading distribution resembles that of

a minimum-induced loss design, with a peak around a radial coordinate of $0.85R$. For the negative thrust conditions, a completely different distribution is obtained where most of the contribution comes from the inboard section with a relatively flat distribution up to the radial coordinate of $0.6R$. The power at outboard sections drops to zero and even goes to positive values at the tip. The positive power at the tip, along with the negative thrust, indicates that the tip is separated to the extent that the power is consumed by that specific part of the blade (instead of being extracted from the flow) to drag the tip along with the rest of the blade. As the pitch angle is decreased from 25° to 10° , the increased flow separation around the blade tip increases the fraction of the span operating at positive power. The negative power magnitude increases along the whole span from 25° to 20° pitch. The further decrease in pitch from 20° to 15° only redistributes the power along the blade span. The power contribution from the inboard part of the blade increases and from the outboard part decreases with the decrease of the pitch angle, resulting in almost similar power levels at 15° and 20° pitch settings as already seen in Fig. 4.2a. A further decrease from 15° to 10° results in a decrease in negative power magnitude from the outboard sections; however, there is a negligible increase in power from the inboard sections, resulting in a lower negative power magnitude overall. The local maxima around $0.45R$ can also be seen in the power distribution of the 10° pitch setting, which results from a decrease in local lift magnitude, as explained before.

4.2.2. UNSTEADY AERODYNAMIC PERFORMANCE ANALYSIS

As the propeller is operating at 0° inflow angle, the blade loading is expected to be axisymmetric. That is indeed the case for the positive thrust regime as shown in Fig. 4.4a, in which the radial distribution of instantaneous thrust coefficient (T'_c) along the blade span is shown as a function of circumferential position. However, the same is not true for the negative thrust regime, as shown in Fig. 4.4b. It should be noted that the sign of the instantaneous thrust coefficient (T'_c) has been reversed in Fig. 4.4b to make the comparison easier with Fig. 4.4a. The thrust distribution for the 20° pitch angle shows significant fluctuations over the rotation (amplitude of up to 18% for inboard sections and up to 30% for the blade tip compared to the time-averaged loads). These fluctuations are the result of the flow separation on the back side (suction) of the propeller (Fig. 4.1b). The high amplitude and frequency of these fluctuations in the negative thrust regime make the blade loads dynamic rather than static. These changes in the loading may have an impact on the structural integrity of the propeller blades in the negative thrust regime.

The effect of the load fluctuations on the integrated thrust performance (from all blades together) is shown in Fig. 4.5a for a total of six rotations. In the positive thrust regime, the fluctuations in the integrated thrust coefficient are below $\pm 1\%$ of the time-averaged thrust coefficient, in contrast to the negative thrust regime fluctuations, which are up to $\pm 3\%$. The fluctuation in the integrated thrust might lead to additional requirements in the power train due to the excitation of the shaft. The amplitude of these fluctuations depends upon the negative thrust level (or the pitch setting in this case). As the negative thrust level increases (i.e., a decrease in pitch angle in this case), the flow separation around the blades increases, leading to an increase in load fluctuations. Figure 4.5b shows the standard deviation of the integrated thrust normalised with the time-averaged thrust value. The average fluctuation amplitude increases from 0.7% to 1.5% as

the negative T_C increases from -0.04 to -0.14 . In the positive thrust regime, the sudden increase of the average fluctuation amplitude to 1.2% for $T_C = 0.01$ results from the low normalising value (T_C). In contrast to the negative thrust regime, the amplitude of fluctuation is below 0.5% for all the positive thrust conditions. Eventually, the fluctuations in the positive thrust regime would increase once significant flow separation is encountered (at higher pitch settings); however, those settings are considered irrelevant in the current study.

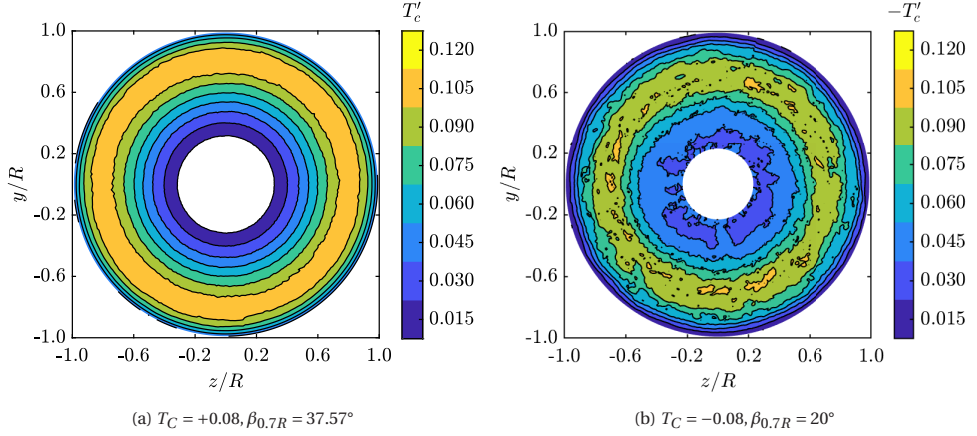


Figure 4.4: Radial distribution of instantaneous thrust coefficient (T'_c) along the propeller blade span over a rotation as a function of circumferential position for $T_C = \pm 0.08$ at $J = 1.34$, $M_\infty = 0.29$

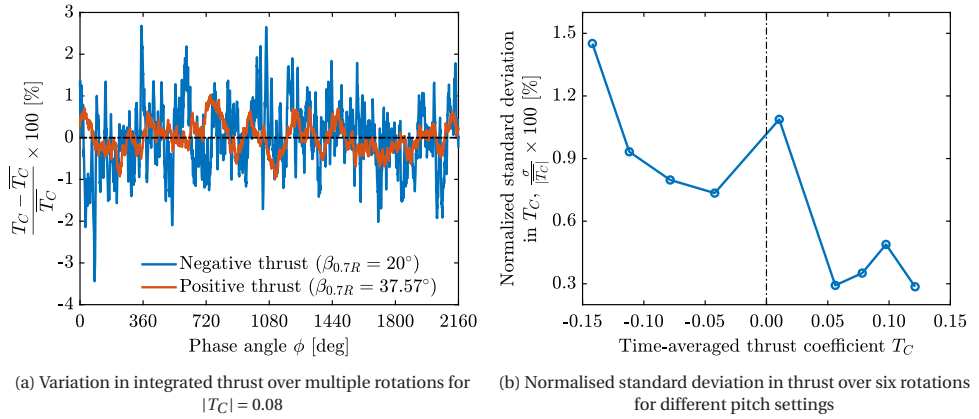


Figure 4.5: Time-accurate integrated thrust performance at $J = 1.34$, $M_\infty = 0.29$

4.2.3. SLIPSTREAM

The slipstream in a negative thrust condition is expected to have significantly different characteristics than in a conventional positive thrust condition. The time-accurate data

in the slipstream was available from simulations with a 5° resolution for one propeller rotation leading to 72 time instances. From each time instance, three slices aligned with the three propeller blades were extracted. The resulting 216 slices were averaged (given their expected symmetry for uniform inflow) to obtain the final phase-locked results. The phase-locked axial and tangential velocity contours in the propeller slipstream have been compared in Figs. 4.6 and 4.7 at an absolute thrust level of $|T_C| = 0.08$, corresponding to pitch angles of 20° and 37.57° for negative and positive thrust respectively. Figures 4.6a and 4.7a show the contours of the mean of the phase-locked velocities and Figs. 4.6b and 4.7b show contours of the standard deviation of the phase-locked velocities. In these figures, the slipstream contours on the top side of the nacelle show the negative thrust condition, and the slipstream in the positive thrust condition is shown on the bottom side.

4

As expected, the operation at negative thrust results in decreased axial velocity in the slipstream compared to the freestream condition, whereas the positive thrust results in increased axial velocity. This difference in the axial velocity causes an axial shift of the tip vortex between the two conditions; see Fig. 4.6a. Also, the radial gradients where the tip vortex cuts the measurement plane are much higher in the positive thrust case than in the negative thrust condition. As the radial gradients due to the tip vortex at $x/R \approx 1.0$ are diffused over a larger region in the negative thrust case, the region with a higher standard deviation is also spread over a larger region compared to the positive thrust case, as can be seen in Fig. 4.6b. These plots also highlight the difference in the shape of the blade wake and tip vortex between the two thrust conditions. In the positive thrust condition, the blade wake is downstream of the tip vortex due to the increased axial velocity. However, the axial velocity is reduced in the negative thrust condition, leading to the tip vortex being downstream of the blade wake.

From the results shown in Fig. 4.6, three main inferences can be drawn regarding the nature of fluctuations experienced by a wing surface immersed in such a slipstream. Firstly, an aerodynamic surface immersed in a slipstream at a negative thrust setting would experience reduced dynamic pressure, resulting in a reduction in local lift. In contrast, an aerodynamic surface immersed in a slipstream at a positive thrust would experience an increase in local lift. Secondly, as the vortices in the negative thrust regime are expected to be closer to each other due to reduced pitch between the tip vortices (Fig. 4.6a), this results in more pressure fluctuations over a wing immersed in a slipstream with negative thrust condition than the positive thrust condition over a given axial distance. Lastly, as can be noticed in Fig. 4.6b, the fluctuations due to the tip vortex are concentrated over a small region compared to the negative thrust condition. Therefore, a wing immersed in a slipstream at a positive thrust condition would experience high-amplitude periodic impingement of the tip vortex. On the other hand, a wing immersed in a slipstream at a negative thrust condition would experience comparatively low-amplitude periodic impingement scattered over a comparatively larger area. These inferences will be tested in the follow-up work with the installed configuration.

Figure 4.7 shows the tangential velocity in the slipstream. This study defines the tangential velocity as positive in the clockwise direction. As expected, the direction of the propeller-induced swirl is in the direction of the rotation of the propeller (anticlockwise) in the conventional positive thrust regime, see Fig. 4.7a. In contrast, as the

direction of the torque is reversed in the negative thrust condition, the direction of the propeller-induced swirl is also reversed, i.e., opposite to the propeller rotation. Therefore, the interaction effects with a body immersed in the propeller slipstream operating at negative thrust would be reversed compared to the effects in the positive thrust condition. Moreover, the gradients in the axial direction near the propeller plane are stronger in the negative thrust condition compared to the positive thrust condition. These differences between the two regimes originate from the differences in blade loading distribution, resulting in a different vortex system and leading to different inductions in the slipstream. Figure 4.7b shows the contours of the standard deviation of the phase-locked tangential velocity in the propeller slipstream. The trends are similar to those shown in Fig. 4.6b, i.e., the strong fluctuations in the tangential velocity are concentrated in the region where the tip vortex cuts the measurement plane. Similar to Fig. 4.6b, Fig. 4.7b also shows that the high fluctuation region (around $x/R = 1.0$) is spread over a larger region in the negative thrust condition compared to the positive thrust condition.

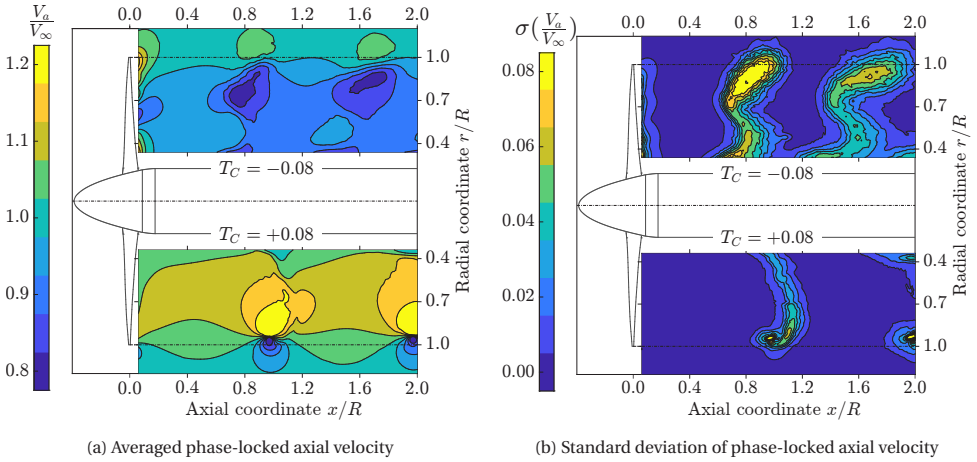


Figure 4.6: Comparison of axial velocity contours in negative ($\beta_{0.7R} = 20^\circ$) and positive ($\beta_{0.7R} = 37.57^\circ$) thrust condition at absolute thrust level of $|T_C| = 0.08$ (Phase-locked)

Figure 4.8 shows the radial distributions of time-averaged axial and tangential velocity in the slipstream at $1R$ downstream of the propeller center. The axial location for the comparison was based on its relevance for an installed case. The radial distributions of axial velocity in Fig. 4.8a display the expected increase in velocity with the increase in thrust for the positive thrust conditions with pitch settings between 30° and 45° . Similarly, the negative thrust conditions show an expected decrease in axial velocity with the increasingly negative thrust value. The radial distributions of axial velocity for 10° and 15° show a local maximum similar to the one seen in the blade loading distributions in Fig. 4.2c. In the positive thrust regime, the strong radial gradients of the axial velocity near $r/R = 1$ result from the high spanwise gradients of the loading distribution seen in Fig. 4.2c. In contrast, as the spanwise loading gradients are comparatively lower in the negative thrust regime near $r/R = 1$, the corresponding radial gradients of the axial velocity are also lower. The slope steepens with an increase in the magnitude of the neg-

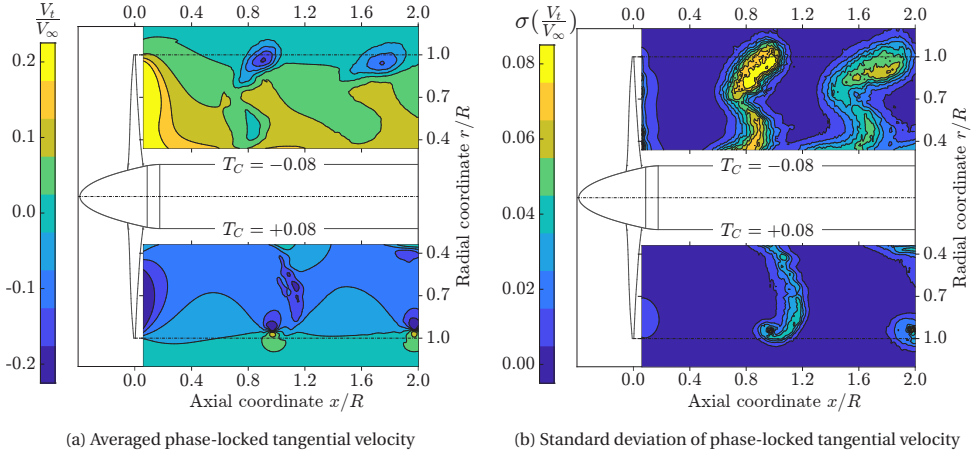


Figure 4.7: Comparison of tangential velocity contours in negative ($\beta_{0.7R} = 20^\circ$) and positive ($\beta_{0.7R} = 37.57^\circ$) thrust condition at absolute thrust level of $|T_C| = 0.08$ (Phase-locked)

ative thrust due to the increase in the corresponding spanwise loading gradients. The increasing blade loading at the inboard sections with the decreasing pitch settings results in decreasing axial velocities in the wake at the corresponding radial coordinates in Fig. 4.8a.

As expected, the tangential velocities are opposite in negative thrust conditions compared to the positive thrust condition due to the opposite direction of torque, see Fig. 4.8b. High loading at the inboard blade sections in the negative thrust regime results in high tangential velocities at the corresponding radial coordinates in the wake. With the increasing radial coordinate, though the dynamic pressure increases, the power coefficient stays almost constant (Fig. 4.2d), resulting in decreasing tangential velocities in the wake. This explains the large radial gradients observed in the negative thrust conditions in Fig. 4.8b. In contrast, in positive thrust conditions, the power coefficient increases with the increasing radial coordinate resulting in almost constant tangential velocities in the wake at a given axial location, as can be seen in Fig. 4.8b. At the radial coordinate of 0.9, the power coefficient becomes positive in the negative thrust conditions resulting in negative tangential velocities. From these trends, it becomes clear that a wing immersed in the slipstream of a negative thrust condition will perceive a changed effective angle of attack compared to a positive thrust condition.

4.3. FAR-FIELD ACOUSTIC CHARACTERISTICS

The changes in the aerodynamics of the negative thrust regime compared to the conventional positive thrust regime are expected to modify the resulting acoustic emissions. The tonal noise is sensitive to both blade loading and thickness, making it difficult to isolate the changes in the noise sources between the two regimes (positive and negative thrust). Building upon the previous section's discussion, the current section also analyses the cases with the fixed tip Mach number (different thrust settings achieved through

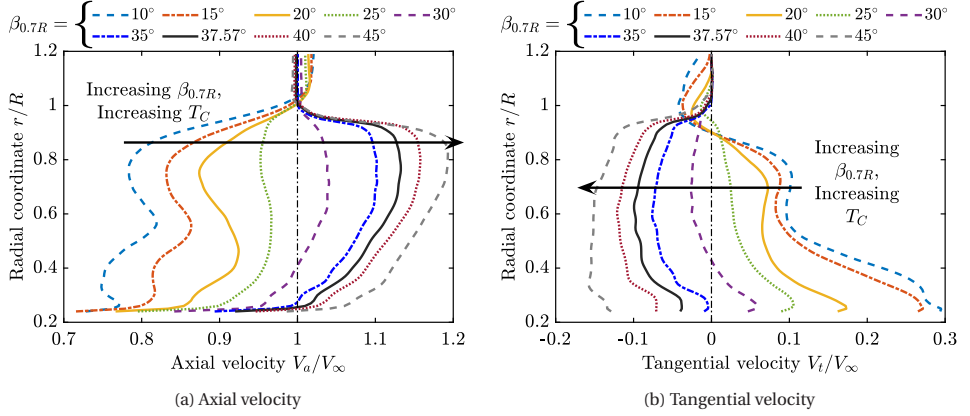


Figure 4.8: Radial distributions of time-averaged axial and tangential velocity in the propeller slipstream at 1R downstream of the propeller center

variation in blade pitch setting). This strategy allows studying the changes in the noise characteristics solely due to the change in the blade loading characteristics and not due to a change in thickness noise. The convection effects have been neglected in this analysis as the main interest is in the change of noise mechanism.

4.3.1. FAR-FIELD NOISE DIRECTIVITY AND POWER SPECTRUM DENSITY

Figure 4.9a shows the resulting far-field noise directivity at a distance of $20R$. The noise directivity has been calculated in two ways. The dash lines with markers are obtained by propagating the pressure signal captured at the blade surface to the far field using the FWH analogy. Therefore, these lines represent the total noise generated by the propeller blades, i.e., the sum of tonal and broadband noise. The solid lines (without markers) are obtained by feeding the time-averaged blade loading shown in Figs. 4.2c and 4.2d to Hanson's model [54] to calculate the tonal noise due to the time-averaged blade loading. The noise can be decomposed into two components using the FWH analogy: loading noise and thickness noise, based on their respective integral terms [97]. The advantage of using Hanson's model is that it further decomposes the loading noise into the noise due to the thrust and torque.

The dashed black line shows the thickness noise obtained from the FWH analogy, whereas the dotted black line shows the thickness noise obtained using Hanson's model. The FWH analogy gives the total noise obtained from the high-fidelity simulations, whereas Hanson's model gives further insight into the loading noise sources. Comparing the noise levels obtained from the two approaches shows that Hanson's model overpredicts the tonal noise by 2-3 dB for both positive and negative thrust conditions, which originates from the simplifications inherent in Hanson's model [54]. The thickness noise is also overpredicted by 3 dB in the propeller plane. As broadband noise is the primary source of the noise near the propeller axis, the total noise level (predicted by FWH analogy) is higher than the tonal noise levels (predicted by Hanson's model) for $0^\circ \leq \theta < 30^\circ$ and $150^\circ < \theta \leq 180^\circ$. For approximately $30^\circ \leq \theta \leq 150^\circ$, Hanson's model agrees qualita-

tively with the FWH analogy and can be used to understand the relative importance of different tonal noise sources. Therefore, this analysis with the Hanson model has been used to gain more insight into these noise sources.

The positive thrust condition has 10 dB higher noise in the propeller plane than the negative thrust condition, which is also reflected in the PSD plot shown in Fig. 4.10b. This difference in the tonal noise is expected to originate from two sources: a) higher noise due to torque in the positive thrust condition (due to higher torque, see Fig. 4.2d); b) differences in blade loading distribution between the two conditions as seen in Fig. 4.2c. These sources of difference between the loading noise at positive and negative thrust have been analyzed further by decomposing the loading noise into noise produced by thrust and torque using Hanson's model, see Fig. 4.9b. Though the absolute thrust level is the same for both conditions, the more outboard loading in the positive thrust condition leads to a 4 dB higher noise due to thrust. Despite the constant absolute thrust level, the magnitude of the torque is approximately three times higher in the positive thrust condition than in the negative thrust condition. The higher torque amplitude results in up to 12 dB higher noise in the positive thrust condition than in the negative thrust condition. As evident from Fig. 4.9b, noise due to torque is the dominant noise for the positive thrust condition for the given operating condition. In contrast, the noise produced by thrust and torque is comparable in the negative thrust condition. For both regimes, the noise due to thrust has two lobes, with the front lobe interfering destructively with the noise due to torque and the back lobe interfering constructively with the noise due to torque, irrespective of thrust direction. This interference trend between noise produced by thrust and torque agrees with the previous studies [96, 98]. As noise levels produced by thrust and torque are comparable in the negative thrust condition, the destructive interference results in a decreased loading noise in front of the propeller plane, as can also be seen in the FWH analogy results in Fig. 4.9a. In the positive thrust condition, the noise due to thrust has a small effect on the overall loading noise.

Along the propeller axis ($0^\circ \leq \theta \leq 30^\circ$ and $150^\circ \leq \theta \leq 180^\circ$), the negative thrust condition results in 13-15 dB higher noise than the positive thrust condition along the propeller axis; see the FWH analogy results in Fig. 4.9a. This is an expected result of the increased flow separation in the negative thrust condition compared to the positive thrust condition, as seen in Fig. 4.1. The increased broadband noise can also be seen in the PSD plot shown in Fig. 4.10a.

4.3.2. NOISE SOURCE MAP

To further understand the difference between the noise sources in positive and negative thrust conditions, a post-processing tool from 3DS named OptydB-PFNOISESCAN was used. This tool calculates the noise contribution per unit surface area emitted towards a given microphone at every time step, and then Fourier transforms the unsteady surface field to provide output for a given frequency range. The noise contribution of the surfels is calculated in terms of power density, i.e., Pa^2/m^2 and then the resulting value is converted into dB by taking the log, resulting in the units of dB/m^2 . It should be noted that this tool uses the assumption of a compact source, which is a reasonable assumption for the first two BPFs ($Mc_o/\lambda < 0.1$) for the given operating conditions ($M_\infty = 0.29$, $M_{ht} = 0.74$). Nine time instances of the obtained results are shown for one

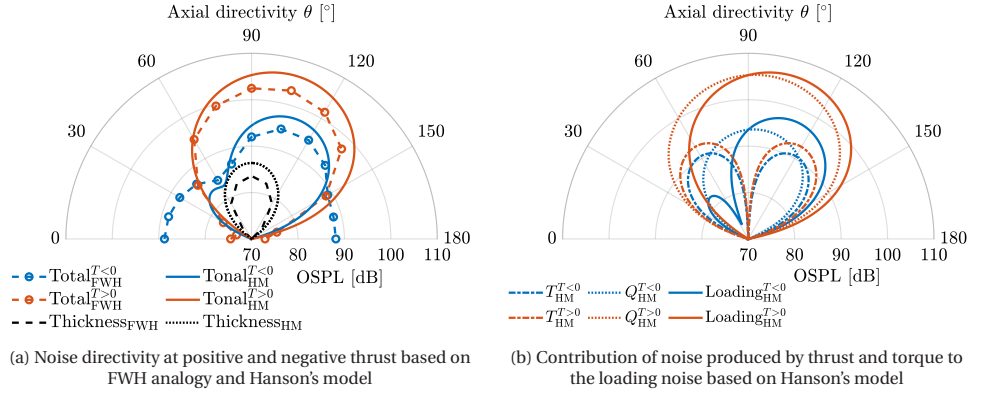


Figure 4.9: Far-field noise directivity of the propeller in positive and negative thrust regimes at absolute thrust level of $|T_C| = 0.08$

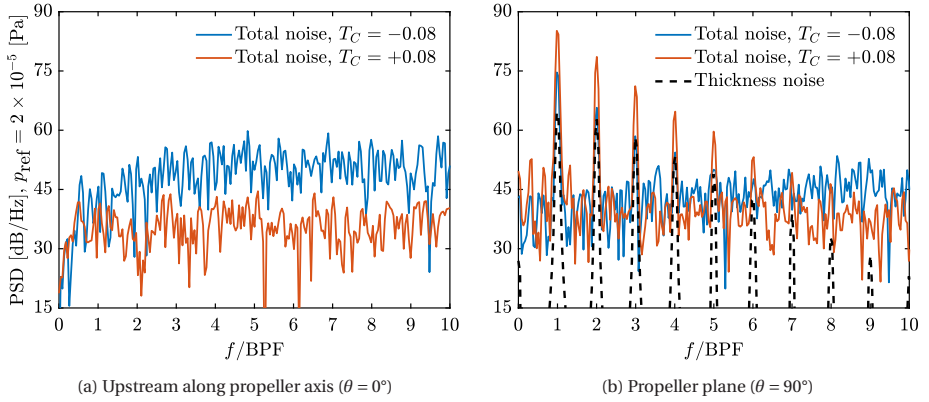


Figure 4.10: Power spectrum density at $\theta = 0^\circ$ and 90° for absolute thrust level of $|T_C| = 0.08$

of the blades in Fig. 4.11 and Fig. 4.12 for $\theta = 0^\circ$ and 90° respectively. For $\theta = 0^\circ$, the frequency range was chosen to be 1 - 2 BPF, given the considerable difference in PSD between the two operating conditions seen in Fig. 4.10a and constraints imposed by the assumption of a compact source. Similarly, for $\theta = 90^\circ$, the first BPF was chosen to compare the location of tonal noise sources at the given operating conditions based on Fig. 4.10b.

Figures 4.11a and 4.11c show the noise source maps of the front and back sides of the propeller respectively for a microphone located along the propeller axis ($\theta = 0^\circ$) for $T_C = +0.08$ ($\beta_{0.7R} = 37.57^\circ$). Similarly, Figs. 4.11b and 4.11d show the noise source maps of the front and back sides of the propeller respectively for the same microphone location for $T_C = -0.08$ ($\beta_{0.7R} = 20^\circ$). As the microphone is located along the propeller axis, the noise source contribution is independent of the circumferential position in Fig. 4.11. As can be noticed from the figure, broadband noise is dominant for this observer location (Fig. 4.10a). Since the inflow turbulence is negligible, the two main sources of broadband noise are trailing-edge noise and flow separation. For the front side of the propeller

(Fig. 4.11a), the noise mainly comes from the trailing edge. The strong noise sources near the trailing edge can be related to the trailing-edge separation seen in Fig. 4.1a. Similarly, on the back side of the propeller, the noise sources are observed at the inboard sections corresponding to the separation bubble seen in Fig. 4.1a along with trailing-edge noise sources located relatively outboard.

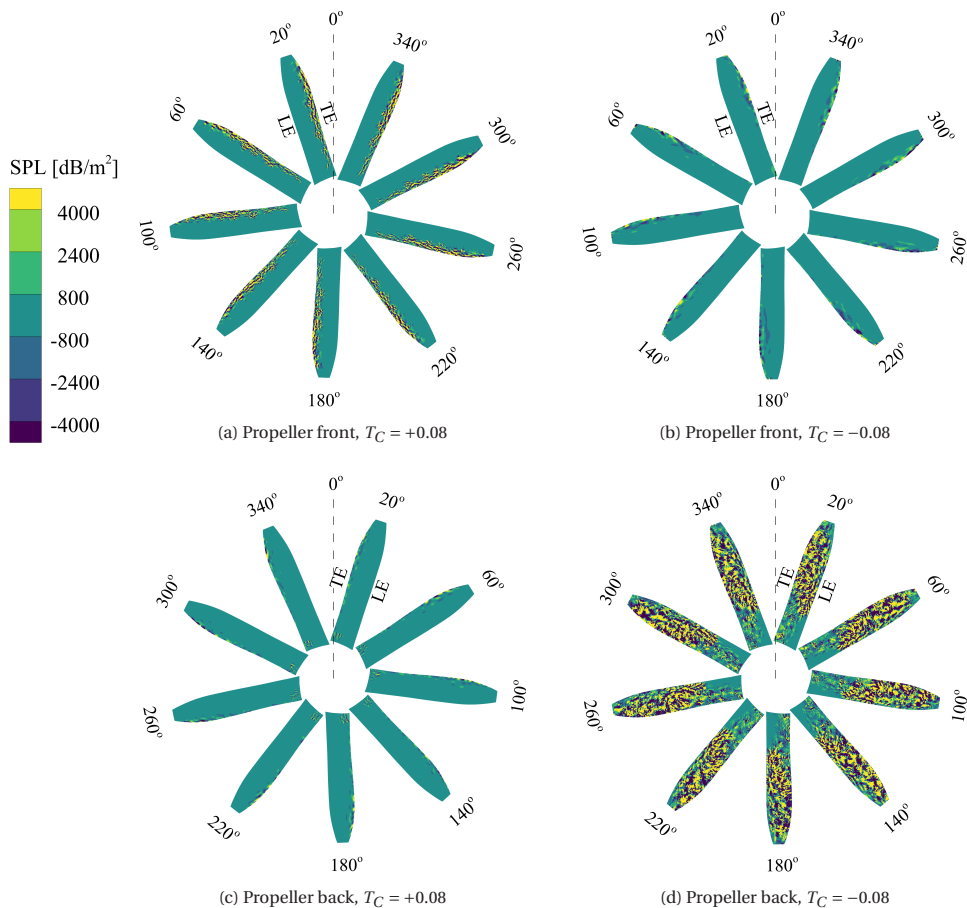


Figure 4.11: Noise source map (1 - 2 BPF) on a single propeller blade for an observer located along the propeller axis ($\theta = 0^\circ$) at positive and negative thrust conditions

In contrast, the extensive flow separation on the back side of the propeller in the negative thrust condition (as shown in Fig. 4.1b) leads to a dominant broadband noise contribution from the whole back surface of the blade, see Fig. 4.11d. Again, the inboard region with the attached flow in Fig. 4.1b features negligible noise generation radiated to the given microphone. With the increase in local Mach number and pressure amplitude (due to the increased dynamic pressure) in the radial direction, the extent of flow separation also increases from the root to the tip, enhancing the strength of the broadband noise source. For the conventional regime, i.e., positive thrust condition, the front side

is the dominant source of broadband noise. In contrast, the back side is the dominant broadband noise source in the negative thrust condition.

To compare the distribution of tonal noise source for the two operating conditions, the noise source map for $\theta = 90^\circ$ at the first BPF is shown in Fig. 4.12. Because the microphone is located in the propeller plane along the 0° line depicted in the figure, the source contribution varies with the circumferential position. This is a consequence of the varying distance between the blade surface and the microphone due to the rotation of the blade surface. Due to the increase in local Mach number and pressure amplitude (due to the increased dynamic pressure) in the radial direction, the outboard part of the blade has the most dominant contribution to the noise in the propeller plane in the conventional positive thrust regime on both the front and the back side of the propeller (Figs. 4.12a and 4.12c). In the negative thrust case as well, a clear dominant noise source can be seen on the outboard part of the blade on the front side of the propeller (Fig. 4.12b) contributing to the tonal noise. However, on the back side of the propeller, random fluctuations are superimposed on a circumferential variation of the source amplitude (Fig. 4.12d). This indicates the presence of a combination of tonal and broadband noise. The tonal noise in the positive thrust condition is higher than in the negative thrust case in Fig. 4.12 because of higher torque in the positive thrust case, as explained previously.

4.3.3. EFFECT OF THRUST COEFFICIENT ON OSPL

This section evaluates the effect of the thrust setting on the OSPL. Figure 4.13a shows the variation of OSPL with the absolute thrust coefficient for both positive and negative thrust regimes using the FWH analogy along the propeller axis ($\theta = 0^\circ$) and in the vicinity of the propeller plane ($75^\circ \leq \theta \leq 105^\circ$). The tonal noise in the vicinity of the propeller plane has been decomposed further by using Hanson's model into thrust, torque, and thickness noise, see Fig. 4.13b. In Fig. 4.13a, the dash-dotted lines show the noise levels along the propeller axis ($\theta = 0^\circ$), where the main contribution comes from the broadband noise sources. The solid lines show the maximum OSPL level between 75° – 105° , where the OSPL is expected to be dominated by tonal noise (see Fig. 4.10b). The dashed-black line shows the level of thickness noise for the given operating condition. The OSPL for the positive thrust condition increases from 71 dB to 80 dB along the propeller axis (dash-dot orange line) when the thrust coefficient increases from 0.01 to approximately 0.12. This is a result of the increase in the broadband noise caused by an increase in trailing-edge separation (Fig. 4.1a) with the increase in T_C . Even with the trailing-edge separation, the broadband-dominated noise of the positive thrust regime is considerably lower than that of the negative thrust regime (dash-dot blue line) at all the thrust levels (as expected). The noise along the propeller axis for the negative thrust conditions has a higher positive slope than the positive thrust regime. After a certain thrust level, the broadband-dominated noise level exceeds the tonal-dominated noise levels and becomes the dominant source of the noise. This is a consequence of the significant increase in the broadband noise levels caused by the increasing separation as the magnitude of negative thrust increases.

On the other hand, the tonal-dominated noise for the positive thrust regime (solid orange line) is considerably higher than the tonal-dominated noise for the negative thrust

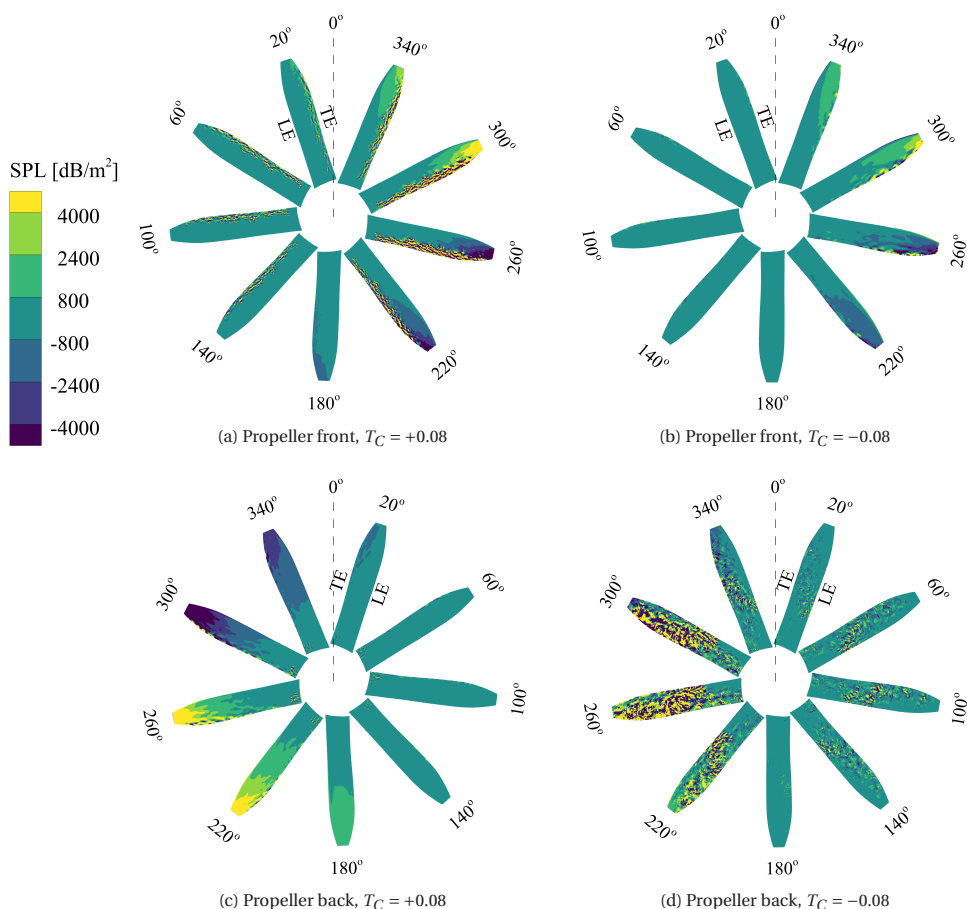


Figure 4.12: Noise source map (1st BPF) on a single propeller blade for an observer located in the propeller plane ($\theta = 90^\circ$) at positive and negative thrust conditions

regime (solid blue line). In the vicinity of the propeller plane, the negative thrust condition with a thrust coefficient of $T_C = -0.04$ produces approximately similar noise as produced in the positive thrust regime at $T_C = +0.01$. The positive thrust regime has a much steeper slope along the whole range of thrust levels than the negative thrust regime (Fig. 4.13). In contrast, there is a little increase in the noise near the propeller plane for $|T_C| \geq 0.08$ in the negative thrust regime. These trends can be explained by decomposing the tonal noise into thrust, torque, and thickness noise using Hanson's model, which is shown in Fig. 4.13b. Hanson's model predicts trends similar to those of the FWH analogy for the noise in the given directivity range. In the vicinity of the propeller plane, the noise due to torque (dotted orange line) is the dominant noise source for the whole thrust range in the positive thrust regime. The same is true for the negative thrust regime up to the maximum regeneration point. As a result, even though the absolute thrust magnitude in the negative thrust condition ($T_C = -0.04$) is approximately

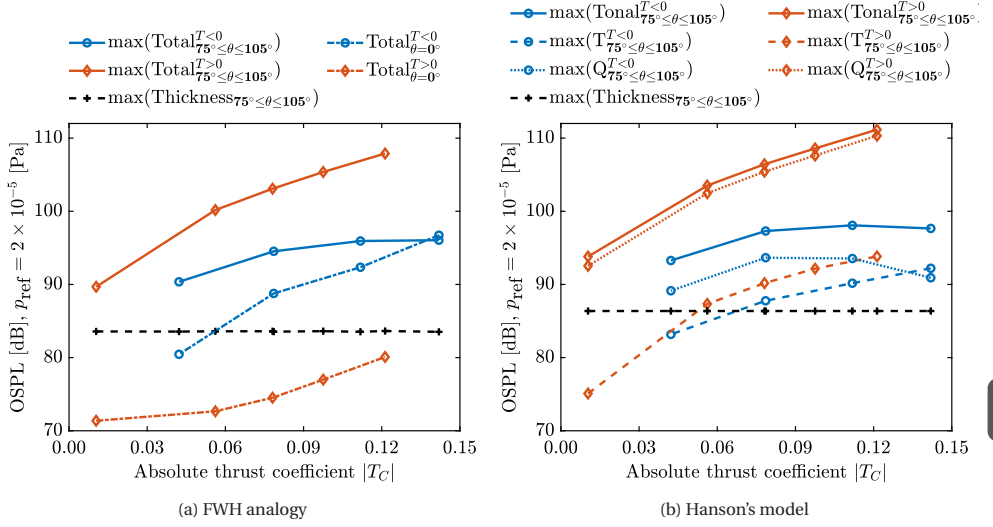


Figure 4.13: Effect of thrust coefficient on the noise sources in positive and negative thrust regimes for a propeller operating at a constant rotational speed ($M_\infty = 0.29$, $M_{ht} = 0.74$)

four times higher than the positive thrust condition ($T_C = +0.01$), the tonal noise levels are similar due to the similar magnitude of P_C ($|P_C| = 0.02$), see Fig. 4.2a. As in the positive thrust regime, the torque increases with the increasing thrust magnitude, and the tonal noise levels also increase. However, in the negative thrust regime, the operating conditions with $T_C = -0.08$ and -0.11 have similar values of P_C (Fig. 4.2a), resulting in similar tonal noise levels. After the maximum regeneration point, the magnitude of the negative torque starts to decrease, whereas the magnitude of the negative thrust continues to increase. As a result, noise due to thrust becomes the dominant noise source after a certain point; see Fig. 4.13b. However, such an operating condition probably would not be relevant for an aircraft due to the high magnitude of the negative thrust coefficient.

4.3.4. MAIN INFERENCES FOR LANDING USING NEGATIVE THRUST SETTINGS

Three main inferences can be drawn from the trends observed in Fig. 4.13. Firstly, it can be concluded that for a given absolute thrust level, the negative thrust regime can be expected to have lower noise in the propeller plane than the positive thrust regime based on two facts: a) For a given thrust level, the noise due to thrust in positive thrust condition can be expected to be always higher than the noise due to negative thrust due to more outboard loading; b) As concluded in the earlier work [98] as well, the torque required to generate a given thrust level can be expected to be always higher than the torque regenerated at the same absolute thrust level in the negative thrust regime (for a conventional propeller design). As a result, the sum of the noise due to both thrust and torque is expected to be lower in the negative thrust regime compared to the positive thrust regime for a given absolute thrust; therefore, the resulting tonal noise is also ex-

pected to be lower. Secondly, it can be concluded that for a conventional propeller, the negative thrust regime is expected to be noisier along the propeller axis than the positive thrust regime, irrespective of the thrust or torque level. Lastly, the noise due to torque is expected to be the dominant noise source in the operating conditions (moderate thrust levels) relevant for a landing using negative thrust. When the negative torque is below the torque required to operate the propeller in a conventional landing, the noise near the propeller plane can be expected to be either lower or similar to the noise generated by the propeller in a conventional landing. A similar torque level in the two regimes is achieved at a higher absolute thrust in the negative thrust regime compared to the conventional positive thrust regime. It essentially means that a steeper descent is possible without increasing the tonal noise (without considering the effects of inflow angle on the tonal noise). Moreover, the steeper descent means that the vicinity of the airport is exposed to the noise for a shorter time and generally at larger distances. This would lead to reduced noise hindrance even at a constant source noise level.

4.4. KEY FINDINGS

A propeller operating at a constant rotational speed but varying pitch angle was used to investigate the far-field noise characteristics with a freestream Mach number of 0.29 and helicoidal tip rotational Mach number of 0.74. Such a configuration ensures that the thickness noise stays constant as the loading is changed with the variation of pitch setting. The resulting absolute thrust coefficient lies in the range of 0.01 - 0.12 for the positive thrust regime and between 0.04 - 0.14 for the negative thrust regime. As expected, thrust shows a monotonic decreasing trend with the increase in pitch angle in the negative thrust regime. Power reaches a maximum at a unique pitch setting (for the studied propeller at 15°). The blade loading distributions show that the peak in the radial distribution of thrust is located inboard (0.7R) compared to the spanwise location of maximum loading (0.85R) for the positive thrust regime. Moreover, most of the negative power comes from the inboard part of the blade (up to 0.6R) compared to the positive thrust regime, where the maximum power loading is around 0.85R. The flow separation around the blades in the negative thrust regime increases average fluctuations from 0.7% at $T_C \approx -0.04$ to 1.5% at $T_C \approx -0.14$ in the integrated thrust. In comparison, the fluctuations are below 0.5% for all thrust settings in the positive thrust regime. Further, the blade loading in the negative thrust regime shows the amplitude of fluctuations of up to 18% for inboard sections and up to 30% near the blade tip compared to the time-averaged loads. The analysis of the slipstream flowfields shows that an aerodynamic body immersed in a slipstream at a negative thrust setting will experience reduced dynamic pressure and opposite tangential velocity compared to those experienced at a positive thrust setting.

The analysis of the far-field noise characteristics shows that a conventional propeller operating in the negative thrust regime can be expected to produce more broadband noise than in positive thrust conditions at all practical thrust settings. The tonal noise in the positive thrust regime is higher than in the negative thrust regime for a given absolute thrust. This difference arises from two sources. Firstly, the higher torque leads to higher noise due to torque in the positive thrust regime. Secondly, the higher absolute loading on the inboard blade segments results in a lower noise due to thrust in the negative thrust

regime, even though the absolute thrust level is the same. As the noise due to torque is the dominant noise source for low to moderate thrust settings, a steeper and quieter descent compared to a conventional descent is possible using negative thrust as long as the negative torque produced is equal to or lower than the torque required to operate the propeller in a conventional landing (without considering the effect of inflow angle on propeller noise). Additional reduction in noise hindrance is expected due to the steeper descent leading to shorter exposure time to the community noise.

5

PROPELLER AERODYNAMICS AND AEROACOUSTICS AT NON-ZERO ANGLE OF ATTACK

Even at 0° AoA, the operation of conventional propellers at negative thrust conditions leads to flow separation around the blades as seen in Chapter 4. The flow separation is likely to be further amplified when operating at a non-zero AoA. The periodic perturbations in the inflow conditions due to the operation at a non-zero AoA are hypothesised to potentially result in periodic stall of the blade sections, impacting both aerodynamic and aeroacoustic performance. Understanding such effects is crucial for designing propellers that optimise energy regeneration while minimising noise emissions. To address this knowledge gap, this chapter investigates the effect of a non-zero AoA on the aerodynamic and aeroacoustic performance of a propeller operating at negative thrust compared to positive thrust. This chapter utilises LB-VLESS_{y⁺ ≥ 15} previously validated in Chapter 3 and employed for the 0° AoA case in Chapter 4.

The chapter begins with a description of physical mechanisms and reference frames used for the analysis in Section 5.1. It then delves into the analysis of aerodynamic performance, focusing on the changes in the integrated propeller performance, blade loading, loading fluctuations, and propeller slipstream to understand the differences in the aerodynamic performance at 0° and non-zero AoA in Section 5.2. Finally, the changes in the aeroacoustic performance are characterised by comparing the far-field noise at 0° and non-zero AoA in Section 5.3, with key findings summarised in Section 5.4.

5.1. PHYSICAL MECHANISMS AND REFERENCE FRAMES FOR OPERATION OF A PROPELLER AT A NON-ZERO ANGLE OF ATTACK

This section establishes the conventions and reference frames used to describe the physical mechanisms governing propeller operation at non-zero AoA.

5.1.1. AZIMUTHAL POSITION

When the propeller operates at a non-zero AoA, the incoming flow no longer aligns with the propeller axis. This misalignment results in a varying propeller blade performance with the azimuthal position. The convention for the phase angle (ϕ) defining the azimuthal position of the blade is illustrated in Fig. 5.1.

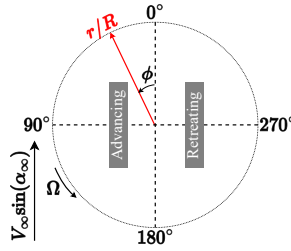


Figure 5.1: Definition of phase angle (ϕ) and conventions used in this thesis

5.1.2. LOCAL ADVANCE RATIO

The in-plane velocity resulting from the non-zero AoA induces a variation in the local advance ratio for each blade section during the rotation, as shown in Fig. 5.2. The propeller blade on the advancing side (downward direction, $\phi = 90^\circ$) experiences a higher in-plane velocity, leading to a reduced local advance ratio compared to the uniform inflow. Conversely, the propeller blade on the retreating side (upward direction, $\phi = 270^\circ$) experiences a lower in-plane velocity, resulting in an increased local advance ratio. This variation is particularly pronounced in the negative thrust condition ($J = 1.10$) due to its higher baseline advance ratio, as evident in Fig. 5.2b.

The local advance ratio directly influences the local geometric AoA at each blade section for a given pitch and twist distribution. A higher local advance ratio (on the retreating side) reduces the local geometric AoA compared to uniform inflow and vice-versa. Consequently, the most significant changes in the local geometric AoA occur at the blade root, with the highest increase at $\phi = 90^\circ$ (advancing side) and the highest decrease at $\phi = 270^\circ$ (retreating side), see Fig. 5.2.

5.1.3. IN-PLANE FORCE AND DELAYED AERODYNAMIC RESPONSE

The variations in local J result in varying thrust and tangential forces over the rotation. The differences in the tangential force on the advancing and retreating sides result in an in-plane force. This in-plane force acts at a delayed $\Delta\phi$ with respect to $\phi = 90^\circ$. This delay

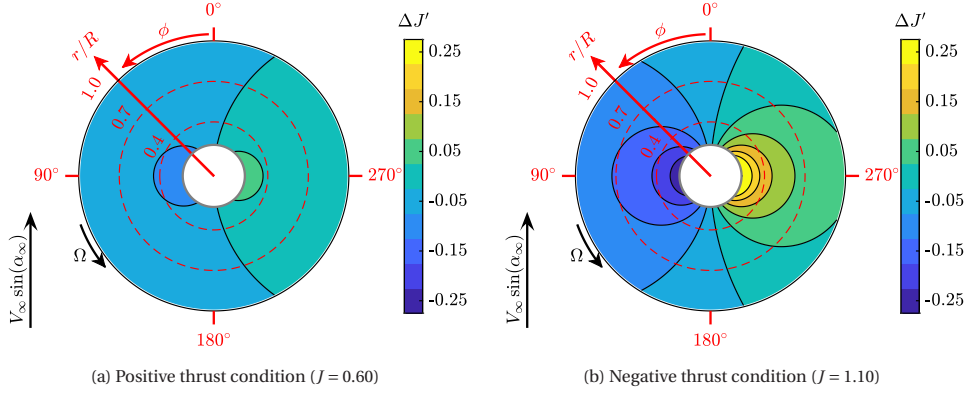


Figure 5.2: Change in the local advance ratio over a rotation at 10° angle of attack compared to 0° angle of attack

is a consequence of the sinusoidal variation in the local inflow conditions at blade sections over the rotation, similar to the delay of the forces observed on an airfoil subjected to an unsteady inflow [100]. Due to this aerodynamic delay, the in-plane force can be decomposed into normal (N_C) and side forces (Y_C), which relate to $\Delta\phi$ as per Eq. (5.1). Here, the normal force is considered positive in the direction of $\phi = 0^\circ$, and the side force is considered positive in the direction of $\phi = 90^\circ$ as shown in Fig. 5.3.

Figure 5.3 shows a vector diagram illustrating the convention for normal (N_C) and side forces (Y_C). The diagram shows a circular path with a red arrow indicating the rotation direction Ω . The vertical axis is labeled $V_\infty \sin(\alpha_\infty)$. The normal force N_C is shown as a red vector pointing towards the center, and the side force Y_C is shown as a red vector pointing tangentially. The angle ϕ is marked at 0° and 90°.

$$\Delta\phi = \tan^{-1} \left(\frac{Y_C}{N_C} \right) \quad (5.1)$$

Figure 5.3: Convention for normal (N_C) and side forces (Y_C)

5.1.4. FREESTREAM-ALIGNED PERFORMANCE PARAMETERS

The performance parameters projected along the propeller axis are crucial for understanding the isolated propeller performance, while the performance parameters projected along the freestream direction are relevant for the performance of the system at the aircraft level. Therefore, two types of definitions are used for comparing the propeller performance parameters: 1) aligned with the propeller axis, and 2) aligned with the freestream (∞). The parameters aligned with the freestream, derived from those aligned with the propeller axis, are illustrated in Fig. 5.4 and defined by Eqs. (5.2) to (5.4).

5.2. AERODYNAMIC RESULTS

This section presents the aerodynamic results, which are divided into five parts. Initially, the effect of the AoA on the integrated performance is analysed for both positive and neg-

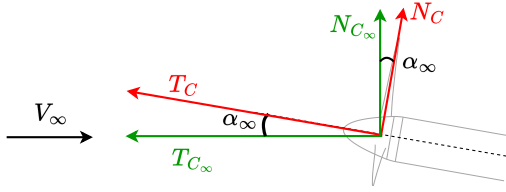


Figure 5.4: Components of propeller performance parameters in propeller axis aligned and freestream aligned reference frames

$$T_{C_\infty} = T_C \cos \alpha_\infty - N_C \sin \alpha_\infty \quad (5.2)$$

$$N_{C_\infty} = N_C \cos \alpha_\infty + T_C \sin \alpha_\infty \quad (5.3)$$

$$\eta_{p_\infty} = \frac{T_{C_\infty}}{P_C} \quad (5.4)$$

ative thrust conditions. This is followed by an analysis of the changes in the blade loading distribution with the change in the AoA. The observed changes are then explained by examining the flow characteristics around the blade sections. Subsequently, a comparison of periodic and broadband fluctuations in the blade loading is presented. Finally, the propeller slipstream characteristics are analysed.

5.2.1. INTEGRATED PERFORMANCE

This section investigates the influence of angle of attack (AoA) on integrated propeller performance using data from numerical simulations previously reported in Tables 3.5 and 3.6, and repeated here in Table 5.1 for ease of reference. At positive thrust, increasing the AoA from 0° to 10° increases both thrust and power magnitudes along the propeller axis by 7% and 4%, respectively. Conversely, at negative thrust, increasing AoA results in decreases in both thrust and power magnitudes along the propeller axis by 7% and 10%, respectively. These changes translate to a 3% increase in propeller efficiency (η_p) for the positive thrust case, whereas a 3% reduction in the turbine efficiency (η_t) for the negative thrust case, both calculated along the propeller axis. The observed changes in the integrated performance with the change in AoA are the result of two effects: 1) the operation of the propeller at a slightly lower freestream advance ratio due to reduced axial inflow ($V_\infty \cos \alpha_\infty$), and 2) the nonlinear nature of the $T_C - J$ and $P_C - J$ curves. A detailed explanation for these trends is given when analysing the blade loading distributions in Section 5.2.2.

Table 5.1: Propeller performance at 0° and 10° angles of attack (calculated using LB-VLES simulations)

J	$\alpha_\infty [^\circ]$	T_C	P_C	η_t	T_{C_∞}	η_{t_∞}	Y_C	N_C	N_{C_∞}	$\Delta\phi [^\circ]$
0.60	0°	0.1135	0.1645	0.6898	0.1135	0.6898	0	0	0	--
	10°	0.1219	0.1710	0.7131	0.1174	0.6868	0.0044	0.0152	0.0362	16.08°
	$\Delta\alpha_\infty\%$	7.42%	3.91%	3.38%	3.46%	-0.43%	--	--	--	--
1.10	0°	-0.0985	-0.0483	0.4908	-0.0985	0.4908	0	0	0	--
	10°	-0.0914	-0.0433	0.4741	-0.0920	0.4712	0.0030	0.0113	-0.0047	14.99°
	$\Delta\alpha_\infty\%$	-7.18%	-10.33%	-3.39%	-6.60%	-3.99%	--	--	--	--

The direction of normal and side forces remains unaffected by the reversal of the

thrust and torque direction between positive and negative thrust cases. This results in a phase difference of about 15° for both positive and negative thrust cases. For the positive thrust case, the normal force perpendicular to the freestream direction (N_{C_∞}) becomes more than double the normal force perpendicular to the propeller axis (N_C) due to the positive contribution from thrust (T_C). This translates to a positive lift force ($0.30T_{C_\infty}$) being generated in the positive thrust case. Conversely, at negative thrust, the normal force perpendicular to the freestream direction (N_{C_∞}) becomes negative (reversed in direction) due to the opposing contribution from the thrust component (refer to Eq. (5.3)). This translates to a small negative lift force ($0.05T_{C_\infty}$) being generated in the negative thrust case.

Further, in the positive thrust case, the contribution from the normal force reduces the thrust magnitude along the freestream direction ($T_{C_\infty} = 0.1174$) compared to that along the propeller axis ($T_C = 0.1219$). In contrast, at negative thrust, the contribution from the normal force results in a higher thrust magnitude along the freestream direction ($|T_{C_\infty}| = 0.0920$) than that along the propeller axis ($|T_C| = 0.0914$). Consequently, though the propeller efficiency along the propeller axis (η_p) is higher at 10° AoA compared to 0° AoA for the positive thrust case, the propeller efficiency along the freestream direction (η_{p_∞}) remains nearly unaffected when changing the AoA.

Given that operating the propeller at a positive thrust and positive AoA generates a positive lift, installing the propeller at such an AoA may prove beneficial at aircraft level. However, at negative thrust, the turbine efficiency along the freestream direction (η_{t_∞}) is reduced by 4% at 10° AoA compared to 0° AoA. Therefore, such an installation would yield a lower harvested energy than the operation at 0° AoA and the generation of a negative lift when operated at negative thrust.

5.2.2. PROPELLER BLADE LOADING

This section analyses the impact of the non-zero AoA ($\alpha_\infty = 10^\circ$) on the propeller blade loading compared to the baseline case ($\alpha_\infty = 0^\circ$). Figures 5.5a and 5.6a show the change in the magnitude of the phase-locked local thrust coefficient ($|\Delta|\overline{T}_c^l(r, \phi)| = |\overline{T}_c^l(r, \phi)|_{\alpha_\infty=10^\circ} - |\overline{T}_c^l(r, \phi)|_{\alpha_\infty=0^\circ}$) at 10° AoA compared to 0° AoA. The phase-locked averaging is performed using the data from eight rotations and all the blades, resulting in a total of 24 samples for each radial and azimuthal location. Positive values indicate increased thrust magnitude, while negative values indicate decreased thrust magnitude. The noisy fluctuations in these figures are attributed to the limited data available (eight rotations) due to computational constraints. Despite the fluctuations, the presented results provide valuable insights into the blade loading changes under non-zero angles of attack. Further, Figs. 5.5b and 5.6b show the azimuthal average of the phase-locked thrust coefficient to represent a mean blade loading ($\overline{T}_c^{\text{mean}}(r) = \frac{1}{2\pi} \int_0^{2\pi} \overline{T}_c^l(r, \phi) d\phi$) experienced by the propeller blade at both 0° and 10° AoA. Along with this mean, the spread of phase-locked thrust distribution over the azimuth ($\overline{T}_c^{\text{spread}}(r) = [\min(\overline{T}_c^l(r, \phi)), \max(\overline{T}_c^l(r, \phi))]$) is also shown to indicate the periodic variation in the blade loading over a rotation.

POSITIVE THRUST CONDITION ($J = 0.60$)

The effect of non-zero AoA on propeller blade loading is well established for the positive thrust conditions [45, 101, 102]. As shown in Fig. 5.5a, the decrease in the local advance ratio on the advancing side leads to an increase in thrust, while the opposite is seen on the retreating side. At positive thrust, $T_C \propto J^{-2}$ and $P_C \propto J^{-3}$. Consequently, a decrease in the advance ratio on the advancing side results in a more pronounced increase in thrust and power compared to the decrease experienced on the retreating side, due to the corresponding increase in its advance ratio. Hence, operating a propeller at non-zero AoA in positive thrust conditions always leads to a higher thrust and power along the propeller axis [45, 101, 102]. This is also evident from Fig. 5.5b. The mean thrust distribution at the 10° AoA is higher than at 0° AoA along the whole blade span, resulting in a 7% increase in the time-averaged integrated thrust, as reported in Table 3.5.

Though the maximum change in advance ratio occurs at $\phi = 90^\circ$ and 180° (Fig. 5.2a), the highest change in thrust distribution occurs around $\phi = 0^\circ$ and 285° (Fig. 5.5a). This shift in the maximum and minimum thrust distribution location is a consequence of the delay in the aerodynamic response to the sinusoidal variation in inflow angle [100]. A similar delay in the tangential force leads to a side force, as explained previously in Section 5.1.3.

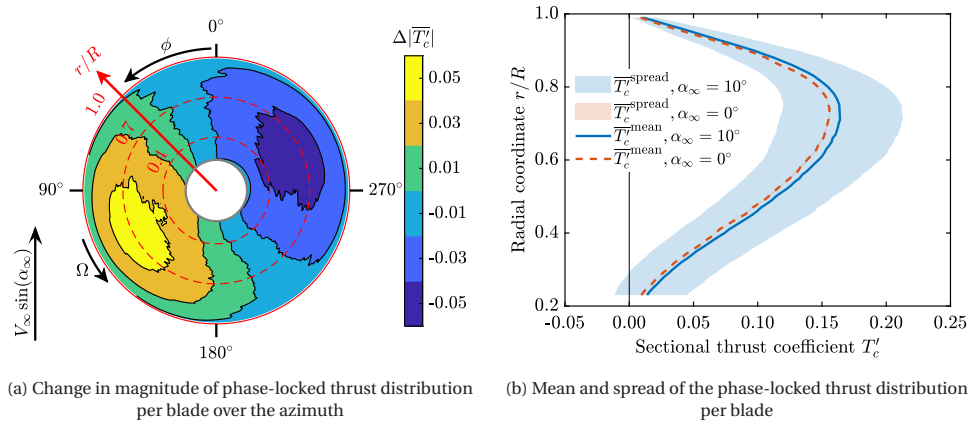


Figure 5.5: Effect of non-zero angle of attack (10°) on the phase-locked thrust distribution per blade compared to 0° angle of attack at the positive thrust condition ($J = 0.60$)

In Fig. 5.5b, the maximum absolute increase in the mean blade loading is observed near the peak of the loading distribution ($0.6R$ - $0.8R$). As expected, the spread of the phase-locked thrust over the azimuth is negligible at 0° AoA due to the almost steady solution for this operation condition. In contrast, at 10° AoA, the highest absolute spread occurs at the radial locations with the maximum loading at 0° AoA, i.e., around $0.7R$. The smallest thrust spread is seen near the propeller tip due to the combined effects of the lowest change in advance ratio and the comparatively low absolute blade loading. Notably, the region near the hub experiences a significant spread in the phase-locked thrust over the azimuth despite low absolute blade loading, primarily driven by the maximum change in advance ratio, as seen in Fig. 5.2a.

NEGATIVE THRUST CONDITION ($J = 1.10$)

Previous studies investigating propeller operation at negative thrust [39, 98, 103] observed a non-monotonic trend for the $T_C - J$ and $P_C - J$ curves. Upto the maximum power output point, both T_C and P_C magnitude increase with the increase in J . In other words, the gradients of the absolute value of the thrust and power coefficients with advance ratio $\left(\frac{\partial|T_C|}{\partial J}, \frac{\partial|P_C|}{\partial J}\right)$ in negative thrust conditions have an opposite sign as compared to positive thrust conditions upto the maximum power output point. Beyond this point, the T_C and P_C magnitudes decrease with the increase in J , resembling the performance trend of positive thrust conditions, albeit with reduced gradient. Therefore, the performance change in the negative thrust condition with the change in AoA depends upon the chosen operating condition.

For the investigated propeller, the maximum power output occurs at approximately $J = 1.15$ [103]. Since the freestream advance ratio ($J = 1.10$) is lower than at the maximum power output point ($J = 1.15$), the decrease in the local advance ratio on the advancing side at 10° AoA compared to 0° AoA results in a decrease in the absolute thrust values (Fig. 5.6a), contrary to positive thrust conditions. On the retreating side, $\frac{\partial|T_C|}{\partial J}$ approaches a plateau with the increase in the local advance ratio resulting in only a small increase in thrust as evident in Fig. 5.6a.

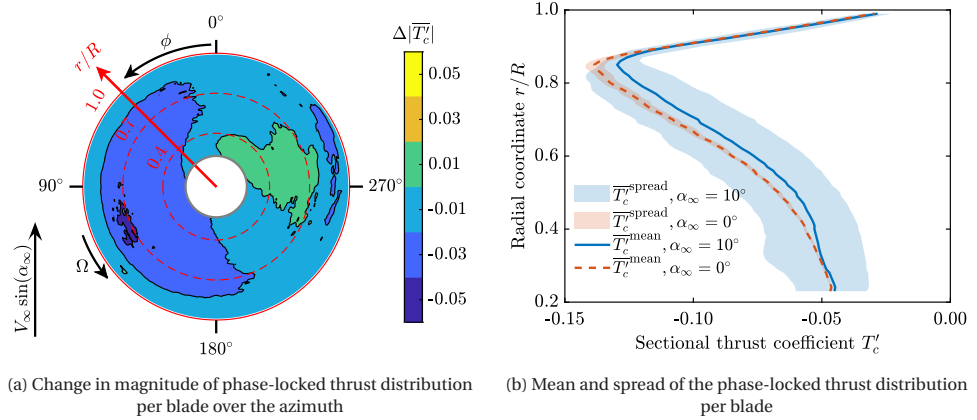


Figure 5.6: Effect of non-zero angle of attack (10°) on the phase-locked thrust distribution per blade compared to 0° angle of attack at the negative thrust condition ($J = 1.10$)

Figure 5.6b presents the mean thrust distribution along with the spread of phase-locked thrust over the azimuth. Due to the dominance of flow separation in negative thrust conditions, the spread of phase-locked thrust over the azimuth is also visible at 0° AoA, with a maximum spread of $\pm 3\%$ occurring at the radial location with the peak blade loading ($0.85R$). This spread is a consequence of the flow separation around the blades, resulting in unsteady flow behaviour in the negative thrust condition even at 0° AoA. Compared to the 0° AoA case, the 10° AoA case exhibits a lower absolute mean blade loading across the entire blade span, resulting in a 7% lower integrated thrust as

reported in Table 3.6. Interestingly, the maximum spread of phase-locked thrust at 10° AoA occurs near the hub region, contrasting with the positive thrust condition where the maximum spread was observed around the radial location of peak loading. This different behaviour is attributed to the dynamic stall of the blade sections near the hub (discussed in Section 5.2.3) and completely separated blade sections outboard, leading to a more pronounced spread of phase-locked thrust over the azimuth near the hub and the smallest spread at the blade tip.

5.2.3. FLOW AROUND THE BLADE SECTIONS

This section analyses the influence of the varying in-plane velocity component over the azimuth on the aerodynamics of blade sections at two radial locations: near the root ($r/R = 0.30$) and the region of maximum loading ($r/R = 0.70$). For this purpose, chordwise pressure distributions have been analysed for both positive and negative thrust conditions. The change in chordwise pressure distributions is explained with the help of variation of the geometric AoA over the azimuth. In addition, the streamlines and local static pressure contours are also shown around these blade sections at different azimuth positions.

5

POSITIVE THRUST CONDITION ($J = 0.60$)

Figure 5.7a shows the change in the local geometric AoA at $\alpha_\infty = 10^\circ$ compared to $\alpha_\infty = 0^\circ$ ($\Delta\alpha_{g_r} = \alpha_{g_r, \alpha_\infty=10^\circ} - \alpha_{g_r, \alpha_\infty=0^\circ}$) for the positive thrust condition. The geometric AoA is changed slightly ($< 0.5^\circ$) at $\phi = 0^\circ$ and 180° for $\alpha_\infty = 10^\circ$ compared to $\alpha_\infty = 0^\circ$ due to the reduced axial inflow ($V_\infty \cos \alpha_\infty$). As expected, the maximum change in geometric angle occurs at $\phi = 90^\circ$ and 270° with the inboard section ($r/R = 0.30$) experiencing a higher change than the outboard section ($r/R = 0.70$).

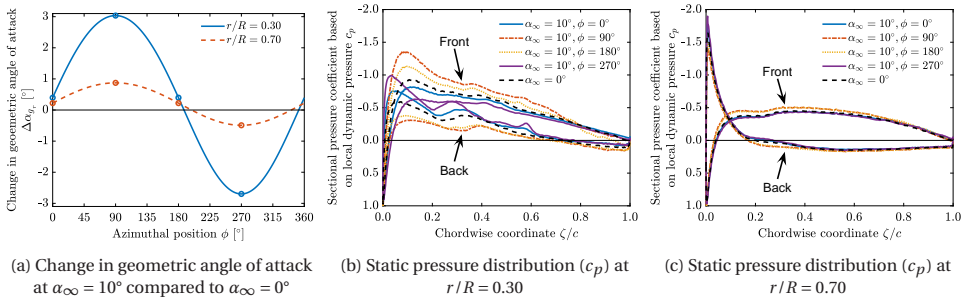


Figure 5.7: Influence of freestream angle of attack (α_∞) on the local geometric angle of attack (α_{g_r}) and chordwise static pressure distribution (c_p) for the positive thrust condition ($J = 0.60$)

Figures 5.7b and 5.7c show the variation in the chordwise static pressure distributions during the rotation, and Fig. 5.8 shows the streamlines around the blade sections over the azimuth at $r/R = 0.30$ and 0.70 for the positive thrust condition, respectively. It should be noted that the y-axis of the chordwise pressure distributions has been reversed to keep the front side of the propeller on top (same as Fig. 5.8). A direct impact of the variations in geometric angles of attack can be seen on the chordwise pressure

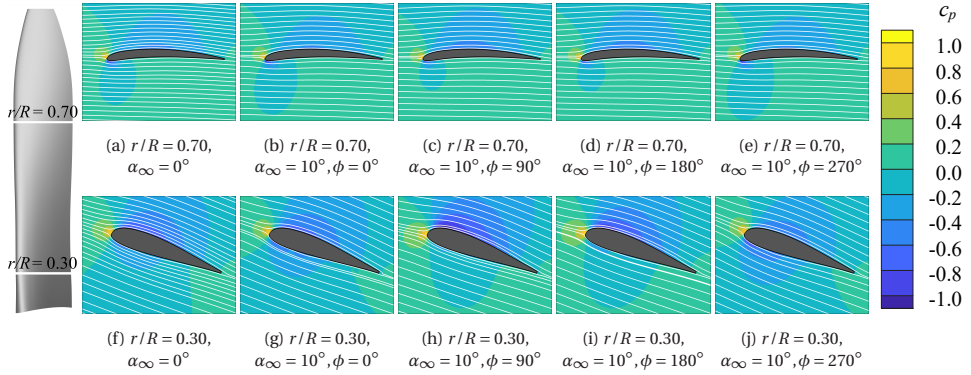


Figure 5.8: Phase-locked, time-averaged streamlines around blade sections along with c_p contours at different radial locations (r/R) for the positive thrust condition ($J = 0.60$)

distributions in Figs. 5.7b and 5.8g to 5.8j for $r/R = 0.30$. As the highest AoA is expected at $\phi = 90^\circ$ for $\alpha_\infty = 10^\circ$ case, the highest pressure difference between the front and back sides of the blade section is also observed at $\phi = 90^\circ$. As the AoA decreases from $\phi = 90^\circ$ to $\phi = 270^\circ$, the pressure difference between the front and back sides also decreases. Though the geometrical AoA is the same at $\phi = 0^\circ$ and $\phi = 180^\circ$, the former shows a lower pressure difference between the front and back sides of the blade section compared to the latter due to the aerodynamic delay in response to the sinusoidal variation in the geometric AoA. As a result of this aerodynamic delay, though the $\phi = 0^\circ$ for $\alpha_\infty = 10^\circ$ case has a higher geometrical AoA than $\alpha_\infty = 0^\circ$ case, the pressure difference between the front and back sides is lower for the former.

At $r/R = 0.70$, the geometric AoA changes by only 1° and -0.5° at $\phi = 90^\circ$ and 270° , respectively, with respect to $\alpha_\infty = 0^\circ$; see Fig. 5.7a. The change is comparatively small in the local static pressure coefficient between different azimuthal positions; see Figs. 5.7c and 5.8b to 5.8e. The highest pressure difference between the front and back sides of the blade section is seen at $\phi = 90^\circ$ due to the highest geometric AoA, and the lowest pressure difference between the front and back sides is seen at $\phi = 270^\circ$ due to the lowest geometric AoA. This shows that the dominant effect is the variation in the local dynamic pressure at this blade section, leading to a significant change in the local thrust coefficient over the azimuth (Fig. 5.5a) and is only marginally affected directly by the blade section performance.

NEGATIVE THRUST CONDITION ($J = 1.10$)

At $J = 1.10$, the cross-flow component results in a larger change in the geometric AoA compared to the $J = 0.60$ case. Specifically, at $r/R = 0.30$, there is a $\pm 6^\circ$ change in geometric AoA at $\phi = 90^\circ$ and 270° , respectively, whereas at $r/R = 0.70$, the respective change is 3° and -2° ; see Fig. 5.9a. The highest positive change in the AoA at $\phi = 90^\circ$ results in an absolute lower AoA at the blade section, resulting in the smallest separation bubble at the blade sections for both $r/R = 0.30$ and 0.70 in Figs. 5.9b and 5.9c. Streamline visualisations in Figs. 5.10c and 5.10h further support this observation. As the AoA becomes more negative from $\phi = 90^\circ$ to $\phi = 270^\circ$, the size of the separation bubble increases for both ra-

dial locations (Fig. 5.10). Though $\phi = 0^\circ$ and $\phi = 180^\circ$ have the same geometric AoA, the separation bubble is larger at $\phi = 0^\circ$ compared to $\phi = 180^\circ$; see Figs. 5.9b and 5.9c. This is a consequence of the delay in the aerodynamic response to the sinusoidal variation in the geometric AoA. These sinusoidal variations in the geometric AoA experienced by the blade sections are analogous to a plunging airfoil, leading to dynamic stall conditions at the negative thrust condition. This dynamic stall leads to a hysteresis effect in the aerodynamic response, resulting in varying pitch moments over the azimuth. Such unsteady loading can pose challenges for structural integrity and complicate control system design.

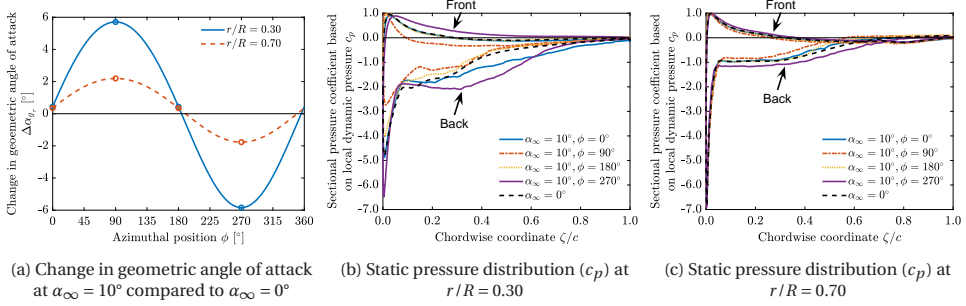


Figure 5.9: Influence of freestream angle of attack (α_∞) on the local geometric angle of attack (α_{gr}) and chordwise static pressure distribution (c_p) for the negative thrust condition ($J = 1.10$)

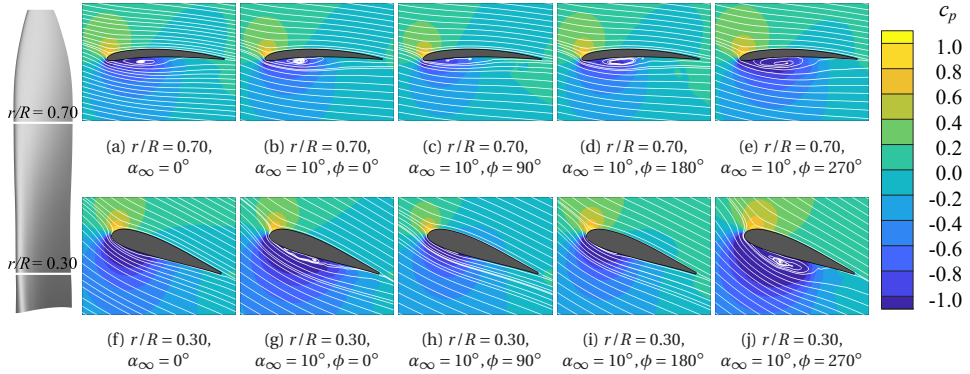


Figure 5.10: Phase-locked, time-averaged streamlines around blade sections along with c_p contours at different radial locations (r/R) for the negative thrust condition ($J = 1.10$)

5.2.4. BROADBAND FLUCTUATIONS

When propeller blades operate in negative thrust conditions, the flow separation around them causes broadband fluctuations in blade loading (Chapter 4), which act as sources of both noise and structural vibrations. To obtain the broadband fluctuations over the azimuth, the phase-locked local thrust coefficient ($T'_c(r, \phi)$) was subtracted from the instantaneous local thrust coefficient ($T'_c(r, \phi, t_{\text{sim}})$). Figure 5.11 displays the root

mean square (RMS) of the resulting broadband fluctuations of local thrust coefficient ($\sigma(T'_c(r, \phi))$) over eight rotations, normalised with the absolute mean thrust distribution ($|\overline{T'_c}^{\text{mean}}(r)|$), for both the positive and negative thrust conditions.

At 0° AoA, the positive thrust condition ($J = 0.60$) has negligible broadband fluctuations as evident from Fig. 5.11a. In contrast, significant fluctuations can be observed at the negative thrust condition ($J = 1.10$) in Fig. 5.11b. The fluctuations increase in the negative thrust condition with radial location due to the increasing separation as observed previously in Chapter 4. For the inboard part of the blade, where the flow is attached, the fluctuations are nearly negligible up to $r/R = 0.40$. However, in the mid-board sections ($0.40 < r/R < 0.70$), the fluctuations are around 2%-3% of the mean thrust level and increase up to 10% or even more at the blade tip.

The 10° AoA case also shows negligible broadband fluctuations in the positive thrust condition; see Fig. 5.11c. In contrast, the operation of the propeller at 10° in the negative thrust condition changes the distribution of broadband fluctuations over the blade as compared to 0° AoA; see Figs. 5.11b and 5.11d. As the inboard part of the blade exhibits dynamic stall (Fig. 5.10), during the part of the rotation ($\phi = 75^\circ - -195^\circ$) over which the flow is almost fully attached, fluctuations with negligible amplitude are observed for $r/R \leq 0.70$. However, as the separation bubble extends to the trailing edge on the retreating side, it leads to fluctuations of around 5% of the mean thrust level. Even on the outer part of the blade, the fluctuations are amplified on the retreating side and are comparatively reduced on the advancing side, as expected.

RELATIVE AMPLITUDES OF PERIODIC AND BROADBAND FLUCTUATIONS

Given the increased broadband fluctuations in the negative thrust condition, a quantitative analysis of the relative amplitudes of periodic and broadband fluctuations is necessary. For this purpose, the absolute mean thrust value ($|\overline{T'_c}^{\text{mean}}(r)|$), previously shown in Figs. 5.5b and 5.6b, has been subtracted from the phase-locked thrust coefficient ($\overline{T'_c}(r, \phi)$). The resulting quantity has been normalised with the absolute mean thrust value ($|\overline{T'_c}^{\text{mean}}(r)|$) to assess the periodic variation in the local thrust coefficient. The amplitude of broadband fluctuations has been indicated with the shaded regions showing the standard deviation of the quantity.

Figure 5.12 displays the periodic variations along with broadband fluctuations of the local thrust coefficient at three radial stations: $r/R = 0.30$, 0.70 , and 0.90 , which correspond to the near blade root, maximum-loading region, and near blade tip, respectively. There is almost 180° phase difference between positive and negative thrust conditions due to the opposite change in the absolute thrust on the advancing and retreating side as seen previously in Figs. 5.5a and 5.6a.

At $r/R = 0.30$ in Fig. 5.12a, the positive thrust condition displays a larger range of periodic variations in the local thrust coefficient (-94% to 109%) compared to the negative thrust condition (-33% to 41%). This contrasts with the larger variations in the local advance ratio observed in the negative thrust condition in Fig. 5.2. It can be attributed to two factors. Firstly, the given blade section has a lower mean loading in the positive thrust condition ($|\overline{T'_c}^{\text{mean}}| = 0.034$) than the negative thrust condition ($|\overline{T'_c}^{\text{mean}}| = 0.049$), as shown in Figs. 5.5b and 5.6b. This results in a higher relative periodic variation in the positive thrust condition even for similar absolute changes in the thrust coefficient.

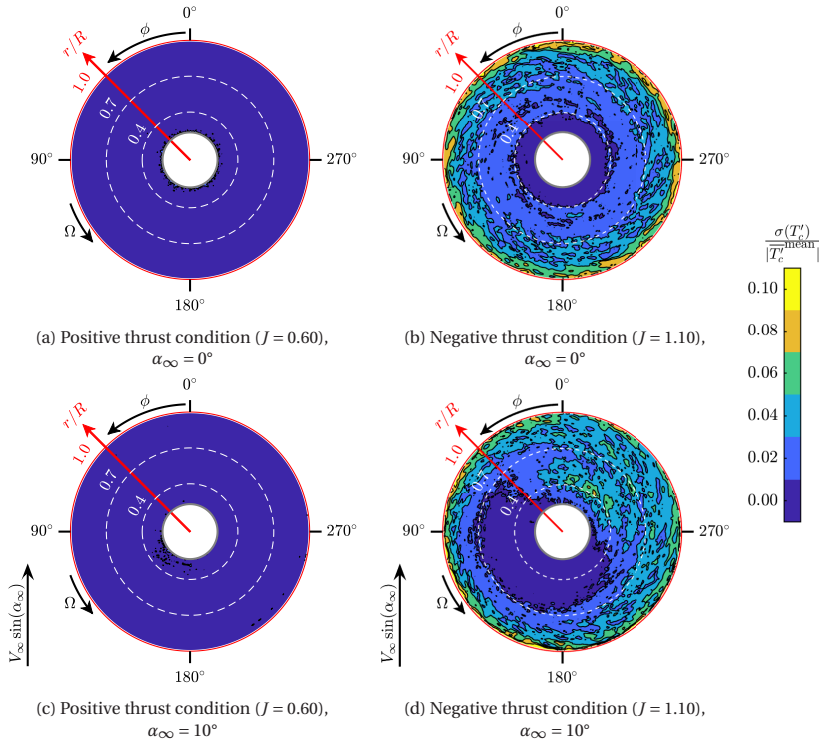


Figure 5.11: Normalised broadband fluctuations in phase-locked thrust distribution at 0° and 10° angle of attack at the positive ($J = 0.60$) and negative ($J = 1.10$) thrust conditions

Secondly, the thrust coefficient has reduced sensitivity to the changes in the advance ratio at negative thrust conditions, as depicted in the $T_C - J$ curve in previous studies [39, 98, 103]. Specifically, the blade section operates at high negative angles of attack, which leads to the formation of a leading-edge separation bubble that reduces the $C_l - \alpha$ slope, consequently reducing the sensitivity of the thrust coefficient to advance ratio variations. The positive thrust condition exhibits broadband fluctuations amplitude up to $\pm 2\%$ of the mean thrust value, whereas the negative thrust condition shows broadband fluctuations of up to $\pm 4\%$ of the mean thrust value. The higher broadband fluctuations in the negative thrust condition are caused by the observed separation bubble at this radial location in Fig. 5.10.

At $r/R = 0.70$, the relative maximum amplitude of the periodic variation in thrust coefficient is reduced to 30% and 25% of the mean thrust value for the positive and negative thrust conditions, respectively. The broadband fluctuations are negligible in the positive thrust condition, with variations of up to $\pm 1\%$ of the mean thrust value. In contrast, they are noticeable in the negative thrust condition, reaching up to $\pm 7\%$ of the mean thrust value between $180^\circ \leq \phi \leq 360^\circ$. The increased broadband fluctuations on the retreating side are attributed to the periodic appearance of the separation bubble, as seen in Fig. 5.10.

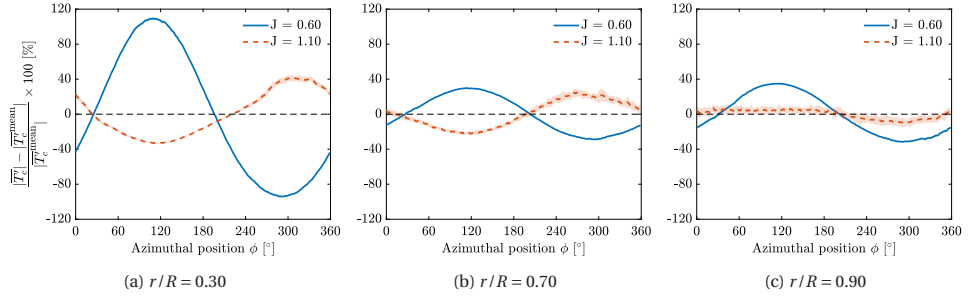


Figure 5.12: Change in the absolute phase-locked thrust coefficient ($|T_c^T|$) with respect to the absolute mean value ($|T_c^{\text{mean}}|$) over the azimuthal position (ϕ)

At $r/R = 0.90$, the positive thrust condition shows the relative amplitude of periodic variations of up to 35% of the mean thrust value with negligible amplitude of broadband fluctuations (up to $\pm 2\%$ of the mean thrust value). Interestingly, the negative thrust condition no longer displays a sinusoidal pattern observed at inboard sections (Fig. 5.12c). The periodic fluctuations become non-sinusoidal and exhibit a reversal in trend compared to the inboard sections. This is expected to be the consequence of the operation of the blade section in the deep stall region, where the increase of the absolute AoA on the retreating side ($180^\circ \leq \phi \leq 360^\circ$) leads to a decreased C_l and the corresponding lower thrust coefficient. At this radial station, the broadband fluctuations (up to $\pm 7\%$ of the mean thrust value) appear to be almost as significant as the periodic fluctuations, which range from -10% to 7% of the mean thrust value.

5.2.5. PROPELLER SLIPSTREAM

In a tractor propeller-wing configuration, the interaction between the propeller slipstream and wing significantly affects the wing performance. These changes are mainly determined by two parameters: the swirl angle induced by the propeller slipstream and the modification of the dynamic pressure. Therefore, this section presents an analysis of these two parameters for the positive and negative thrust conditions, both at zero and non-zero angles of attack. All the results presented in this section are obtained at $x/R = 1.0$ on a plane parallel to the propeller plane. This axial position has been based on the potential location of a lifting surface (wing). The projected propeller disk is shown in the figures with the help of a dashed-red line indicating $r/R = 1.0$.

SWIRL ANGLE

Figure 5.13 shows the time-averaged swirl angle (θ_{swirl}) calculated using Eq. (5.5). The swirl angle has been defined as positive in the direction of propeller rotation. It is important to highlight that the in-plane freestream velocity component has been subtracted from the tangential velocity to isolate and account for the swirl induced solely by the propeller.

$$\theta_{\text{swirl}} = \tan^{-1} \left(\frac{V_t - V_\infty \sin(\alpha_\infty) \sin(\phi)}{V_x} \right) \quad (5.5)$$

At $\alpha_\infty = 0^\circ$, as expected, there is an axisymmetric swirl in the propeller slipstream, see Figs. 5.13a and 5.13b. The operation at the positive thrust condition ($J = 0.60$) introduces a positive swirl of about 3° to 4° (Fig. 5.13a), with contraction of the slipstream to $0.93R$ at $x/R = 1.0$ (indicated by the outer edge of the positive swirl contour). On the other hand, in the negative thrust condition ($J = 1.10$), the propeller introduces a negative swirl in the slipstream with strong radial gradients. Near the hub, the swirl angle is about -12° , reducing to -5° at $0.5R$ and -4° to -2° in the outboard region (Fig. 5.13b). This steep radial gradient of swirl angle in the inboard sections results from high inboard torque loading in the negative thrust conditions (Chapter 4). Additionally, the stall of the propeller tip leads to positive torque loading on the blade tip, resulting in a positive swirl (2°) near the edge of the slipstream.

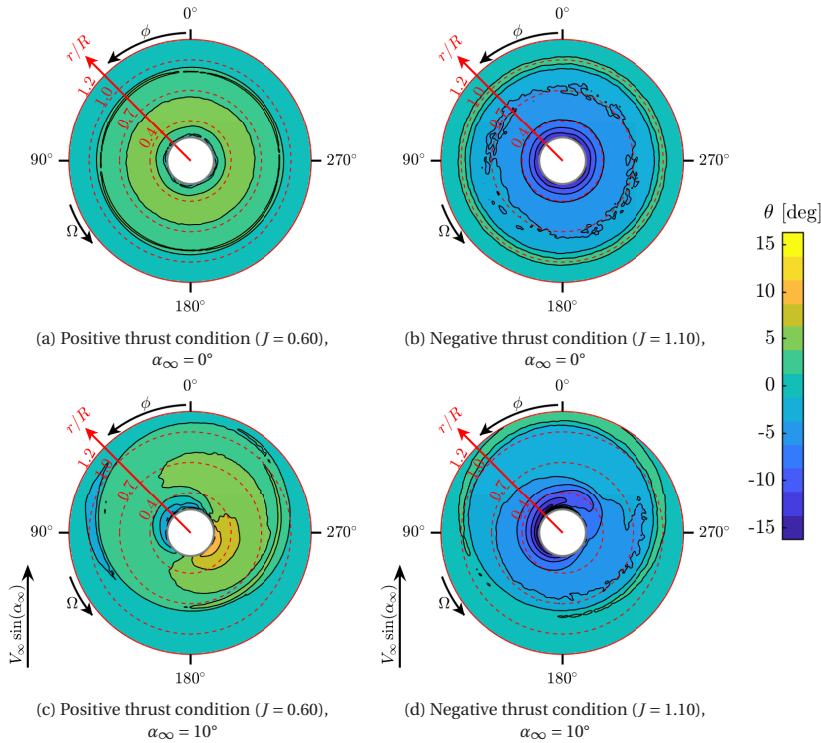


Figure 5.13: Time-averaged swirl angle (θ_{swirl}) in the propeller slipstream at $x/R = 1.0$

At the 10° AoA, the slipstream is deflected outside the projected propeller region ($r/R > 1.0$) above the nacelle and distorted beneath it due to the in-plane velocity component of the freestream ($V_\infty \sin \alpha_\infty$); see Figs. 5.13c and 5.13d. In the inboard region, the root vortices induce a negative swirl, whereas the potential flowfield induced by the nacelle (due to the in-plane velocity component) generates a negative swirl on the advancing side and a positive swirl on the retreating side. The combined effect of the two (root vortex and potential flowfield induced by nacelle) results in a negative swirl on the advancing side for both positive and negative thrust conditions Figs. 5.13c and 5.13d.

Conversely, on the retreating side, these effects partially cancel out, leading to a positive swirl for the positive thrust condition and a small negative swirl for the negative thrust condition.

Away from the nacelle ($r/R \geq 0.7$), the increased tangential velocity on the advancing side relative to the 0° AoA case is balanced by the corresponding increase in axial velocity, while the decreased tangential velocity on the retreating side is balanced by the decrease in axial velocity. This results in similar swirl values as in the case of 0° AoA for both positive and negative thrust conditions. For the negative thrust condition, as the stall of the blade tip is more pronounced on the retreating side (shown previously in Fig. 5.10), a positive torque is required to propel the tip along with the blade, resulting in a slight positive swirl around $r/R = 1$ on the retreating side as shown in Fig. 5.13d.

Additionally, in Fig. 5.13c, the slipstream appears slightly shifted towards the retreating side in the positive thrust condition due to a more significant contraction on the advancing side than on the retreating side. Conversely, the retreating side experiences more expansion in the negative thrust condition, leading to a similar apparent shift in Fig. 5.13d.

DYNAMIC PRESSURE

Figure 5.14 shows the squared magnitude of the normalised velocity within the propeller slipstream. This quantity directly reflects changes in dynamic pressure compared to the freestream condition. At the 0° AoA, the dynamic pressure distribution in the slipstream exhibits axisymmetric behaviour for both positive and negative thrust conditions. Operation under positive thrust conditions (Fig. 5.14a) results in increased dynamic pressure in the slipstream compared to the freestream, reaching approximately 30% around $0.4R$ and 40% between $0.5R$ - $0.8R$ for the selected thrust setting ($T_C = 0.11$); see Fig. 5.14a. On the other hand, the operation at negative thrust (Fig. 5.14b) results in a decrease in dynamic pressure within the slipstream compared to the freestream. This decrease is approximately 20% between $0.3R$ - $0.7R$ and 30% between $0.7R$ - $0.9R$ for the selected thrust setting ($T_C = -0.10$); see Fig. 5.14b.

Upon increasing the AoA from 0° to 10° , the dynamic pressure distribution within the propeller slipstream is no longer axisymmetric (as expected). In the positive thrust condition (Fig. 5.14c), the advancing side experiences a dynamic pressure increase of up to 60% compared to the freestream, while the retreating side sees a maximum increase of 40%. Consequently, there is effectively higher dynamic pressure on the advancing side and lower dynamic pressure on the retreating side compared to the 0° AoA case. These variations in dynamic pressure are directly related to the changes in the blade loading distribution shown in Fig. 5.5a. In the inboard regions, the presence of the nacelle disrupts the in-plane velocity component of the freestream, resulting in a region of reduced dynamic pressure (deficit) above it, as observed in Fig. 5.14c. This region of the deficit is further amplified by the negative blade loading in the inboard part of the blade on the retreating side, as indicated by the lower bound of the $\overline{T'_c}^{\text{spread}}$ in Fig. 5.5b.

For the negative thrust condition (Fig. 5.14d), the advancing side experiences up to 20% lower dynamic pressure compared to the freestream for $r/R \geq 0.60$, while the retreating side experiences a decrease of up to 30%. Again, this results in a higher dynamic pressure on the advancing side and lower dynamic pressure on the retreating side as

compared to the 0° AoA case. These changes in the dynamic pressure correspond directly to the observed changes in the blade loading in Fig. 5.6. For $r/R < 0.60$, the combined effects of the tangential velocity induced by the propeller and the velocity induced by the nacelle's potential flowfield result in up to 5% decrease in dynamic pressure on the advancing side and up to 40% decrease on the retreating side.

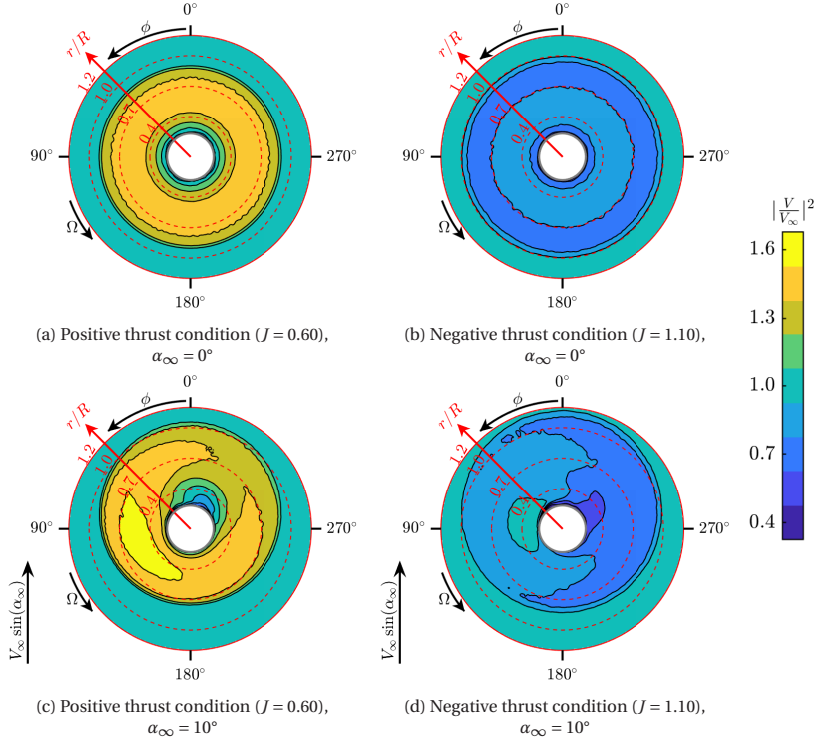


Figure 5.14: Time-averaged dynamic pressure $\left(\left|\frac{V}{V_\infty}\right|^2\right)$ in the propeller slipstream at $x/R = 1.0$

INFERENCES FOR A WING IMMERSED IN A PROPELLER SLIPSTREAM

Based on the results shown in Figs. 5.13 and 5.14, it is evident that a wing immersed in a slipstream experiences distinct effects depending on the thrust condition and AoA. At a negative thrust condition at 0° AoA, the slipstream induces a negative swirl and a reduced dynamic pressure compared to the slipstream at a positive thrust condition. The negative swirl increases the effective AoA on the advancing side while decreasing it on the retreating side. Therefore, the part of the wing located on the retreating side experiences a double negative effect: decreased dynamic pressure and a decreased AoA due to the swirl. In contrast, on the advancing side, the effect of the decreased dynamic pressure is partially compensated by the increased AoA induced by the swirl. Therefore, the impingement of the slipstream of a propeller operating at negative thrust conditions results in a higher reduction in the lift on the retreating side than on the advancing side.

Operation of a propeller at negative thrust conditions at a non-zero AoA results in a higher dynamic pressure on the advancing side and a lower dynamic pressure on the retreating side compared to the 0° AoA. The higher dynamic pressure, coupled with the beneficial impact of the negative swirl on the AoA, enhances lift generation on the advancing side compared to 0° AoA. Conversely, on the retreating side, the lower dynamic pressure and the adverse effect of the negative swirl on the AoA result in a lower lift generation than at 0° AoA. Therefore, a non-zero AoA further amplifies the differences in the lift generated on the advancing and retreating sides at negative thrust conditions.

In the positive thrust condition, the positive swirl induced by the slipstream reduces the effective AoA on the advancing side and increases the effective AoA on the retreating side. On the advancing side, the decrease in the effective AoA due to the swirl is partially countered by the increase in the dynamic pressure. Conversely, on the retreating side, both the increased dynamic pressure and the increased effective AoA due to the swirl angle result in an increase in lift. At a non-zero AoA, the part of the wing on the advancing side experiences a higher dynamic pressure and lower positive swirl, leading to a higher lift compared to the 0° AoA scenario. Conversely, on the retreating side, the decrease in dynamic pressure results in a lower lift generation than the 0° AoA case. Therefore, in contrast to the negative thrust conditions, a non-zero AoA tends to reduce the differences in the lift generated on the advancing and retreating sides at positive thrust conditions.

5.3. FAR-FIELD AEROACOUSTIC RESULTS

The operation of a propeller at non-zero angles of attack significantly changes the noise characteristics compared to its operation at 0° AoA [104, 105]. Two mechanisms account for these changes: the periodic variations in blade loading and the asymmetric phase modulation of the strength of noise sources. The asymmetric phase modulation is the kinematic/acoustic effect, which is a result of the periodic variation of observer-source relative Mach number for an observer rigidly rotating with the blade [104, 106, 107]. The present study investigates the relative importance of these two effects by conducting FW-H computations with and without the convective effects due to the freestream cross-flow velocity component ($V_\infty \sin \alpha_\infty$) when the propeller operates at the 10° AoA.

The far-field noise was computed on a circular array with a radius of $10D$, centred around the propeller centre. The array included 24 evenly spaced virtual microphones in two planes: the plane of propeller rotation (YZ plane) and the plane along the axis of the propeller (XZ plane). To isolate the impact of the AoA on the noise generation mechanisms, the microphones were fixed relative to the propeller itself, meaning the microphones were kept in the same location even when the freestream was tilted to change the AoA.

In both planes, the total noise at the circular arrays was further decomposed into thickness and loading noise using the monopole and dipole terms, respectively, in the so-called solid FW-H formulation [81, 82]. The noise directivity was plotted in terms of overall sound pressure level (OSPL) in two different frequency ranges: $0.9 \leq \text{BPF} \leq 10$ and $0.9 \leq \text{BPF} \leq 1.1$, where BPF refers to blade passing frequency. The former represents the overall sound pressure level directivity, whereas the latter is used to investigate the directivity of tonal noise at the most dominant harmonic, i.e., the first BPF. Here, the

lower bound of 0.9 BPF eliminates potential contributions from numerical noise sources arising due to differences in blade loading on the propeller blades. These variations are inherent to the limitations of LB-VLES working with Cartesian meshes, leading to up to $\pm 4\%$ difference in blade loadings for $J = 0.60$ and $\pm 1\%$ difference in blade loadings for $J = 1.10$ compared to the blade-averaged loading.

5.3.1. NOISE DIRECTIVITY IN THE PLANE OF PROPELLER ROTATION

POSITIVE THRUST CONDITION ($J = 0.60$)

Figure 5.15 shows the far-field noise directivity in the plane of propeller rotation at the positive thrust condition ($J = 0.60$). Figures 5.15a and 5.15b display the noise directivity at 0° and 10° AoA, respectively, for the frequency range of $0.9 \leq \text{BPF} \leq 10$. Similarly, Figures 5.15c and 5.15d show the noise directivity for the frequency range of $0.9 \leq \text{BPF} \leq 1.1$. In Figs. 5.15b and 5.15d, an additional noise directivity denoted as "Total (no cross-flow)" is shown with blue-cross markers. It has been calculated without accounting for the convection effects of the freestream cross-flow velocity component ($V_\infty \sin \alpha_\infty$) and is used to illustrate the relevance of the aforementioned asymmetric phase modulation for the given operating condition. The corresponding PSD plots are presented in Fig. 5.16 for $\phi = 0^\circ$ and 180° .

The noise directivity at 0° AoA shows expected axisymmetry around the propeller axis, see Figs. 5.15a and 5.15c. However, when the AoA is changed from 0° to 10° , the noise is no longer axisymmetric around the propeller axis (Figs. 5.15b and 5.15d). The total noise increases in the region from which the propeller is tilted away, i.e., $90^\circ < \phi < 270^\circ$ and decreases in the opposite region, i.e., $270^\circ < \phi \leq 90^\circ$. These changes are in agreement with the literature [104, 108–110]. The change in the noise directivity is caused by unsteady (periodic) loading on the propeller blades. The total noise calculated without accounting for the convection effects of the freestream cross-flow velocity component (blue-cross markers) shows results similar to those obtained when including these convection effects. Therefore, the influence of asymmetric acoustic modulation by the cross-flow velocity component is minor compared to the impact of unsteady blade loading for the given case.

The change in the AoA from 0° to 10° results in a maximum increment of 5 dB in noise emissions occurring at $\phi = 195^\circ$ and a maximum reduction of 8 dB occurring at $\phi = 15^\circ$ in the loading noise. This increase and decrease are direct results of the change in the blade loading at 10° AoA compared to 0° (Fig. 5.5). Since the loading noise generated by the propeller blades primarily radiates in the perpendicular direction, the maximum and minimum noise locations are located 90° ahead of the maximum and minimum blade loading locations, respectively.

In contrast to the loading noise, the thickness noise exhibits a negligible change (± 0.5 dB) with the varying AoA. This can be attributed to the relatively smaller variation in the effective velocity at the outboard sections ($\pm 3\%$ at the blade tip) compared to the corresponding variation in the blade loading, as previously shown in Fig. 5.12. At 0° AoA, the thickness noise is almost as significant as the loading noise. However, at the 10° AoA, the thickness noise becomes dominant between $300^\circ < \phi < 60^\circ$ due to the decrease in the loading noise, whereas the loading noise remains dominant for the rest of the azimuth.

For further insights into the spectral content of the propeller noise emissions, the

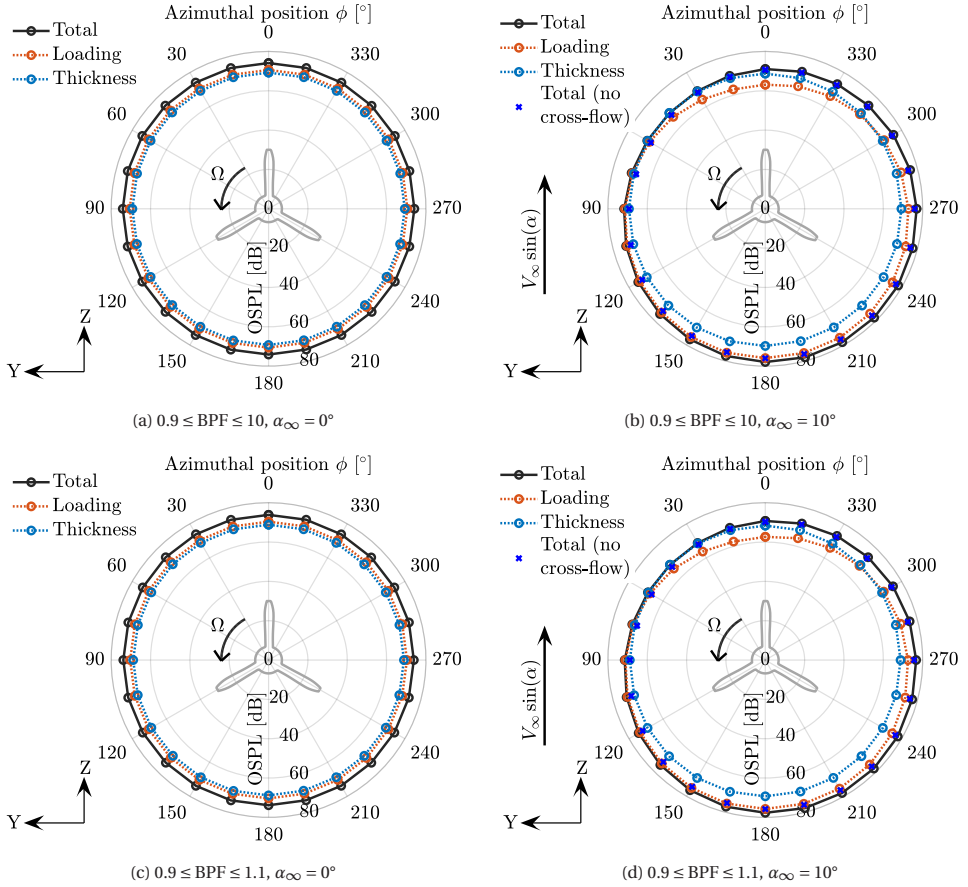


Figure 5.15: Effect of angle of attack on the azimuthal noise directivity in the plane of propeller rotation at the positive thrust condition ($J = 0.60$)

PSD of the pressure signal obtained at virtual microphones is shown in Fig. 5.16. The PSD is presented for two azimuthal positions, 0° and 180° , which correspond to the regions of maximum decrease and increase of the loading noise, respectively. At 10° AoA, a decrease is observed in the first BPF at $\phi = 0^\circ$ and an increase at $\phi = 180^\circ$, consistent with the noise directivity plots. Similar trends can be observed for the second BPF.

NEGATIVE THRUST CONDITION ($J = 1.10$)

The noise directivity plots for the negative thrust condition ($J = 1.10$) are shown in Fig. 5.17. An axisymmetric trend is observed at 0° AoA, as expected. Unlike the positive thrust case ($J = 0.60$), the thickness noise is no longer the dominant noise source. This is because the reduced tip Mach number at $J = 1.10$ compared to $J = 0.60$ decreases the thickness noise, which is more sensitive to the tip Mach number than the loading noise. Additionally, the loading noise is significantly lower in the negative thrust condition compared to the positive thrust condition. This is due to the lower magnitude of T_C

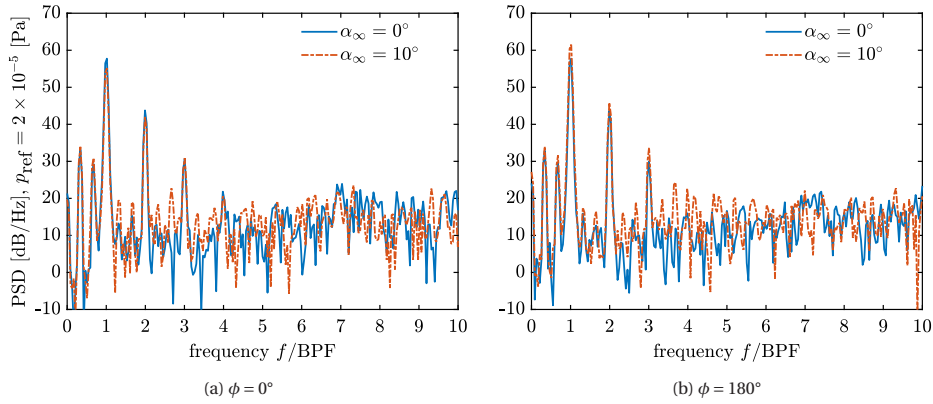


Figure 5.16: Effect of angle of attack on the power spectrum density of the pressure signal obtained at virtual microphones located in the plane of propeller rotation at the positive thrust condition ($J = 0.60$)

5

(Table 3.5), lower tip Mach number, and the inboard shift of the power distribution [98] in the negative thrust case compared to the positive thrust case.

Similar to $J = 0.60$, the blue-cross markers in Figs. 5.17b and 5.17d represent the noise directivity when neglecting the convection effect of the cross-flow component. These markers show results very similar to the total noise with the cross-flow component (Fig. 5.17b), indicating that the unsteady blade loading again dominates the change in the noise directivity. At 10° AoA, the total noise increases by up to 4 dB between $270^\circ \leq \phi \leq 90^\circ$ and decreases by up to 2 dB between $90^\circ \leq \phi \leq 270^\circ$ compared to 0° ; see Fig. 5.17b. Similar changes can also be observed in the noise directivity at the first BPF in Fig. 5.17d. The change in AoA from 0° to 10° results in a decrease of up to 12 dB in the loading noise in the region from which the propeller is tilted away ($90^\circ \leq \phi \leq 270^\circ$) and an increment of up to 6 dB in the opposite direction ($270^\circ \leq \phi \leq 90^\circ$) as shown in Fig. 5.17c. This trend differs from the positive thrust condition (Fig. 5.15b), where a decrease was observed between $270^\circ \leq \phi \leq 90^\circ$ and an increase between $90^\circ \leq \phi \leq 270^\circ$.

The difference in the noise directivity between the positive and negative thrust conditions can be explained by revisiting the changes in blade loading shown in Fig. 5.12. As the variation in the absolute blade loading in the negative thrust condition is 180° out of phase as compared to the positive thrust condition, the corresponding changes in the loading noise directivity are also out of phase by 180° . Surprisingly, for this operating condition, the interference between the thickness and the loading noise becomes destructive between $120^\circ < \phi < 210^\circ$, resulting in a decreased tonal noise. This effect is also observable in Fig. 5.17b, where the total noise level is slightly lower than the loading noise levels between the aforementioned azimuthal positions. The detailed investigation into the reasons behind the observed destructive interference is presented in Section 5.3.1.

The relative level of tonal and broadband noise can be observed by examining the PSD at two azimuthal positions: $\phi = 0^\circ$ and $\phi = 180^\circ$, as shown in Fig. 5.18. Figure 5.18a depicts an increase in the noise at the first BPF at $\alpha_\infty = 10^\circ$, consistent with the results presented in Fig. 5.17d. The broadband noise levels are comparable at both α_∞ values.

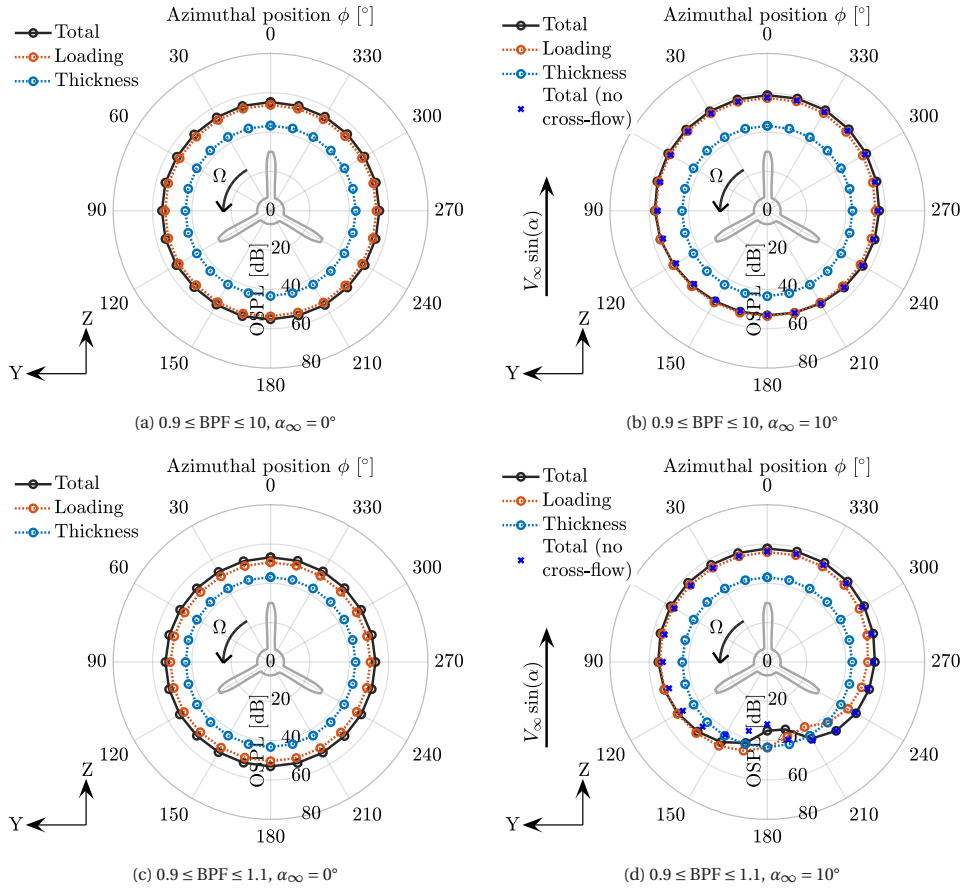


Figure 5.17: Effect of angle of attack on the azimuthal noise directivity in the plane of propeller rotation at the negative thrust condition ($J = 1.10$)

At $\phi = 180^\circ$, the noise level at the first BPF is significantly reduced. However, there is an observable increase in broadband noise between 1-5 BPFs, which partially compensates for the decrease of the tonal noise at the first BPF. This increase in broadband noise is a result of the stalling of the blade tip, as seen in Fig. 5.12c.

PRESSURE SIGNAL PEAK AMPLITUDE AND PHASE DIFFERENCE BETWEEN LOADING AND THICKNESS NOISE SIGNALS

The destructive interference observed between loading and thickness noise for $120^\circ < \phi < 210^\circ$ in Fig. 5.17d is further investigated by band passing the loading and thickness noise pressure signal at the microphones for the first BPF ($0.9 \leq \text{BPF} \leq 1.1$). Figures 5.19a and 5.19b show the peak amplitude of the resulting pressure signal for both thickness and loading components for the positive ($J = 0.60$) and negative ($J = 1.10$) thrust conditions, respectively. Further, Fig. 5.19c shows the phase difference between the peak amplitudes of the resulting loading and thickness noise pressure signals.

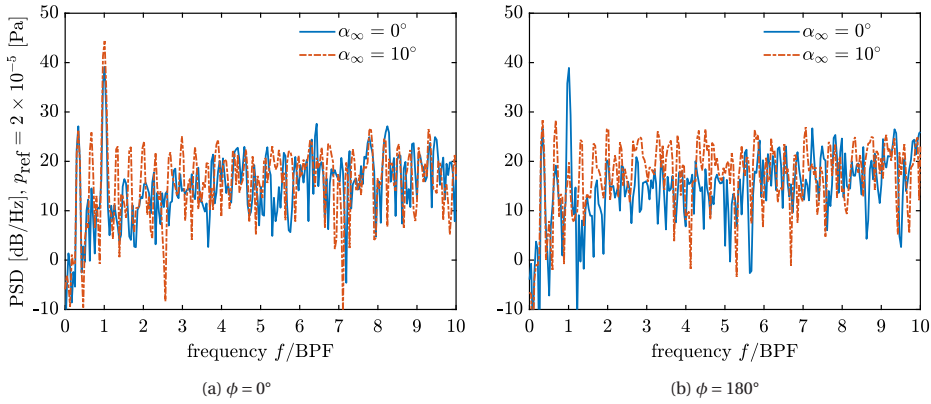


Figure 5.18: Effect of angle of attack on the power spectrum density of the pressure signal obtained at virtual microphones located in the plane of propeller rotation at the negative thrust condition ($J = 1.10$)

5

At $\alpha_\infty = 0^\circ$, the pressure signal peak amplitudes for both thickness and loading noise exhibit minimal variation with the azimuthal position for both thrust conditions ($J = 0.60$ and 1.10); see Figures 5.19a and 5.19b. The small variations in the loading noise peak amplitude at $J = 1.10$ result from the extensive flow separation at this condition. The pressure signal peak amplitudes at $J = 1.10$ are one order lower than at $J = 0.60$, which agrees with the previously observed lower loading and thickness noise for the former condition.

At $\alpha_\infty = 10^\circ$, the peak amplitude of the pressure signal of the thickness noise shows a slight variation with the azimuth as a consequence of the varying tip Mach number due to the cross-flow, particularly evident for $J = 0.60$ in Fig. 5.19a. Removing the cross-flow component confirmed this, resulting in similar and almost constant thickness noise peak amplitudes at both α_∞ values. The variation in the peak amplitude of the pressure signal of the loading noise at $\alpha_\infty = 10^\circ$ is dominated by the unsteady blade loading effect for both $J = 0.60$ and 1.10 . Therefore, this variation directly corresponds to the variation in the blade loading seen in Fig. 5.12 with a shift of 90° as the loading noise is radiated in the perpendicular direction.

In addition to the variation in the peak amplitude of the pressure signal of the loading noise with the azimuth, the phase difference between the loading and thickness noise signals also varies at a non-zero AoA as shown in Fig. 5.19c. At $\alpha_\infty = 0^\circ$, the loading noise signal is 94° ahead of the thickness noise signal at the positive thrust condition ($J = 0.60$) with negligible variations in the phase difference with the azimuthal position. On the other hand, the loading noise signal lags behind the thickness noise signal by approximately 102° in the negative thrust condition ($J = 1.10$).

However, a non-zero α_∞ introduces ϕ -dependent variations in the phase difference, irrespective of the thrust condition. For $J = 0.60$, the phase difference increases between $0^\circ \leq \phi \leq 60^\circ$ reaching a maximum phase difference of 133° at $\phi = 60^\circ$ and then starts to decrease between $60^\circ \leq \phi \leq 300^\circ$ reaching a minimum phase difference of 55° at $\phi = 300^\circ$ and then it increases again. For the negative thrust condition, the phase difference between the loading and thickness noise signals decreases from -96° at $\phi = 0^\circ$ to -172°

at $\phi = 150^\circ$. The phase difference between the loading and thickness noise signals decreases beyond -180° for $\phi > 150^\circ$. It is shown as a positive phase difference by adding the 360° to the phase difference values due to the cyclic nature of the effect of the phase difference on the total noise. The phase difference between the loading and thickness noise signals decreases from 179° at $\phi = 165^\circ$ to -96° at $\phi = 360^\circ$. As the pressure signals of the loading and thickness noise are nearly out of phase for $120^\circ \leq \phi \leq 210^\circ$ for the negative thrust condition, their sum results in a lower total noise level compared to when they are in phase or partially in phase at other azimuthal positions as seen in Fig. 5.17d.

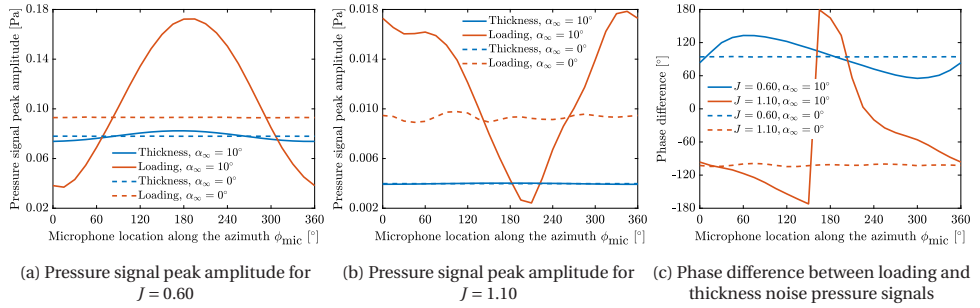


Figure 5.19: Effect of angle of attack on the bandpassed pressure signal ($0.9 \leq \text{BPF} \leq 1.1$) obtained at virtual microphones located at $10D$ in the plane of propeller rotation

These results show that, at non-zero angles of attack, two key factors influence the azimuthal variation in total noise: changes in peak amplitude and the changing phase difference between loading and thickness noise over the azimuth. The thickness noise signal remains nearly constant over the azimuth. The key physical phenomenon driving both the peak amplitude change and the phase difference variation is the varying blade loading over the azimuth. The variation in phase difference between thickness and loading noise presents a potential new parameter for propeller noise optimisation, potentially allowing for reduced noise without compromising aerodynamic performance. Further research using the analytical solution of the FWH analogy is necessary to validate these findings.

5.3.2. NOISE DIRECTIVITY IN THE PLANE ALONG THE PROPELLER AXIS POSITIVE THRUST CONDITION ($J = 0.60$)

Figure 5.20 illustrates the noise directivity along the propeller axis for the positive thrust condition ($J = 0.60$). As thickness noise is a tonal noise source, it mainly radiates in the propeller plane (69 dB) and has zero contribution along the propeller axis, as seen in Fig. 5.20a. On the other hand, the loading noise has both broadband and tonal noise components, leading to a noise level of up to 61 dB along the propeller axis and 71 dB in the propeller plane. This is also evident in the noise directivity of the first BPF in Fig. 5.20c, where the tonal noise mainly propagates in the propeller plane, resulting in a total noise level of 74 dB at $\theta = 90^\circ$, compared to the noise level of 31-32 dB along the propeller axis.

While the noise directivity is symmetric around the propeller axis at 0° AoA (as ex-

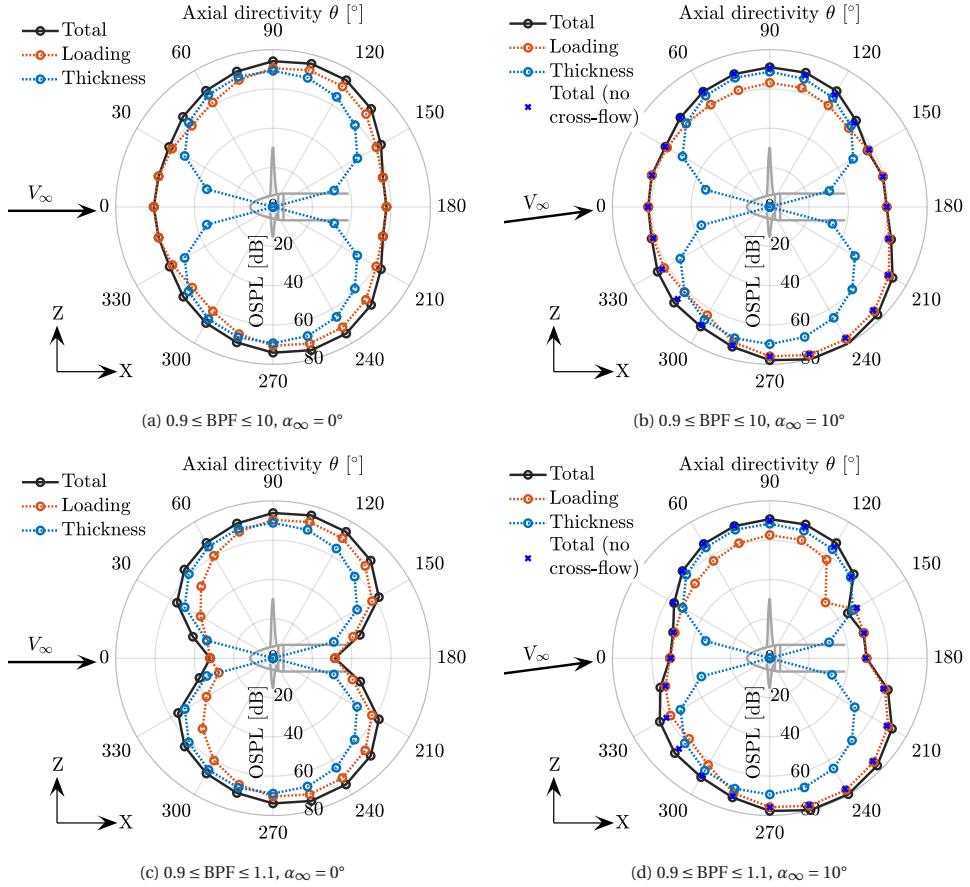


Figure 5.20: Effect of angle of attack on the noise directivity along the propeller axis at the positive thrust condition ($J = 0.60$)

pected), the same is not true at the 10° AoA. For the positive thrust condition, the total noise increases in the region where the propeller is tilted away and vice versa, as shown in Fig. 5.20b, which agrees with the trends seen in Section 5.3.1. The change in the noise directivity is mainly driven by changes in the loading noise at the first BPF, as observed in Figs. 5.20b and 5.20d. The maximum change in the total noise is up to ± 8 dB at $\theta = 210^\circ$ and 135° , respectively, due to the significant change in the loading noise. As a result, the thickness noise becomes the dominant source of noise for $45^\circ \leq \theta \leq 135^\circ$ in Figs. 5.20b and 5.20d.

Although the tonal noise changes significantly with the AoA, the broadband noise remains almost constant. This can be observed from the PSD plots shown in Fig. 5.21. There is no tonal noise at 0° AoA (as expected), but tonal peaks appear, albeit small, at $\alpha_\infty = 10^\circ$. It is important to acknowledge that the peaks at $(1/3)$ and $(1/6)$ BPF likely stem from numerical artifacts due to slight variations in blade loading across propeller blades,

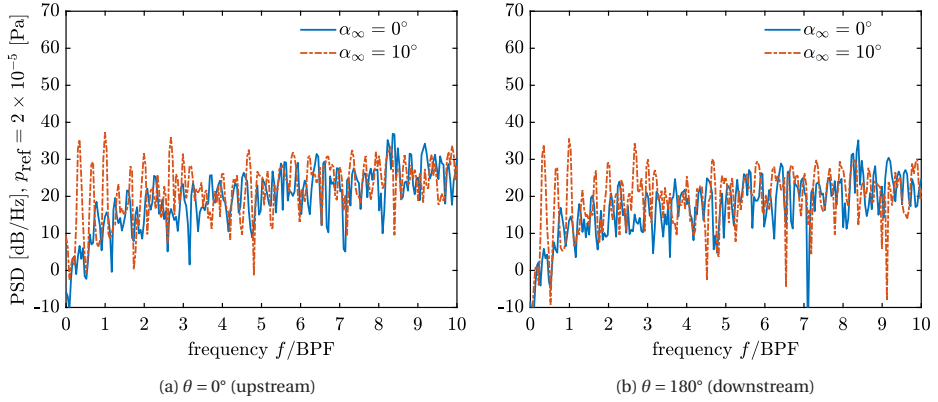


Figure 5.21: Effect of angle of attack on the power spectrum density of the pressure signal obtained at virtual microphones located along the propeller axis at the positive thrust condition ($J = 0.60$)

as mentioned at the start of this section. Despite these numerical artifacts, a tonal peak is visible at the first BPF for the 10° AoA case compared to the 0° AoA case. Therefore, unsteady blade loading leads to the propagation of noise along the propeller axis, which is in agreement with the literature [105, 107].

Similar to the previous Section 5.3.1, the noise without the convective effect of the cross-flow velocity component (blue-cross markers) shows similar trends as the noise with the convective effect of the cross-flow velocity (Figs. 5.20b and 5.20d). Therefore, the asymmetric modulation of the noise sources is also irrelevant in the plane perpendicular to the plane of rotation.

NEGATIVE THRUST CONDITION ($J = 1.10$)

Figure 5.22 shows the noise directivity in the plane aligned with the propeller axis for the negative thrust condition ($J = 1.10$). As previously mentioned in Section 5.3.1, the thickness noise is significantly reduced at $J = 1.10$ compared to $J = 0.60$, making the loading noise the dominant source of noise at both 0° and 10° AoA. The loading noise is higher along the propeller axis (63 dB at $\theta = 0^\circ$ and 62 dB at 180°) than in the propeller plane (54 dB at $\theta = 90^\circ$ and 270°), as shown in Fig. 5.22a. This is a consequence of significant broadband noise in the negative thrust condition due to extensive flow separation around the propeller blades. The reduced tonal noise compared to the positive thrust condition is partially due to the reduced absolute loading and reduced tip Mach number but also due to the change in the loading distribution along the blade span. Again, the noise directivity at 0° AoA is symmetric around the propeller axis as expected.

The directivity of noise at the first harmonic at 0° AoA (Fig. 5.22c) shows a significant noise level along the propeller axis (41 dB) due to the presence of broadband noise between $0.9 \leq BPF \leq 1.1$, as can be seen in the PSD plots in Fig. 5.23. Interestingly, the directivity at the first BPF shows destructive interference between loading and thickness noise at $0^\circ < \theta < 75^\circ$, resulting in lower total noise at these axial directivity angles. This is expected to be the consequence of the same mechanism explained earlier in Section 5.3.1.

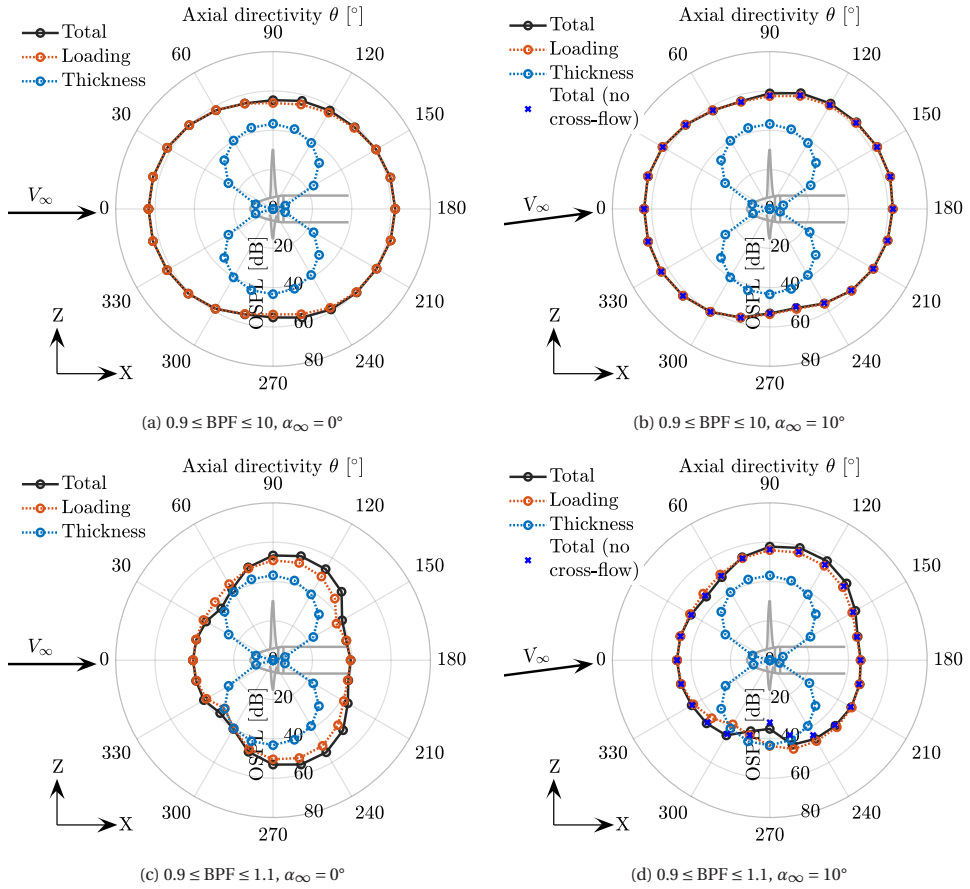


Figure 5.22: Effect of angle of attack on the noise directivity along the propeller axis at the negative thrust condition ($J = 1.10$)

At the 10° AoA, the directivity of noise is significantly altered with respect to the 0° AoA case, as can be seen in Fig. 5.22. The loading noise is increased up to 4 dB between $90^\circ \leq \theta \leq 180^\circ$ and reduced up to 3 dB between $180^\circ \leq \theta \leq 270^\circ$ compared to 0° AoA, as shown in Fig. 5.22b. These changes in the noise levels are opposite to the trends seen for $J = 0.60$. As explained before in Section 5.3.1, the differences in the noise directivity between negative and positive thrust conditions at non-zero angles of attack are the consequence of different variations in the absolute blade loading over the advancing and retreating sides (Fig. 5.12). Like all previous results, the total noise without convection effects shows identical results as the total noise with convection effects, indicating that the dominant mechanism responsible for changes in noise directivity at the 10° AoA is unsteady loading.

The directivity of loading noise at the first BPF (Fig. 5.22d) also shows similar changes with the change in the AoA. However, an interesting change can be seen in the inter-

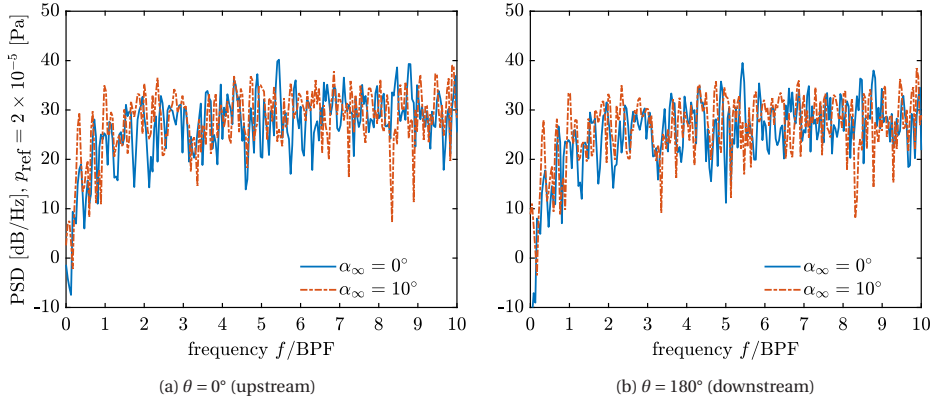


Figure 5.23: Effect of angle of attack on the power spectrum density of the pressure signal obtained at virtual microphones located along the propeller axis at the negative thrust condition ($J = 1.10$)

ference of the loading and thickness noise. In addition to the observed destructive interference between loading and thickness noise for $0^\circ < \theta < 75^\circ$ at 0° AoA, there is also destructive interference for $210^\circ \leq \theta < 300^\circ$ at 10° AoA, which reduces total noise in the lower part of the plane. This phenomenon has been explained earlier in Section 5.3.1.

Contrary to expectations, the broadband noise stays almost constant with the change of AoA. This can also be seen from PSD plots shown in Fig. 5.23. Unlike the positive thrust case, no clear tonal peaks are observed along the propeller axis at the 10° AoA due to the lower tonal noise compared to the broadband noise in this case.

5.4. KEY FINDINGS

This chapter investigated the impact of a non-zero AoA on aerodynamics and far-field noise characteristics of an isolated propeller operating at positive and negative thrust conditions. The direction of the normal and side forces remained constant in the propeller axis aligned reference frame, while thrust and torque directions reversed between positive and negative thrust regimes. The combined effects of the positive thrust and positive normal force resulted in a significant positive lift ($0.30T_{C_\infty}$) in the positive thrust condition. In contrast, the positive normal force counters the negative thrust component in the negative thrust condition, resulting in a small negative lift ($0.05T_{C_\infty}$). Along the freestream direction, the propeller efficiency (η_{p_∞}) remained nearly unaffected by AoA in positive thrust conditions. Given that operating the propeller at a positive thrust and a positive AoA generates positive lift without affecting η_{p_∞} , installing the propeller at such an AoA may prove beneficial at the aircraft level. In contrast, such an installation would yield a lower harvested energy than the equivalent operation at 0° AoA and the generation of a negative lift when operated at negative thrust.

At a negative thrust condition with a 10° AoA, a dynamic stall was observed on the inboard sections of the propeller blade, with flow attaching on the advancing side and separating on the retreating side. Meanwhile, the outboard sections, already stalled at the 0° AoA, undergo changes in the extent of separation with azimuthal position (with

a noticeable increase in broadband fluctuations on the retreating side). Near the blade tip ($r/R = 0.90$), the periodic fluctuations deviate from a sinusoidal pattern due to the operation of blade sections in a deep stall region, where broadband fluctuations in the local thrust coefficient ($\pm 7\%$ of the mean thrust level) are comparable in magnitude to the periodic variations (-10% to $+7\%$ of the mean thrust level).

The operation at a non-zero AoA results in an asymmetry in the slipstream as a result of sinusoidal variation in the geometric AoA over the azimuth. The operation of the propeller at 10° AoA results in a higher dynamic pressure on the advancing side compared to the retreating side for both positive and negative thrust conditions. A wing immersed in such propeller slipstream experiences distinct effects depending on the thrust condition and AoA. In positive thrust conditions, when the propeller and wing have the same sign of AoA (both positive or both negative), differences in slipstream dynamic pressure between the advancing and retreating sides tend to reduce the differences in lift increase between the upgoing and downgoing blade sides compared to the 0° case. In negative thrust conditions, when the propeller and wing have the same sign of AoA, differences in slipstream dynamic pressure between the advancing and retreating sides amplify the differences in lift reduction between the upgoing and downgoing blade sides compared to the 0° case, with a greater reduction in lift on the upgoing blade side.

The changes in the propeller blade loading lead to changes in the far-field aeroacoustic performance. In the plane of propeller rotation, the first blade passing frequency (BPF) exhibits increased noise (up to 5 dB) in the region away from the tilt direction and decreased noise (up to 8 dB) towards the tilt direction for the positive thrust condition. This trend reverses in the negative thrust case, with increased noise towards the tilt direction (up to 6 dB) and decreased noise away from it (up to 12 dB) at the first BPF. These opposing trends are a direct consequence of the opposite changes in absolute blade loading caused by the AoA. In the plane along the propeller axis (in which the freestream is tilted to change AoA), noise levels are higher along the propeller axis (62-63 dB) than in the plane of rotation (54-59 dB) in the negative thrust condition for both angles of attack (0° and 10°). In contrast, positive thrust exhibits lower noise levels along the propeller axis (58-62 dB) compared to the plane of rotation (71-78 dB). This is a consequence of higher broadband noise and lower tonal noise in the negative thrust condition than in the positive thrust condition.

Furthermore, in the negative thrust condition, destructive interference between thickness noise and loading noise reduces the total noise in specific regions: $120^\circ < \phi < 210^\circ$ in the propeller plane and $210^\circ \leq \theta < 300^\circ$ in the plane along the propeller axis. This destructive interference results from the approximately $\pm 180^\circ$ phase difference between the loading and thickness noise signal at the specified locations. The phase difference between the loading and the thickness noise signals varies over the azimuth for the non-zero AoA as a consequence of the varying blade loading over the azimuth. The variation in phase difference between thickness and loading noise presents a potential new parameter for propeller noise optimisation, potentially allowing for reduced noise without compromising aerodynamic performance. Further research using the analytical solution of the FWH analogy is necessary to validate these findings.

PART III

ASSESSMENT OF AERODYNAMIC MODELS

6

BENCHMARKING OF AERODYNAMIC MODELS FOR PROPELLERS

Given the complex aerodynamics associated with the propeller operation at negative thrust conditions, as detailed in Chapters 4 and 5, models that perform well under positive thrust may not be reliable for negative thrust conditions. Thus, it is critical to benchmark the capabilities of different aerodynamic models in the negative thrust regime compared to the positive thrust regime. This chapter addresses this need by systematically evaluating numerical methods of varying fidelity against experimental data. The spectrum of fidelity encompasses low-fidelity tools: BEM and LL, mid-fidelity through SRANS, and high-fidelity simulations involving URANS and LB-VLESs.

The chapter begins with an overview of the operating conditions simulated using the different numerical tools in Section 6.1. Given the significance of integrated performance as a fundamental metric in design optimisation studies, it is the first one presented in the analysis in Section 6.2. Differences in performance are further examined through skin friction contours and streamlines around blade sections in Section 6.3. Next, the total pressure coefficient in the propeller slipstream and blade loading distributions are compared in Section 6.4. The analysis concludes with a comparison of phase-locked out-of-plane vorticity within the propeller slipstream in Section 6.5, deemed relevant for investigations of propeller-wing interactions. The key findings derived from these analyses are presented method by method in Section 6.6.

The contents of this chapter have been adapted from Ref. [49].

6.1. OVERVIEW OF OPERATING CONDITIONS

Multiple additional operating conditions were simulated besides those listed in Table 2.2 for the comparison of the numerical methods against the available experimental data [46]. The low-fidelity tools BEM and LL were evaluated at numerous advance ratios ranging from $J = 0.55$ to 1.48 due to their lower computational cost. SRANS, URANS, and LB-VLES $_{y^+ \geq 15}$ were evaluated at eight advance ratios. Due to the considerably higher computational cost associated with LB-VLES $_{y^+ \leq 10}$ (refer to Tables 2.3 and 2.4), only two advance ratios ($J = 0.60, 1.10$) were simulated using this high-fidelity tool. Table 6.1 details the different advance ratios simulated using mid- and high-fidelity tools.

Table 6.1: List of operating conditions simulated using mid and high-fidelity numerical methods

J	$T > 0$		$T < 0$					
	0.60	0.61	0.75	0.89	1.09	1.10	1.28	1.48
SRANS	✓	✓	✓	✓	✓	✓	✓	✓
URANS	✓	✓	✓	✓	✓	✓	✓	✓
LB-VLES $_{y^+ \geq 15}$	✓	✓	✓	✓	✓	✓	✓	✓
LB-VLES $_{y^+ \leq 10}$	✓					✓		

6

6.2. TIME-AVERAGED INTEGRATED PERFORMANCE

This section presents a comparative analysis of five distinct parameters as a function of advance ratio (J): thrust coefficient (C_T), power coefficient (C_P), energy-harvesting efficiency (η_{eh}), as well as propeller and turbine efficiency (η_p, η_t). The variation of these parameters with the advance ratio is plotted in Fig. 6.1, showing the predictions from different numerical tools compared to experimental results. Additionally, Tables 6.2 and 6.3 quantify the differences in the integrated performance calculated using different numerical tools as compared to the experimental data for a positive ($J = 0.60$) and a negative thrust condition ($J = 1.10$), respectively. The uncertainties in the experimental data calculated for a 95% confidence interval are depicted by the shaded-blue region in the figure and as \pm values in the tables. However, the shaded blue region is only visible for η_p in Fig. 6.1 due to the small values of uncertainty for other parameters.

Figures 6.1a and 6.1b show the comparison of C_T vs J and C_P vs J , respectively. The uncertainty (95% confidence interval) in the experimental C_T and C_P values at $J = 0.60$ is $\pm 2\%$ and $\pm 3\%$, respectively. The LB-VLES $_{y^+ \leq 10}$, available only for two operating points, display a good agreement with the experiment for C_T at both conditions, with a 3% error at the positive thrust condition ($J = 0.60$) and less than 1% error at the negative thrust condition ($J = 1.10$). In contrast, C_P shows an 8% error at the positive thrust condition ($J = 0.60$) and almost no error at the negative thrust condition ($J = 1.10$) compared to the experiment; see Tables 6.2 and 6.3.

The LB-VLES $_{y^+ \geq 15}$ follow the trend of variation of C_T with J for the whole range of advance ratios, as can be seen in Fig. 6.1a. However, the same cannot be said for C_P ; see Fig. 6.1b. These simulations significantly overpredict C_P beyond the maximum power output point ($J > 1.10$), reaching up to 26% deviation at $J = 1.48$ compared to the ex-

periment. Closer examination (Table 6.2) reveals underpredictions of both C_T and C_P by approximately 4% and 15%, respectively, at the positive thrust condition ($J = 0.60$). In contrast, the negative thrust condition ($J = 1.10$) exhibits a considerable increase in errors (Table 6.3), reaching 8% and 16% for C_T and C_P , respectively. These significant inaccuracies, particularly for $J \geq 1.10$, are likely caused by the delayed transition from modeled to resolved turbulence, leading to errors in predicting complex flow phenomena such as separation and reattachment. This argument is further supported by the superior agreement of LB-VLESS $_{y^+ \leq 10}$ with experimental data at $J = 1.10$ compared to LB-VLESS $_{y^+ \geq 15}$. Section 6.3 will discuss this in more detail.

The SRANS and URANS simulations show near-identical solutions in the positive thrust regime ($J = 0.60$), showing errors of approximately 3-4% for C_T and 7-8% for C_P ; see Table 6.2. The significant underprediction of C_P by the RANS, as well as LB-VLES simulations at $J = 0.60$, is expected to be a consequence of the lower drag prediction in the simulations than experiment. In contrast, at the negative thrust condition near the maximum power output point ($J = 1.10$), the errors in both C_T (1%-2%) and C_P (less than 1%) drop significantly compared to the positive thrust regime; see Table 6.3.

The differences between SRANS and URANS simulations become more pronounced as the advance ratio increases in the negative thrust regime (Figs. 6.1a and 6.1b). The rising discrepancies between the two highlight the growing significance of unsteadiness with increasing advance ratio due to the increase in flow separation in the negative thrust regime. Moreover, the errors in C_T and C_P values for URANS simulations, relative to the experiment, increase with the increase in the advance ratio. For instance, at $J = 1.48$, the errors in C_T and C_P values increase to 3% and 6%, respectively. The increasing error can be attributed to the inaccuracies introduced by turbulence modelling in URANS simulations.

Table 6.2: Integrated performance of the propeller at the positive thrust condition ($J = 0.60$) calculated using different methods

Method	C_T	$\Delta C_T\%$	C_P	$\Delta C_P\%$	η_p	$\Delta \eta_p\%$
Experiment	0.04234 ± 0.00103	$\pm 2.44\%$	0.04160 ± 0.00056	$\pm 1.35\%$	0.6107 ± 0.0171	$\pm 2.79\%$
LB-VLES $_{y^+ \leq 10}$	0.04109	-2.96%	0.03810	-8.40%	0.6469	+5.93%
LB-VLES $_{y^+ \geq 15}$	0.04085	-3.51%	0.03554	-14.58%	0.6898	+12.95%
URANS	0.04055	-4.22%	0.03841	-7.66%	0.6335	+3.73%
SRANS	0.04097	-3.23%	0.03853	-7.39%	0.6381	+4.48%
LL	0.04713	+11.31%	0.03864	-7.12%	0.7318	+19.84%
BEM	0.04512	+6.56%	0.03785	-9.01%	0.7152	+17.11%

While negative thrust conditions were expected to be more challenging to simulate, comparisons of Tables 6.2 and 6.3 show that mid and high-fidelity simulations (except for LB-VLESS $_{y^+ \geq 15}$) exhibit higher errors for the positive thrust condition ($J = 0.60$) than the negative thrust condition ($J = 1.10$). This unexpected trend can be attributed to the operation of the propeller at a relatively low Reynolds number based on chord and effective velocity ($2 \times 10^5 - 3 \times 10^5$) for these operating conditions. As a result, laminar separation bubbles are likely present in the experiments, whereas the simulations assume

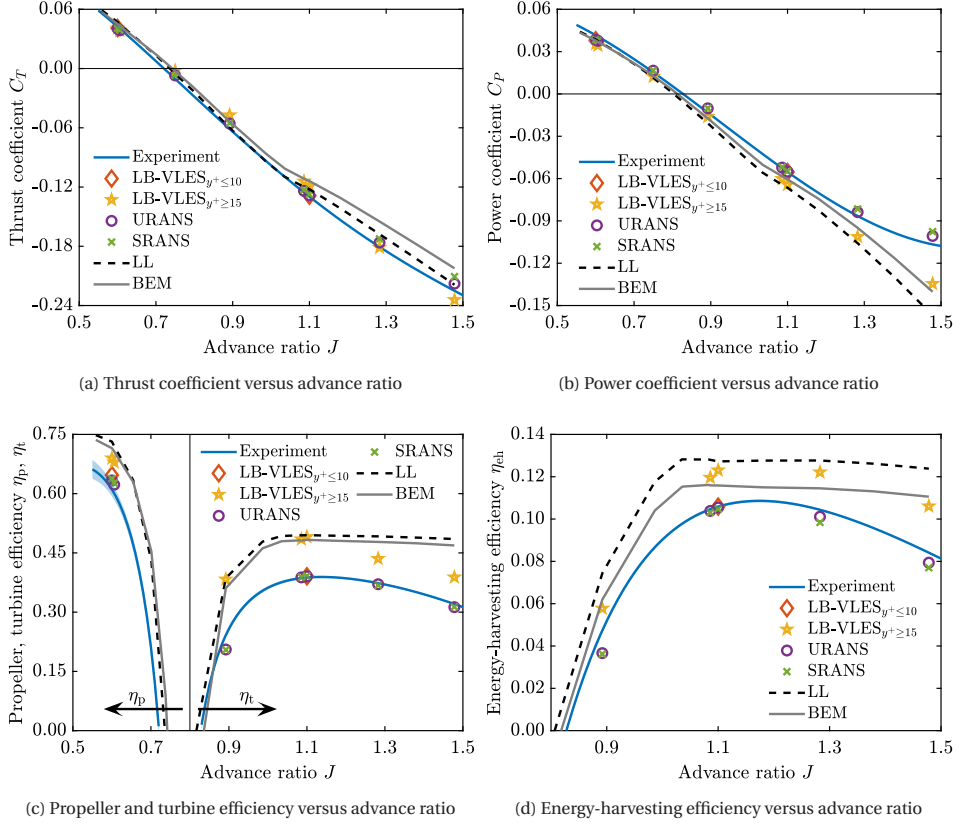


Figure 6.1: Comparison of integrated performance estimated using different numerical methods with the experimental data

 Table 6.3: Integrated performance of the propeller at the negative thrust condition ($J = 1.10$) calculated using different methods

Method	C_T	$\Delta C_T\%$	C_P	$\Delta C_P\%$	η_t	$\Delta \eta_t\%$
Experiment	-0.12978 ± 0.00069	$\pm 0.53\%$	-0.05534 ± 0.00035	$\pm 0.63\%$	0.3877 ± 0.0032	$\pm 0.83\%$
LB-VLES $_{y^+ \leq 10}$	-0.12878	-0.77%	-0.05535	+0.01%	0.3907	+0.79%
LB-VLES $_{y^+ \geq 15}$	-0.11918	-8.17%	-0.06434	+16.26%	0.4908	+26.61%
URANS	-0.12835	-1.11%	-0.05514	-0.37%	0.3905	+0.74%
SRANS	-0.12724	-1.96%	-0.05480	-0.98%	0.3915	+1.00%
LL	-0.12217	-5.87%	-0.06651	+20.18%	0.4949	+27.67%
BEM	-0.11398	-12.18%	-0.06056	+9.42%	0.4830	+24.60%

a fully turbulent flow. The presence of laminar separation bubbles in the experiments leads to a higher drag compared to the mid- and high-fidelity simulations, resulting in

the observed differences for the positive thrust condition. This effect was verified by estimating the performance of blade sections using XFOIL with and without forced transition. Additionally, experimental measurements show a negative total pressure coefficient (C_{pt}) at the blade tip (discussed later in Section 6.4.1), which is not replicated in the mid and high-fidelity simulations, further amplifying the difference in the experimental and simulated integrated performance for the positive thrust condition.

In contrast, the negative thrust condition ($J = 1.10$) experiences flow separation along most of the blade span (shown later in Section 6.3.2). Fully separated flows are comparatively easier to simulate than the prediction of laminar separation bubbles. Consequently, a closer match between experiments and mid and high-fidelity simulations (except for LB-VLESS _{$y^+ \geq 15$}) is observed for the negative thrust condition ($J = 1.10$) compared to the positive thrust condition ($J = 0.60$).

The low-fidelity tools BEM and LL showcase a reasonable agreement with experimental gradients for both C_T and C_P with respect to J up to $J \leq 1.10$ (close to the maximum power output point); see Figures 6.1a and 6.1b. However, as the advance ratio increases further, both tools struggle to capture even the gradients accurately for both C_T and C_P with respect to J . In the positive thrust regime ($J = 0.60$), the LL model overestimates C_T by 11% and underestimates C_P by 7%; see Table 6.2. At the negative thrust condition ($J = 1.10$), the error in C_T reduces to 6%, but with a significant jump in C_P error to 20%, as listed in Table 6.3. The BEM model exhibits a rise in C_T error from 7% to 12% between $J = 0.60$ and $J = 1.10$, while the error in C_P stays almost unaffected (9%) across both advance ratios.

The underprediction of $|C_T|$ and overprediction of $|C_P|$ by BEM and LL for $J \geq 1.10$ is expected to be the consequence of neglecting 3D flow effects in BEM and LL theories and their impact on the boundary layer of blade sections, resulting in a delayed stall prediction in RFOIL [59, 60].

Figure 6.1c shows the variation of propeller efficiency for positive thrust conditions and turbine efficiency for negative thrust conditions. The LB-VLESS _{$y^+ \leq 10$} show errors of 6% and 1% compared to experimental data for positive and negative thrust conditions, respectively. The higher error at $J = 0.60$ (positive thrust) can be traced back to the 8% underprediction of C_P in this simulation. However, the LB-VLESS _{$y^+ \geq 15$} consistently overpredict both propeller and turbine efficiency across the entire advance ratio range, with overpredictions of 13% at $J = 0.60$ and 27% at $J = 1.10$. This significant overestimation of turbine efficiency directly reflects the overprediction of C_P values in this simulation setup. While the absolute values are inaccurate, it is worth noting that these simulations still capture the overall gradients of turbine efficiency with J , as seen in Fig. 6.1c.

As SRANS and URANS simulations are in reasonable agreement with the experimental data for C_T and C_P in Figs. 6.1a and 6.1b, it results in a reasonable agreement for propeller and turbine efficiencies over the whole range of advance ratio, see Fig. 6.1c. The RANS simulations show an error of 4%-5% for propeller efficiency at $J = 0.60$ and less than 1% error for turbine efficiency at $J = 1.10$; see Tables 6.2 and 6.3. BEM and LL methods manage to capture the gradient of propeller efficiency with respect to J but with an offset in values compared to experimental data. The significant offset, with BEM and LL predicting 17%-20% higher propeller efficiency than the experiment at $J = 0.60$, cannot be only due to the errors in the profile performance (L/D ratio) predicted by RFOIL

but is also a consequence of the incorrect induction predictions by BEM and LL theories leading to incorrect inflow angles. In contrast, BEM and LL fail to capture the gradients of turbine efficiency with respect to J altogether, with their predictions flattening out as the advance ratio increases for $J \geq 1.10$.

Figure 6.1d shows the energy-harvesting efficiency of the propeller obtained using the different methods. At the negative thrust condition ($J = 1.10$), the LB-VLES $_{y^+ \leq 10}$ closely aligns with the experimental value, as also expected from C_P values in Table 6.3. This remarkable agreement highlights the effectiveness of this simulation setup in capturing complex flow phenomena under challenging operating conditions. In contrast, the LB-VLES $_{y^+ \geq 15}$ significantly overestimate energy-harvesting efficiency (by 16% at $J = 1.10$) compared to the experiment. Such a stark difference between LB-VLES $_{y^+ \leq 10}$ and LB-VLES $_{y^+ \geq 15}$ at $J = 1.10$ is a consequence of significant flow separation around the blade at this operating condition, making it necessary to accurately capture separation and resolve turbulence at this operating condition. While the absolute values may be overpredicted, it is noteworthy that the LB-VLES $_{y^+ \geq 15}$ still capture the overall gradients of energy-harvesting efficiency with J .

The SRANS and URANS simulations, on the other hand, deliver consistently close predictions to the experiments across the entire advance ratio range, with errors of 6%-8% at $J = 1.48$ (Fig. 6.1d). Similar to the gradients observed for turbine efficiency with respect to J in Fig. 6.1c, both BEM and LL methods generate an almost flat line for energy-harvesting efficiency in Fig. 6.1d for $J \geq 1.10$. This indicates that BEM and LL can only be used up to a certain advance ratio in negative thrust conditions (up to maximum power output point in this case).

6.3. FLOW AROUND THE PROPELLER BLADES

This section describes the complexity of the flow phenomena around the propeller blades that is the cause of inaccurate performance predictions by BEM, LL, and LB-VLES $_{y^+ \geq 15}$. Figure 6.2 shows the contours of the skin-friction coefficient (C_f) on the blade surface along with shearlines for $J = 0.60$ (positive thrust) for the mid- and high-fidelity simulations. The figure also displays flow streamlines at three radial stations: $r/R = 0.3, 0.6$, and 0.9 . Complementing these visualisations, Fig. 6.3 presents chordwise pressure distributions (C_{p_s}) at the aforementioned radial stations for $J = 0.60$. Similarly, Figs. 6.4 and 6.5 show the skin-friction coefficient contours (C_f) and chordwise pressure distributions (C_{p_s}) for $J = 1.10$ (negative thrust).

C_{p_s} is defined based on the local dynamic pressure calculated using the effective velocity ($V_{\text{eff}} = \sqrt{V_\infty^2 + (\Omega r)^2}$). The chordwise pressure distributions for BEM and LL have been obtained using RFOIL. To ensure clarity and conciseness, URANS data have been omitted from the chordwise pressure distribution comparisons as SRANS and URANS show almost identical solutions in Figs. 6.2 and 6.4 and thus the pressure distributions were also almost identical.

To quantify the discrepancies in chordwise pressure distributions across different numerical methods, the normal-force coefficient was calculated by integrating the chordwise pressure distributions with normalised chordwise coordinates (ζ/c). The resulting values of the normal-force coefficient ($C_n = \int_0^1 C_{p_s} d\zeta/c$) for $J = 0.60$ and $J = 1.10$

are listed in Tables 6.4 and 6.5, respectively. Considering the LB-VLES $_{y^+ \leq 10}$ as the reference, the relative change in normal-force coefficient was calculated as follows:

$$\Delta C_n \% = \frac{C_{n_{\text{method}}} - C_{n_{\text{LB-VLES}_{y^+ \leq 10}}}}{C_{n_{\text{LB-VLES}_{y^+ \leq 10}}}} \times 100 \quad (6.1)$$

6.3.1. POSITIVE THRUST CONDITION ($J = 0.60$)

Figure 6.2 shows the visualisation of flow around the propeller blades at $J = 0.60$ as predicted by SRANS, URANS, LB-VLES $_{y^+ \geq 15}$ and LB-VLES $_{y^+ \leq 10}$. Notably, SRANS and URANS simulations yield nearly identical solutions, both indicating the presence of a leading-edge separation bubble on the back side of the blade, primarily in the outboard region. This is evident from shearlines (see Figs. 6.2a and 6.2b). The reattachment location along the blade span for different simulations is indicated in the figure using dashed cyan-colored lines.

In contrast, the LB-VLES $_{y^+ \geq 15}$ shows a separation bubble extending up to $r/R \approx 0.4$ on both sides of the blade, as evident from the shearlines in Fig. 6.2c. Another interesting phenomenon that can be noticed in Fig. 6.2c is the radial outboard pumping of the flow when the flow is separated or about to separate. The centrifugal force pushes the flow in stagnant regions towards the tip, which results in a Coriolis force and acts as a favorable pressure gradient, delaying the stall and resulting in higher lift coefficients compared to a non-rotating blade. This phenomenon is known as the Himmelskamp effect [111] and is shown along the blade span in the figure using dashed yellow-colored lines.

Figure 6.2d shows the flow around the propeller blades predicted by LB-VLES $_{y^+ \leq 10}$ for $J = 0.60$. The skin friction contours seem more discontinuous compared to other simulations. This can be attributed to the increased surface resolution in LB-VLES $_{y^+ \leq 10}$, which allows the capture of small-scale flow fluctuations that remain unresolved in the other simulations. The LB-VLES $_{y^+ \leq 10}$ also exhibits a separation bubble in the inboard sections, similar to the LB-VLES $_{y^+ \geq 15}$. In addition, the LB-VLES $_{y^+ \leq 10}$ shows small separation bubbles in outboard sections very close to the leading edge on the back side of the blade. These outboard characteristics resemble those observed in RANS simulations, albeit with somewhat reduced intensity. These separation bubbles are the result of the operation of the propeller at low Reynolds numbers. The presence of the separation bubbles makes it challenging to have a good agreement between different numerical methods due to the sensitivity of the separation bubble length to the resolution of the boundary layer (y^+) besides other parameters, such as incoming turbulence, surface roughness, and subgrid-scale modelling [92–95].

The chordwise pressure distributions (C_{p_s}) at different radial stations offer further insights into the discrepancies between the solutions obtained from the different methods. At $r/R = 0.30$, separation bubbles in LB-VLES simulations are evident in the chordwise pressure distribution; see Fig. 6.3a. The size and location of the predicted separation bubble are observed to be sensitive to the boundary layer resolution (LB-VLES $_{y^+ \leq 10}$ vs LB-VLES $_{y^+ \geq 15}$ results), as anticipated. In contrast, the SRANS simulation does not predict any separation bubble, resulting in a chordwise pressure distribution similar to those obtained using BEM and LL theories combined with RFOIL, with the exception of the solution near the trailing edge. Notably, the chordwise pressure distribution from the

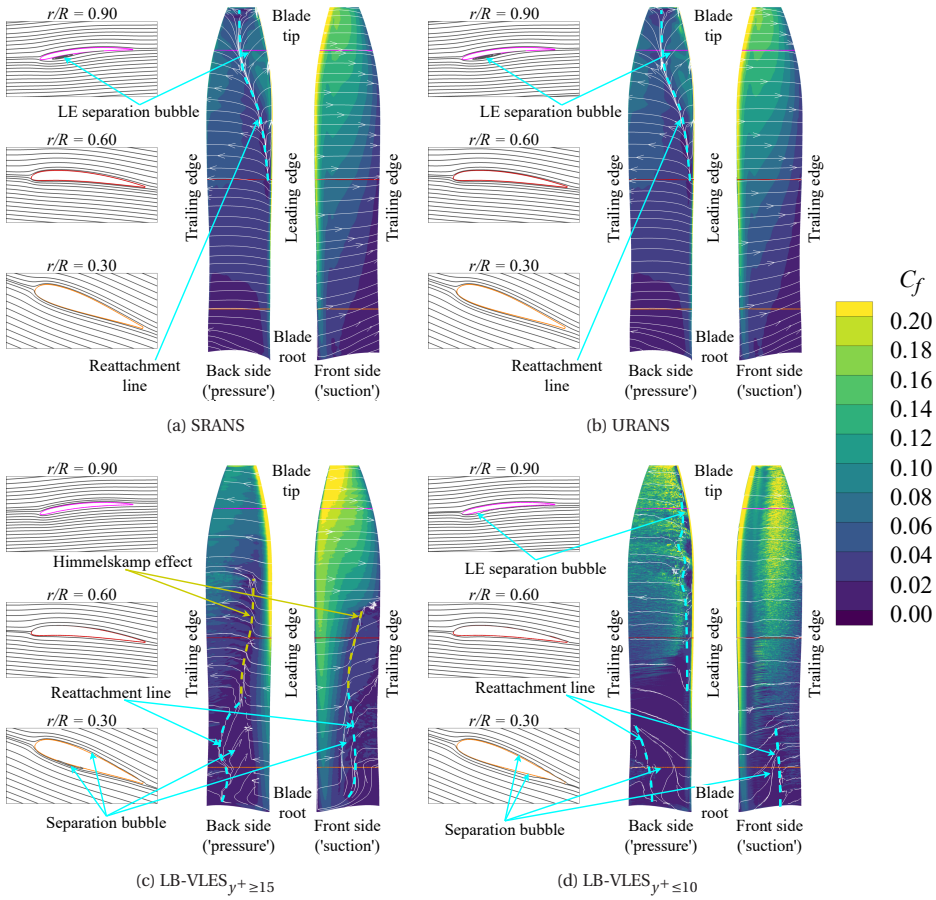
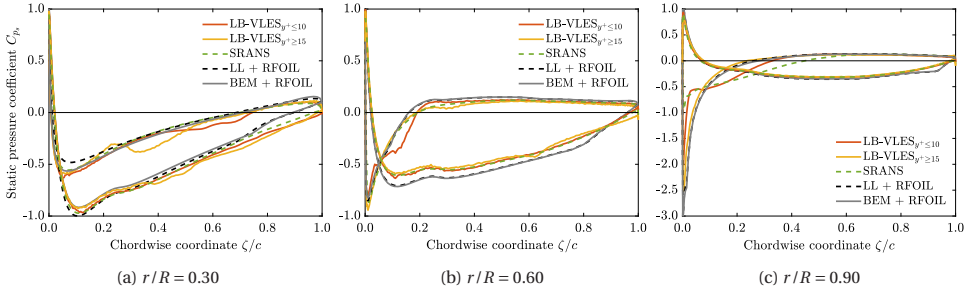


Figure 6.2: Visualisation of flow around propeller blades at the positive thrust condition ($J = 0.60$) using skin friction coefficient and shear lines

SRANS simulation at the trailing edge matches that of LB-VLES simulations, suggesting a possible similarity in the vortices shed at the trailing edge.

The differences in chordwise pressure distributions are quantified in Table 6.4. The differences in separation bubble size and location in LB-VLES simulations result in a 3% difference in the normal-force coefficient at $r/R = 0.30$ between the two LB-VLES approaches. Compared with the LB-VLES $_{y^+ \leq 10}$ as the reference, the SRANS simulation predicts an 8% higher normal-force coefficient at $r/R = 0.30$ due to the absence of a separation bubble. The LL and BEM theories coupled with RFOIL predict 8% higher and 12% lower normal-force coefficients, respectively, compared to the LB-VLES $_{y^+ \leq 10}$. The significantly lower normal-force coefficient in BEM theory, compared to LL theory, is suspected to be a consequence of the higher hub loss in BEM theory calculated through the Prandtl tip and hub loss correction. This higher hub loss results in a lower angle of attack and, consequently, a lower normal-force coefficient than LL theory.

Figure 6.3: Chordwise pressure coefficient distributions (C_{ps}) at the positive thrust condition ($J = 0.60$)Table 6.4: Normal-force coefficient (C_n) at different radial stations at the positive thrust condition ($J = 0.60$)

Method	$r/R = 0.30$		$r/R = 0.60$		$r/R = 0.90$	
	C_n	$\Delta C_n \%$	C_n	$\Delta C_n \%$	C_n	$\Delta C_n \%$
LB-VLES $_{y^+ \leq 10}$	-0.2861	--	-0.3794	--	-0.1213	--
LB-VLES $_{y^+ \geq 15}$	-0.2934	+2.53%	-0.3614	-4.73%	-0.1285	+5.94%
SRANS	-0.3101	+8.39%	-0.3870	+2.01%	-0.1002	-17.34%
LL + RFOIL	-0.3088	+7.93%	-0.4750	+25.21%	-0.1454	+19.92%
BEM + RFOIL	-0.2509	-12.31%	-0.4820	+27.04%	-0.1279	+5.49%

At $r/R = 0.60$, the LB-VLES $_{y^+ \leq 10}$ exhibits a small leading-edge separation bubble, consistent with earlier observations in Fig. 6.2d. This feature is absent in other numerical methods. The LB-VLES $_{y^+ \geq 15}$, influenced by the Himmelskamp effect, shows a thicker boundary layer at the trailing edge compared to LB-VLES $_{y^+ \leq 10}$ (Fig. 6.3b), resulting in a 5% lower normal-force coefficient (Fig. 6.3). The SRANS simulation, lacking the leading-edge bubble, differs by 2% compared to LB-VLES $_{y^+ \leq 10}$. In contrast, both LL and BEM theories, with their overestimation of suction force, show an overestimation of the normal-force coefficient by 25% and 27%, respectively, compared to the LB-VLES $_{y^+ \leq 10}$. This increased suction force could result from either an inaccurate prediction of the angle of attack by BEM and LL theories, or an inaccurate prediction of blade section performance by RFOIL at a given angle of attack, or a combination of both these factors.

Significant differences can be seen in the chordwise pressure distribution at $r/R = 0.90$ near the leading edge; see Fig. 6.3c. Both SRANS and LB-VLES $_{y^+ \leq 10}$ predict a leading-edge separation bubble, consistent with the visualisation in Fig. 6.2. The differences in the size and location of these bubbles result in a notable difference in chordwise pressure distributions up to $\zeta/c = 0.6$. These differences in chordwise pressure distributions translate to a 17% lower normal-force coefficient for the SRANS simulation compared to the LB-VLES $_{y^+ \leq 10}$. Interestingly, the absence of a leading-edge separation bubble in the LB-VLES $_{y^+ \geq 15}$ results in almost identical chordwise pressure distributions as predicted using BEM and LL theories combined with RFOIL.

These observations underscore the significance of accurately predicting separation bubbles in simulations and highlight the critical role of boundary layer resolution in capturing complex flow phenomena. Despite the apparent inability of BEM and LL theories

combined with RFOIL to capture the separation bubbles accurately, these methods offer a qualitatively reasonable estimate of chordwise pressure distributions for all considered radial stations at $J = 0.60$. The quantitative differences between the normal-force coefficient obtained from BEM and LL theories combined with RFOIL and LB-VLES $_{y^+ \leq 10}$ may have been aggravated due to the selected case for which the blade sections were operating at low Reynolds number.

6.3.2. NEGATIVE THRUST CONDITION ($J = 1.10$)

Figure 6.4 shows the visualisation of flow around the propeller blades at $J = 1.10$ as predicted by SRANS, URANS, LB-VLES $_{y^+ \geq 15}$ and LB-VLES $_{y^+ \leq 10}$. Once again, SRANS and URANS simulations exhibit near-identical solutions despite flow separation in the outboard section of the blade, as evident in Figs. 6.4a and 6.4b. This separation, attributed to the operation at negative angles of attack, manifests as a leading-edge separation bubble in the inboard sections on the back side of the blade. This bubble progressively expands towards the tip, leading to complete flow separation beyond $r/R = 0.60$.

On the other hand, the LB-VLES $_{y^+ \geq 15}$ predicts that the separation bubble reaches the trailing edge at $r/R = 0.85$; see Fig. 6.4c. Additionally, the LB-VLES $_{y^+ \geq 15}$ also predicts trailing-edge separation on the front side of the blade, which is not observed in other methods.

Interestingly, the LB-VLES $_{y^+ \leq 10}$ in Fig. 6.4d predicts similar results as seen in the RANS simulations, i.e., a leading-edge separation bubble in the inboard sections on the back side of the blade extending to the trailing edge at around $r/R = 0.60$. Unlike the LB-VLES $_{y^+ \geq 15}$, no trailing-edge separation is predicted on the front side of the blade in the LB-VLES $_{y^+ \leq 10}$. As the flow stays attached up to a higher radial coordinate in the LB-VLES $_{y^+ \geq 15}$ (Fig. 6.4c), it leads to higher $|C_p|$ compared to the RANS and LB-VLES $_{y^+ \leq 10}$ as shown before in Fig. 6.1b.

Expanding this analysis further, the chordwise pressure distributions (C_{p_s}) are compared in Fig. 6.5 and the resulting normal-force coefficients are listed in Table 6.5. At $r/R = 0.30$, BEM and LL theories combined with RFOIL show a leading-edge separation bubble similar to that observed in mid and high-fidelity simulations (Fig. 6.5a). However, the size of this bubble is notably smaller in BEM and LL theories combined with RFOIL, leading to underestimations of the normal-force coefficient by 28% and 18% compared to the LB-VLES $_{y^+ \leq 10}$ (Table 6.5). Similarly, the difference in size and location of the separation bubbles in the LB-VLES $_{y^+ \geq 15}$ and SRANS simulations as compared to the LB-VLES $_{y^+ \leq 10}$ results in 9% and 7% lower normal-force coefficient, respectively.

The difference in the size and location of the separation bubbles at $r/R = 0.60$ is evident in the chordwise pressure distributions of the SRANS and LB-VLES simulations in Fig. 6.5b. While the SRANS simulation exhibits a separation bubble size similar to the LB-VLES $_{y^+ \leq 10}$, the significant difference in the suction peak magnitude results in a 6% normal-force underestimation compared to the LB-VLES $_{y^+ \leq 10}$. The LB-VLES $_{y^+ \geq 15}$, on the other hand, showcases a smaller separation bubble and higher suction peak, leading to a 17% underestimation of the normal-force coefficient compared to the LB-VLES $_{y^+ \leq 10}$. In contrast, the chordwise pressure distributions from BEM and LL theories combined with RFOIL do not predict any separation bubble, resulting in a 19% and 17% lower normal-force coefficient, respectively, compared to the LB-VLES $_{y^+ \leq 10}$.

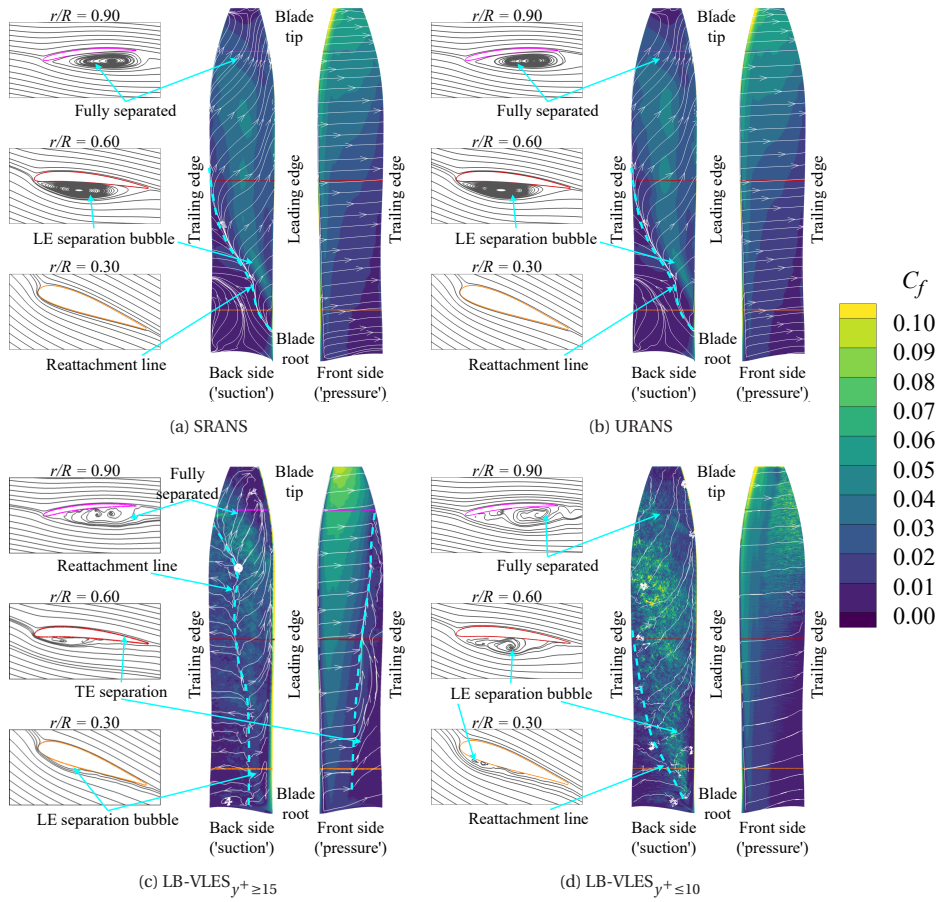


Figure 6.4: Visualisation of flow around propeller blades at the negative thrust condition ($J = 1.10$) using skin friction coefficient and shear lines

At $r/R = 0.90$ in Fig. 6.5c, the SRANS and both LB-VLES simulations predict qualitatively similar chordwise pressure distributions, indicating diminishing discrepancies as the flow fully separates. Despite the qualitative similarity, the LB-VLES $_{y^+ \geq 15}$ predicts a 34% higher normal-force coefficient compared to the LB-VLES $_{y^+ \leq 10}$ due to its higher suction and pressure values. In contrast to higher-fidelity simulations, the chordwise pressure distributions from BEM and LL theories combined with RFOIL predict attached flow without a separation bubble, resulting in a 56% and 59% higher normal-force coefficient, respectively, compared to the LB-VLES $_{y^+ \leq 10}$. This observation substantiates the delayed stall prediction in RFOIL is a contributing factor to the underprediction of $|C_T|$ and the overprediction of $|C_P|$ by BEM and LL in negative thrust conditions, seen before in Figs. 6.1a and 6.1b.

Considering the LB-VLES $_{y^+ \leq 10}$ as the reference, it is evident that RANS modelling with a resolved boundary layer can provide more accurate predictions of mean flow

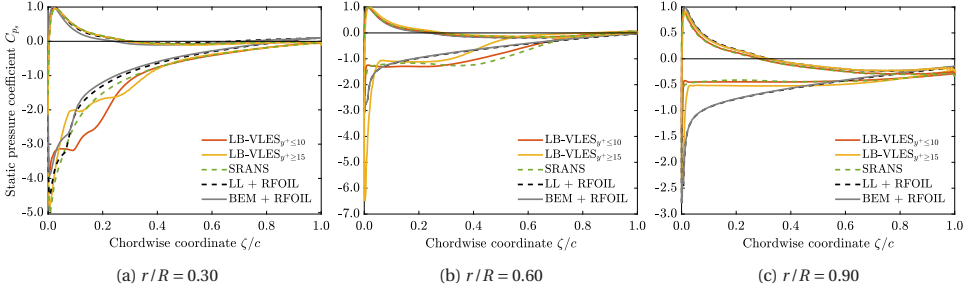

 Figure 6.5: Chordwise pressure coefficient distributions (C_{ps}) at the negative thrust condition ($J = 1.10$)

 Table 6.5: Normal-force coefficient (C_n) at different radial stations at the negative thrust condition ($J = 1.10$)

Method	$r/R = 0.30$		$r/R = 0.60$		$r/R = 0.90$	
	C_n	$\Delta C_n \%$	C_n	$\Delta C_n \%$	C_n	$\Delta C_n \%$
LB-VLES $_{y^+ \leq 10}$	1.0981	--	0.7261	--	0.3430	--
LB-VLES $_{y^+ \geq 15}$	0.9990	-9.02%	0.6033	-16.91%	0.4599	+34.08%
SRANS	1.0171	-7.38%	0.7727	+6.41%	0.3282	-4.32%
LL + RFOIL	0.9017	-17.89%	0.6053	-16.63%	0.5462	+59.23%
BEM + RFOIL	0.7890	-28.15%	0.5878	-19.04%	0.5349	+55.92%

characteristics compared to the LB-VLES $_{y^+ \geq 15}$. This is an expected conclusion given the extent of separation along the propeller blade, making it necessary to either resolve the boundary layer (as done in RANS simulations) or to use the enhanced modeled to resolved turbulence transition capabilities of the LB-VLES solver (PowerFLOW) by ensuring $y^+ \leq 10$ [73]. The BEM and LL theories combined with RFOIL provide qualitatively reasonable chordwise pressure distribution for the blade sections where the flow remains attached ($r/R = 0.30$). However, these models prove to be inadequate for the blade sections with fully separated flow due to their inherent assumptions of 2D flow, leading to significant errors, as seen for $r/R = 0.90$ for this operating condition.

6.4. TOTAL PRESSURE COEFFICIENT AND BLADE LOADING

Besides integrated performance, the radial blade loading distributions are essential inputs for studies in aeroacoustics and optimisation. Therefore, evaluating the predictive accuracy of numerical tools in capturing blade loading distributions is essential. However, directly measuring blade loading through experiments remains a challenge. Instead, the radial distributions of total pressure coefficient (C_{pt}) measured using a 5-hole pressure probe at a fixed azimuthal position at $x/R = 0.15$ downstream of the propeller offer an indirect measure of blade loading. The total pressure coefficient profiles obtained using different numerical methods have been compared with the experimental data for the same advance ratios considered in the preceding section: $J = 0.60$ and 1.10 (positive and negative thrust, respectively). As the flow is still expected to be partially attached at $J = 1.10$ (Fig. 6.4), blade loading has also been evaluated for $J = 1.48$ to un-

derstand how the differences between numerical methods are affected when the flow is fully separated along the whole blade span. Note that experimental total pressure coefficient profiles for $J = 1.48$ are unavailable, and therefore, for this condition, only a comparison between the different numerical solutions is available.

The total pressure coefficient profiles for SRANS, URANS, LB-VLES $_{y^+ \geq 15}$ and LB-VLES $_{y^+ \leq 10}$ are directly available from the simulation data. However, BEM and LL require alternative methods. Given the close proximity of the measurement location to the propeller plane of rotation ($x/R = 0.15$), the change in total pressure across the propeller can be estimated from the thrust distribution as outlined in Eq. (6.3). This approach neglects the contribution of the swirl, viscous losses, and slipstream contraction at the measurement location. The assumption of no contraction is at least partially mitigated by the flow displacement due to the nacelle thickness.

$$\delta P(r) = \frac{\delta T(r)}{2\pi r \delta r}, \quad (6.2)$$

$$C_{p_t}(r) = \frac{\delta P(r)}{q_\infty}. \quad (6.3)$$

6.4.1. POSITIVE THRUST CONDITION ($J = 0.60$)

Figure 6.6a shows the comparison of radial distribution of total pressure coefficient at $0.15R$ downstream of the propeller center for $J = 0.60$. The solid blue line represents the experimental data, with a shaded blue area denoting the estimated experimental uncertainty (estimated to be around 3% at the peak value). The BEM prediction shows agreement with the experimental total pressure distribution with a 6% overprediction of the peak. Additionally, BEM predicts a negative total pressure coefficient for $0.95 \leq r/R \leq 1$, whereas the experiment shows a negative total pressure coefficient between $0.92 \leq r/R \leq 1$. Similarly, the LL method overestimates the peak value by 5% as compared to the experiment and predicts a negative total pressure coefficient for $0.97 < r/R \leq 1$. The overprediction of the total pressure coefficient by BEM and LL theories is in agreement with the observed overprediction of C_T with respect to the experiment, as listed in Table 6.2.

In contrast to the BEM and LL theories, all the higher-fidelity simulations underpredict the peak total pressure coefficient value compared to the experimental data. Both SRANS and URANS simulations show an 11% underprediction of the peak, while LB-VLES $_{y^+ \leq 10}$ and LB-VLES $_{y^+ \geq 15}$ underestimate the peak by 12% and 16%, respectively. Additionally, the SRANS and URANS simulations fail to capture the negative total pressure coefficient observed in the experiment at $0.92 \leq r/R \leq 1$. In both the LB-VLES simulations, the total pressure coefficient is negative only between $0.98 \leq r/R \leq 1$. The underprediction of the total pressure coefficient is in agreement with the previously seen underprediction of C_T and C_P by the mid- and high-fidelity simulations in Table 6.2.

The total pressure distribution seems to be better predicted by BEM and LL theories, even though these models exhibit higher discrepancies in integrated performance compared to higher-fidelity simulations (Table 6.2). This seemingly contradictory observation can be attributed to multiple effects.

The mid- and high-fidelity simulations do not predict the negative C_{p_t} at the blade tip observed in the experiments. This negative C_{p_t} indicates negative thrust being pro-

duced by the blade tip in the experiments. Consequently, this would lead to a higher underestimation of the blade loading peak/total pressure peak by simulations compared to experiments than the underprediction of the integrated thrust listed in Table 6.2. Besides, the lower predicted power in the mid- and high-fidelity simulations translates to underpredicted momentum added to the flow in the swirl direction. This underprediction of swirl momentum contributes to increasing the discrepancy in the total pressure peak observed in higher-fidelity simulations compared to experiments.

In contrast, two effects are neglected in the calculation of the total pressure coefficient for BEM and LL theories, which, if accounted for, would lead to a greater overprediction of the total pressure coefficient than is currently observed. The first is the neglect of the swirl momentum, which is estimated to account for an additional 1-2% of the total pressure coefficient (away from root and tip) based on SRANS results. Secondly, BEM and LL theories do not account for slipstream contraction, which would further increase the overprediction of the peak value of C_{pt} . These effects are partially countered by neglecting the viscous losses and slipstream displacement due to the presence of the nacelle. This neglect of all these effects combined results in the observed 5-6% overprediction of the peak value of C_{pt} by BEM and LL theories as compared to experiments.

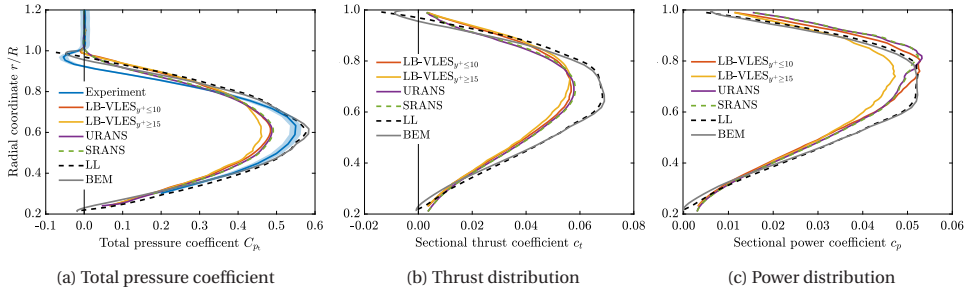


Figure 6.6: Total pressure coefficient (C_{pt}) at $0.15R$ downstream of propeller center and blade loading at the positive thrust condition ($J = 0.60$)

Figures 6.6b and 6.6c present the thrust and power distribution along the propeller blade for $J = 0.60$, respectively. Since total pressure coefficient and thrust distributions are interconnected through Eq. (6.3), discrepancies in thrust distribution mirror those observed in the total pressure coefficient profile. Interestingly, the viscous losses in the tip vortices lead to a positive thrust and power in the outboard region despite the negative total pressure coefficients in this region.

In terms of power distribution along the blade span, the RANS and LB-VLES $_{\gamma^+ \leq 10}$ show similar results, except that the RANS simulations predict the peak location to be slightly outboard (at $0.80R$) compared to the LB-VLES $_{\gamma^+ \leq 10}$ (at $0.75R$). The LB-VLES $_{\gamma^+ \geq 15}$ predicts a power distribution profile similar to the LB-VLES $_{\gamma^+ \leq 10}$, but the peak loading of the former is underpredicted by 10% compared to the latter. BEM and LL predict a higher inboard torque loading and a lower outboard torque loading than the higher-fidelity simulations. Also, the power peak is inboard (at $0.65R$) compared to higher-fidelity simulations (around $0.75R - 0.80R$).

6.4.2. NEGATIVE THRUST CONDITIONS ($J = 1.10, 1.48$)

The comparison of the total pressure coefficient and blade loading for the negative thrust condition with $J = 1.10$ can be seen in Fig. 6.7. As mentioned before, this advance ratio is close to the point of maximum negative shaft power. The experimental data has an uncertainty of 3-4% up to $r/R \leq 0.8$ as compared to the mean value, as indicated by the shaded blue area around the solid-blue line; see Fig. 6.7a.

The LB-VLES $_{y^+ \leq 10}$ exhibits good agreement with the experiment up to $r/R = 0.70$, with a maximum difference of 6% compared to the experimental mean values. However, further outboard, the LB-VLES $_{y^+ \leq 10}$ predicts a 12% lower total pressure coefficient at $r/R = 0.80$ than the experimental mean value. However, the LB-VLES $_{y^+ \leq 10}$ fails to predict the strong gradients in the outboard region for $r/R > 0.80$. Conversely, the LB-VLES $_{y^+ \geq 15}$ captures the radial gradients of the total pressure coefficient but underestimates its magnitude by up to 21% for $r/R \leq 0.90$. This is consistent with the observed underprediction of $|C_T|$ for this operational condition in Fig. 6.1a. This underprediction is attributed to an inaccurate separation bubble size observed previously in Figs. 6.4 and 6.5.

The SRANS and URANS simulations show a good agreement with experimental data up to $r/R = 0.70$, with a maximum difference of 5% as compared to the experimental mean values. Similar to the LB-VLES $_{y^+ \leq 10}$, the RANS simulations also fail to predict the strong gradients at higher radial coordinates, resulting in a 15% lower total pressure coefficient at $r/R = 0.80$ as compared to the experimental mean values; see Fig. 6.7a. Though the BEM and LL theories capture the radial gradients of the total pressure coefficient up to $r/R \leq 0.8$, the absolute values significantly diverge from the experimental data, underestimating the total pressure coefficient by up to 30% and 23% for $r/R \leq 0.8$. This is in agreement with the previously seen discrepancies in the normal-force coefficient in Table 6.5.

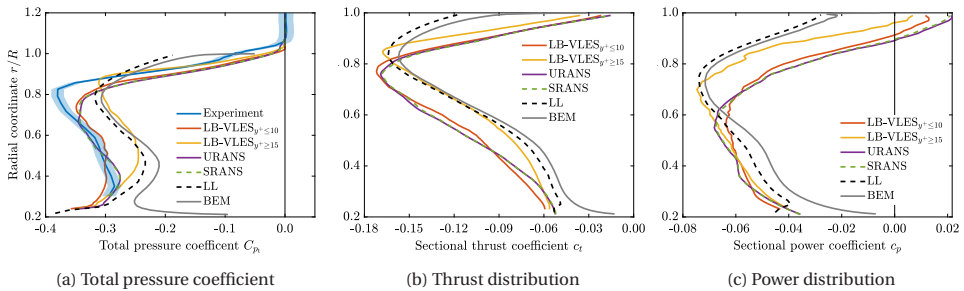


Figure 6.7: Total pressure coefficient (C_{p_t}) at $0.15R$ downstream of propeller center and blade loading at a negative thrust condition ($J = 1.10$) near the maximum power output point

Figure 6.7b compares the thrust distributions obtained from the different numerical methods for $J = 1.10$. As expected, similar differences are present in the thrust distribution as observed in the total pressure coefficient profiles in Fig. 6.7a. Besides the radial location and amplitude of the loading peak (based on Fig. 6.7a), the LB-VLES $_{y^+ \leq 10}$ is deemed to represent the thrust distribution well. Therefore, LB-VLES $_{y^+ \leq 10}$ has been used as the reference for comparing power distribution along the blade span in Fig. 6.7c.

The BEM and LL methods predict a considerably different power distribution from

the LB-VLES $_{y^+ \leq 10}$. These methods underpredict the power distribution in the inboard part of the blade by 20-30% and overpredict the power distribution in the outboard part of the blade ($r/R \geq 0.60$) by more than 40% as compared to the LB-VLES $_{y^+ \leq 10}$. The SRANS and URANS simulations have a power distribution similar to the LB-VLES $_{y^+ \leq 10}$, except for the 6% overprediction of power peak by the former compared to the latter. The LB-VLES $_{y^+ \geq 15}$ has a similar distribution as the LB-VLES $_{y^+ \leq 10}$ for the inboard part of the blade ($r/R \leq 0.60$) with a difference of less than 10% up to $r/R \leq 0.60$. However, the LB-VLES $_{y^+ \geq 15}$ significantly overpredicts the power distribution in the outboard part of the blade (more than 30%), resulting in a 16% higher integrated power than LB-VLES $_{y^+ \leq 10}$ as observed in Table 6.3.

Lastly, blade loading comparisons were conducted for $J = 1.48$, representing the highest advance ratio considered in this study. As the experimental total pressure coefficient profile is unavailable for this condition, only the thrust and power distributions have been compared between different numerical methods; see Fig. 6.8. Given the good match between the experimental data and URANS simulations in integrated performance in Fig. 6.1, and in the absence of other pertinent data, URANS simulations are considered the reference for comparing blade loading distributions.

Compared to higher-fidelity simulations, BEM and LL predict completely different loading distributions in Fig. 6.8. As mentioned before, these deviations may not be solely due to inaccuracies in polar data; they might be rooted in the breakdown of underlying assumptions inherent to these methods due to extensive flow separation. Though SRANS and URANS have an identical solution in all the previous results, some differences can be observed between the two for $J = 1.48$ in Fig. 6.8. These variations underline the increasing significance of unsteadiness with the increase in advance ratio due to the increase in flow separation. In contrast to the results seen in Fig. 6.7 for $J = 1.10$, LB-VLES $_{y^+ \geq 15}$ for $J = 1.48$ predict similar radial gradients as URANS simulations for both thrust and power distributions. This shows that fully separated flow is comparatively easier to simulate using wall models than flows with reattachment zones. Consequently, it strengthens the argument that the LB-VLES $_{y^+ \geq 15}$ are suitable for capturing the general trend of the propeller performance in negative thrust conditions.

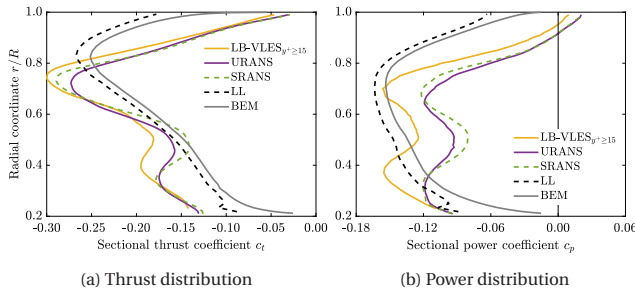


Figure 6.8: Comparison of blade loading at a negative thrust condition with fully separated flow ($J = 1.48$)

6.5. PHASE-LOCKED FLOWFIELD IN THE PROPELLER SLIPSTREAM

In this section, the non-dimensional phase-locked out-of-plane vorticity ($\vec{\omega}_t^*$) component has been compared in the propeller slipstream. The purpose of comparing $\vec{\omega}_t^*$ is twofold. Firstly, to assess the efficacy of various simulations in preserving the wake structure in the slipstream, given the current mesh and computational cost. Secondly, to evaluate the sensitivity of the wake structure to discrepancies observed in blade loadings in the preceding section. These aspects hold significant relevance for future investigations related to propeller-wing interactions. The same advance ratios have been considered in this section as before: $J = 0.60$ (positive thrust) and 1.10 (negative thrust). Due to a similar flowfield in SRANS and URANS simulations, this section excludes URANS simulations to maintain brevity.

6.5.1. POSITIVE THRUST CONDITION ($J = 0.60$)

Figure 6.9 compares the phase-locked non-dimensional out-of-plane vorticity component in the propeller slipstream for the positive thrust condition ($J = 0.60$). The figure depicts two distinct wake structures, which will be referred to as the upstream and downstream wake structures in the following discussion.

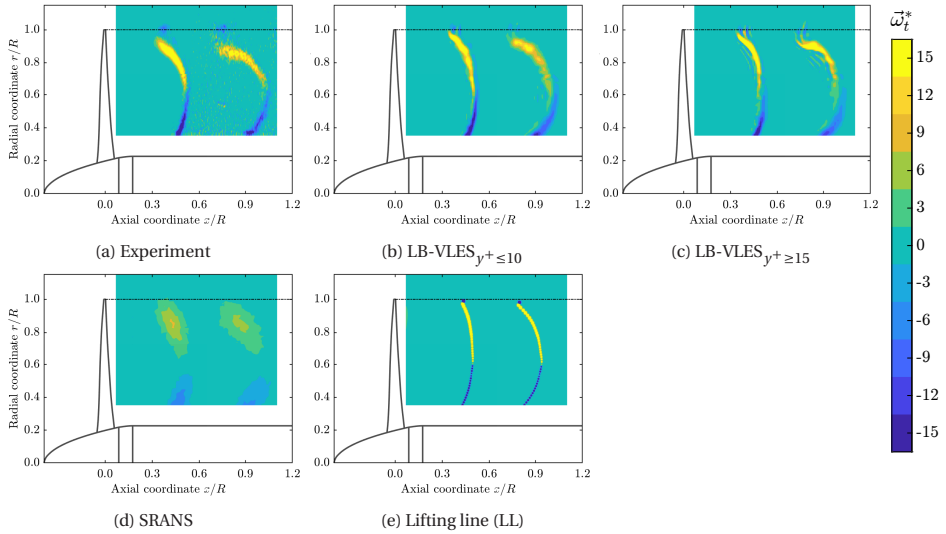


Figure 6.9: Comparison of phase-locked non-dimensional out-of-plane vorticity component ($\vec{\omega}_t^*$) at the positive thrust condition ($J = 0.60$)

The LB-VLES $_{\gamma^+ \leq 10}$ shows blade-wake and tip-vortex structures similar to the experiment. The negative out-of-plane vorticity region of the upstream wake around $r/R \approx 1.0$ extends up to $0.97R$ in the LB-VLES $_{\gamma^+ \leq 10}$ as compared to up to $0.95R$ in the experiment, which agrees with the differences previously observed in the radial distribution of total pressure in Fig. 6.6a. Also, the region with positive vorticity in the downstream wake

structure extends up to $0.95R$ as compared to $0.90R$ in the experiment. This is the consequence of the underprediction of the blade loading peak, resulting in decreased slipstream contraction in the LB-VLES $_{y^+ \leq 10}$. Nevertheless, the blade wakes from the inboard part of the blade in the LB-VLES $_{y^+ \leq 10}$ agree well with the experimental data.

The LB-VLES $_{y^+ \geq 15}$ have a similar mesh in the propeller slipstream as LB-VLES $_{y^+ \leq 10}$. Though both have similar blade-wake and tip-vortex structures, some differences can be noticed upon careful observation; see Figs. 6.9b and 6.9c. The most significant difference is the presence of the secondary vortices around the blade-wake and tip-vortex structures in the LB-VLES $_{y^+ \geq 15}$, which are absent in the LB-VLES $_{y^+ \leq 10}$. The secondary vortices are expected to be the result of different blade loading and flow features around the propeller blades in the LB-VLES $_{y^+ \geq 15}$ as compared to the LB-VLES $_{y^+ \leq 10}$ as seen in the preceding sections.

The SRANS simulation shows diffused tip and root vortex regions at locations broadly consistent with the experiment; see Fig. 6.9d. The diffusion of blade wake and tip vortex in SRANS simulations is expected to be a consequence of two factors: the relatively coarse mesh in the propeller wake in RANS simulations as compared to LB-VLES simulations and the inherently higher numerical diffusion characteristic of RANS simulations compared to LB-VLES simulations [112, 113]. It should be noted that the current RANS mesh was not set up for maximum preservation of the wake structures, and better results may be achievable with a focus on wake preservation with a similar computational cost.

Finally, Fig. 6.9e presents the vorticity distribution in the slipstream as obtained from LL using the slipstream contraction model (Eq. (2.1)). Though qualitatively LL shows somewhat similar wake structures as the experiment, quantitatively significant differences are present. The upstream tip vortex cuts the plane around $x/R = 0.43$ in the LL slipstream as compared to $x/R = 0.38$ in the experiment. Similarly, the second tip vortex passes through the plane at $x/R = 0.8$ in the LL slipstream as compared to $x/R = 0.75$ in the experiment. The differences in the location of the blade wake between LL and experimental slipstreams increase from the upstream wake to the downstream wake due to the lower axial slipstream velocity in the former. For instance, at $r/R = 0.5$, the blade wakes in the LL flowfield are located at $x/R = 0.48$ and 0.92 as compared to $x/R = 0.51$ and 1.02 in the experimental flowfield. This suggests a lower convection velocity of the wake structures in LL than experiment despite the higher total pressure coefficient in the former; see Fig. 6.6a. These discrepancies can be partially attributed to the absence of the nacelle in the LL simulation and partially to the assumptions made in the slipstream contraction model. Despite this, considering the substantially lower computational cost of the LL method as compared to other numerical methods, the LL method provides a valuable first approximation of the slipstream vorticity distribution in the wake.

6.5.2. NEGATIVE THRUST CONDITION ($J = 1.10$)

Figure 6.10 compares the non-dimensional out-of-plane vorticity component for the negative thrust condition, i.e. $J = 1.10$. Again, the LB-VLES $_{y^+ \leq 10}$ shows a wake structure similar to the experiment at approximately the same location; see Figs. 6.10a and 6.10b. However, the tip-vortex shape in the LB-VLES $_{y^+ \leq 10}$ is slightly different than in the experiment.

The LB-VLES $_{y^+ \geq 15}$ in Fig. 6.10c predicts the blade-wake structure to be compara-

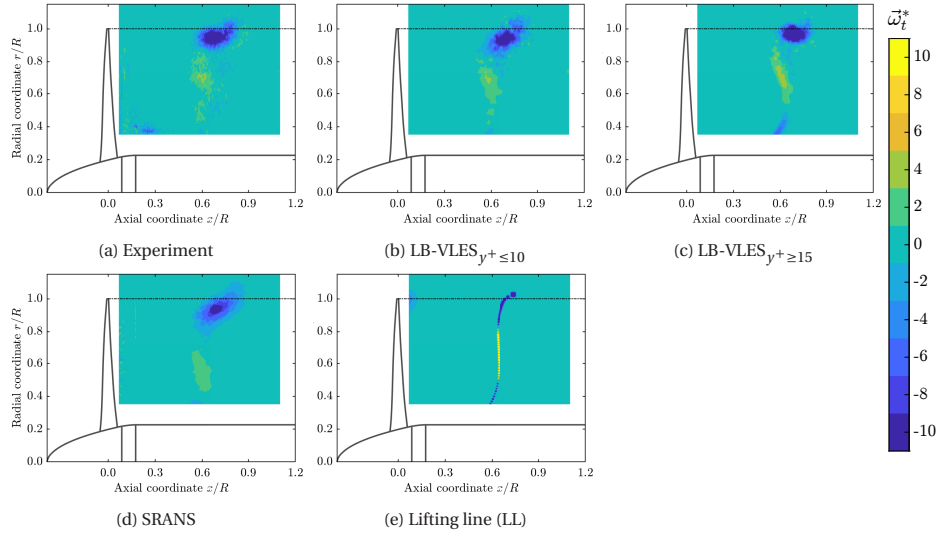


Figure 6.10: Comparison of phase-locked non-dimensional out-of-plane vorticity component ($\vec{\omega}_t^*$) at the negative thrust condition ($J = 1.10$)

tively more concentrated and well-defined, which could be attributed to the underpredicted flow separation as seen in Fig. 6.4c. The overall wake structure and tip vortex shape are somewhat similar to the experiment, as expected from Fig. 6.7a, given the good agreement between the LB-VLES $_{y^+ \geq 15}$ and experiment in terms of radial gradients.

In the case of the SRANS simulations, a diffused region of tip vortex and blade wake can be observed approximately at the same location as the experiment; see Fig. 6.10d. However, further insights are hindered by the numerical diffusion inherent in SRANS simulations. Examining the LL slipstream in Fig. 6.10e, a well-defined tip vortex and blade wake structure are evident, with blade wake and tip vortex located at approximately the same location as the experimental flowfield. Notably, while providing a reasonable initial estimate of the vorticity distribution in the wake, the LL model does not capture the diffusion and dissipation of wake structures due to the absence of viscous losses and wake mixing.

6.6. KEY FINDINGS

This study systematically evaluated various numerical methods for modelling the aerodynamic performance of propellers across both positive and negative thrust regimes. The findings from this study provide valuable guidance for researchers seeking the optimal approach for investigating propeller performance across a diverse range of operating conditions depending upon the desired accuracy.

6.6.1. BEM AND LL THEORIES

The comparison of integrated performance (C_T and C_P) showed that BEM and LL can predict the trends of propeller performance in the positive thrust regime, though with

an offset, for instance, an offset of 7%-11% at $J = 0.60$ for the propeller and pitch setting considered in this study. The total pressure distribution in the slipstream also shows reasonable agreement with experimental data (overestimating the peak by 5-6%). Despite the differences, BEM and LL methods combined with RFOIL offer qualitatively reasonable chordwise pressure distributions at positive thrust.

In the negative thrust conditions, while BEM and LL initially follow experimental trends in thrust and power up to the maximum power output point ($J = 1.10$ in this study), they quickly diverge from experiments for higher advance ratios, underestimating thrust magnitude and significantly overestimating power magnitude (by more than 25% at $J = 1.48$). This is a consequence of the fact that the blade loading distributions derived from BEM and LL theories cease to be representative of the actual expected distribution as per higher-fidelity simulations.

Therefore, while BEM and LL theories are suitable for predicting general trends and optimising propeller performance in positive thrust conditions, their applicability in the negative thrust regime is limited to conditions without significant flow separation around the blades. In this study, this limitation manifested before the maximum power output point. The inaccuracies in performance prediction by BEM and LL are suspected to arise not just from polar data limitations but also from the breakdown of the inherent assumption in these methods. Further research is needed to thoroughly explore and validate these assumptions in the negative thrust regime.

Besides the propeller performance prediction, the vorticity distribution in the propeller wake calculated using LL theory provided a good first approximation for both positive and negative thrust conditions (up to maximum power output point) and, therefore, can be a useful tool for propeller-wing interaction studies.

6.6.2. RANS SIMULATIONS

The SRANS and URANS simulations showcase near-identical solutions across almost the entire range of advance ratios. At the positive thrust condition ($J = 0.60$), the errors in C_T and C_P range from 3%-4% and 7%-8%, respectively, with an 11% underprediction of the total pressure peak in the slipstream compared to the experiment. On the contrary, these errors decrease to 1%-2% in C_T and less than 1% in C_P at the negative thrust condition ($J = 1.10$). The difference between RANS simulations and experimental data increases with the advance ratio in the negative thrust regime, reaching a 3% error in C_T for URANS simulations at $J = 1.48$ due to the error introduced by the turbulence modelling in predicting separated flows. Also, the differences between the SRANS and URANS become apparent at this condition due to the increasing influence of unsteadiness induced by the separated flow.

While RANS simulations offer a viable choice for comprehensively studying propeller performance within both positive and negative thrust regimes, it is essential to note that the blade wake and tip vortex structures tend to diffuse rapidly in RANS-simulated cases. This diffusion results from the coarser mesh resolution and comparatively higher numerical diffusion in RANS simulations than in LB-VLES simulations. Therefore, while RANS simulations are suitable for predicting propeller performance, their use for capturing phase-locked slipstream data requires refinement of the mesh beyond the point required for predicting integrated performance.

6.6.3. LB-VLES SIMULATIONS

The comparison of LB-VLES simulations with experimental data highlights the crucial role of using $y^+ \leq 10$ for accurate solutions, particularly in negative thrust conditions. The LB-VLESs _{$y^+ \leq 10$} align well with experimental data (error < 1% at $J = 1.10$), albeit with significantly increased computational resources (over 30 times compared to LB-VLESs _{$y^+ \geq 15$}). In contrast, though the computation cost of the LB-VLESs _{$y^+ \geq 15$} is similar to URANS simulations, the LB-VLESs _{$y^+ \geq 15$} overestimates the power magnitude by 16% when compared to experimental data at $J = 1.10$ (close to the maximum power output point). This disparity primarily arises from inaccuracies in modelling reattachment locations along the blade span. Despite the errors in absolute values, LB-VLESs _{$y^+ \geq 15$} offer an alternative option for capturing the general trend of propeller performance. Both types of LB-VLES simulations effectively preserve propeller wake structures due to their inherent lower numerical diffusion and lower computational cost per mesh element compared to RANS simulations. This characteristic could be useful for propeller-wing interaction studies.

6.6.4. CHOOSING THE OPTIMAL METHOD

Ultimately, the most suitable numerical method depends on the specific research objectives and available resources. BEM and LL theories are good tools for predicting general trends of propeller performance and optimisation in the positive thrust regime. However, these methods should be used with caution in the negative thrust regime. LL theory provides a good first estimation of the phase-locked propeller slipstream and can be useful for studies interested in accounting for propeller-wing interactions in aircraft design studies. Both SRANS and URANS simulations with $y^+ < 1$ provide a good balance between accuracy and computational cost for propeller performance studies in both positive and negative thrust regimes. However, special attention is needed while meshing for the preservation of tip-vortex and blade wake structures in the propeller slipstream. LB-VLESs _{$y^+ \geq 15$} can be used as an alternative for studies interested in propeller-wing interactions due to their reduced numerical diffusion and competitive computational cost compared to URANS simulations. However, one must be cautious of errors introduced by wall modelling in LB-VLESs _{$y^+ \geq 15$} . Though LB-VLESs _{$y^+ \leq 10$} provide excellent agreement with the experiments in negative thrust conditions, this accuracy comes at a tremendous computational cost (over 30 times LB-VLESs _{$y^+ \geq 15$}) and may not be practical.

These findings highlight the importance of carefully selecting the numerical method based on specific research objectives and computational resources. Future experiments focused on measuring surface quantities such as skin friction and pressure distribution could provide valuable insight into flow separation, further enhancing the assessment of the accuracy of numerical models.

7

PROPELLER BLADE LOADING FROM EXPERIMENTAL SLIPSTREAM DATA

Direct comparison between the experimental data and numerical methods is often hindered by the absence of experimental blade loading distributions. Chapter 6 highlights this issue, where the total pressure coefficient in the slipstream was used as a proxy for blade loading distributions. This chapter addresses this challenge by evaluating the efficacy of a potential flow method, referred to here as the “wake-informed lifting line” method, which estimates blade loading distributions from phase-locked slipstream velocity data.

The chapter begins with an overview of traditional methods for obtaining experimental blade loading distributions and their limitations in Section 7.1, followed by a brief description of different lifting line models in Section 7.2. Then, a detailed description of the setup of the wake-informed lifting line model is provided in Section 7.3. Subsequently, the method is validated using CFD data in Section 7.4, for which the data available from SRANS simulations utilised in Chapter 6 are used. After validation, the model is applied to experimental data to assess its efficacy in practical scenarios in Section 7.5, with key findings summarised in Section 7.6.

7.1. INTRODUCTION

Blade loading distributions are essential for assessing the aerodynamic and aeroacoustic performance of rotor designs. Conventionally, obtaining blade loading data directly from experiments requires the use of intrusive measurement techniques, involving the installation of complex and costly surface pressure sensors on blade surfaces [115, 116]. These sensors typically offer low spatial resolution due to several factors: their size relative to the thin blades of scaled models, the high cost of individual sensors, and the expense of high-bandwidth data transfer systems needed to transmit data from the rotating to the stationary domain [117]. These challenges are further amplified when dealing with off-the-shelf rotors, where customisation of the rotor blades to accommodate pressure sensors is impractical. Additionally, limited information about the geometry of off-the-shelf rotors often necessitates 3D scanning before numerical simulations can be performed, complicating the characterisation of commercially available rotors.

Alternatively, multi-hole probes can be placed directly behind the blades to estimate total loads using momentum-based analysis techniques. However, accurately tracing these loads back to their exact radial origin on the rotor blades is not feasible, and measurements may be affected by viscous phenomena in the slipstream. Non-intrusive techniques, such as particle image velocimetry (PIV), encounter similar challenges. While it is possible to reconstruct the pressure distribution around a blade segment using the stereoscopic velocity field obtained through PIV [118], this method encounters difficulties with optical access and increased uncertainty near the blade surface, potentially leading to significant inaccuracies in the reconstructed blade loading [119, 120].

Another non-intrusive measurement technique is the use of pressure-sensitive paint (PSP) paired with optical measurements, which can be used for off-the-shelf rotors [121, 122]. While PSP techniques offer high spatial resolution for surface pressure measurements, their application to rotating propeller blades is constrained by challenges such as insufficient signal strength, pressure and temperature sensitivity, illumination requirements, and the complexities of calibrating on moving surfaces [123, 124].

An alternative approach was proposed by Haans et al. [125], who used a lifting-line-based method to estimate local flow conditions and blade loads using wake measurements. They reconstructed the wake geometry assuming the trailing vorticity sheet rolls up into tip and root vortices at the boundary of the very near ($0 \leq x/R \leq 0.15$) and the near wake ($0.15 < x/R \leq 1$) regions. Subsequently, they solved for the unknown bound circulation based on velocities obtained from wake measurements, employing Kelvin's circulation theorem and the Biot-Savart law. While this approach demonstrated potential, its application was limited to a simplified rotor blade geometry consisting of a NACA0012 airfoil without twist or taper and was primarily tested in wind turbine conditions. These conditions differ significantly from those encountered by aircraft propellers, particularly in terms of tip speed ratio (advance ratio). Additionally, their study lacked comprehensive validation, as it only compared local angles of attack derived from the potential flow method with experimentally estimated values.

In this thesis, the method proposed by Haans et al. has been extended. Although the theoretical formulation remains unchanged, the wake reconstruction methodology has been updated; the trailing vorticity sheet maintains its path and does not roll up into the tip and root vortices. This modification allows accounting for the variations in convec-

tive velocity along the radial direction. Furthermore, it has been adapted for application to propellers, with a focus on evaluating its effectiveness in estimating blade loading distributions directly from wake measurements under both attached and separated flow conditions. The method in the current thesis is referred to as the “wake-informed lifting line” model and is used in combination with phase-locked slipstream data containing all three velocity components.

7.2. LIFTING LINE MODELS

This section provides a brief description of the conventional LL model. Subsequently, the theory of the wake-informed LL model is presented. Lastly, an additional way of solving the LL model, referred to as the ‘load-informed LL’ model, is explained, which is used as an intermediary validation tool in subsequent analyses.

7.2.1. CONVENTIONAL LIFTING LINE MODEL

Conventionally, a lifting-line analysis of a rotor is performed to compute rotor performance based on prescribed blade geometry and airfoil polar data, with the rotor wake typically modelled as an incompressible, inviscid vortex system of fixed shape [64]. The strength of the shed vortices from the rotor corresponds to the spanwise gradient in bound vortex strength as per Kelvin’s theorem, and the velocity induced by these vortices at any point on the rotor blade is calculated using the classical Biot-Savart law. For a given wake geometry and bound circulation strength, the induced velocity at the rotor blade can be calculated, which in turn can be used to determine the angle of attack at each blade section. To compute the resulting local lift and drag coefficients, polar data for different blade sections are required from an external source, which further requires knowledge of blade section geometry. This whole process is iterated until a converged solution is obtained, as shown in Fig. 7.1a. However, the conventional LL approach is applicable only to rotors with known geometries, and its accuracy is inherently limited by the precision of the polar data and prescribed wake shape.

7.2.2. WAKE-INFORMED LIFTING LINE MODEL¹

The wake-informed LL model is a modification of the conventional prescribed wake LL model that partially eliminates the need for airfoil polar data and blade section geometry to determine blade loading distributions. Instead, it uses the information available from input slipstream data, including the blade wake and tip vortex locations, as well as the induced velocity vectors to estimate the bound circulation.

In this model, the process begins by constructing a wake vortex system based on the blade wake and tip vortex locations identified in the slipstream data. An initial guess of the bound circulation is used to calculate the resulting induced velocities at prescribed locations in the slipstream, referred to as ‘control points’. These control points are strategically positioned where the induced velocity vectors are available from the input slipstream data, avoiding regions dominated by viscous effects, such as the boundary layer of the nacelle. The bound circulation is then iteratively adjusted using non-linear least

¹The source code of the wake-informed LL model used in this study can be found on 4TU.ResearchData repository [126].

squares fitting to minimise the root sum square of the errors between the velocity vectors induced by the wake vortex system and the induced velocity vectors obtained from the input slipstream data at the control points. The trust-region-reflective (gradient-based) algorithm [127, 128] was used for this optimisation, though alternative algorithms could also be utilised. A detailed description of each step in setting up the model is provided in Section 7.3.

Once the fitting process converges, the resulting bound circulation distribution is used to compute the induced velocities at the blade sections, similar to the conventional LL model. However, it is important to note that the wake-informed LL model does not calculate the profile drag component without supplementary polar data; it only determines the lift component of the blade loading distribution. The computational procedure for the wake-informed LL model is shown in Fig. 7.1b.

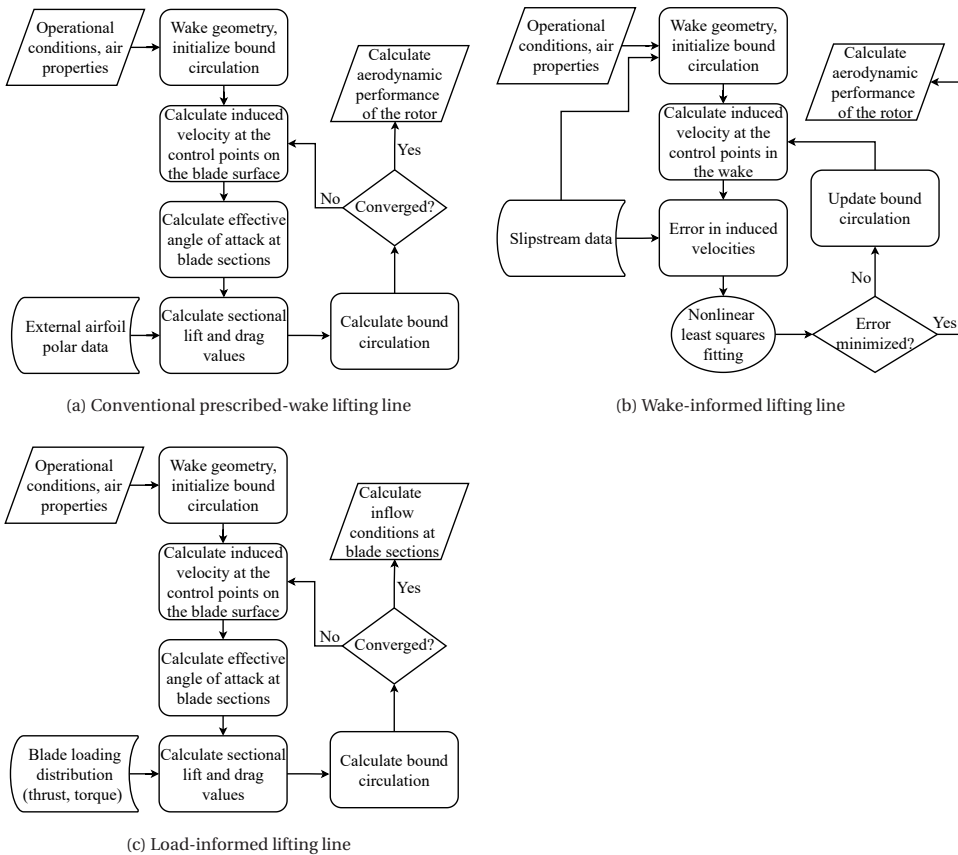


Figure 7.1: Computational procedure to solve the conventional prescribed-wake lifting line, wake-informed lifting line, and load-informed lifting line models

7.2.3. LOAD-INFORMED LIFTING LINE MODEL

To enable a more direct comparison between the wake-informed LL model and validation data, this study also employs an alternative formulation, referred to as the “load-informed lifting line” model. Unlike conventional LL models, where the blade loading distributions (thrust and torque distributions) are obtained as outputs, this model takes the blade loading distributions as input from an external source and decomposes them into their corresponding lift and drag components.

The load-informed LL model serves two purposes. Firstly, by decomposing the thrust and torque distributions obtained from validation data into lift and profile drag components, it enables a more fair comparison between the wake-informed LL model and validation data. This is particularly important because the wake-informed LL model, as mentioned in Section 7.2.2, does not provide the profile drag component. This decomposition also provides insight into the significance of the profile drag component for thrust and torque distributions.

Secondly, the load-informed LL model provides the equivalent potential flow solution for the given blade loading distribution. The induced velocities in the slipstream, calculated using the load-informed LL model, serve as a benchmark for evaluating the wake-informed LL model. Assuming the fundamental assumptions of LL theory hold, the wake-informed LL model should theoretically converge to the load-informed LL solution. Significant discrepancies between the load-informed LL and wake-informed LL solutions would indicate that potential flow solutions obtained using LL models cannot reconcile the given combination of blade loading and the induced velocities in the slipstream for a given operating condition, or in other words, the fundamental assumptions of the LL models are not representative of the given operating condition.

To achieve this, the computational procedure for the load-informed LL model begins with a predefined helical wake structure and an initial guess for the bound circulation. The model then calculates the induced velocities at the quarter-chord points of the blade sections, which are then used to determine the local inflow angles ($\varphi(r)$). Using Eqs. (7.1) and (7.2) and the input blade loading distributions, the corresponding lift and drag forces are computed. The calculated lift is subsequently employed to update the bound circulation. This iterative process continues until a converged bound circulation is obtained. The computational procedure is shown in Fig. 7.1c.

$$T'(r) = L'(r) \cos \varphi(r) - D'(r) \sin \varphi(r) \quad (7.1)$$

$$Q'(r) = (L'(r) \sin \varphi(r) + D'(r) \cos \varphi(r)) r \quad (7.2)$$

To ensure consistency, all load-informed LL solutions in this study use the same helical wake system as the wake-informed LL model, thereby avoiding discrepancies due to variations in wake geometry.

7.3. SETUP OF THE WAKE-INFORMED LIFTING LINE MODEL

This section details the problem setup for the wake-informed LL model. It begins with a description of the required slipstream data for the model, followed by the procedure for identifying blade wake and tip vortex structures using these input data. Next, the

methodology for setting up the helical wake system and choosing the control points is described. Then, the objective function minimised to obtain the solution is described. Finally, the post-processing of the results is discussed.

7.3.1. SLIPSTREAM DATA

The setup of the wake-informed LL model requires phase-locked slipstream data. While the axial velocity component is essential for the wake-informed LL model and must be available in the slipstream data, the inclusion of the radial and tangential velocity components, when available, contributes to achieving a more accurate and representative solution.

For the rest of this section, slipstream data derived from SRANS simulations described in Chapter 2 are used as examples. These data are also employed later for validation in Section 7.4. The slipstream data consist of phase-locked velocity vectors calculated in a plane behind the propeller blade, extending to approximately $1.2R$ in both axial and radial directions. This measurement plane aligns with the dimensions and location of the plane employed in particle image velocimetry (PIV) experiments conducted by Nederlof et al. [46] for the same propeller. These PIV measurements will be used later for a real-world test case of the model in Section 7.5. The input slipstream data from the SRANS simulations include all three velocity components. The availability of the axial and radial velocity components from SRANS simulations enabled the identification of the blade wake and tip vortex shapes and locations using the out-of-plane vorticity field.

Figure 7.2 shows the corresponding phase-locked out-of-plane vorticity field for both attached and separated flow conditions. For the attached flow condition (Fig. 7.2a), two blade wakes are observed in the specified plane. In contrast, for the separated flow condition (Fig. 7.2b), only one blade wake is visible. This difference results from the lower advance ratio in the attached flow condition compared to the separated flow condition. In the attached flow condition, the blade wakes show the expected shape, with the mid-board part of the blade wake convecting faster than the wake from the tip and root regions. Conversely, in the separated flow condition, the blade wake originating from the inboard part of the blades convects slower than the outboard region due to higher negative loading in the inboard region.

7.3.2. IDENTIFYING SHAPE AND LOCATION OF BLADE WAKE AND TIP VORTEX

Identifying blade wake and tip vortex locations is crucial for setting up the vortex wake system for the wake-informed LL model. In this study, these features are determined using vorticity fields. However, if vorticity fields are unavailable due to the absence of radial velocity data, an alternative approach is to use the axial velocity gradient in the axial direction $\left(\frac{\partial V_x}{\partial x}\right)$ as a substitute, as discussed subsequently in this section. The procedure followed in this study to identify these features using the vorticity field is detailed below:

1. A Gaussian filter ($\mathcal{G}(\vec{r})$) is applied to the input $\vec{\omega}_t^*$ values to mitigate noise in the measurement plane, which is especially important when dealing with experimental data.
2. A vorticity ($\vec{\omega}_t^*$) threshold is defined to identify regions where vorticity values ex-

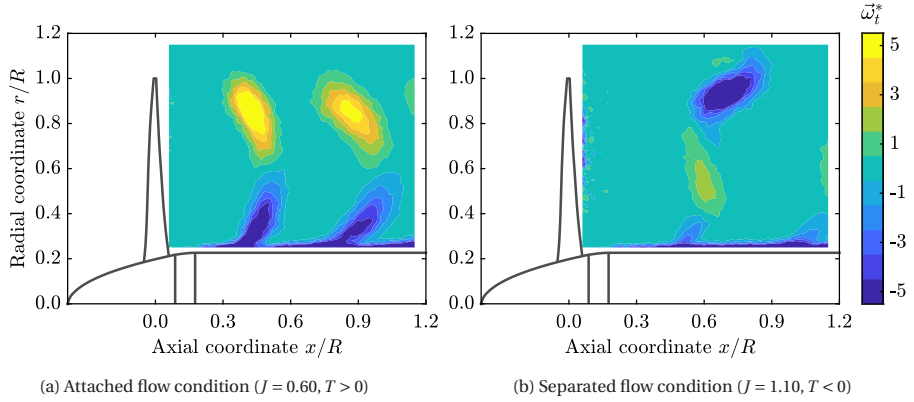


Figure 7.2: Phase-locked non-dimensional out-of-plane vorticity component ($\vec{\omega}_t^*$) obtained from SRANS simulations

ceed the threshold magnitude. These regions are expected to correspond to the desired features, such as blade wakes and tip vortices. However, the filtering process may also capture unwanted features, such as the boundary layer of the nacelle. In this study, a threshold of $\vec{\omega}_t^* < -3.5 \vee \vec{\omega}_t^* > 3.5$ was applied for the attached flow case, while a threshold of $\vec{\omega}_t^* < -1.5 \vee \vec{\omega}_t^* > 0.6$ was used for the separated flow case.

3. Additional constraints, informed by the vorticity field visualisation (Fig. 7.2), are defined to exclude regions associated with boundary layers and other extraneous features, such as support struts in experimental setups. These constraints may be applied to the axial coordinate, radial coordinate, vorticity values, or a combination of these parameters.
4. In case of multiple wakes in the measurement plane, the remaining measurement points are divided into distinct bins. These bins are defined based on the minimum and maximum axial locations for each blade wake and tip vortex, as informed by the vorticity field visualisation (Fig. 7.2). For instance, for the attached flow condition ($J = 0.60$), two bins were defined: the first bin corresponds to $x/R \leq 0.60$, and the second bin corresponds to $x/R > 0.60$. No binning was necessary for the separated flow condition, as only one blade wake was present in the measurement plane.
5. A polynomial curve is fitted along the radial direction through the remaining points in each bin to obtain the shape of the blade wake in the specified plane. The initial polynomial orders were determined by minimising the root mean square errors (RMSE). Subsequently, terms with a probability greater than 5% of having a non-zero coefficient due to random error were eliminated to obtain the final polynomial curve [53]. A practical approach to validate the identified shape is to overlay it on the $\vec{\omega}_t^*$ plot (Fig. 7.3). This step helps assess whether the determined shape is physically realistic, particularly near the nacelle where input slipstream

data may be sparse or unavailable. In this study, third-order and sixth-order polynomials were used for attached and separated flow conditions, respectively, for the input SRANS data.

Figure 7.3 shows the resulting Gaussian-filtered vorticity field, overlaid with red points where the vorticity magnitude exceeds the threshold values. Additionally, the final polynomial curves, fitted through these high-vorticity points, are also displayed. These polynomial curves extend from the nacelle ($r/R = 0.24$) to the blade tip ($r/R = 1.0$).

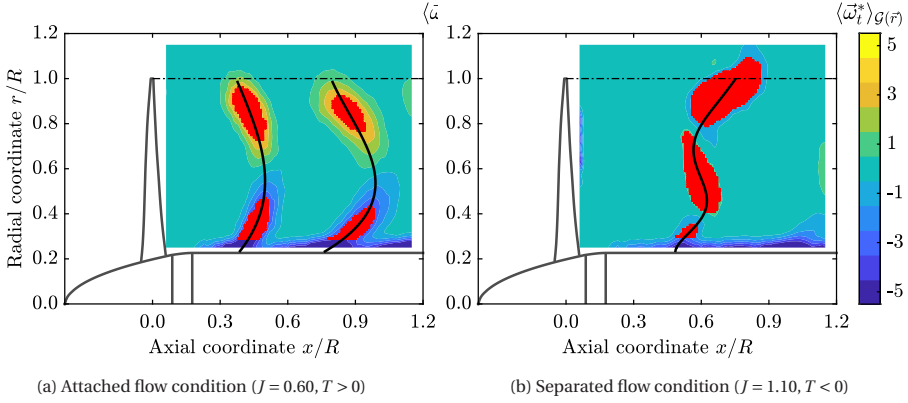


Figure 7.3: Identified shape of blade wakes and tip vortices

7

ADAPTATION OF THE BLADE WAKE IDENTIFICATION PROCESS IN THE ABSENCE OF VORTICITY FIELD

In cases where only the axial velocity component is available, $\tilde{\omega}_t^*$ values cannot be computed, necessitating an alternative approach to determine the location and shape of the blade wake. A viable method is to analyse the gradient of the axial velocity in the axial direction $\left(\frac{\partial V_x}{\partial x}\right)$. Since the blade wake is a viscous region characterised by a locally reduced axial velocity, this gradient is expected to be negative within the wake.

This approach is demonstrated in Fig. 7.4, where the non-dimensionalised gradient of the axial velocity, $\left(\frac{\partial V_x}{\partial x} \frac{D}{V_\infty}\right)$, is plotted alongside the previously detected blade wake and tip vortex shapes derived from $\tilde{\omega}_t^*$ values using the method outlined earlier in this section (indicated by solid black lines). The strong alignment of the previously identified blade wake and tip vortex with regions of negative $\frac{\partial V_x}{\partial x} \frac{D}{V_\infty}$ values validates the proposed approach.

7.3.3. SETUP OF HELICAL WAKE SYSTEM

For simplicity, this study assumes no wake contraction when setting up the helical wake system. However, when necessary, contraction can be accounted for using Eq. (2.1). The helical wake system is defined by calculating the convection velocity at each radial station. The convection velocity of each blade wake is determined by dividing the axial distance between consecutive wakes by the time interval between their passage through

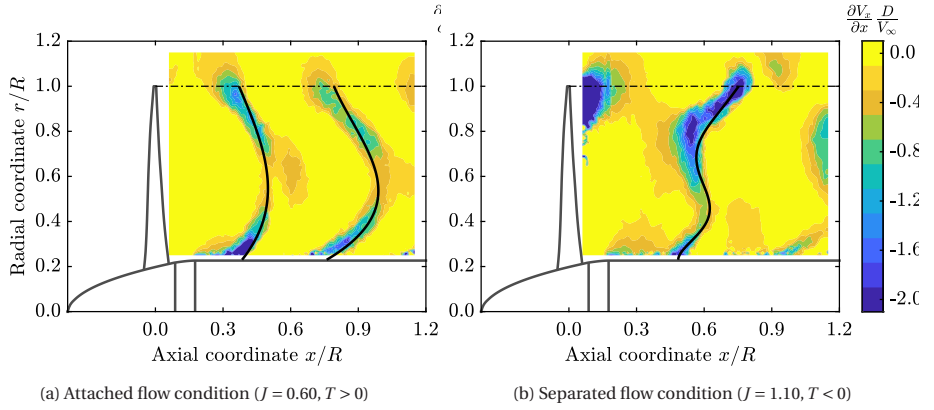


Figure 7.4: Phase-locked non-dimensional gradient of the axial velocity in the axial direction $\left(\frac{\partial V_x}{\partial x} \frac{D}{V_\infty}\right)$ obtained from SRANS simulations

the measurement plane $\left(\frac{1}{nB}\right)$. For the first blade wake, the axial distance is measured from the propeller plane, taking into account the phase angle of the measurement plane relative to the reference propeller blade (0° in this study). In cases where multiple wake structures are detected in the slipstream data, the convection velocity of the blade wake varies between consecutive wakes; i.e., the convection velocity between the propeller plane and the 1st wake differs from the convection velocity between the 1st and 2nd wakes, and so on. The convection velocity of the wake beyond the last wake structure is assumed to be the same as that calculated between the second-last and last wake structures.

The resulting helical wake systems can be seen in Figs. 7.5a and 7.5c for the attached and separated flow conditions, respectively, along with the zoomed-in views in Figs. 7.5b and 7.5d. In the setup, the length of the wake is defined to be $5R$ for the vortex line shed from the blade tip based on sensitivity studies investigating the influence of wake length on bound circulation. However, because of the variation in convection velocity with radial location, the resulting helical wake system stretches out for both conditions. In the attached flow condition, the blade wake convects at a higher speed in the mid-board region than in the root and tip regions, resulting in a wake extending up to approximately $6R$ in the mid-board area. In contrast, the convection speed is highest at the blade tip in the separated flow condition. Therefore, the wake extends between $4R$ - $5R$ depending on the radial location for the separated flow condition in Fig. 7.5c.

RADIAL DISCRETISATION

Defining the vortex wake system requires selecting an appropriate number of radial stations from which vortex lines emanate and convect in the slipstream. A sensitivity study was conducted for various radial discretisations, with the resulting non-dimensionalised bound circulations shown in Fig. 7.6. For all the radial discretisations, the two innermost vortex lines were consistently located at $r/R = 0.24$ and $r/R = 0.30$. The first vortex line corresponds to the root vortex and is determined by the nacelle diameter, while the sec-

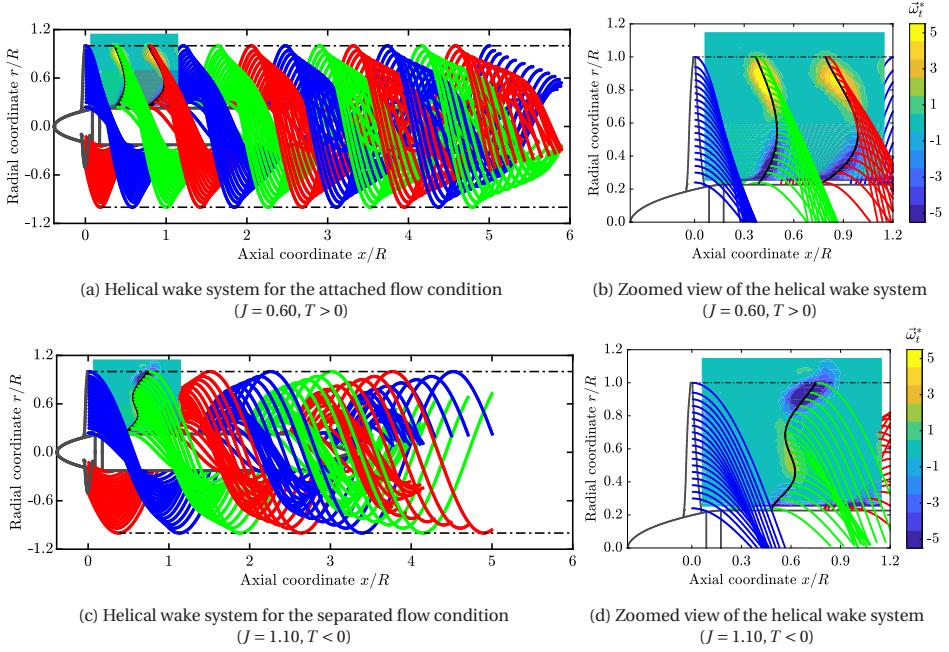


Figure 7.5: Setup of helical wake geometry for the wake-informed lifting line method

7

and one was selected to ensure that the vortex line intersects the input measurement plane. This avoids placing multiple vortex lines at radial locations lacking input velocity data, which could otherwise introduce high uncertainty. Without this restriction, vortex lines might cluster too closely relative to their nearest control point, making the solution overly sensitive to the placement of control points. This sensitivity arises because the induced velocities, as per Biot-Savart's law, are inversely proportional to the square of the distance between the vortex line and the control point.

The impact of such clustering is evident in the finest discretisation (47 radial stations) considered in the sensitivity study, where oscillatory behaviour is observed, particularly for the attached flow case (Fig. 7.6a). Similar oscillations were observed for the second-finest discretisation (36 radial stations) for both attached and separated flow cases. Conversely, the coarsest resolution (8 radial stations) leads to an underprediction of the peak value of the circulation magnitude. Therefore, to balance accuracy and stability, a sensitivity analysis is recommended for each case to identify the optimal radial resolution. For this study, 18 radial stations were chosen for further sensitivity studies conducted in Section 7.3.4 and validation of the model against SRANS data for both attached and separated flow conditions.

7.3.4. SETUP OF CONTROL POINTS

After defining the helical wake system, the next step is to set up the control points, which are used to inform the non-linear least squares fitting to obtain the bound circulation on

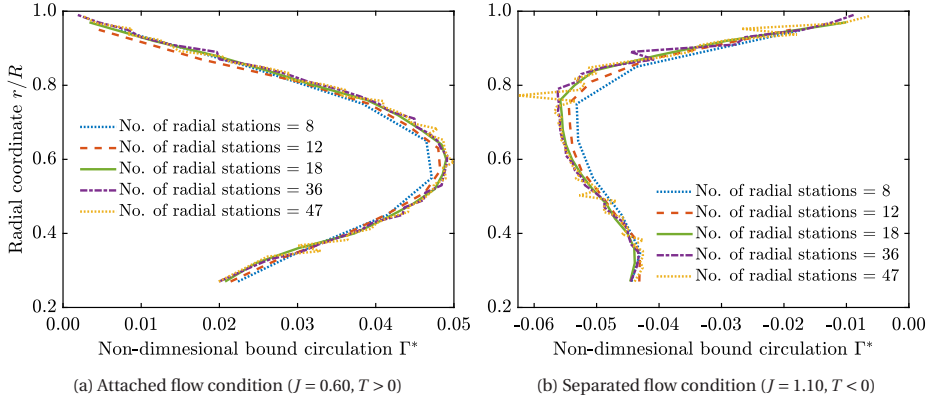


Figure 7.6: Effect of radial discretisation on the non-dimensionalised bound circulation for the wake-informed lifting line method

the propeller blades. The positions of the control points need to be chosen carefully as the fitting process aims to minimise the root sum square of the errors between the velocities induced by the helical system and the input slipstream data. The following procedure is used to position the control points:

1. Start by populating the measurement plane with a certain number of random points. In this study, 1000 points were used for this process.
2. Remove points that are too close to the propeller blades to avoid areas influenced by the blade thickness effect, which is not accounted for by LL models. Based on the sensitivity study presented later in *Sensitivity to Threshold Distance from Propeller Blade*, points within a threshold distance of $x/R < 0.20$ from the propeller blades were excluded for the attached flow condition, while for the separated flow condition, a threshold distance of $x/R < 0.30$ was used. This can be seen in Fig. 7.7.
3. To ensure numerical stability, the control points within a specified axial distance from the identified blade wake (from previous steps) are excluded to avoid having points too close to the helical element that can result in destabilising the solution. In this study, this tolerance was chosen to be $x/R < 0.010$ based on the sensitivity study presented later in *Sensitivity to Threshold Distance from Wake Structures*, and the affected regions are indicated with dashed blade lines in Fig. 7.7.
4. Finally, remove control points located within the boundary layer of the nacelle based on their axial or radial coordinates or the out-of-plane vorticity values, as potential flow methods cannot simulate boundary layer effects.

Theoretically, control points located within high-vorticity regions near the blade wakes and tip vortices should be removed, as LL models do not explicitly simulate viscous effects. However, viscous effects still influence blade loading distributions in real-world scenarios. Therefore, control points in high-vorticity regions are retained to derive a

non-linear least squares solution that aligns with the blade loading distributions implied by the input slipstream data.

This process resulted in approximately 800 control points for the present study. An example of the resulting control point distribution is shown in Fig. 7.7. Alternatively, one could have first masked the domain and then distributed a set number of random points across the remaining measurement plane.

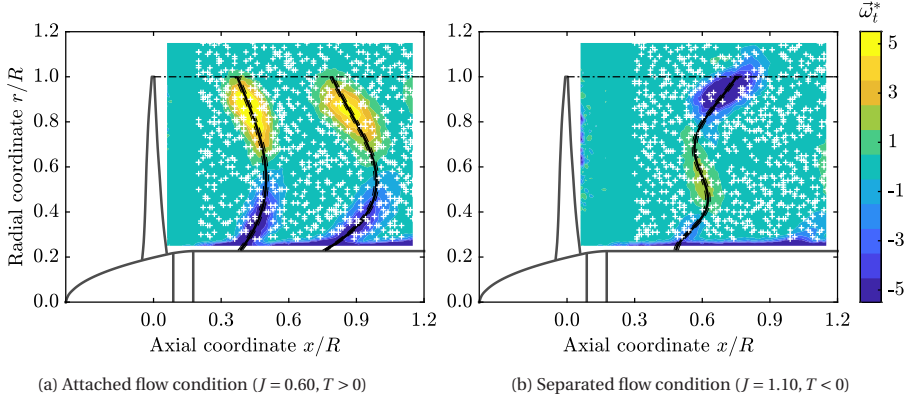


Figure 7.7: Setup of control points for the wake-informed lifting line method

STATISTICAL CONVERGENCE

The solution is expected to be sensitive to the choice of the control points. To mitigate this sensitivity and achieve statistical convergence, the model needs to be solved multiple times using a randomly distributed set of control points in each iteration, with the bound circulation averaged over these iterations.

Figure 7.8 presents the averaged bound circulations obtained from the wake-informed LL model for different numbers of randomly distributed control point sets under both attached and separated flow conditions. After just 10 passes, the solution exhibited less than 1% deviation from the 100-pass result across most of the blade span, excluding the tip region. Therefore, the additional passes beyond 10 have minimal impact on the converged bound circulation. However, to ensure statistical robustness and establish a 95% confidence interval, the 100-pass solution was used in this study. The corresponding confidence interval is shown as a shaded region around the mean solution in the figure.

SENSITIVITY TO THRESHOLD DISTANCE FROM PROPELLER BLADE

Figure 7.9 shows the sensitivity of the non-dimensionalised bound circulations (after 10 passes) to the threshold distance from the propeller blade. Since the mean values were already shown to converge after 10 passes in the previous section, only 10 passes were used for this sensitivity study. The threshold distance was varied from $x/R < 0.06$, representing the axial location where the input slipstream data begins, to $x/R < 0.40$.

For the attached flow condition (Fig. 7.9a), increasing the threshold distance from $x/R < 0.06$ to $x/R < 0.20$ results in a 4.1% increase in the peak value of the bound cir-

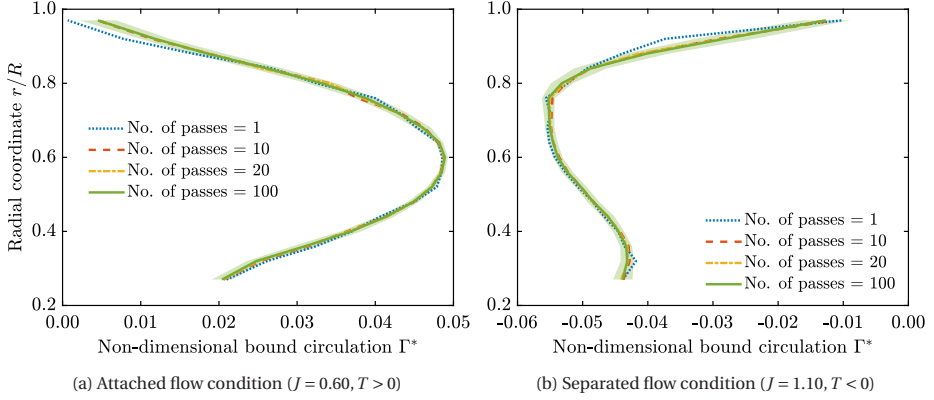


Figure 7.8: Statistical convergence of the wake-informed lifting line solution

culation (using $x/R < 0.20$ as the reference). This change underlines the influence of the blade thickness effect in regions closer to the propeller. Beyond $x/R < 0.20$, further increases in the threshold distance lead to minimal variations in the bound circulation, with only a 0.7% change in the peak value.

For the separated flow condition (Fig. 7.9b), increasing the threshold distance from $x/R < 0.06$ to $x/R < 0.20$ leads to an 11.6% change in the peak value, again using $x/R < 0.20$ as the reference. A further increase in the threshold distance from $x/R < 0.20$ to $x/R < 0.30$ results in a 1.6% change, with negligible variations beyond $x/R < 0.30$. The higher threshold distance required for the separated flow condition, compared to the attached flow condition, is a result of flow separation around the blades. This separation effectively makes the blade thicker in the separated flow case than in the attached flow case.

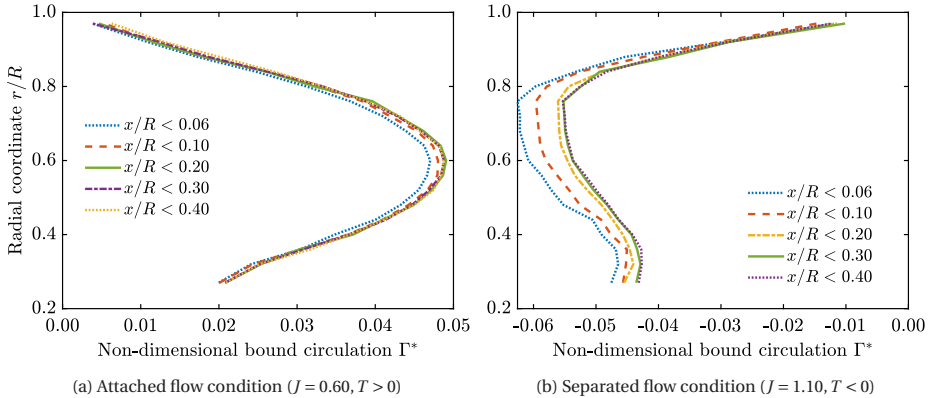


Figure 7.9: Sensitivity analysis of the wake-informed lifting line solution to the threshold distance from propeller blade

Based on these observations, threshold distances of $x/R < 0.20$ and $x/R < 0.30$ were

selected for the attached and separated flow conditions, respectively, to minimise the influence of the blade thickness effect on the wake-informed LL solution.

SENSITIVITY TO THRESHOLD DISTANCE FROM WAKE STRUCTURES

Figure 7.10 shows the sensitivity of the non-dimensionalised bound circulations (after 10 passes) to the variations in the threshold distance from wake structures, ranging from $\Delta x/R < 0.005$ to $\Delta x/R < 0.030$. For the threshold distance of $\Delta x/R < 0.030$, the solution exhibits some fluctuations in the bound circulation, particularly for the attached flow condition. These fluctuations arise because the distance of the closest control point ($\Delta x/R = 0.030$) becomes comparable to the distance between adjacent vortex lines ($0.04R$) for the chosen radial discretisation with 18 radial stations. The comparable distances make the solution overly sensitive to the placement of control points, as previously discussed in Section 7.3.3. Reducing the threshold distance results in a smoother solution for both attached and separated flow cases.

For the attached flow condition (Fig. 7.10a), reducing the threshold distance from $\Delta x/R < 0.030$ to $\Delta x/R < 0.010$ decreases the peak bound circulation by 2.6% (with $\Delta x/R < 0.010$ as the reference). Further reducing the threshold to $\Delta x/R < 0.005$ results in negligible changes to the bound circulation distribution along the blade span, with a marginal decrease of 0.8% for the peak value. Similarly, for the separated flow condition (Fig. 7.10b), reducing the threshold distance from $\Delta x/R < 0.030$ to $\Delta x/R < 0.010$ decreases the peak value by 3.2%. A further reduction of the threshold distance to $\Delta x/R < 0.005$ results in minimal impact on the distribution and a 1% decrease in the peak value (relative to $\Delta x/R < 0.010$).

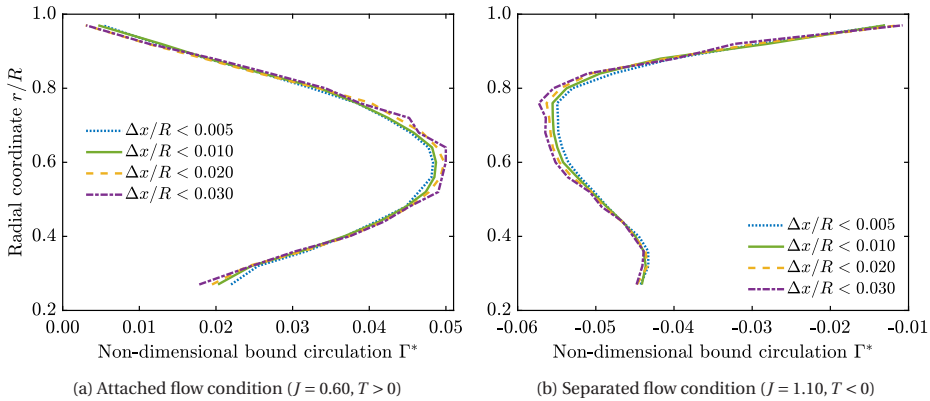


Figure 7.10: Sensitivity analysis of the wake-informed lifting line solution to the threshold distance from wake structures

Based on these results, the threshold distance of $\Delta x/R < 0.010$ was deemed suitable for further analysis. This choice provides a smooth solution by avoiding the placement of control points too close to the wake structures, which could destabilise the solution due to the inverse-square dependence of induction on the distance between control points and wake structures.

7.3.5. OBJECTIVE FUNCTION AND SOLUTION ALGORITHM

The bound circulation is determined by minimising the root sum square of the errors between the velocity vectors induced by the helical wake system, as set up in Section 7.3.3, and the induced velocity vectors obtained from the input slipstream data at the control points. Mathematically, this can be expressed using Eq. (7.3).

$$\min_{\Gamma(r)} \sum_{i=1}^N \left\| \mathbf{V}_{\text{ind},i}^{\text{Helix}}(\Gamma) - \mathbf{V}_{\text{ind},i}^{\text{Slipstream}} \right\|^2 \quad (7.3)$$

where $\mathbf{V}_{\text{ind},i}^{\text{Helix}}(\Gamma)$ represents the velocity vector induced by the helical wake system at control point i , and $\mathbf{V}_{\text{ind},i}^{\text{Slipstream}}$ is the corresponding velocity vector from the input slipstream data.

This minimisation is performed using non-linear least squares fitting. This study employed the trust-region-reflective (gradient-based) algorithm [127, 128] for the minimisation, though other algorithms could also be used.

7.3.6. POST-PROCESSING

The wake-informed LL model provides the converged bound circulation distribution along the blade span. This distribution, combined with the helical wake system, allows for the determination of all three components of the induced velocities at the quarter-chord point of each blade section and other desired locations. Using the induced velocities at the quarter-chord point of blade sections, the local inflow angle and local velocity vector at each blade section can be calculated. These parameters, along with the bound circulation, can be used to calculate the lift force contribution to thrust and torque as per Eqs. (7.4) and (7.5). Additionally, the local lift coefficient and angle of attack can be calculated using Eqs. (7.6) and (7.7), provided the chord and twist distributions along the blade span are known.

$$T'_L(r) = \rho_\infty V(r) \Gamma(r) \cos \varphi(r) \quad (7.4)$$

$$Q'_L(r) = \rho_\infty V(r) \Gamma(r) \sin \varphi(r) r \quad (7.5)$$

$$c_l(r) = \frac{2\Gamma(r)}{V(r)c(r)} \quad (7.6)$$

$$\alpha(r) = \beta(r) - \varphi(r) \quad (7.7)$$

To incorporate the missing drag force contribution in the thrust and torque (Eqs. (7.8) and (7.9)), external polar data are required. In this study, the polar data were generated using RFOIL [57], which is a modification of the well-known 2D-panel method XFOIL [58]. RFOIL was selected for its better lift and drag coefficient prediction in the post-stall region [61]. Moreover, the quasi-3D model available in RFOIL was utilised to account for the influence of Coriolis and centrifugal forces on the boundary-layer characteristics of rotating airfoils [59, 60]. To address compressibility and Reynolds number effects, polar data were generated at various Mach and Reynolds numbers for 24 radial stations using RFOIL.

$$T'_D(r) = -0.5\rho_\infty V^2(r)c(r)c_d(r) \sin \varphi(r) \quad (7.8)$$

$$Q'_D(r) = 0.5\rho_\infty V^2(r)c(r)c_d(r) \cos \varphi(r) r \quad (7.9)$$

These resulting polar data were interpolated with respect to radial position, local Reynolds number, and local Mach number based on the local effective velocity ($V(r)$) and chord of the blade sections ($c(r)$) to obtain the drag coefficient (c_d). Interpolation with respect to radial position is necessary because the chosen radial discretisation may not align with the stations for which the airfoil geometry and corresponding polar data are available. This interpolation was performed in two steps. Firstly, the polar data were interpolated using Delaunay triangulation of the sample points to obtain the drag coefficient for each radial location and local Reynolds number across all input Mach numbers at a given lift coefficient ($c_l(r)$) based on the solution from the wake-informed LL model. In the subsequent step, the resulting drag coefficient values were linearly interpolated to obtain the values at the specified local effective Mach number. A similar procedure was used to obtain the corresponding angle of attack values from the polar data, allowing for comparison with the angle of attack values derived from the wake-informed LL model.

7.4. VALIDATION OF WAKE-INFORMED LIFTING LINE MODEL

In this section, the wake-informed LL method is validated by comparing its results with those obtained from SRANS simulations, using the load-informed LL method as an intermediate tool for validation. The validation process begins with a comparison of axial induction in the slipstream, followed by an evaluation of blade loading distributions. Finally, the integrated thrust values obtained from the wake-informed LL model are compared against those from SRANS simulations.

7.4.1. AXIAL INDUCTION

Minimising the root-sum-square error between induced velocity components from the wake-informed LL model and the input data does not necessarily result in identical induced velocities due to inherent limitations of LL models, such as their inability to account for viscous effects, blade thickness, and nacelle presence. Consequently, these differences serve as a measure of the solution's accuracy. This section compares axial inductions from the wake-informed LL model with input inductions from SRANS data in the slipstream, starting with the attached flow condition, followed by the separated flow condition.

ATTACHED FLOW CONDITION ($J = 0.60$)

Figure 7.11 compares axial inductions obtained from SRANS, load-informed LL, and wake-informed LL in the plane directly behind the propeller blade for the attached flow condition. Contour plots of axial induction for each method are shown in Figs. 7.11a to 7.11c. The solid-black lines in these figures indicate the locations where the helical wake system of the LL models intersects the plane, also shown on top of the SRANS data for reference. Additionally, Figs. 7.11d and 7.11e show the comparison of the axial induction along the radial and axial lines located at $x/R = 0.6$ and $r/R = 0.6$ respectively, with dashed black lines marking their locations in the contour plots. The comparison between the load-informed LL and wake-informed LL models (Figs. 7.11b to 7.11e) show negligible differences, confirming the validity of the assumptions inherent to the LL models for this operating condition.

The comparison of contour plots (Figs. 7.11a to 7.11c) shows significant differences near the blade ($x/R < 0.20$) between both LL models and SRANS simulations. This discrepancy is due to the inability of the LL models to replicate the thickness effect of the propeller blade, and as a result, the control points were removed from this region (Section 7.3.4). However, away from the blade ($x/R \geq 0.20$), all three methods show qualitative similarities. As LL models do not simulate the presence of a nacelle, differences compared to SRANS data are apparent near the nacelle. This is further confirmed by the line plot at $x/R = 0.60$ in Fig. 7.11d, where the nacelle boundary layer is evident in the SRANS data. Despite this limitation, both LL models show good agreement with SRANS data except for the underprediction of the peak value of the induction near $r/R = 0.60$ by approximately 9%. This discrepancy is likely due to the omission of slipstream contraction in the LL models, as implemented in this study.

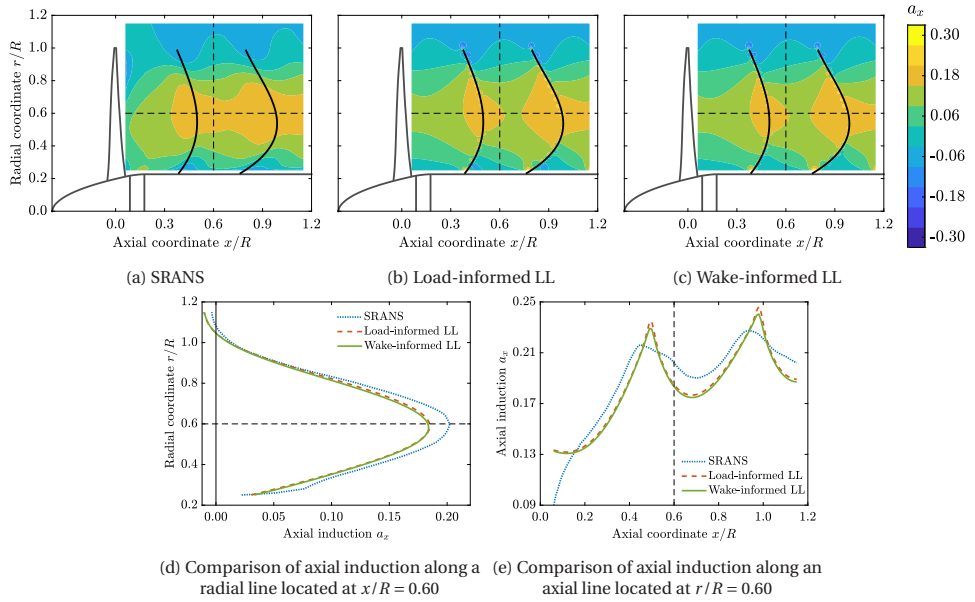


Figure 7.11: Comparison of axial induction in the slipstream for the attached flow condition ($J = 0.60$, $T > 0$)

The comparison along the axial direction at $r/R = 0.60$ (Fig. 7.11e) shows a good qualitative agreement between LL models and SRANS except near the blade ($x/R \leq 0.20$), as discussed earlier. LL models exhibit a sharp peak near blade wakes due to the inviscid flow assumption, while SRANS data show a flattened peak due to viscous effects and numerical diffusion. Also, there is an apparent axial offset between the axial induction distributions obtained from SRANS and LL models. This discrepancy is likely due to the blade wake (the position where the helical wake system cuts the measurement plane) being defined at a slightly different position in the LL models compared to its position in the SRANS simulations.

SEPARATED FLOW CONDITION ($J = 1.10$)

Figure 7.12 compares axial inductions in the slipstream behind the propeller blade for the separated flow condition. The differences near the nacelle between SRANS and LL models (Figs. 7.12a to 7.12c) are again due to the inability of LL models to account for the presence of nacelle, confirmed by the radial line plot at $x/R = 0.90$ in Fig. 7.12d. However, away from the nacelle ($r/R > 0.40$), a qualitative agreement can be observed between the three methods, with differences of up to 21% and 30% observed for the wake-informed LL and load-informed LL models, respectively, within the range $0.4 \leq r/R \leq 0.9$, when compared to SRANS data. Similar to the attached flow case, the flowfield close to the propeller blades ($x/R < 0.30$) is significantly different due to the inability of the LL models to simulate thickness effects. These differences are evident in the axial line plot at $r/R = 0.60$ in Fig. 7.12e. However, away from the blade ($x/R \geq 0.30$), a qualitative agreement can be observed between the three methods, with a difference of up to 12% for wake-informed LL and up to 19% for load-informed LL as compared to SRANS at the intersection of the blade wake with the specified plane (shown with solid-black line in contour plots). Since the wake-informed LL model uses SRANS slipstream data as an objective function for the solution, it exhibits a lower error than the load-informed LL model.

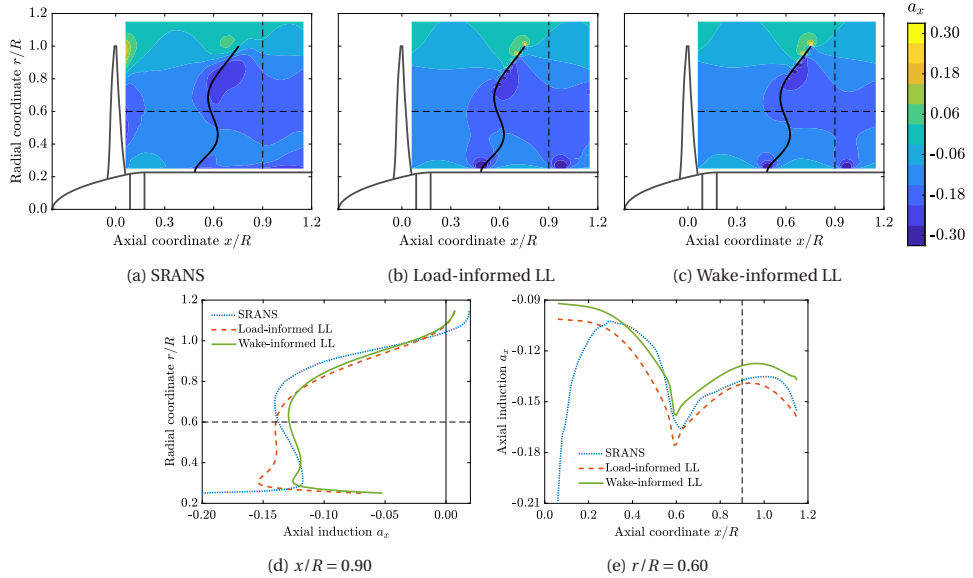


Figure 7.12: Comparison of axial induction in the slipstream for the separated flow condition ($J = 1.10$, $T < 0$)

Overall, higher discrepancies are observed for the separated flow condition between the wake-informed LL model and SRANS data as compared to the attached flow condition. These increased differences suggest that the inherent assumptions of the wake-informed LL model, such as perfectly helical wake and inviscid flow assumptions, may not accurately represent this operating condition. This is further confirmed by the observed increased differences between the wake-informed LL and the load-informed LL

models.

7.4.2. BLADE LOADING DISTRIBUTIONS

This section evaluates the accuracy of the wake-informed LL model in predicting blade loading distributions. To this end, thrust and power distributions obtained from the wake-informed LL model are compared with those from SRANS simulations. As a potential flow method, the wake-informed LL model inherently captures only lift force contributions (c_{t_L} , c_{p_L}) to thrust and power distributions (Eq. (7.10)) and requires external polar data for the estimation of the profile drag contributions (c_{t_D} , c_{p_D}).

$$c_t = c_{t_L} + c_{t_D}, \quad c_p = c_{p_L} + c_{p_D} \quad (7.10)$$

While a direct comparison with SRANS data is informative for practical applications, it is not suitable for a comprehensive model assessment. To address this, two types of comparisons are conducted:

1. **Evaluation of Importance of Drag Force Contribution to Blade Loads:** The load-informed LL model is used to decompose the blade loading distribution from SRANS into its lift and profile drag components. Comparing the lift contribution from the load-informed LL model with the total blade loading from SRANS provides insights into the importance of the drag contribution for the given blade loading distribution. Additionally, the lift force contribution from the wake-informed LL model is compared with the total blade loading from SRANS to assess the feasibility of using the wake-informed LL model without external polar data.
2. **Total Blade Loading Comparison:** Using external polar data, the profile drag contributions are estimated and combined with the lift force contributions from the wake-informed LL model to calculate total thrust and power distributions. These results are then compared with SRANS data for a practical evaluation of the performance of the wake-informed LL model.

First, the comparisons are presented for the attached flow condition, followed by the separated flow condition.

ATTACHED FLOW CONDITION ($J = 0.60$)

Figure 7.13 presents the comparison of thrust and power distributions for the attached flow condition. The mean solution obtained using the wake-informed LL is depicted with solid lines, and the 95% confidence interval is shown as a shaded area. The mean values and the confidence interval are based on 100 different sets of control points, which have been shown to provide converged results; see Fig. 7.8.

Figure 7.13a demonstrates excellent agreement between the wake-informed LL model and SRANS results for the thrust distribution, both with and without the profile drag contribution. Without the profile drag contribution, the c_{t_L} values predicted using the wake-informed LL model slightly overpredict the peak value by 0.3% with a $\pm 2.1\%$ uncertainty compared to the total thrust distribution from SRANS. Incorporating the profile drag component into the wake-informed LL model using polar data results in a 1.0% underprediction of the peak with a similar $\pm 2.1\%$ uncertainty. In contrast, the

load-informed LL model suggests a 1.8% drag contribution by comparing its c_{tL} distribution to the SRANS c_t . These observations indicate potential underestimations in both the profile drag values from polar data and the lift values from the wake-informed LL model. Nonetheless, these results validate the wake-informed LL method for estimating thrust distributions from slipstream data, both with and without profile drag estimation. It should be noted that the profile drag estimation requires detailed propeller geometry information.

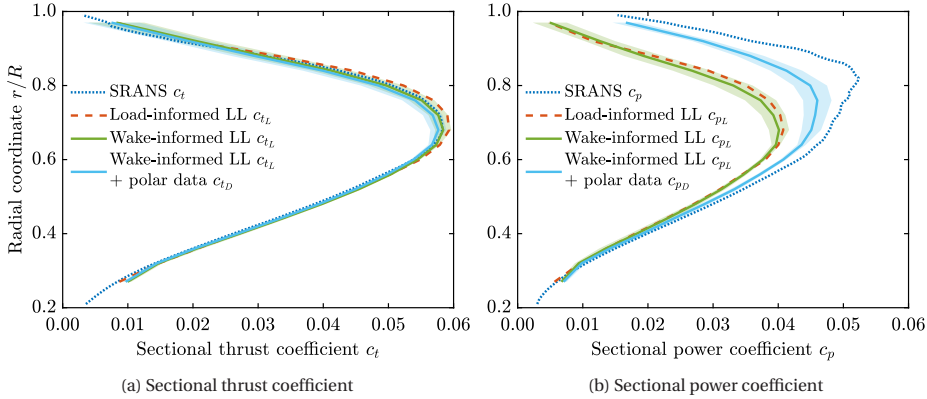


Figure 7.13: Comparison of blade loading distribution for the attached flow condition ($J = 0.60$, $T > 0$)

Figure 7.13b shows the comparison of power distributions. The comparison of the lift component of the power distribution (c_{pL}) from the load-informed LL model and total power distribution (c_p) from SRANS shows that the profile drag contribution (c_{pD}) constitutes up to 10% of the c_p for $r/R \leq 0.50$, increasing to about 20% at $r/R = 0.75$, and even higher further outboard. Therefore, while the wake-informed LL model shows good agreement with the c_{pL} obtained using the load-informed LL model, significant differences are observed when compared to c_p from SRANS. When the profile drag contribution is included, the resulting power distributions from the wake-informed LL model become more representative. However, there is still an underprediction of up to 8% for $r/R \leq 0.75$, increasing to 13% at $r/R = 0.80$, and becoming even more pronounced further outboard when compared to the total power distribution. This underprediction is attributed to the underestimation of profile drag values in the polar data, as well as inaccuracies in the predicted induced angles of attack by LL models that result in an incorrect lift contribution to the power distribution.

Given the significance of the drag contribution, the wake-informed LL model should not be used for obtaining power distributions without accounting for the profile drag contribution via external polar data, which necessitates knowledge of the propeller geometry.

SEPARATED FLOW CONDITION ($J = 1.10$)

Figure 7.14 shows the comparison of blade loading distributions for the separated flow condition. The flow separation around blades (Chapters 4 and 6) increases the importance of the drag contribution in the total thrust and power distributions. As per the

load-informed LL model, profile drag accounts for 8.9% of the total thrust magnitude at $r/R = 0.76$, as shown by the comparison of c_t from SRANS and c_{tL} from the load-informed LL model in Fig. 7.14a.

The wake-informed LL model captures the radial gradients and overall shape of the thrust distribution seen in SRANS but shows significant quantitative differences. These differences include a shift in the peak location from $r/R = 0.76$ in the SRANS data to $r/R = 0.80$ and a 10.4% underprediction of the peak value with a $\pm 3.2\%$ uncertainty when not accounting for profile drag. Incorporating profile drag into the wake-informed LL model reduces the underprediction of the peak value to 3.9% with an associated uncertainty of $\pm 3.4\%$ as compared to SRANS. These differences are attributed to the inviscid flow assumptions of the LL model, inaccuracies in the polar data, and the unaccounted influence of the presence of the spinner and nacelle (Appendix B). While the slipstream data used in the wake-informed LL model implicitly incorporates some effects of the spinner and nacelle, the model does not explicitly account for their impact on blade loading.

Large differences are observed between the c_{tL} values from load-informed and wake-informed LL models, with a 1.8% difference in the peak values and up to 20% difference near the root ($r/R \leq 0.40$), with load-informed LL as the reference. These larger discrepancies align with the significant differences observed in axial inductions in the slipstream in Fig. 7.12. These differences between load-informed LL and wake-informed LL are a consequence of pronounced viscous effects in the separated flow condition due to the flow separation around the blades [49], leading to different potential flow solutions obtained using direct blade loads and slipstream data.

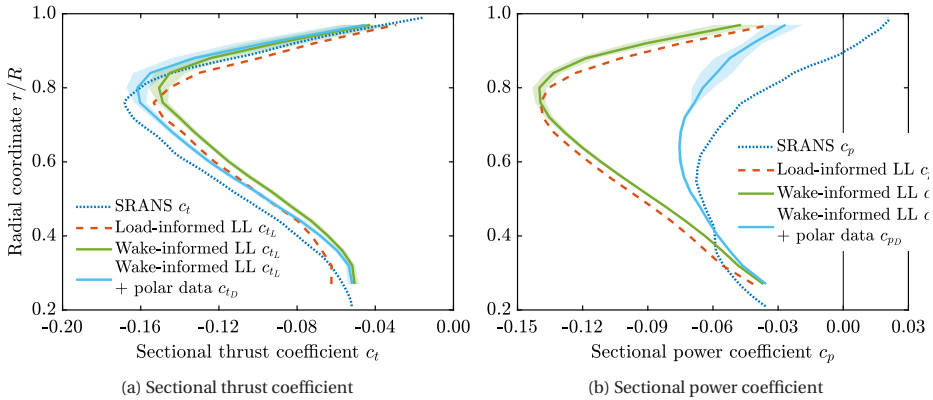


Figure 7.14: Comparison of blade loading distribution for the separated flow condition ($J = 1.10, T < 0$)

Figure 7.14b shows the comparison of power distributions for the separated flow condition. When profile drag is not accounted for, the wake-informed LL model overpredicts the power distribution by more than 100% for $r/R \geq 0.65$ as compared to SRANS. Incorporating profile drag estimates from polar data into the wake-informed LL model improves the radial trends, aligning it better with the power distribution from SRANS. However, significant discrepancies are observed in absolute values, particularly in the

outboard region, with a difference of 20% and higher for $r/R \geq 0.65$. Additionally, increased uncertainties of approximately 13% or more (with mean values as the reference) are observed for $r/R \geq 0.80$.

The increased uncertainty can be attributed to vortices being shed by the propeller blade in this outboard region due to flow separation. Consequently, the wake-informed LL model shows high sensitivity to the placement of control points, resulting in significant uncertainty in the converged bound circulation. The resultant uncertainty is reflected in the corresponding lift coefficient, which impacts the calculated drag coefficient from polar data and, subsequently, the power distribution.

7.4.3. INTEGRATED THRUST AND POWER

This section compares the integrated thrust and power values from the wake-informed LL method with those obtained from SRANS simulations. In practical applications, the contributions of the blade and spinner are typically inseparable. However, the wake-informed LL model does not account for the influence of the spinner. Therefore, to provide an estimate of the expected difference caused by the presence of the spinner, the wake-informed LL model is compared to both blade-only and blade + spinner results from SRANS simulations.

Table 7.1 lists the integrated thrust and power coefficient values for the attached flow condition. The comparison of the integrated values with and without the spinner shows that the spinner accounts for 1.3% and 0.7% of the total integrated thrust and power, respectively. When the profile drag is not included, the wake-informed LL model slightly overpredicts the integrated thrust by 0.4% with an uncertainty of 1.3% relative to the total integrated thrust from SRANS. This corresponds to a 1.7% overprediction compared to the blade-only contribution in SRANS simulations. Conversely, incorporating the profile drag contribution via external polar data results in a 1.6% underprediction of integrated thrust compared to the total value, with a negligible underprediction (0.3%) relative to the SRANS blade-only contribution.

For power, the wake-informed LL model exhibits significant errors compared to SRANS. Without accounting for the profile drag contribution, the wake-informed LL model underpredicts the power by 28.1% as compared to the total integrated power from SRANS. Incorporating the profile drag contribution via external polar data reduces this underprediction to 11.0%.

Table 7.1: Comparison of integrated thrust and power between SRANS and the wake-informed lifting line model for the attached flow condition ($J = 0.60$, $T > 0$)

Method	Components	C_T	$\Delta C_T\%$	C_P	$\Delta C_P\%$
SRANS	Blades + spinner	+0.0410	--	0.0385	--
SRANS	Blades	+0.0405	-1.3%	0.0382	-0.7%
Wake-informed LL	Blades	$+0.0411 \pm 0.0005$	$+0.4\% \pm 1.3\%$	0.0277 ± 0.0004	$-28.1\% \pm 1.0\%$
Wake-informed LL + polar data	Blades	$+0.0403 \pm 0.0005$	$-1.6\% \pm 1.3\%$	0.0343 ± 0.0003	$-11.0\% \pm 0.8\%$

Therefore, while the wake-informed LL model shows strong agreement with SRANS for thrust predictions, even without accounting for profile drag, significant errors are ob-

served in the integrated power values even after including the profile drag contribution. These findings are consistent with previous comparisons of the radial thrust and power distribution shown in Figs. 7.13a and 7.13b.

Table 7.2 lists the integrated thrust and power values for the separated flow condition. In this case, the spinner accounts for 1.9% of the total thrust magnitude. The wake-informed LL model underpredicts thrust magnitude by 13.1% with an uncertainty of 2.0% as compared to the total integrated thrust magnitude obtained from SRANS. Including the profile drag contribution using external polar data reduces this underprediction to 6.8% with an uncertainty of 2.1%. This improvement highlights the increased significance of profile drag in the separated flow condition due to flow separation. These error magnitudes align with the discrepancies observed in the thrust distributions shown in Fig. 7.14a.

For the power, the spinner has a significant contribution of 6.6% to the total power, as also detailed in Appendix B. When not accounting for the profile drag contribution, the wake-informed LL model overpredicts the power magnitude by 92.6% due to the increased importance of the profile drag contribution due to the flow separation. Incorporating profile drag using polar data reduces this overprediction to 21.1%. These discrepancies are a result of delayed stall prediction in the polar data, leading to underestimated profile drag and an overpredicted power. Additionally, errors in the induced angle of attack also affect the lift contribution to power.

Table 7.2: Comparison of integrated thrust between SRANS and the wake-informed lifting line model for the separated flow condition ($J = 1.10$, $T < 0$)

Method	Components	C_T	$\Delta C_T\%$	C_P	$\Delta C_P\%$
SRANS	Blades + spinner	-0.1272	--	-0.0548	--
SRANS	Blades	-0.1248	-1.9%	-0.0512	-6.6%
Wake-informed LL	Blades	-0.1106 ± 0.0025	$-13.1\% \pm 2.0\%$	-0.1056 ± 0.0021	$92.6\% \pm 3.8\%$
Wake-informed LL + polar data	Blades	-0.1186 ± 0.0027	$-6.8\% \pm 2.1\%$	-0.0663 ± 0.0011	$21.1\% \pm 2.0\%$

7.5. EXPERIMENTAL TEST CASE

This section applies the wake-informed LL model to experimental PIV data from Nederlof et al. [46] to demonstrate its capabilities and potential for expanding experimental analyses. The model was applied to the same operating conditions ($J = 0.60, 1.10$) for which the model was validated in the previous section using SRANS data. Figure 7.15 shows the phase-locked out-of-plane vorticity field obtained from PIV measurements for both operating conditions, along with the identified shape of the blade wake intersecting the measurement plane, represented by solid black lines. A fifth-order polynomial was used to define the blade wake shapes for the attached flow condition, while a sixth-order polynomial was used for the separated flow condition (obtained using the procedure defined in Section 7.3.2).

The analysis begins by comparing input axial inductions from PIV with output axial inductions from the wake-informed LL model. Subsequently, measured thrust is

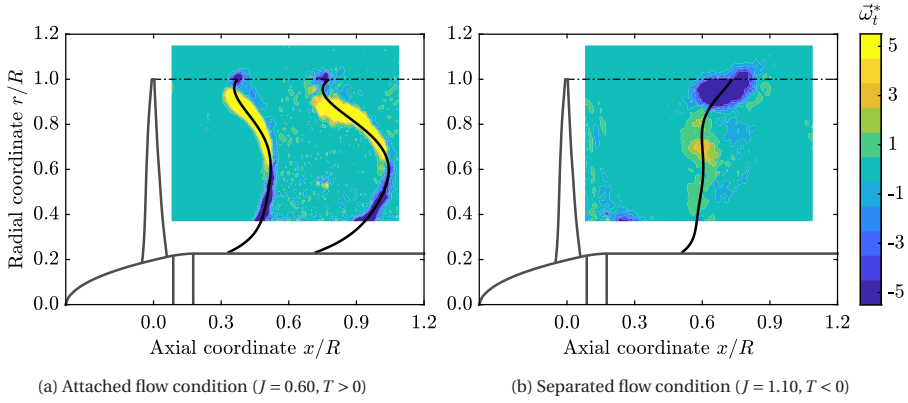


Figure 7.15: Phase-locked non-dimensional out-of-plane vorticity component ($\bar{\omega}_t^*$) obtained from PIV measurement along with the identified shape of blade wakes and tip vortices

compared with thrust obtained from the wake-informed LL model. Finally, thrust distributions, local angles of attack, and sectional lift coefficients derived from the wake-informed LL model are presented.

7.5.1. AXIAL INDUCTION

Figure 7.16 shows the comparison of axial inductions from PIV data and wake-informed LL model for the attached flow condition. Similar to the validation case, the most significant errors are observed close to the blade due to the inability of the LL models to simulate the thickness effect of the propeller blades; see Figs. 7.16a and 7.16b. Away from the propeller blades ($x/R \geq 0.20$), there is a good agreement between the experimental inductions and those obtained from the wake-informed LL model. This agreement is further confirmed in the radial and axial line plots at $x/R = 0.60$ and $r/R = 0.60$, respectively, as seen in Figs. 7.16c and 7.16d. The line plot at $x/R = 0.60$ shows good agreement except for an underprediction of the peak value by 2.9% (Fig. 7.16c).

Similarly, good agreement is also observed along the axial line at $r/R = 0.60$ in Fig. 7.16d, except for $x/R \leq 0.20$. Notably, the peak values near blade wakes are sharper in LL models due to their inviscid flow assumption, contrasting with the more flattened peaks in experiments (due to viscous effects). Additionally, some noise can be observed in the experimental data in the line plot, particularly between $0.6 \leq x/R \leq 1.0$, which is not simulated by the wake-informed LL model. Given the minimal differences between the experimental and wake-informed LL axial inductions, it is expected that the thrust distributions obtained from the latter method should closely represent the experimental blade loading for the considered operating condition.

Figure 7.17 shows the comparison of axial induction in the slipstream for the separated flow condition. As expected, significant discrepancies are observed close to the propeller for $x/R \leq 0.30$ (due to the blade thickness effect). Away from the blade, a qualitative agreement is observed between the experimental and wake-informed LL axial inductions. However, some differences are evident in the contour plots near the tip vortex

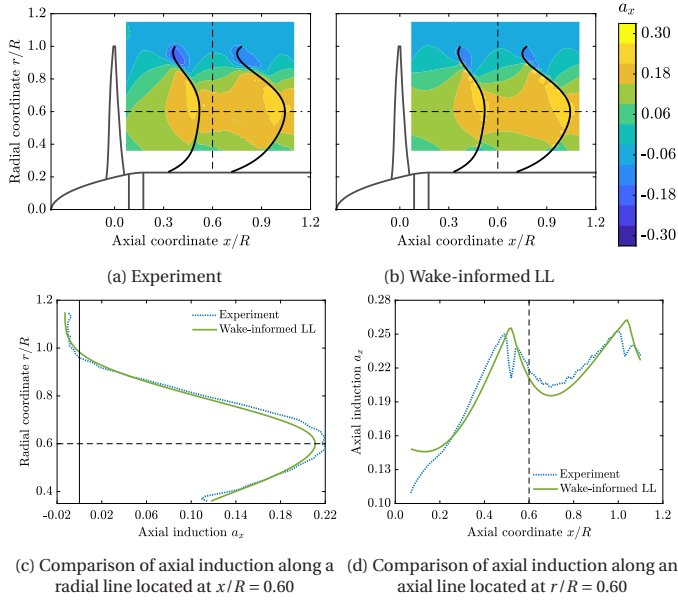


Figure 7.16: Comparison of axial induction in the slipstream for the attached flow condition ($J = 0.60$, $T > 0$)

region. The vorticity shed by the blades due to the flow separation in this operating condition is not accurately modelled by the wake-informed LL model due to the inviscid assumption.

To further analyse these discrepancies, two line plots are presented: a radial line at $x/R = 0.90$ and an axial line at $r/R = 0.60$. The comparison along the radial line ($x/R = 0.90$) shows that the wake-informed LL model captures the radial gradients, although there are differences in absolute values. The differences are negligible for $r/R \leq 0.60$ but increase to 10% in the outboard region ($r/R = 0.80$). The axial line plot at $r/R = 0.60$ shows significant discrepancies between the experiment and wake-informed LL model, particularly for $x/R \leq 0.30$ due to the thickness effect of the propeller blade. Beyond this region, the trends are captured, but with notable differences in the gradients. The wake-informed LL model exhibits a steeper gradient for axial induction increase for $x/R \leq 0.60$ and a lower gradient for $x/R \geq 0.80$ compared to the experiment. These differences in the gradient are expected to be a consequence of assumptions made about wake geometry and convection velocity within the LL model. Besides, as the axial line passes the location where the blade wake intersects through the plane (near $x/R = 0.60$), a local peak is seen in the wake-informed LL model, whereas a sudden drop in the axial induction values is seen in the experimental data. This discrepancy is attributed to the inviscid flow assumption of the LL model, while the experimental data captures the viscous nature of the blade wake, which is not concentrated around the assumed vortex line.

Given the significant differences between the axial inductions obtained from the experiment and the wake-informed LL model, it can be concluded that the thrust distributions obtained from the wake-informed LL model for this separated flow condition

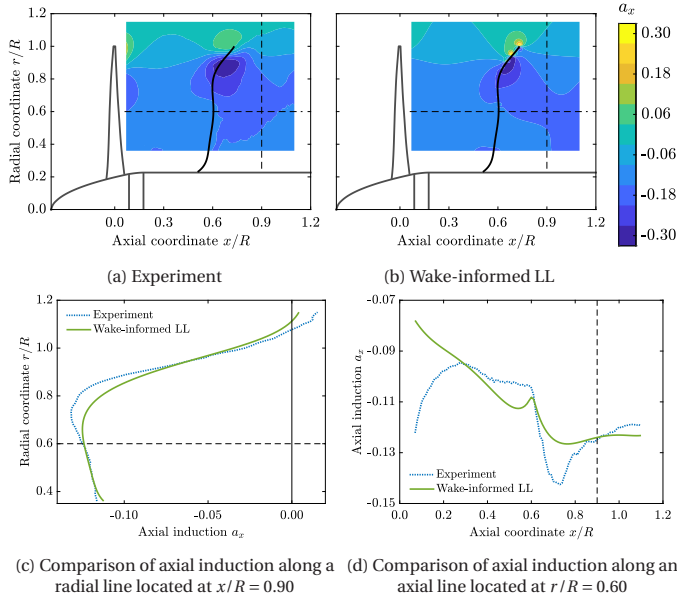


Figure 7.17: Comparison of axial induction in the slipstream for the separated flow condition ($J = 1.10$, $T < 0$)

are expected to have significant errors in terms of absolute values. However, the model might still be able to capture the radial gradients of the experimental thrust distribution, as evident from the comparison of the axial inductions along the radial line at $x/R = 0.90$.

7.5.2. INTEGRATED THRUST AND POWER

In cases where the measured integrated thrust and power values are available, comparing them to wake-informed LL model predictions provides an additional means to estimate the potential error in the predicted thrust and power distribution. This section compares the integrated thrust obtained using the wake-informed LL model with those measured in the experiments. The experimental values reported here were corrected for wind-tunnel boundary interference (Chapter 2).

Table 7.3 lists the integrated thrust and power values from the experiment and the wake-informed LL model for the attached flow condition. The experimental thrust and power have uncertainties of 2.4% and 1.3%, respectively. The wake-informed LL model underpredicts thrust by 2.2% (with a 2.6% uncertainty) and power by 31.5% (with a 1.5% uncertainty) compared to experimental values. Incorporating drag contributions using polar data increases the thrust underprediction to 4.2% due to negative drag contributions in the thrust direction while reducing the power underprediction to 14.2% due to significant positive drag contributions in the torque direction. A part of these discrepancies can be attributed to the presence of the spinner and nacelle in the experiments, which are not modelled in the wake-informed LL model. The error in the thrust is of the same order as observed in the validation case for the same operating condition. The underprediction of integrated thrust, with and without polar data, being comparable to the

uncertainty in experimental measurements, suggests that the wake-informed LL model can provide reasonable thrust distribution predictions for this attached flow condition. However, the power distributions obtained from the wake-informed LL model should be interpreted with caution while ensuring that profile drag contributions are accurately accounted for.

Table 7.3: Comparison of integrated thrust and power between the experiment and wake-informed lifting line model for the attached flow condition ($J = 0.60, T > 0$)

Method	Components	C_T	ΔC_T %	C_P	ΔC_P %
Experiment	Blades + spinner	$+0.0423 \pm 0.0010$	$\pm 2.4\%$	$+0.0416 \pm 0.0006$	$\pm 1.3\%$
Wake-informed LL	Blades	$+0.0414 \pm 0.0003$	$-2.2\% \pm 2.6\%$	$+0.0285 \pm 0.0002$	$-31.5\% \pm 1.5\%$
Wake-informed LL + polar data	Blades	$+0.0406 \pm 0.0003$	$-4.2\% \pm 2.6\%$	$+0.0357 \pm 0.0003$	$-14.2\% \pm 1.5\%$

Table 7.4 lists the integrated thrust and power values for the separated flow condition. Unlike the attached flow case, the uncertainties in the experimental values are rather small ($\pm 0.5\% - \pm 0.6\%$). For this condition, the wake-informed LL model without polar data underpredicts thrust by 12.7% (with a 2.5% uncertainty) and overpredicts power by 95.4% (with a 4.6% uncertainty) for this condition. These larger errors in the integrated values for the separated flow case, compared to the attached flow case, are consistent with previously observed increased discrepancies in axial induction between experiments and the wake-informed LL model for the former (Fig. 7.17). The increased drag contribution in this operating condition, caused by flow separation, combined with the inherent limitations of the LL model, exacerbates these errors. Incorporating drag contributions reduces the thrust underprediction to 6.3% and the power overprediction to 19.1%. These results highlight the necessity of accounting for drag contributions using external polar data when predicting thrust and power distributions with the wake-informed LL model in separated flow conditions.

Table 7.4: Comparison of integrated thrust and power between the experiment and the wake-informed lifting line model for the separated flow condition ($J = 1.10, T < 0$)

Method	Components	C_T	ΔC_T %	C_P	ΔC_P %
Experiment	Blades + spinner	-0.1298 ± 0.0007	$\pm 0.5\%$	-0.0553 ± 0.0003	$\pm 0.6\%$
Wake-informed LL	Blades	-0.1133 ± 0.0031	$-12.7\% \pm 2.5\%$	-0.1081 ± 0.0025	$+95.4\% \pm 4.6\%$
Wake-informed LL + polar data	Blades	-0.1216 ± 0.0034	$-6.3\% \pm 2.7\%$	-0.0659 ± 0.0016	$+19.1\% \pm 2.9\%$

7.5.3. BLADE LOADING DISTRIBUTIONS

This section gives an example of the blade loading parameters that can be derived from the slipstream velocity field of an experimental test case. In addition to thrust and power distributions in Fig. 7.18, the sectional lift coefficient, drag coefficient, and local angles of attack at the blade sections are also presented in Fig. 7.19.

Figure 7.18a shows the radial distributions of the sectional thrust coefficient obtained using the wake-informed LL model, both with and without estimated drag contri-

butions using the polar data. For the attached flow condition ($J = 0.60$), the peak loading is observed around $r/R \approx 0.7$, while for the separated flow condition ($J = 1.10$), it shifts to $r/R \approx 0.85$ as per the wake-informed LL model. The attached flow condition exhibits negative loading at the tip, consistent with previous studies for this propeller and operating condition [46]. The attached flow case has a relatively small uncertainty of $\pm 1.0\%$, whereas the separated flow case shows an uncertainty of $\pm 4.2\%$ at the peak. Incorporating drag contributions has a minimal impact on the thrust distribution for the attached flow condition, with changes of around 1%-2% along the entire blade span. In contrast, for the separated flow condition, drag contributions significantly influence the thrust distribution due to the increased importance of drag as a result of the flow separation, resulting in up to 9% changes along the blade span when compared to the distribution without drag contributions.

Figure 7.18b shows the power distributions along the blade span obtained using the wake-informed LL model with and without estimated drag contributions. For the attached flow case, the power values predicted without the drag contribution exhibit similar trends and magnitudes as those including drag for $r/R \leq 0.50$. However, drag contributions become increasingly significant outboard, accounting for 10% at $r/R = 0.70$ and 33% at $r/R = 0.80$, compared to the power distribution without drag contributions as the reference. In the separated flow condition, the drag contribution dramatically alters the power distribution along the entire span, reducing power by 10% at $r/R = 0.40$, increasing to a 70% reduction at $r/R = 0.90$ when compared to the distribution without drag contributions.

Notably, power distributions with drag contributions exhibit significant uncertainty (up to 38%) for $r/R \geq 0.80$ in the separated flow condition. This uncertainty arises due to the shedding of vortices in the outboard region caused by flow separation. Consequently, the wake-informed LL model shows increased sensitivity to the placement of control points in this region, resulting in increased uncertainty in the converged bound circulation. The resulting uncertainty is reflected in the corresponding lift coefficient (Fig. 7.19a), which impacts the calculated drag coefficient from polar data and, subsequently, the power distribution.

The distribution of the sectional lift coefficient along the blade span obtained from the wake-informed LL model is shown in Fig. 7.19a. In the attached flow case, the lift coefficient reaches a maximum of 0.5 near $r/R = 0.5$, then decreases with the increasing radial coordinate and goes below zero for $r/R > 0.9$. In contrast, the sectional lift coefficient in the separated flow condition decreases from -1.0 to -0.5 up to the radial coordinate of 0.90 and then quickly drops towards zero at the tip.

Figure 7.19b shows the distribution of the drag coefficient along the blade span, obtained by interpolating the polar data at the c_l values obtained using the wake-informed LL model. The drag values for the separated flow condition are nearly an order of magnitude higher than those for the attached flow condition, therefore justifying the previously observed increased importance of the drag contribution in the thrust and power distributions. In the outboard region ($r/R > 0.80$), the drag coefficient exhibits significant uncertainty (upto 28%) for the separated flow condition. This is attributed to the higher uncertainty in the converged bound circulation (as explained before), which was also reflected in the power distribution in Fig. 7.18b.

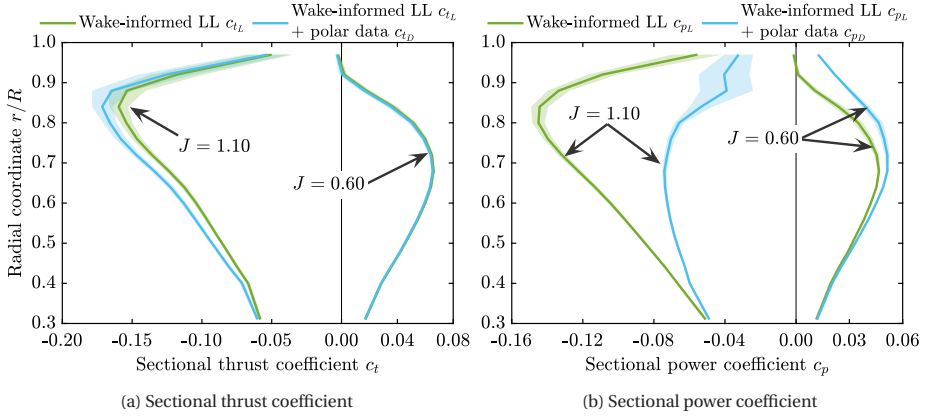


Figure 7.18: Comparison of blade loading distributions for the attached and separated flow conditions obtained using the wake-informed lifting line model with PIV data as input

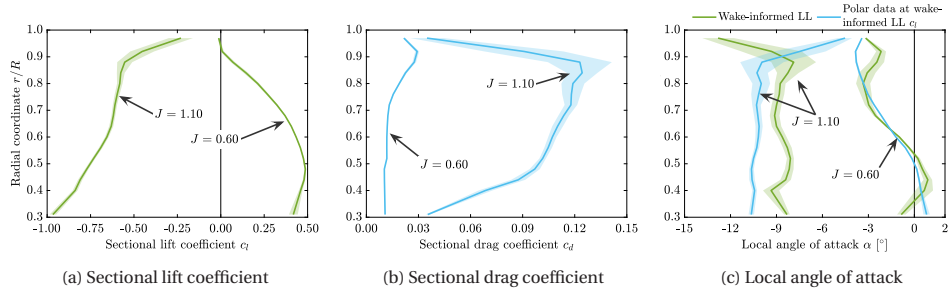


Figure 7.19: Comparison of blade sectional parameters for the attached and separated flow conditions obtained using the wake-informed lifting line model with PIV data as input

Figure 7.19c shows the distribution of the local angle of attack at blade sections. As per the wake-informed LL model, the positively cambered airfoils of the propeller blade operate at a significantly higher absolute angle of attack in the separated flow conditions compared to the attached flow condition. While the separated flow condition maintains relatively constant local angles of attack (between -10° to -8°) up to $r/R \leq 0.9$, the attached flow condition exhibits a broader range of -4° to 1° . The angles of attack obtained from the polar data for the given c_l based on the wake-informed LL model are also plotted in the figure. For the attached flow condition, polar data predictions align well with wake-informed LL model trends, with differences of less than 0.5° (except at the root and the tip). However, for the separated flow condition, the use of the polar data overpredicts the required angles of attack to obtain the given c_l by $1.1^\circ - 2.5^\circ$ along the whole blade span (except at the tip). This mismatch could either be the consequence of the inaccuracies in the polar data and/or due to the assumptions of the LL model being challenged under these conditions, potentially leading to an incorrect induced angle of attack at the blade.

7.6. KEY FINDINGS

This chapter evaluated the performance of the so-called “wake-informed lifting line” model in estimating blade loading distributions from slipstream velocity data. The method was validated by comparing its results with those obtained from SRANS simulations and subsequently applied to a test case based on experimental input data. Since the wake-informed LL model only predicts the lift component of the blade loading distribution, drag contributions were incorporated using external polar data.

In the attached flow condition, the wake-informed LL model demonstrated excellent agreement with SRANS predictions for thrust distribution, with errors below 1% in the peak value, even without accounting for the drag contribution. In the separated flow condition, while the model qualitatively captured the radial trends and overall thrust distribution shape, discrepancies of 10%-20% were observed in absolute values when drag contributions were not included. Accounting for drag reduced these errors to 8%–16%, with the remaining discrepancies attributed to the limitations of potential flow models in separated flows, inaccuracies in external polar data, and unaccounted influence of the spinner.

Irrespective of the flow condition (attached or separated), the drag contribution is crucial in the torque direction and must be accounted for when estimating the power distribution using the wake-informed LL model, necessitating the use of external polar data. Even with the drag contribution included, power values were underestimated by 10-25% in the outboard region ($r/R \geq 0.80$) in the attached flow condition and more than 20% for the separated flow condition beyond $r/R \geq 0.65$. This underprediction is attributed to two factors: the underestimation of drag in the polar data and inaccuracies in the induced angles of attack predicted by the wake-informed LL model, leading to an inaccurate lift contribution to the power distribution.

When applied to experimental data, the model provided the thrust distribution, sectional lift coefficients, and local angles of attack post-priori from slipstream velocity measurements, without the need for propeller geometry or external polar data (assuming drag contributions are negligible). The resulting axial induction and integrated thrust obtained using this method showed errors of approximately 2%-3% for the attached flow condition and more than 10% for the separated flow condition.

In conclusion, the wake-informed LL model offers a promising, non-intrusive approach for estimating blade loading distributions and local flow conditions at the blade, post-priori from slipstream velocity measurements. It offers significant value for practical applications, particularly in predicting thrust distributions when propeller geometry is unknown or inaccessible, as well as in situations where blade instrumentation is not feasible. However, for the estimation of power distribution, external polar data is required, which inherently requires the knowledge of propeller geometry. While the model excels in attached flow conditions, its limitations in separated flow necessitate caution in its application under such conditions.

PART IV

CONCLUSION

8

CONCLUSIONS AND RECOMMENDATIONS

The next generation of regional and short to medium-range aircraft are poised to embrace propellers as a sustainable solution, possibly combined with (hybrid-)electric propulsion systems, offering innovative integration opportunities. The presence of electric motors and propellers in such configurations presents a unique opportunity to leverage propellers as airbrakes, enabling steeper descents, reduced community noise, and shorter landing runs, while the regenerative capabilities of electric motors allow for energy harvesting. To adopt this concept successfully, a deeper understanding of the aerodynamic and aeroacoustic characteristics of propellers operating in both positive and negative thrust modes is crucial. Therefore, this thesis focused on this critical research question:

How do the aerodynamic and aeroacoustic characteristics of an unducted propeller change when operated in negative thrust mode compared to conventional propulsive mode?

To address this research question, multi-fidelity numerical simulations were employed. The conclusions drawn from this work are presented in Section 8.1. Subsequently, Section 8.2 outlines recommendations for further research endeavours.

8.1. CONCLUSIONS

Four sub-questions were addressed to tackle the main research question. The conclusions for each sub-question are summarized below, reflecting the key findings presented at the ends of Chapters 4 to 7, respectively.

8.1.1. AERODYNAMIC AND AEROACOUSTIC CHARACTERISTIC ANALYSIS

To understand the physical phenomena driving the performance of the propeller in negative thrust conditions, in-depth investigations have been carried out based on the fol-

lowing two subquestions, discussed one by one:

RQ1. What physical mechanisms drive the low regenerative efficiency observed for the conventional propellers operating in the negative thrust mode, and how do these mechanisms influence the resulting blade loading, slipstream, and far-field noise characteristics when compared to the conventional positive thrust mode?

To answer this sub-question, Chapter 4 presented a comprehensive analysis of the aerodynamic and aeroacoustic characteristics of a conventional propeller operating at a 0° AoA in the isolated configuration under both positive and negative thrust conditions. The analysis was carried out using lattice-Boltzmann very large-eddy simulations (LB-VLESs) at a constant rotational speed while varying the pitch angle (10° – 45°) to enable a direct comparison of the aerodynamic and aeroacoustic characteristics of positive and negative thrust conditions at a constant tip Mach number and Reynolds numbers. This approach allowed for the isolation of loading noise effects on the overall acoustic signature while keeping the thickness noise contribution constant. The key findings from this analysis are summarised below:

- In the positive thrust regime, the thrust and power magnitude increases with an increase in pitch angle (within the considered range). Conversely, in the negative thrust regime, thrust magnitude decreases monotonically with the increase in pitch angle, and power magnitude reaches a maximum at a unique pitch setting (at 15° for the considered propeller). This is a consequence of the fact that both lift and drag force components add up for the thrust in negative thrust conditions, whereas they counteract each other for the power.
- Flow separation in the outboard sections of the blade in the negative thrust mode significantly alters the radial distribution of thrust and power as compared to the positive thrust mode. For the considered propeller, the peak of the radial distribution of thrust is located more inboard in negative thrust conditions than in positive thrust conditions. Additionally, most of the negative power originates from the inboard part of the blade during negative thrust conditions, whereas in positive thrust conditions, the maximum power is generated comparatively outboard.
- The flow separation also results in an increase in the broadband fluctuations in the blade loading and integrated performance. These fluctuations increase with the increase in thrust coefficient (due to the increasing flow separation). For the considered case, the fluctuations in the integrated thrust increased from 0.7% to 1.5% as $|T_C|$ increased from 0.04 to 0.14. In comparison, the fluctuations in the integrated thrust were below 0.5% for all the thrust settings considered for the positive thrust conditions. Further, the blade loading in the negative thrust regime for the given absolute thrust coefficient ($|T_C| = 0.08$) showed the amplitude of fluctuations of up to 18% for inboard sections and up to 30% near the blade tip relative to the time-averaged loads, whereas the fluctuations in the blade loading in the positive thrust regime were negligible ($< 1\%$).
- Propeller operation under negative thrust conditions results in a reduced dynamic pressure compared to the freestream and generates a swirl opposite to the direction of propeller rotation. This contrasts with positive thrust conditions, where

dynamic pressure is increased, and the swirl in the slipstream aligns with the direction of propeller rotation. Consequently, a wing immersed in such a slipstream would experience different effects on the upgoing and downgoing blade sides, depending on the thrust condition. For a propeller operating under negative thrust, the slipstream would cause a greater reduction in lift on the upgoing blade side compared to the downgoing blade side. Conversely, under positive thrust conditions, the slipstream would lead to a greater increase in lift on the upgoing blade side than on the downgoing blade side.

- The comparison of the far-field noise (at $10D$) showed that the noise produced along the axial direction, which is primarily dominated by the broadband noise, is about 15–20 dB higher in negative thrust conditions than positive thrust conditions for all the whole range of thrust coefficient (0.01–0.14) considered in the study. This is a consequence of increased flow separation in negative thrust conditions, which leads to higher fluctuations in blade loading and enhanced vortex shedding. These factors result in increased broadband noise, which exhibits dominant directivity along the propeller axis.
- At a given absolute thrust magnitude, the tonal noise produced in the propeller plane is higher under positive thrust conditions compared to negative thrust conditions. This is primarily due to the noise due to torque being the dominant contributor. For a given thrust at a constant advance ratio, the torque required to generate that thrust (positive thrust condition) is always higher than the torque regenerated (negative thrust condition) at the same absolute thrust level. Therefore, the resulting tonal noise is higher for the positive thrust condition.
- Given that the noise due to torque is the predominant source of noise in the propeller plane for low to moderate thrust settings, a steeper and quieter descent compared to conventional approaches can be achieved using negative thrust, provided that the negative torque generated is equal to or less than the torque required for conventional propeller operation during landing (without considering the effect of inflow angle on propeller noise). Additionally, the steeper descent associated with negative thrust is expected to further reduce community noise exposure by decreasing the duration of noise impact. Although broadband noise increases along the axial direction in negative thrust conditions, it is considered less relevant for community noise exposure since the community typically lies below the aircraft.

The subsequent analysis focused on examining the effect of the inflow angle on the aerodynamic and aeroacoustic characteristics of the propeller, addressing the following subquestion:

- RQ2. How do the key physical phenomena that drive the aerodynamic and aeroacoustic performance of a propeller in positive and negative thrust mode change when operating at non-zero angles of attack?

The findings related to this subquestion are detailed in Chapter 5, where the simulation setup validated in Chapter 4 was used for the analysis at an AoA of 10° . The following

conclusions were drawn from this analysis about the changes in the physical phenomena that affect the aerodynamic performance at non-zero angles of attack:

- Operating the propeller at a non-zero AoA results in increased thrust and power along the propeller axis in positive thrust conditions. Conversely, in negative thrust conditions, a non-zero AoA leads to a decrease in both thrust and power magnitudes along the propeller axis compared to the 0° AoA case.
- In both positive and negative thrust conditions, thrust and torque are higher on the advancing side and lower on the retreating side, so the directions of normal and side forces remain unchanged in the propeller-axis aligned reference frame. However, thrust and torque directions are reversed when transitioning from positive to negative thrust conditions. In positive thrust conditions, the combination of positive thrust and positive normal force results in a substantial positive lift force in the freestream-aligned reference frame (30% of the thrust in the freestream-aligned reference frame for the considered condition). Conversely, in negative thrust conditions, the positive normal force opposes the negative thrust component, leading to a relatively small negative lift force in the freestream-aligned reference frame (5% of the thrust in the freestream-aligned reference frame for the considered condition).
- The propeller efficiency along the freestream direction (η_{p_∞}) remains nearly unchanged by AoA in positive thrust conditions. Therefore, operating a propeller at a positive thrust with a positive AoA generates beneficial positive lift without impacting η_{p_∞} , indicating that such an installation could be advantageous at the aircraft level. In contrast, for negative thrust conditions, this setup would result in lower energy-harvesting efficiency (10% lower for the considered case) compared to operation at 0° AoA, along with the generation of negative lift.
- In negative thrust conditions at non-zero angles of attack, conventional propellers experience dynamic stall, particularly on the inboard sections of the blade, with flow attaching on the advancing side and separating on the retreating side. The outboard sections, which are already stalled at 0° AoA, show significant variation in the extent of separation with the azimuthal position, resulting in increased broadband fluctuations on the retreating side. For the considered case, the periodic fluctuations deviate from a sinusoidal pattern due to the operation of blade sections in a deep stall region, where broadband fluctuations in the local thrust coefficient ($\pm 7\%$ of the mean thrust level) are comparable in magnitude to the periodic variations (-10% to $+7\%$ of the mean thrust level) near the blade tip ($r/R = 0.90$).
- Operation at a non-zero AoA induces asymmetry in the propeller slipstream due to periodic variations in the geometric AoA over the azimuth. For both positive and negative thrust conditions, the dynamic pressure on the advancing side is higher than on the retreating side at a non-zero AoA. A wing immersed in such a slipstream would experience varying effects depending on the thrust condition and AoA.

- In positive thrust conditions, when the propeller and wing have the same sign of AoA (both positive or both negative), differences in slipstream dynamic pressure between the advancing and retreating sides tend to reduce the differences in lift increase between the upgoing and downgoing blade sides compared to the 0° case. However, if the propeller's incidence angle results in an effective inflow angle opposite in sign to the wing's AoA, the differences in lift increase between the upgoing and downgoing blade sides are amplified compared to the 0° case, with a greater increase in lift on the downgoing blade side.
- In negative thrust conditions, when the propeller and wing have the same sign of AoA, differences in slipstream dynamic pressure between the advancing and retreating sides amplify the differences in lift reduction between the upgoing and downgoing blade sides compared to the 0° case, with a greater reduction in lift on the upgoing blade side. However, if the propeller's incidence angle results in an effective inflow angle opposite in sign to the wing's AoA, the differences in lift reduction between the upgoing and downgoing blade sides are diminished compared to the 0° case.

The operation of a propeller at non-zero angles of attack significantly changes the noise characteristics compared to its operation at 0° AoA. These changes are primarily due to two mechanisms: the periodic variations in blade loading and the asymmetric phase modulation of the strength of noise sources. To assess these effects, far-field noise was computed on a circular array with a radius of $10D$, centred around the propeller centre. This array consisted of 24 evenly spaced virtual microphones positioned in two planes: the plane of propeller rotation and the plane along the axis of the propeller. To isolate the impact of the AoA on the noise generation mechanisms, the microphones were fixed relative to the propeller axis for both 0° and non-zero AoA conditions. The following conclusions were drawn from this analysis:

- For positive thrust conditions, a non-zero AoA leads to a significant increase in noise levels in the plane of propeller rotation in regions opposite the tilt direction, with an increase of up to 5 dB in the studied case. Conversely, there is a notable reduction in noise towards the tilt direction (up to 8 dB in the studied case) compared to the 0° AoA case. This trend reverses in the negative thrust case, with increased noise towards the tilt direction (up to 6 dB for the considered case) and decreased noise away from it (up to 12 dB for the considered case) as compared to the 0° AoA case. These contrasting changes in noise directivity can be directly attributed to the opposing changes in absolute blade loading induced by the AoA. From this observation, it can be inferred that operating the propeller at negative thrust during the approach phase of flight could be beneficial for community noise reduction, as the community typically lies below the aircraft, away from the tilt direction.
- Noise levels are generally higher along the propeller axis (62–63 dB) than in the plane of rotation (54–59 dB) in the negative thrust condition for both angles of attack (0° and 10°). In contrast, positive thrust exhibits lower noise levels along the

propeller axis (58–62 dB) compared to the plane of rotation (71–78 dB). This is a consequence of higher broadband noise along the propeller axis and lower tonal noise in the plane of rotation in the negative thrust condition than in the positive thrust condition. The lower tonal noise levels in negative thrust are due to the higher advance ratio, while the higher broadband noise can be attributed to flow separation.

- The phase difference between the loading and the thickness noise signals varies over the azimuth for the non-zero AoA as a consequence of the varying blade loading. In negative thrust conditions, this phase difference can approach $\pm 180^\circ$, leading to destructive interference between the loading and thickness noise signals at specific azimuthal angles ($120^\circ \leq \phi \leq 210^\circ$ and $210^\circ \leq \phi \leq 300^\circ$ for the considered case). Therefore, the variation in phase difference between thickness and loading noise at non-zero AoA presents a potential new parameter for optimising propeller noise. By leveraging this phase difference, it may be possible to reduce noise levels locally while maintaining aerodynamic performance.

These conclusions contribute to the state-of-the-art by providing insights into the aerodynamic and aeroacoustic characteristics of conventional propellers operating in positive and negative thrust conditions at zero and non-zero angles of attack.

8.1.2. AERODYNAMIC MODELLING

The capabilities of different numerical methods for modelling the above-discussed physical phenomena that drive the aerodynamic performance of a propeller in both positive and negative thrust regimes were investigated based on the following subquestion:

RQ3. How do various numerical models compare against experimental data in their ability to predict the aerodynamic performance of propellers in both positive and negative thrust conditions?

8

To answer this sub-question, Chapter 6 presented a comprehensive evaluation of numerical methods of varying fidelity against experimental data to assess their capabilities in predicting propeller aerodynamic performance. The spectrum of fidelity encompasses low-fidelity tools like blade element momentum theory (BEM) and lifting line theory (LL), mid-fidelity through steady RANS (SRANS), and high-fidelity simulations involving unsteady RANS (URANS), lattice-Boltzmann (LB) very large eddy simulations (VLESs). The key parameters considered in this evaluation include blade loading distribution along the blade span and pressure distribution along the chord of blade sections. These parameters are critical for accurately predicting the loading noise, which is a major contributor to the total tonal noise. The insights gained from this comparative analysis are discussed in the following subsections:

BEM AND LL THEORIES

- For positive thrust conditions, BEM and LL theories showed a reasonable agreement with the experimental data. These theories effectively predicted the trends of propeller performance (C_T and C_P), though with an offset. For instance, an

offset of 7–11% was observed at $J = 0.60$ for the propeller and pitch setting considered in this study. The total pressure distribution in the slipstream also showed reasonable agreement with experimental data, albeit with a 5–6% overestimation of the peak pressure. Despite the differences, BEM and LL methods combined with RFOIL provided qualitatively reasonable chordwise pressure distributions. Therefore, BEM and LL theories are suitable for predicting general trends of propeller performance in positive thrust conditions, particularly up to moderate thrust settings where flow remains attached.

- The applicability of BEM and LL theories in the negative thrust regime is limited by flow separation around the blades. For the case considered, this limitation manifested even before the maximum power output point at $J = 1.10$. The flow separation results in inaccuracies in performance prediction by BEM and LL theories, not only due to the limitations of polar data but also from the breakdown of the inherent assumptions in these methods. This results in an underprediction of the thrust magnitude and an overestimation of the power magnitude (by more than 25% at $J = 1.48$) for operating conditions beyond the maximum power output point. Consequently, the blade loading distributions predicted by BEM and LL theories are not representative of those obtained from higher-fidelity simulations (the comparison was made with high-fidelity simulations due to the lack of experimental blade loading data).
- The vorticity distribution in the propeller wake, as calculated using LL theory, provides a good initial approximation for both positive and negative thrust conditions, but only up to the maximum power output point. This makes LL theory a valuable tool for preliminary design studies, particularly when considering propeller-wing interactions.

RANS SIMULATIONS

- The SRANS and URANS simulations provide nearly identical results across the entire range of advance ratios considered for propeller operation at 0° AoA with uniform inflow. However, differences emerge at high advance ratios (negative thrust), where the flow around the blades becomes fully separated. In these conditions, the influence of unsteadiness induced by the separated flow becomes more pronounced, highlighting the advantages of URANS simulations. Thus, while URANS simulations offer no significant advantage over SRANS under attached flow conditions, they become valuable when dealing with fully separated flow scenarios.
- RANS simulations offer a viable choice for comprehensively studying propeller performance within both positive and negative thrust regimes. For instance, at the positive thrust condition with $J = 0.60$, the errors in C_T and C_P range from 3–4% and 7–8%, respectively, with an 11% underprediction of the total pressure peak in the slipstream compared to the experiment. On the contrary, these errors decrease to 1–2% in C_T and less than 1% in C_P at the negative thrust condition with $J = 1.10$. The difference between RANS simulations and experimental data increases with the advance ratio in the negative thrust regime, reaching a 3% error

in C_T for URANS simulations at $J = 1.48$ (highest advance ratio considered) due to the error introduced by the turbulence modelling in predicting separated flows.

- In RANS simulations, the blade wake and tip vortex structures tend to diffuse more rapidly than in LB-VLES simulations due to coarser mesh resolution and comparatively higher numerical diffusion. Consequently, while RANS simulations are adequate for predicting propeller performance, capturing detailed phase-locked slip-stream data necessitates a finer mesh than what is typically required for accurate performance prediction.

LB-VLES SIMULATIONS

Two types of LB-VLES simulations were carried out for the analysis: 1) LB-VLES with $y^+ \geq 15$, and 2) LB-VLES with $y^+ \leq 10$. Unlike traditional RANS simulations, where stretched cells can be used to achieve low y^+ values, the LB-VLES solver that was used requires cells with a strict aspect ratio of 1 and a Courant number below 1. Consequently, achieving $y^+ \leq 10$ in LB-VLESs incurs approximately 30 times the computational cost compared to LB-VLES with $y^+ \geq 15$ or URANS simulations. Therefore, most practical studies use $y^+ \geq 15$ to balance detail and computational expense. Considering this, both types of LB-VLES simulations were conducted for the comparative analysis, leading to the following conclusions:

- The comparison of LB-VLES simulations with experimental data showed that it is crucial to use $y^+ \leq 10$ for accurate solutions, especially when flow separation is expected, such as in negative thrust conditions. For the considered case, the LB-VLES simulations with $y^+ \leq 10$ showed an error of less than 1% as compared to the experimental data, albeit with significantly increased computational resources.
- The LB-VLES simulations with $y^+ \geq 15$ have a computational cost similar to that of URANS simulations. However, with this boundary-layer resolution, LB-VLES simulations overestimate the power magnitude by 16% compared to experimental data at $J = 1.10$ (close to the maximum power output point). This discrepancy arises due to inaccuracies in modelling reattachment locations along the blade span. Despite the errors in absolute values, LB-VLES simulations with $y^+ \geq 15$ offer an alternative option for capturing the general trend of propeller performance. Compared to RANS simulations, the advantage of LB-VLES simulations with $y^+ \geq 15$ lies in better preservation of propeller wake structures due to lower numerical diffusion and a lower computational cost per mesh element, making them valuable for studies of propeller-wing interactions.

The conclusions from these comparative analyses showed that the choice of method should be informed by the desired accuracy and computational resources available, balancing the trade-offs between resolution and overall cost.

8.1.3. BLADE LOADING DISTRIBUTIONS FROM WAKE MEASUREMENTS

While comparing different numerical methods, it became apparent that such comparisons are often hindered by the absence of the blade loading distributions from experiments. To address this gap, the following subquestion was investigated:

RQ4. How accurately can the blade loading distributions be extracted a posteriori from wake measurements using potential flow methods in both positive and negative thrust conditions?

To answer this question, the so-called “wake-informed lifting line” method was used to estimate the thrust and power distributions along propeller blades using phase-locked slipstream velocity data. The validity of the method was first assessed by comparing its results with those obtained from SRANS simulations. Subsequently, it was applied to experimental data to test its performance in real-world scenarios. The following conclusions were drawn about the efficacy and accuracy of the wake-informed lifting line model:

- In the attached flow condition, the wake-informed LL model provides excellent results for thrust distribution. For the considered case, the model demonstrated errors below 1% in the peak value as compared to RANS predictions, even without accounting for the drag contribution.
- While the model performs well in attached flow conditions, its application in separated flow conditions requires caution. For the considered separated flow case, the model qualitatively captured the radial trends and overall thrust distribution shape; however, discrepancies of 10%-20% were observed in absolute values when drag contributions were not included. Accounting for drag reduced these errors to 8%–16%, with the remaining discrepancies attributed to the limitations of potential flow models in separated flows, inaccuracies in external polar data, and unaccounted influence of the spinner.
- Irrespective of the flow condition (attached or separated), the drag contribution is crucial in the torque direction and must be accounted for when estimating the power distribution using the wake-informed LL model. This necessitates the use of external polar data and, consequently, knowledge of the propeller geometry. For the considered cases, even with the drag contribution included, power values were underestimated by 10-25% in the outboard region ($r/R \geq 0.80$) in the attached flow condition and more than 20% for the separated flow condition beyond $r/R \geq 0.65$. This underprediction is attributed to two factors: the underestimation of drag in the polar data and inaccuracies in the induced angles of attack predicted by the wake-informed LL model, leading to an inaccurate lift contribution to the power distribution.
- The model offers significant value for practical applications, particularly in predicting thrust distributions when propeller geometry is unknown or inaccessible, as well as in situations where blade instrumentation is not feasible. Besides, the model can also provide sectional lift coefficients and local angles of attack.

Therefore, the wake-informed LL model offers a promising, non-intrusive approach for estimating blade loading distributions and local flow conditions at the blade, post-priori from slipstream velocity measurements.

The conclusions from this work offer in-depth insights into the physical phenomena and the modelling options of those phenomena that govern the time-averaged and unsteady integrated performance, blade loading distributions, slipstreams and the resulting far-field acoustic characteristics of propeller operation at zero and non-zero angles of attack under negative thrust conditions. These findings are contextualised by comparing them with the well-studied propulsive conditions. The analyses presented in this thesis attempt to establish a foundation for future research focused on propeller operation, particularly at negative thrust, while addressing the research objectives outlined at the beginning of the thesis in Chapter 1.

8.2. RECOMMENDATIONS

Building upon the comprehensive analysis of propeller aerodynamics and aeroacoustics in negative thrust conditions, this section outlines key recommendations for future research.

SCALING ASPECTS

This study utilised a scaled-down propeller from a previous-generation turboprop aircraft. To bridge the gap between the current study and real-world applications, future research should investigate propeller operation in negative thrust at higher Reynolds numbers and Mach numbers that are more representative of full-scale aircraft. Although some analyses in this thesis were conducted at higher helicoidal tip Mach numbers, the Reynolds number was still an order of magnitude lower than what would be experienced in full-scale flight. Despite these differences, the fundamental physical phenomena identified herein are expected to remain dominant, though their relative influence on propeller performance may change. For instance, increased Reynolds numbers can lead to delayed flow separation on propeller blades to higher advance ratios, potentially improving energy-harvesting efficiency during negative thrust operations. Additionally, tonal and broadband noise exhibit different scaling behaviours with increasing Reynolds numbers and Mach numbers, which might alter their relative importance, particularly in negative thrust conditions. Although broadband noise is expected to remain higher in negative thrust conditions compared to positive thrust conditions, its relative importance compared to tonal noise in negative thrust conditions requires further investigation for full-scale conditions.

PROPELLER DESIGN

The propeller used in this study was not specifically optimised for negative thrust operation. While propeller design is typically dominated by cruise phase requirements for minimising energy consumption, the descent phase may significantly influence the design for short-haul flights. Optimising propeller geometry for both cruise and descent phases could potentially mitigate flow separation in negative thrust conditions, leading to improved energy recovery and overall operational efficiency. Further investigation into propeller design tailored for such flight missions is recommended. Additionally, modern turboprop designs often feature blade sweep, unlike the propeller used in this

study. It is essential to extend this research to swept propeller designs to assess the impact of sweep on negative thrust performance and to validate the findings presented herein.

EXPERIMENTAL VALIDATION

While the aerodynamic performance predicted by high-fidelity simulations was extensively validated against experimental data in this thesis, a similar level of validation for aeroacoustic predictions was not possible due to the unavailability of reliable experimental aeroacoustic data. Although the extensive validation of aerodynamic performance provides confidence in the tonal noise component, the accuracy of the broadband noise component remains uncertain. To address this, future research should prioritise acquiring comprehensive experimental aeroacoustic data, ideally under conditions that represent full-scale flight, as broadband noise and tonal noise scale differently with Reynolds number and Mach number.

Additionally, the observed phase difference between thickness and loading noise signals, which varies with azimuth angle at non-zero angles of attack, offers the potential for noise reduction through destructive interference. Further research is required to validate these findings and assess their practical significance. The validation could be done either experimentally by comparing simulated and measured total noise signatures or by using analytical methods capable of isolating individual noise sources to isolate individual noise sources and quantify the potential for destructive interference.

LIMITATIONS OF MOMENTUM AND LIFTING LINE MODELS

This study showed that the low-fidelity model blade-element momentum theory (BEM) and lifting line (LL) models start to deviate significantly from the experimental data in the negative thrust conditions. While inaccuracies in airfoil polar data contribute to these discrepancies, the breakdown of the inherent 2D assumptions of these models due to flow separation around the blades is likely a primary factor. This hypothesis should be tested in further research by either using reliable polar data or by examining the underlying theories without relying on airfoil polar data.

EXTENSION OF WAKE-INFORMED LIFTING LINE MODEL

The wake-informed lifting line model was evaluated exclusively for 0° AoA in this study. While the theoretical framework of the model can be extended to non-zero angles of attack and installed configurations, further research is necessary to validate its performance and applicability in these more complex scenarios.

INSTALLATION EFFECTS

This thesis focused on isolated propeller configurations, laying the groundwork for the investigation of installed configurations. As shown in the current thesis, the slipstream characteristics change significantly in the negative thrust operation as compared to the positive thrust condition. While some inferences regarding propeller-wing interactions were made, comprehensive numerical and experimental investigations are required to fully understand the impact of negative thrust operation on wing performance and vice-versa. Maintaining lift during descent is crucial, yet negative thrust can induce localised lift reduction on the wing. Additionally, minimising the noise emissions near the ground

is more critical, necessitating detailed studies of the modified aircraft noise signature during negative thrust operation.

Structure-borne noise, exacerbated by the impingement of slipstreams on the wing in configurations with multiple propellers (e.g., distributed propulsion), requires in-depth study for both positive and negative thrust conditions. Future research should investigate the transmission of structure-borne noise into the cabin and develop strategies to mitigate its impact on passenger comfort.

STRUCTURAL ASPECTS

The operation of the propeller at negative thrust will lead to aerodynamic forces acting in opposite directions on the propeller as compared to conventional propulsive conditions. As the propellers are expected to be operated at higher advance ratios to achieve the negative thrust conditions as compared to the positive thrust condition, the relative importance of aerodynamic loads compared to centrifugal forces is expected to be higher in the former. Furthermore, the significant broadband fluctuations in aerodynamic loads, even at zero AoA, and the occurrence of dynamic stall at non-zero angles of attack can induce substantial cyclic stresses on the propeller blades. These cyclic stresses can lead to structural fatigue and potentially compromise propeller integrity. Further research is essential to optimise propeller structural design for both positive and negative thrust conditions to ensure safe and reliable operation. By integrating structural considerations into the design process, it is possible to develop propellers that efficiently operate in both thrust modes, extending component life and minimising overall energy consumption.

ASSESSMENT OF COMMUNITY NOISE

While negative thrust operation offers the potential for steeper descents with reduced noise levels from propellers, further research is necessary to evaluate its impact on the overall noise generated by the aircraft and its effect on community noise. For this purpose, a comprehensive comparison between conventional landing approaches and steeper descent approaches utilising negative thrust is needed. Additionally, the impact of increased broadband noise in negative thrust conditions on perceived noise levels should be carefully assessed. Future comparisons could also consider the influence of noise propagation through varying atmospheric conditions (such as air density, temperature, and wind speed) and across complex terrains on perceived noise levels and community impact.

In conclusion, this thesis has advanced the understanding of propeller aerodynamics and aeroacoustics in negative thrust conditions, providing a foundation for future research and development. The recommendations outlined in this chapter build upon the foundational research conducted in this study, offering a roadmap for future investigations. By addressing scaling aspects, optimising propeller design, validating aeroacoustic predictions, refining modelling techniques, and exploring installation and structural impacts, these recommendations aim to enhance the practical applicability of negative thrust operations in future aircraft, potentially contributing to quieter and environmentally sustainable aviation solutions.

PART V

APPENDICES

A

IMPORTANCE OF ROTATIONAL EFFECTS FOR AERODYNAMIC PERFORMANCE PREDICTIONS

The polar data used as input for BEM and LL models are typically obtained from 2D-panel codes such as XFOIL [58], which often neglect the impact of propeller blade rotation on sectional characteristics. In near-stall conditions, centrifugal forces due to rotation cause the flow in stagnant regions to move towards the blade tip, inducing a Coriolis force that creates a favourable pressure gradient. This effect delays stall and increases lift coefficients compared to non-rotating blades, a phenomenon known as the Himmelskamp effect [111]. This effect is expected to be particularly relevant in the negative thrust regime due to the operation of propeller blade sections in stalled or near-stall conditions. Thus, understanding the relative importance of the Himmelskamp effect in both positive and negative thrust regimes is crucial for predicting aerodynamic performance using BEM and LL models. This appendix first evaluates the influence of rotation on sectional characteristics in Appendix A.1, followed by an assessment of its impact on predicted integrated performance in Appendix A.2.

A.1. EFFECT OF ROTATION ON SECTIONAL CHARACTERISTICS

To account for rotational effects, RFOIL [57] is employed due to its quasi-3D model, which incorporates these effects into the blade section characteristics. The relative change in blade section characteristics when considering the Himmelskamp effect, compared to when it is neglected, is shown in Fig. A.1. As expected, the Himmelskamp effect is most prominent near the root and diminishes towards the tip.

In Fig. A.1a, the normalised difference between the predicted lift coefficient with (c_l) and without ($c_{l_{NR}}$) the rotational effect is plotted for a representative Reynolds number

The contents of this appendix have been adapted from Ref. [98].

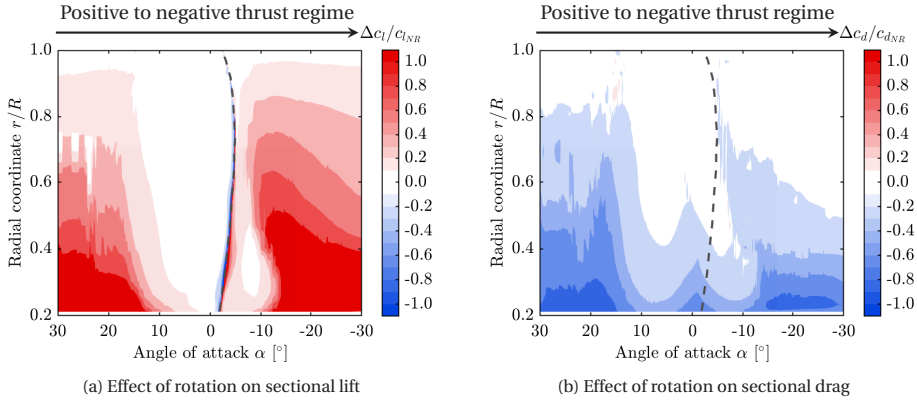


Figure A.1: Effect of rotation on sectional characteristics (estimated using RFOIL)

variation ($1 \times 10^5 - 2 \times 10^5$) along the blade span. The red colour in the plot means that the lift coefficient with rotational effect is higher as compared to the lift coefficient without rotational effect. The red-blue line around 0° angle of attack (indicated by a dashed line) appears due to the normalisation when $c_{l_{NR}}$ goes to 0 and provides a clear distinction between positive (left side) and negative thrust regime (right side). In the positive thrust regime, rotational effects become significant only at higher angles of attack. Conversely, in the negative thrust regime, rotational effects rapidly increase due to the operation of positively cambered airfoils at negative angles of attack, causing an onset of separation. This separation is affected by the rotational effects.

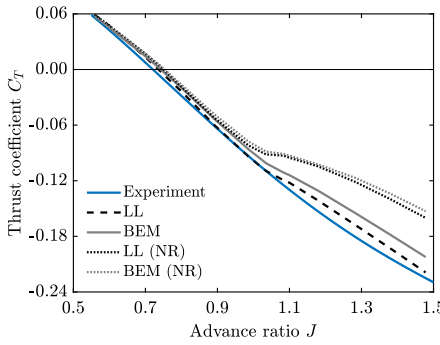
Similar to the lift coefficient, the normalised change in drag coefficient is shown in Fig. A.1b. The blue colour in the plot means that the drag coefficient with rotational effect is lower as compared to the drag coefficient without rotational effect. The large relative change in drag coefficient near 0° angle of attack is due to the very low baseline drag coefficient ($c_{d_{NR}} \rightarrow 0$). The dashed line corresponding to $c_{l_{NR}} = 0$ from Fig. A.1a has been plotted as a reference. It can again be observed that the rotational effect becomes quickly important upon entering the negative thrust regime (right side). Therefore, rotational corrections are essential for the accurate prediction of the performance of conventional propellers in the negative thrust regime, even under low negative thrust conditions, but are only necessary in the positive thrust regime when operating at a comparatively higher thrust magnitude.

A.2. EFFECT OF ROTATION ON INTEGRATED PERFORMANCE PREDICTIONS

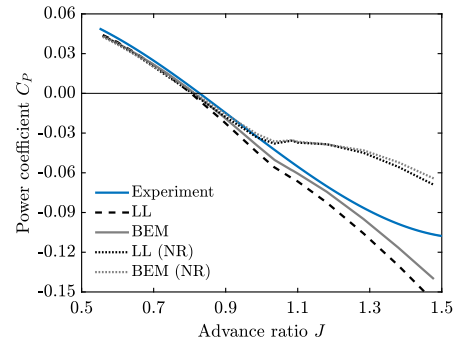
The resulting integrated propeller performance obtained from BEM and LL with and without rotational effects can be seen in Fig. A.2. The results without rotational effects are accompanied by '(NR)' in the figures. For thrust coefficient, shown in Fig. A.2a, the rotational effects have a negligible effect on performance prediction in the positive thrust regime as high positive thrust settings are not considered here. However, in the

negative thrust regime, rotational effects significantly influence propeller performance even at low thrust magnitude. Predictions from BEM (NR) and LL (NR) deviate substantially from experimental data for $J > 1.00$, highlighting the limitations of polar data without rotational corrections. Including rotational effects greatly improves the accuracy of BEM and LL predictions in this operating range, resulting in a good agreement over the whole range of advance ratio. This is the consequence of the operation of positively cambered airfoils at negative angles of attack, where blade sections encounter near-stall and post-stall conditions, making rotational effects increasingly significant.

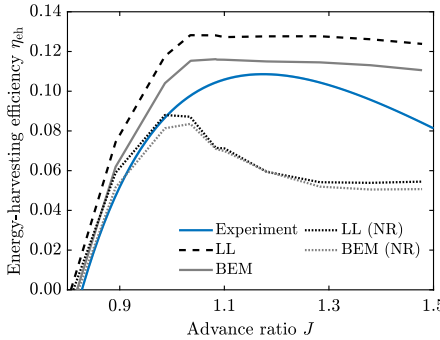
In contrast, for the power coefficient in Fig. A.2b, although the agreement between numerical models (BEM and LL) and experimental data improved with the inclusion of rotational corrections for $1.00 < J < 1.20$, BEM and LL show a significant overprediction of power at higher advance ratios. This overprediction is expected to be a consequence of delayed stall prediction in RFOIL [59, 60], leading to overprediction of lift and underprediction of drag. As in the negative thrust regime, the lift and drag components add up in the thrust force, and the overall effect is reduced, whereas both the components subtract for power, leading to an enhanced effect and a significant deviation from the experiment.



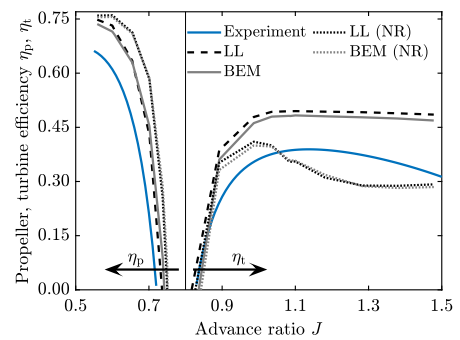
(a) Thrust coefficient versus advance ratio



(b) Power coefficient versus advance ratio



(c) Energy-harvesting efficiency versus advance ratio



(d) Propeller and turbine efficiency versus advance ratio

Figure A.2: Importance of rotational effects for integrated propeller performance prediction using low-fidelity methods

Figure A.2c shows the comparison of energy-harvesting efficiency with and without rotational effects. As seen in the results for thrust and power coefficients, the results without rotational effects deviate significantly compared to the experimental data for $J > 1.00$. With the inclusion of rotational effects, the BEM and LL overpredict the energy-harvesting efficiency, and the resulting line is almost flat with increasing advance ratio for $J \geq 1.10$, indicating that BEM and LL can only be used up to a certain advance ratio in negative thrust conditions.

Figure A.2d shows the comparison of propeller efficiency for positive thrust conditions and turbine efficiency (defined as the inverse of propeller efficiency) for negative thrust conditions. The small but opposite influence of rotational effects on C_T and C_P results in a noticeable impact on the resulting propeller efficiency in positive thrust conditions ($0.55 \leq J \leq 0.70$), where efficiency is overpredicted when rotational effects are excluded. In the negative thrust regime, the inclusion of rotational effects significantly increases turbine efficiency predictions for $J > 0.90$ due to the delayed stall prediction in RFOIL.

In conclusion, the inclusion of rotational effect is specifically important in negative thrust conditions for conventional propeller design performance prediction due to the early onset of separation as a result of the operation of a positively cambered airfoil at a negative angle of attack. However, simply including rotational corrections does not ensure the reliability of BEM and LL in negative thrust regimes due to the significant flow separation encountered under such conditions, as previously discussed in Chapter 6.

B

INFLUENCE OF SPINNER AND NACELLE ON PROPELLER PERFORMANCE

BEM and LL models generally only model the propeller blade and do not model the presence of spinner and nacelle. However, spinner and nacelle are always present in practical scenarios. Therefore, it is important to understand the effect of the presence of the spinner and the nacelle on the propeller performance. For this purpose, additional SRANS simulations (besides the one presented in Chapter 6) were performed without spinner and nacelle geometry for six different advance ratios ($J = 0.60, 0.75, 0.89, 1.10, 1.28, 1.48$). This appendix first compares the integrated performance of the propeller with and without the spinner and nacelle against experimental data, followed by the comparison of blade loading distributions.

B.1. INTEGRATED PERFORMANCE

Figure B.1 shows the integrated propeller performance with and without spinner and nacelle geometry predicted using SRANS simulations. For the comparison, the predictions from BEM, LL and experiments are also plotted. Figure B.1a shows that the presence of nacelle and spinner does not have a noticeable effect on the thrust coefficient in the positive thrust regime for the conditions considered here. However, the same is not true for the negative thrust regime. The SRANS simulations without spinner and nacelle geometry (labelled as 'SRANS w/o nacelle' in the figure) show lower thrust magnitude in the negative thrust regime compared to the SRANS simulations with spinner and nacelle geometry (labelled as 'SRANS'). A similar difference can also be observed in power coefficient plots in Fig. B.1b. The difference between the two increases with an increase in advance ratio (negative thrust regime), indicating the increasing importance of modelling the presence of spinner and nacelle with increasingly negative thrust setting. The thrust coefficient predictions from BEM and LL match better with the values predicted

using SRANS simulation without a spinner and nacelle. In contrast, the power coefficient predictions have a worse match with the values predicted using SRANS simulation without a spinner and nacelle. As explained in Appendix A, this is expected to be the consequence of the delayed stall prediction in RFOIL.

B

The differences observed in Fig. B.1b also translate to the energy-harvesting efficiency plot in Fig. B.1c, i.e., the removal of spinner and nacelle geometry leads to lower energy-harvesting efficiency. Though the energy-harvesting efficiency is reduced, the turbine efficiency is almost unaffected except at $J = 0.90$; see Fig. B.1d. This is a result of a decrease in both thrust and power, leading to almost similar values of turbine efficiency with or without spinner and nacelle geometry.

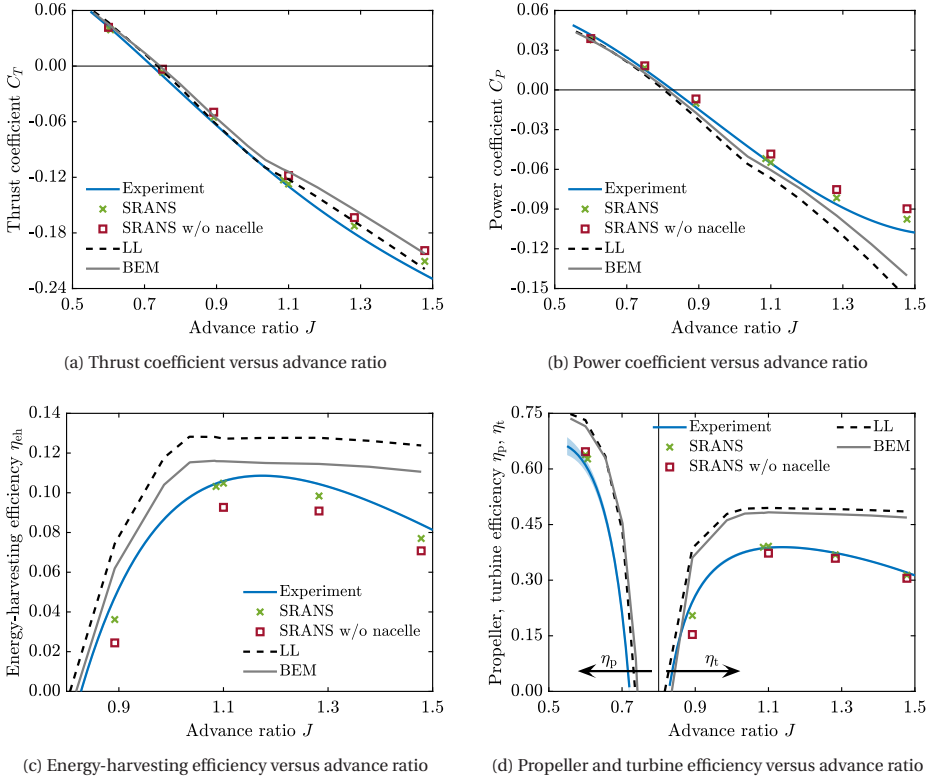


Figure B.1: Effect of the presence of spinner and nacelle on the integrated propeller performance

The integrated performance plots show the increasing importance of the modelling of the spinner and nacelle geometry with the increase in advance ratio in the negative thrust conditions. Therefore, it is important to understand how these differences manifest themselves in the blade loading distributions. For this purpose, the thrust distribution plots are shown for three different advance ratios: 0.60, 1.10 and 1.48 in Appendix B.2. The first advance ratios correspond to the positive thrust condition, whereas the last two advance ratios correspond to negative thrust conditions, with $J = 1.10$ close

to the maximum regeneration point and $J = 1.48$ being the highest advance ratio considered in the thesis.

B.2. BLADE LOADING DISTRIBUTIONS

Figures B.2 and B.3 presents the thrust and power distributions along the blade span for $J = 0.60, 1.10$, and 1.48 , with and without the presence of the spinner and nacelle. For the positive thrust condition ($J = 0.60$), the presence of the spinner and nacelle has a negligible effect on the thrust and power distributions (Figs. B.2a and B.2b), with differences around 1% near the peak value for thrust and 3% for power, using the SRANS results with nacelle and spinner as the reference.

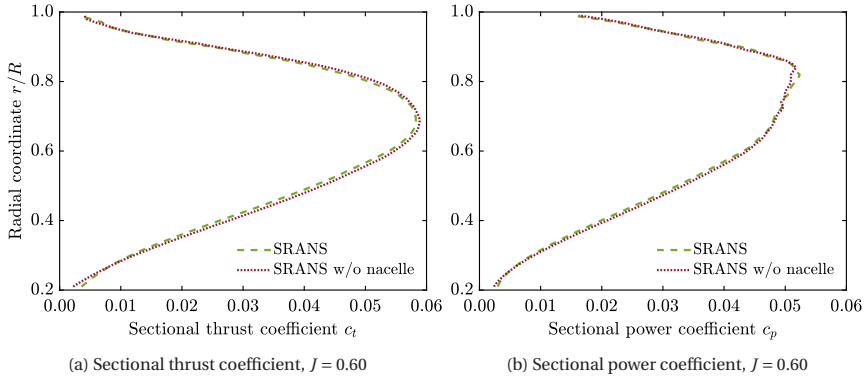


Figure B.2: Effect of the presence of spinner and nacelle on the blade loading for the positive thrust conditions ($J = 0.60$)

In contrast, the spinner and nacelle significantly affect the blade loading distribution in negative thrust conditions (Fig. B.3), particularly for radial positions up to $r/R \approx 0.80$. For $J = 1.10$, the SRANS simulations without the spinner and nacelle underpredict the thrust coefficient by more than 15% for $r/R \leq 0.40$ and between 0-15% for $0.40 \leq r/R \leq 0.65$, along with the underprediction of the peak value by 3%, as compared to the SRANS simulation with the spinner and nacelle. Similar trends are observed for the power distribution, with an error of more than 11% for $r/R \leq 0.40$ and between 2-11% for $0.40 \leq r/R \leq 0.65$. The geometry of the spinner modifies the local pressure gradient near the root, resulting in the observed impact on the thrust and power close to the root. For $J = 1.48$, as the flow is almost fully separated along the whole blade span (Chapter 6), the removal of the spinner and nacelle geometry results in a change in flow separation due to the presence of strong root vortex resulting in a significantly different blade distribution. The blade loading distributions predicted by BEM and LL are completely different than the ones obtained from SRANS simulations, showing the invalidity of the BEM and LL models for this operating condition.

These comparisons reveal that the error from neglecting the spinner and nacelle is more significant under the negative thrust condition than the positive thrust condition. Incorporating the effects of the spinner and nacelle into LL models could be partially achieved through the use of panel methods.

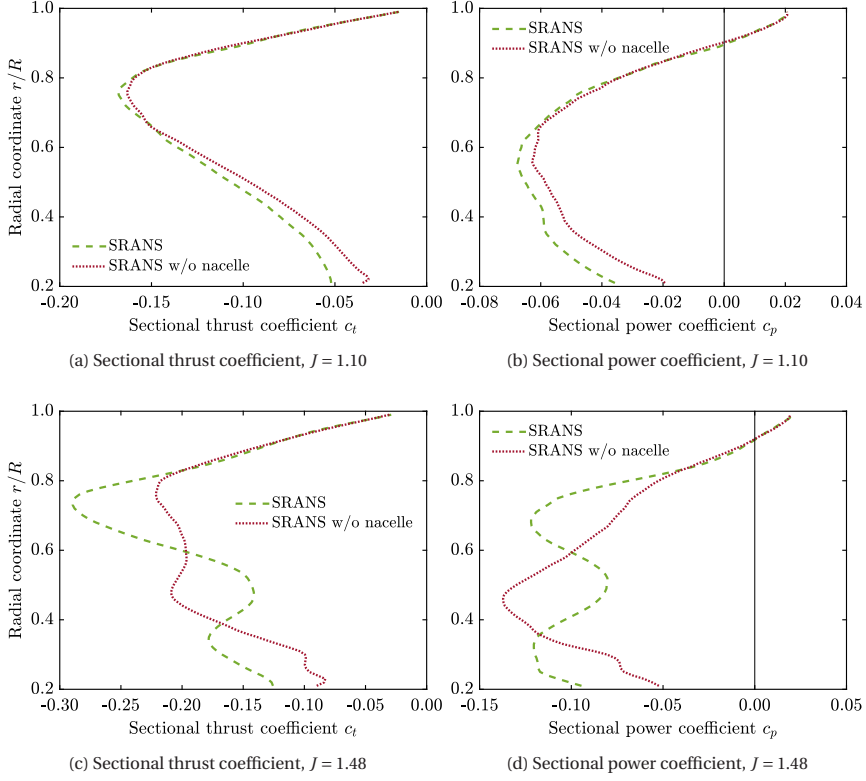


Figure B.3: Effect of the presence of spinner and nacelle on the blade loading for the negative thrust conditions ($J = 1.10, 1.48$)

C

VALIDATION OF MOMENTUM AND LIFTING LINE WAKE MODELLING

The accuracy of BEM and LL theories is typically influenced by the quality of the input polar data, making it challenging to isolate the validity of their underlying wake modelling. This appendix evaluates the validity of the wake modelling theories behind BEM and LL models. To remove the influence of external polar data, the blade loading distributions obtained from SRANS simulations without the spinner and nacelle (refer to Appendix B) are used as input for both models to predict the inductions at the propeller blades. These inductions are then compared with those calculated using the 3D Biot-Savart's law applied to the SRANS flowfield data. This approach enables a direct evaluation of the wake modelling, independent of external polar data. The methodologies are described individually, followed by a comparison of axial inductions under various operating conditions.

C.1. LOAD-INFORMED BEM AND LIFTING LINE

To isolate the momentum theory from the blade-element aspect, SRANS-derived blade loading distributions were used as input. The momentum theory then calculates the corresponding axial and tangential induction distributions along the blade span. A similar approach was also taken for the LL model; refer to Chapter 7. The solution is iterated to get converged circulation and induction distributions using the loading as the input.

The inductions obtained using the momentum theory are effectively smeared out over the actuator disk. In contrast, the solution of the LL model is obtained directly at the blades. To ensure consistency in comparing results between the two, the induced velocities in the load-informed LL were computed at multiple lines situated at 5-degree intervals within the plane of rotation, centred around the propeller axis, using the converged solution. The final induced velocities from the load-informed LL were obtained by averaging the induced velocities over these multiple lines.

C.2. AXIAL INDUCTION BASED ON 3D BIOT-SAVART'S LAW

To provide a reference for the comparison of the axial inductions obtained using load-informed BEM and LL, the 3D formulation of Biot-Savart's law was applied to the flow-field of SRANS simulations without spinner and nacelle. The momentum and LL theories make the assumption that propeller blades are infinitesimally thin and compute the inductions at the $c/4$ line of the propeller blades. To align with this assumption, cells close to the propeller blades were excluded by creating an offset around the blades. Two offsets, referred to as the “near offset” and “far offset”, were used to assess the sensitivity of the results to the removal of cells near the propeller blades. These offsets served two purposes: eliminating viscous effects and mitigating the influence of the thickness of the blade.

As a wedge domain was used in SRANS simulations (refer to Chapter 2), the flow-field was copied and rotated to obtain the solution for the whole propeller geometry. Lastly, using the 3D Biot-Savart's law as given in Eq. (C.1), the induced velocities were computed at multiple lines situated at 5-degree intervals within the plane of rotation, centred around the propeller axis. Similar to the load-informed LL, the final solution was obtained by averaging the induced velocities over these multiple lines.

$$\vec{u}_w = \frac{1}{4\pi} \sum_{i=1}^N \frac{\vec{\omega}_i \times \vec{r}_i}{|\vec{r}_i|^3} dV_i, \quad (\text{C.1})$$

where \vec{u}_w is the velocity induced by the vorticity $\vec{\omega}_i$ at the control point located at \vec{r}_i from the volume dV_i , with cell count going upto N.

Removing cells near the blades eliminates the effect of bound vorticity. While this vorticity doesn't affect axial induction, it does contribute to tangential induction. As a result, the comparison of axial inductions alone is meaningful when assessing the validity of the momentum and LL wake modelling.

C.3. RESULTS

The axial inductions from load-informed BEM and load-informed LL were compared with those from the 3D Biot-Savart's law for various operating conditions. The resulting comparison of axial inductions for $J = 0.60, 1.10$, and 1.48 is shown in Fig. C.1.

For $J = 0.60$ in Fig. C.1a, the choice of offset had minimal impact on the solution obtained using 3D Biot-Savart's law. Both load-informed BEM and load-informed LL theories show a good qualitative agreement with the induction obtained from Biot-Savart's law. However, the peak is overpredicted in the load-informed BEM and load-informed LL theories by 5.4% and 12.6%, respectively, compared to the results obtained by applying 3D Biot-Savart's law with the near offset. The overprediction is expected to be a consequence of the simplification made in the momentum and LL wake modelling, such as neglect of the slipstream contraction, vorticity roll-up, and viscosity losses.

In the negative thrust condition, close to the maximum regeneration point ($J = 1.10$), the difference in the near and far offset axial inductions increases (9.9% at $r/R = 0.70$), indicating the increased influence of the cells in the vicinity of the propeller blade as a result of flow separation. Despite the differences in the axial inductions obtained from the near and far offsets, the radial distributions are qualitatively similar. Both load-informed

BEM and load-informed LL solutions show qualitative similarity with the axial induction distributions obtained using 3D Biot-Savart's law, with differences of 7.0% and 15.0% at $r/R = 0.70$ as compared to 3D Biot-Savart's law with near offset. The good agreement at $J = 1.10$ suggests that the differences seen in the blade loading in Fig. 6.7b were essentially a result of inaccuracies in the polar data and the presence of the nacelle and spinner (refer to Appendix B). These results show that the momentum and lifting line theories are still reasonably valid for this operating condition despite the flow separation.

For $J = 1.48$ in Fig. C.1c, the axial inductions obtained from load-informed BEM and the load-informed LL start to show significant differences compared to Biot-Savart's law, especially in the inboard part of the blade. These deviations indicate the breakdown of the inherent assumptions in these theories, suggesting that the momentum and LL theories do not hold true anymore at this operating condition.

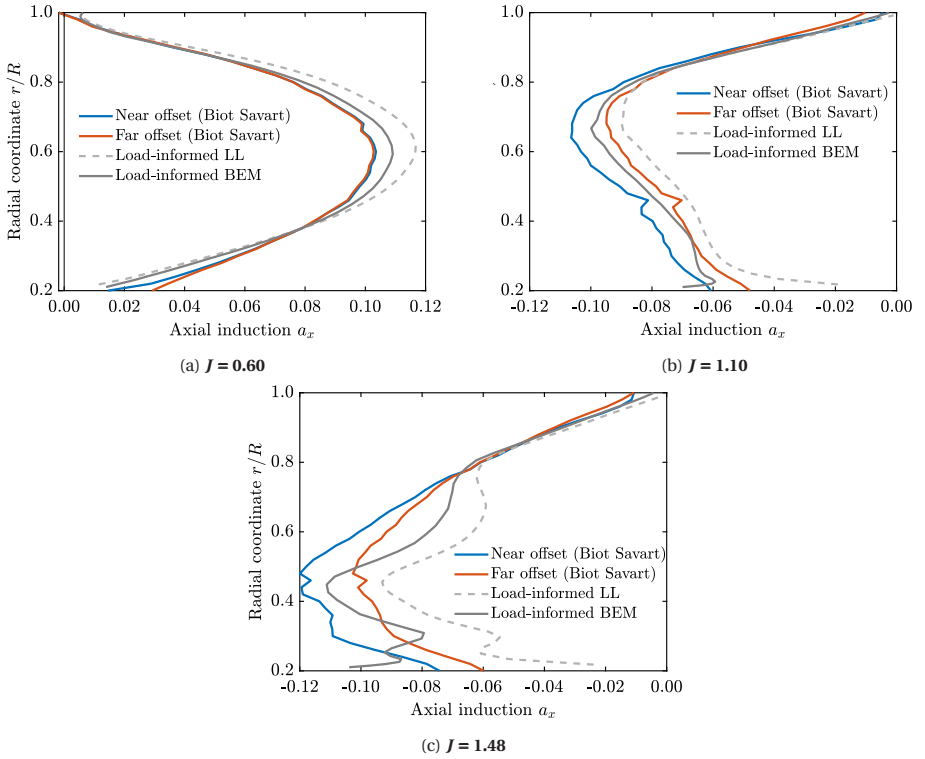


Figure C.1: Validity of momentum and LL wake modelling at different advance ratios based on the inductions from 3D Biot-Savart's law

BIBLIOGRAPHY

- [1] World Meteorological Organization, “Provisional State of the Global Climate 2023,” United Nations, Geneva, Switzerland, 2023. URL <https://wmo.int/files/provisional-state-of-global-climate-2023>.
- [2] Ritchie, H., Rosado, P., and Roser, M., “CO2 and Greenhouse Gas Emissions,” *Our World in Data*, 2023. URL <https://ourworldindata.org/grapher/ghg-emissions-by-sector>.
- [3] United Nations, “Fact Sheet Climate Change,” Sustainable Transport Conference, Beijing, China, 2021. URL https://www.un.org/sites/un2.un.org/files/media_gstc/FACT_SHEET_Climate_Change.pdf.
- [4] Ritchie, H., “Climate change and flying: what share of global CO2 emissions come from aviation?” *Our World in Data*, 2020. URL <https://ourworldindata.org/co2-emissions-from-aviation>.
- [5] Skeie, R. B., Fuglestad, J., Berntsen, T., Lund, M. T., Myhre, G., and Rypdal, K., “Global temperature change from the transport sectors: Historical development and future scenarios,” *Atmospheric Environment*, Vol. 43, No. 39, 2009, pp. 6260–6270. doi:10.1016/j.atmosenv.2009.05.025.
- [6] Lee, D., Pitari, G., Grewe, V., Gierens, K., Penner, J., Petzold, A., Prather, M., Schumann, U., Bais, A., Berntsen, T., Iachetti, D., Lim, L., and Sausen, R., “Transport impacts on atmosphere and climate: Aviation,” *Atmospheric Environment*, Vol. 44, No. 37, 2010, pp. 4678–4734. doi:10.1016/j.atmosenv.2009.06.005.
- [7] Graver, B., Rutherford, D., and Zheng, S., “CO2 emissions from commercial aviation: 2013, 2018, and 2019,” International Council on Clean Transportation, 2020. URL <https://theicct.org/wp-content/uploads/2021/06/CO2-commercial-aviation-oct2020.pdf>.
- [8] Singh, V., and Sharma, S. K., “Fuel consumption optimization in air transport: a review, classification, critique, simple meta-analysis, and future research implications,” *European Transport Research Review*, Vol. 7, No. 2, 2015, p. 12. doi:10.1007/s12544-015-0160-x.
- [9] Airbus, “Global Market Forecast 2023,” , 2023. URL https://www.airbus.com/sites/g/files/jlcbta136/files/2023-06/GMF%202023-2042%20Presentation_0.pdf.

-
- [10] Daggett, D., Hendricks, R., and Walther, R., "Alternative fuels and their potential impact on aviation," *25th Congress of the International Council of the Aeronautical Sciences (ICAS 2006)*, 2006. URL <https://ntrs.nasa.gov/citations/20060051881>.
- [11] Yilmaz, N., and Atmanli, A., "Sustainable alternative fuels in aviation," *Energy*, Vol. 140, 2017, pp. 1378–1386. doi:10.1016/j.energy.2017.07.077.
- [12] Moore, M. D., "Misconceptions of Electric Aircraft and their Emerging Aviation Markets," *52nd Aerospace Sciences Meeting*, AIAA Paper 2014-0535, January 2014. doi:10.2514/6.2014-0535.
- [13] Yaros, S. F., Sexstone, M. G., Huebner, L. D., Lamar, J. E., McKinley Jr, R. E., Torres, A. O., Burley, C. L., Scott, R. C., and Small, W. J., "Synergistic Airframe-Propulsion Interactions and Integrations: A White Paper Prepared by the 1996-1997 Langley Aeronautics Technical Committee," Tech. Rep. TM-1998-207644, NASA, 1998. URL <https://ntrs.nasa.gov/citations/19980055126>.
- [14] Hall, D. K., Huang, A. C., Uranga, A., Greitzer, E. M., Drela, M., and Sato, S., "Boundary Layer Ingestion Propulsion Benefit for Transport Aircraft," *Journal of Propulsion and Power*, Vol. 33, No. 5, 2017, pp. 1118–1129. doi:10.2514/1.B36321.
- [15] Kim, H. D., "Distributed propulsion vehicles," *27th international congress of the aeronautical sciences*, 2010. URL <https://ntrs.nasa.gov/citations/20100036222>.
- [16] Sinnige, T., van Arnhem, N., Stokkermans, T. C. A., Eitelberg, G., and Veldhuis, L. L. M., "Wingtip-Mounted Propellers: Aerodynamic Analysis of Interaction Effects and Comparison with Conventional Layout," *Journal of Aircraft*, Vol. 56, No. 1, 2019, pp. 295–312. doi:10.2514/1.C034978.
- [17] Gnadt, A. R., Speth, R. L., Sabnis, J. S., and Barrett, S. R., "Technical and environmental assessment of all-electric 180-passenger commercial aircraft," *Progress in Aerospace Sciences*, Vol. 105, 2019, pp. 1–30. doi:10.1016/j.paerosci.2018.11.002.
- [18] Guynn, M. D., Berton, J. J., Haller, W. J., Hendricks, E. S., and Tong, M. T., "Performance and environmental assessment of an advanced aircraft with open rotor propulsion," Tech. rep., 2012. URL <https://ntrs.nasa.gov/citations/20120015977>.
- [19] Proesmans, P.-J., and Vos, R., "Airplane Design Optimization for Minimal Global Warming Impact," *Journal of Aircraft*, Vol. 59, No. 5, 2022, pp. 1363–1381. doi:10.2514/1.C036529.
- [20] Thijssen, R., Proesmans, P., and Vos, R., "Propeller Aircraft Design Optimization for Climate Impact Reduction," *33rd Congress of the International Council of the Aeronautical Sciences, ICAS 2022*, International Council of the Aeronautical Science (ICAS), 2022, p. ICAS2022_0819. URL https://www.icas.org/ICAS_ARCHIVE/ICAS2022/data/papers/ICAS2022_0819_paper.pdf.

- [21] Ryerson, M. S., and Hansen, M., "The potential of turboprops for reducing aviation fuel consumption," *Transportation Research Part D: Transport and Environment*, Vol. 15, No. 6, 2010, pp. 305–314. doi:10.1016/j.trd.2010.03.003.
- [22] Junior, C. H. M., Eller, R. d. A. G., and Oliveira, A. V., "Are passengers less willing to pay for flying turboprops? An empirical test of the "turbo aversion hypothesis"," *Journal of Air Transport Management*, Vol. 73, 2018, pp. 58–66. doi:10.1016/j.jairtraman.2018.08.005.
- [23] Hartman, E. P., "Negative Thrust and Torque Characteristics of an Adjustable-pitch Metal Propeller," *Annual Report-National Advisory Committee for Aeronautics*, Vol. 19, 1933, p. 421. URL <http://hdl.handle.net/2060/19930091538>.
- [24] Hedrick, W. S., and Douglass, W. M., "An Experimental Investigation of the Thrust and Torque Produced by Propellers Used as Aerodynamic Brakes," Tech. Rep. NACA-WR-A-27, National Advisory Committee for Aeronautics, 1944. URL <http://hdl.handle.net/2060/19930093338>.
- [25] Thomas, J. L., and Hansman, R. J., "Community Noise Reduction Assessment of Using Windmilling Drag on Approach by Hybrid Electric Aircraft," *AIAA Aviation 2020 Forum*, AIAA Paper 2020-2877, June 2020. doi:10.2514/6.2020-2877.
- [26] MacCready, P., "Regenerative battery-augmented soaring," *Technical Soaring*, Vol. 23, No. 1, 1999, pp. 28–32. URL <https://journals.sfu.ca/ts/index.php/ts/article/view/412>.
- [27] Barnes, J. Philip, "Flight Without Fuel – Regenerative Soaring Feasibility Study," *General Aviation Technology Conference & Exhibition*, SAE International, 2006. doi:10.4271/2006-01-2422.
- [28] Barnes, J. P., "Regenerative Electric Flight: Synergy and Integration of Dual-Role Machines," *53rd AIAA Aerospace Sciences Meeting*, AIAA Paper 2015-1302, Jan. 2015. doi:10.2514/6.2015-1302.
- [29] Galvao, F., "A Note on Glider Electric Propulsion," *Technical Soaring*, Vol. 36, No. 4, 2012, pp. 94–101. URL <https://journals.sfu.ca/ts/index.php/ts/article/view/336>.
- [30] Gunnarsson, G., Skúlason, J. B., Sigurbjarnarson, A., and Enge, S., *Regenerative electric/hybrid drive train for ships RENSEA II*, 2016. URL <https://urn.kb.se/resolve?urn=urn:nbn:se:norden:org:diva-5503>.
- [31] Eržen, D., Andrejašič, M., Lapuh, R., Tomažič, J., Gorup, Č., and Kosel, T., "An Optimal Propeller Design for In-Flight Power Recuperation on an Electric Aircraft," *2018 Aviation Technology, Integration, and Operations Conference*, AIAA Paper 2018-3206, June 2018. doi:10.2514/6.2018-3206.
- [32] JAXA, "Electric and hybrid propulsion system for aircraft," <https://www.aero.jaxa.jp/eng/research/frontier/feather/>, 2015. Accessed: November 25, 2020.

-
- [33] Courty-Audren, S.-K., Binder, N., Carbonneau, X., and Challas, F., "Potential of power recovery of a subsonic axial fan in windmilling operation," *10th European Turbomachinery Conference*, Lappeenranta, Finland, 2013. URL <https://oatao.univ-toulouse.fr/9046/>.
- [34] Gill, A., Von Backström, T. W., and Harms, T. M., "Flow Fields in an Axial Flow Compressor During Four-Quadrant Operation," *Journal of Turbomachinery*, Vol. 136, No. 6, 2013, p. 061007. doi:10.1115/1.4025594.
- [35] García Rosa, N., Dufour, G., Barènes, R., and Lavergne, G., "Experimental Analysis of the Global Performance and the Flow Through a High-Bypass Turbofan in Windmilling Conditions," *Journal of Turbomachinery*, Vol. 137, No. 5, 2015, p. 051001. doi:10.1115/1.4028647.
- [36] Binder, N., Courty-Audren, S.-K., Duplaa, S., Dufour, G., and Carbonneau, X., "Theoretical analysis of the aerodynamics of low-speed fans in free and load-controlled windmilling operation," *Journal of Turbomachinery*, Vol. 137, No. 10, 2015.
- [37] Ortolan, A., Courty-Audren, S.-K., Binder, N., Carbonneau, X., Rosa, N. G., and Challas, F., "Experimental and numerical flow analysis of low-speed fans at highly loaded windmilling conditions," *Journal of Turbomachinery*, Vol. 139, No. 7, 2017.
- [38] Nodama, T., and Sunada, S., "Puropera ni yoru batteri jūden ni kansuru kentō [A Study on battery charging by propellers]," *Proceedings of the Japan Society for Aeronautics and Astronautics*, Vol. 63, No. 1, 2015, pp. 8–12. doi:10.2322/jjsass.63.8.
- [39] Sinnige, T., Stokkermans, T. C. A., van Arnhem, N., and Veldhuis, L. L. M., "Aerodynamic Performance of a Wingtip-Mounted Tractor Propeller Configuration in Windmilling and Energy-Harvesting Conditions," *AIAA Aviation 2019 Forum*, AIAA Paper 2019-3033, June 2019. doi:10.2514/6.2019-3033.
- [40] Veldhuis, L. L. M., "Propeller wing aerodynamic interference," Ph.D. thesis, Delft University of Technology, 2005. URL <http://resolver.tudelft.nl/uuid:8fffbde9c-b483-40de-90e0-97095202fbe3>.
- [41] Sinnige, T., "Aerodynamic and Aeroacoustic Interaction Effects for Tip-Mounted Propellers: An Experimental Study," Ph.D. thesis, Delft University of Technology, Sep. 2018. doi:10.4233/uuid:214e1e9a-c53e-47c7-a12c-b1eb3ec8293b.
- [42] Goldstein, S., and Prandtl, L., "On the vortex theory of screw propellers," *Proceedings of the Royal Society of London. Series A, Containing Papers of a Mathematical and Physical Character*, Vol. 123, No. 792, 1929, pp. 440–465. doi:10.1098/rspa.1929.0078.
- [43] Theodorsen, T., *Theory of propellers*, New York : McGraw-Hill, 1948. URL <http://lib.ugent.be/catalog/rug01:003179678>.
- [44] Wald, Q. R., "The aerodynamics of propellers," *Progress in Aerospace Sciences*, Vol. 42, No. 2, 2006, pp. 85–128. doi:10.1016/j.paerosci.2006.04.001.

- [45] van Arnhem, N., "Unconventional Propeller-Airframe Integration for Transport Aircraft Configurations," Ph.D. thesis, Delft University of Technology, 2022. doi:10.4233/uuid:4d47b0db-1e6a-4f38-af95-aafd33c29402.
- [46] Nederlof, R., Ragni, D., and Sinnige, T., "Energy-Harvesting Performance of an Aircraft Propeller," *Journal of Aircraft*, Vol. 62, No. 2, 2025, pp. 349–369. doi:10.2514/1.C038005.
- [47] Bass, R., "Techniques of Model Propeller Testing," *Business Aircraft Meeting & Exposition*, SAE International TP-830750, April 1983. doi:10.4271/830750.
- [48] Bass, R., "Small scale wind tunnel testing of model propellers," *24th Aerospace Sciences Meeting*, AIAA Paper 1986-0392, January 1986. doi:10.2514/6.1986-392.
- [49] Goyal, J., Sinnige, T., Avallone, F., and Ferreira, C., "Benchmarking of Aerodynamic Models for Isolated Propellers Operating at Positive and Negative Thrust," *AIAA Journal*, 2024. doi:10.2514/1.J064093.
- [50] Goyal, J., Avallone, F., and Sinnige, T., "Isolated propeller aeroacoustics at positive and negative thrust," *Aerospace Science and Technology*, Vol. 147, 2024, p. 109021. doi:10.1016/j.ast.2024.109021.
- [51] Goyal, J., Sinnige, T., Ferreira, C., and Avallone, F., "Effect of Angle of Attack on Propeller Aeroacoustics at Positive and Negative Thrust," *Journal of Aircraft*, 2025. doi:10.2514/1.C038073.
- [52] Barlow, J., Rae, W., and Pope, A., *Low-Speed Wind Tunnel Testing*, Wiley, 1999.
- [53] DeLoach, R., "Improved quality in aerospace testing through the modern design of experiments," *38th Aerospace Sciences Meeting and Exhibit*, 2000, p. 825. doi:10.2514/6.2000-825.
- [54] Hanson, D. B., "Helicoidal surface theory for harmonic noise of propellers in the far field," *ALAA Journal*, Vol. 18, No. 10, 1980, pp. 1213–1220. doi:10.2514/3.50873.
- [55] Rwigema, M. K., "Propeller Blade Element Momentum Theory with Vortex Wake Deflection," *27th International congress of the aeronautical sciences*, ICAS Paper 2010-2.3.3, 2010. URL http://www.icas.org/ICAS_ARCHIVE/ICAS2010/PAPERS/434.PDF.
- [56] Burton, T., Sharpe, D., Jenkins, N., and Bossanyi, E., *Wind energy handbook*, Vol. 2, Wiley Online Library, 2001. doi:10.1002/9781119992714.
- [57] van Rooij, R., "Modification of the boundary layer calculation in RFOIL for improved airfoil stall prediction," Report IW-96087R Delft University of Technology, the Netherlands, Sep. 1996. URL <https://www.osti.gov/etdeweb/biblio/20102159>.
- [58] Drela, M., "XFOIL: An Analysis and Design System for Low Reynolds Number Airfoils," *Low Reynolds Number Aerodynamics*, edited by T. J. Mueller, Springer Berlin Heidelberg, Berlin, Heidelberg, 1989, pp. 1–12. doi:10.1007/978-3-642-84010-4_1.

-
- [59] Snel, H., Houwink, R., and Bosschers, J., "Sectional Prediction of Lift Coefficients on Rotating Wind Turbine Blades in Stall," Report ECN-93-052, Energy Research Center of the Netherlands, Petten, the Netherlands., 1993. URL <https://www.osti.gov/etdeweb/biblio/6693027>.
- [60] Bosschers, J., Montgomerie, B., Brand, A., and van Rooij, R., "Influence of Blade Rotation on the Sectional Aerodynamics of Rotational Blades," *22nd European Rotorcraft Forum, England*, 1996. URL <http://hdl.handle.net/10921/1380>.
- [61] Yu, W., Zhang, M. M., and Xu, J. Z., "Effect of smart rotor control using a deformable trailing edge flap on load reduction under normal and extreme turbulence," *Energies*, Vol. 5, No. 9, 2012, pp. 3608–3626. doi:10.3390/en5093608.
- [62] Goyal, J., "Blade Element Momentum Theory for Positive and Negative Thrust Propellers," *4TU.ResearchData.Software*, 2024. doi:10.4121/e748a68d-5f15-4757-b904-880bce8217b.
- [63] Prandtl, L., and Betz, A., "Vier abhandlungen zur hydrodynamik und aerodynamik," *Göttinger Nachr; Göttingen*, 1927. URL <https://univerlag.uni-goettingen.de/bitstream/handle/3/isbn-978-3-941875-75-3/GKSM3.pdf?sequence=1&isAllowed=y>.
- [64] Katz, J., and Plotkin, A., *Low-speed aerodynamics*, Vol. 13, Cambridge university press, 2001. doi:10.1017/CBO9780511810329.
- [65] Montgomery, Z., and Hunsaker, D. E., "A Propeller Model Based on a Modern Numerical Lifting-Line Algorithm with an Iterative Semi-Free Wake Solver," *2018 AIAA Aerospace Sciences Meeting*, AIAA 2018-1264, January 2018. doi:10.2514/6.2018-1264.
- [66] Anon., "ANSYS® Academic Research Release 2019 R3 Help System, Fluent," ANSYS, inc., Canonsburg, PA, 2019.
- [67] Stokkermans, T. C. A., van Arnhem, N., Sinnige, T., and Veldhuis, L. L. M., "Validation and Comparison of RANS Propeller Modeling Methods for Tip-Mounted Applications," *AIAA Journal*, Vol. 57, No. 2, 2019, pp. 566–580. doi:10.2514/1.J057398.
- [68] van Arnhem, N., Vos, R., and Veldhuis, L. L. M., "Aerodynamic Loads on an Aft-Mounted Propeller Induced by the Wing Wake," *AIAA Scitech 2019 Forum*, AIAA Paper 2019-1093, Jan. 2019. doi:10.2514/6.2019-1093.
- [69] Spalart, P. R., and Allmaras, S. R., "A One-Equation Turbulence Model for Aerodynamic Flows," *30th Aerospace Sciences Meeting*, AIAA Paper 1992-439, June 1992. doi:10.2514/6.1992-439.
- [70] Dacles-Mariani, J., Zilliac, G. G., Chow, J. S., and Bradshaw, P., "Numerical/Experimental Study of a Wingtip Vortex in the Near Field," *AIAA Journal*, Vol. 33, No. 9, 1995, pp. 1561–1568. doi:10.2514/3.12826.

- [71] Succi, S., *The Lattice Boltzmann Equation for Fluid Dynamics and Beyond*, Oxford University Press, 2001. doi:10.1093/oso/9780198503989.001.0001.
- [72] Shan, X., Yuan, X.-F., and Chen, H., “Kinetic theory representation of hydrodynamics: a way beyond the Navier–Stokes equation,” *Journal of Fluid Mechanics*, Vol. 550, 2006, pp. 413–441. doi:10.1017/S0022112005008153.
- [73] Casalino, D., Romani, G., Zhang, R., and Chen, H., “Lattice-Boltzmann calculations of rotor aeroacoustics in transitional boundary layer regime,” *Aerospace Science and Technology*, Vol. 130, 2022, p. 107953. doi:10.1016/j.ast.2022.107953.
- [74] Chen, H., Zhang, R., and Gopalakrishnan, P., “Lattice Boltzmann collision operators enforcing isotropy and Galilean invariance,” , Feb. 21 2017. URL <https://patents.google.com/patent/CA2919062A1/en>.
- [75] Chen, H., Chen, S., and Matthaeus, W. H., “Recovery of the Navier-Stokes equations using a lattice-gas Boltzmann method,” *Physical review A*, Vol. 45, No. 8, 1992, p. R5339. doi:10.1103/PhysRevA.45.R5339.
- [76] Yakhot, V., and Orszag, S. A., “Renormalization group analysis of turbulence. I. Basic theory,” *Journal of scientific computing*, Vol. 1, No. 1, 1986, pp. 3–51. doi:10.1007/BF01061452.
- [77] Teixeira, C. M., “Incorporating turbulence models into the lattice-Boltzmann method,” *International Journal of Modern Physics C*, Vol. 9, No. 08, 1998, pp. 1159–1175. doi:10.1142/S0129183198001060.
- [78] Wilcox, D., *Turbulence Modeling for CFD*, Vol. 1, DCW Industries, 2006. URL <https://books.google.co.in/books?id=tFNNPgAACAAJ>.
- [79] Launder, B. E., and Spalding, D. B., “The numerical computation of turbulent flows,” *Numerical prediction of flow, heat transfer, turbulence and combustion*, Elsevier, 1983, pp. 96–116. doi:10.1016/B978-0-08-030937-8.50016-7.
- [80] Avallone, F., van den Ende, L., Li, Q., Ragni, D., Casalino, D., Eitelberg, G., and Veldhuis, L., “Aerodynamic and Aeroacoustic Effects of Swirl Recovery Vanes Length,” *Journal of Aircraft*, Vol. 56, No. 6, 2019, pp. 2223–2235. doi:10.2514/1.C035552.
- [81] Casalino, D., “An advanced time approach for acoustic analogy predictions,” *Journal of Sound and Vibration*, Vol. 261, No. 4, 2003, pp. 583–612. doi:10.1016/S0022-460X(02)00986-0.
- [82] Farassat, F., and Succi, G. P., “A review of propeller discrete frequency noise prediction technology with emphasis on two current methods for time domain calculations,” *Journal of Sound and Vibration*, Vol. 71, No. 3, 1980, pp. 399–419. doi:10.1016/0022-460X(80)90422-8.
- [83] Turner, J. M., and Kim, J. W., “Quadrupole noise generated from a low-speed aerofoil in near-and full-stall conditions,” *Journal of Fluid Mechanics*, Vol. 936, 2022, p. A34. doi:10.1017/jfm.2022.75.

-
- [84] Gutin, L., "On the Sound Field of a Rotating Propeller," Tech. Rep. NACA-TM-1195, National Advisory Committee for Aeronautics, 1948. URL <http://hdl.handle.net/2060/20030068996>.
- [85] Demming, A. E., "Noise from propellers with symmetrical sections at zero blade angle," Tech. Rep. NACA-TN-605, National Advisory Committee for Aeronautics, 1937. URL <http://hdl.handle.net/2060/19930081380>.
- [86] Barry, F. W., and Magliozzi, B., "Noise detectability prediction method for low tip speed propellers," Tech. Rep. AFAP:-TR-71-37, Air Force Aero Propulsion Laboratory, June 1971. URL <https://apps.dtic.mil/sti/tr/pdf/AD0729432.pdf>.
- [87] Farassat, F., and Succi, G. P., "The prediction of helicopter rotor discrete frequency noise," *American Helicopter Society*, Jan. 1982, pp. 497–507. URL <https://ui.adsabs.harvard.edu/abs/1982ahs..proc..497F>.
- [88] Kotwicz Herniczek, M. T., Feszty, D., Meslioui, S.-A., Park, J., and Nitzsche, F., "Evaluation of acoustic frequency methods for the prediction of propeller noise," *AIAA Journal*, Vol. 57, No. 6, 2019, pp. 2465–2478. doi:10.2514/1.J056658.
- [89] Goyal, J., "Hanson's Model in Frequency Domain - Tonal Noise of Rotors in Uniform Inflow," *4TU.ResearchData.Software*, 2024. doi:10.4121/7DA5AA45-E44B-4FA3-9407-8BF61E835D99.
- [90] Roache, P. J., "Quantification of Uncertainty in Computational Fluid Dynamics," *Annual Review of Fluid Mechanics*, Vol. 29, No. 1, 1997, pp. 123–160. doi:10.1146/annurev.fluid.29.1.123.
- [91] Eça, L., and Hoekstra, M., "Discretization Uncertainty Estimation Based on a Least Squares Version of the Grid Convergence Index," *Proceedings of the Second Workshop on CFD Uncertainty Analysis*, 2006. URL https://maretec.tecnico.ulisboa.pt/html_files/CFD_workshops/html_files_2006/papers/paper_istmarin.pdf.
- [92] O'meara, M., and Mueller, T. J., "Laminar separation bubble characteristics on an airfoil at low Reynolds numbers," *AIAA journal*, Vol. 25, No. 8, 1987, pp. 1033–1041. doi:10.2514/3.9739.
- [93] Ol, M., McCauliffe, B., Hanff, E., Scholz, U., and Kähler, C., "Comparison of laminar separation bubble measurements on a low Reynolds number airfoil in three facilities," *35th AIAA fluid dynamics conference and exhibit*, 2005, p. 5149. doi:10.2514/6.2005-5149.
- [94] Temmerman, L., and Leschziner, M. A., "Large eddy simulation of separated flow in a streamwise periodic channel constriction," *Second Symposium on Turbulence and Shear Flow Phenomena*, Begel House Inc., 2001. doi:10.1615/TSFP2.2300.

- [95] Temmerman, L., Leschziner, M. A., Mellen, C. P., and Fröhlich, J., "Investigation of wall-function approximations and subgrid-scale models in large eddy simulation of separated flow in a channel with streamwise periodic constrictions," *International Journal of Heat and Fluid Flow*, Vol. 24, No. 2, 2003, pp. 157–180. doi:10.1016/S0142-727X(02)00222-9.
- [96] Kurtz, D., and Marte, J., "A review of aerodynamic noise from propellers, rotors, and lift fans," Tech. Rep. 32-1462, Jet Propulsion Laboratory, Jan. 1970. URL <https://ntrs.nasa.gov/citations/19700005920>.
- [97] Williams, J. F., and Hawkings, D., "Theory relating to the noise of rotating machinery," *Journal of Sound and Vibration*, Vol. 10, No. 1, 1969, pp. 10–21. doi:10.1016/0022-460X(69)90125-4.
- [98] Goyal, J., Sinnige, T., Avallone, F., and Ferreira, C., "Aerodynamic and Aeroacoustic Characteristics of an Isolated Propeller at Positive and Negative Thrust," *AIAA Aviation 2021 Forum*, AIAA Paper 2021-2187, June 2021. doi:10.2514/6.2021-2187.
- [99] Goyal, J., Sinnige, T., Ferreira, C., and Avallone, F., "Effect of Angle of Attack on Propeller Aeroacoustics at Positive and Negative Thrust," *Journal of Aircraft*, 2025. doi:10.2514/1.C038073.
- [100] von Karman, T. H., and Sears, W. R., "Airfoil theory for non-uniform motion," *Journal of the aeronautical sciences*, Vol. 5, No. 10, 1938, pp. 379–390. doi:10.2514/8.674.
- [101] De Young, J., "Propeller at high incidence," *Journal of Aircraft*, Vol. 2, No. 3, 1965, pp. 241–250. doi:10.2514/3.43646.
- [102] Ortun, B., Boisard, R., and Gonzalez-Martino, I., "In-plane airloads of a propeller with inflow angle: prediction vs. experiment," *30th AIAA Applied Aerodynamics Conference*, 2012, p. 2778. doi:10.2514/6.2012-2778.
- [103] Nederlof, R., Ragni, D., and Sinnige, T., "Experimental Investigation of the Aerodynamic Performance of a Propeller at Positive and Negative Thrust and Power," *AIAA AVIATION 2022 Forum*, AIAA Paper 2022-3893, June 2022. doi:10.2514/6.2022-3893.
- [104] Mani, R., "The radiation of sound from a propeller at angle of attack," *Proceedings of the Royal Society of London. Series A: Mathematical and Physical Sciences*, Vol. 431, No. 1882, 1990, pp. 203–218. doi:10.1098/rspa.1990.0127.
- [105] Romani, G., Grande, E., Avallone, F., Ragni, D., and Casalino, D., "Computational study of flow incidence effects on the aeroacoustics of low blade-tip Mach number propellers," *Aerospace Science and Technology*, Vol. 120, 2022, p. 107275. doi:10.1016/j.ast.2021.107275.
- [106] Carley, M., "The structure of wobbling sound fields," *Journal of sound and vibration*, Vol. 244, No. 1, 2001, pp. 1–19. doi:10.1006/jsvi.2000.3451.

-
- [107] Hanson, D., "Sound from a propeller at angle of attack: a new theoretical viewpoint," *Proceedings of the Royal Society of London. Series A: Mathematical and Physical Sciences*, Vol. 449, No. 1936, 1995, pp. 315–328. doi:10.1098/rspa.1995.0046.
- [108] Block, P., "The effects of installation on single-and counter-rotation propeller noise," *9th Aeroacoustics Conference*, 1984, p. 2263. doi:10.2514/6.1984-2263.
- [109] Block, P., *Experimental study of the effects of installation on single-and counter-rotation propeller noise*, Vol. 2541, National Aeronautics and Space Administration, Scientific and Technical Information Branch, 1986. URL <https://ntrs.nasa.gov/citations/19860016690>.
- [110] Woodward, R., "Measured noise of a scale model high speed propeller at simulated takeoff/approach conditions," *25th AIAA Aerospace Sciences Meeting*, 1987, p. 526. URL <https://ntrs.nasa.gov/citations/19870043835>.
- [111] Himmelskamp, H., Aerodynamische Versuchsanstalt Göttingen, Great Britain. Ministry of Aircraft Production, and Luftfahrtforschungsanstalt Hermann Georing, *Profile Investigations on a Rotating Aircrew*, ARC-10856, Ministry of Aircraft Production, 1947. URL <https://books.google.co.in/books?id=VlK3tgAACAAJ>.
- [112] Bres, G., Pérot, F., and Freed, D., "Properties of the lattice Boltzmann method for acoustics," *15th AIAA/CEAS Aeroacoustics Conference (30th AIAA Aeroacoustics Conference)*, 2009, p. 3395. doi:10.2514/6.2009-3395.
- [113] Marié, S., Ricot, D., and Sagaut, P., "Comparison between lattice Boltzmann method and Navier–Stokes high order schemes for computational aeroacoustics," *Journal of Computational Physics*, Vol. 228, No. 4, 2009, pp. 1056–1070. doi:10.1016/j.jcp.2008.10.021.
- [114] Goyal, J., Sinnige, T., Avallone, F., and Ferreira, C., "Estimation of Rotor Blade Loading Distribution From Slipstream Velocity Measurements," *AIAA Journal*, 2025. doi:10.2514/1.J064736.
- [115] Philipsen, I., Hoeijmakers, H., and Hegen, S., "An Overview of Advanced Propeller Simulation Tests in the German Dutch Wind Tunnels (DNW)," *22nd AIAA Aerodynamic Measurement Technology and Ground Testing Conference*, AIAA Paper 2002-2920, June 2002. doi:10.2514/6.2002-2920.
- [116] Sinnige, T., Ragni, D., Eitelberg, G., and Veldhuis, L. L. M., "Pusher-Propeller Blade Loading With and Without Pylon Trailing-Edge Blowing," *34th AIAA Applied Aerodynamics Conference*, AIAA Paper 2016-3421, June 2016. doi:10.2514/6.2016-3421.
- [117] Brown, F., Fleming, J., Langford, M., Walton, W., Ng, W., Schwartz, K., Wisda, D., and Burdisso, R., "Reduced-Order Prediction of Unsteady Propeller Loading and Noise from Pylon Wake Ingestion," *AIAA Journal*, Vol. 59, No. 9, 2021, pp. 3304–3316. doi:10.2514/1.J060109.

- [118] Ragni, D., van Oudheusden, B. W., and Scarano, F., “Non-intrusive aerodynamic loads analysis of an aircraft propeller blade,” *Experiments in Fluids*, Vol. 51, 2011, pp. 361–371. doi:10.1007/s00348-011-1057-7.
- [119] del Campo, V. and Ragni, D. and Micallef, D. and Akay, B. and Diez, F. J. and Simão Ferreira, C. J., “3D load estimation on a horizontal axis wind turbine using SPIV,” *Wind Energy*, Vol. 17, No. 11, 2014, pp. 1645–1657. doi:10.1002/we.1658.
- [120] del Campo, V. and Ragni, D. and Micallef, D. and Akay, B. and Diez, F. J. and Simão Ferreira, C. J., “Estimation of loads on a horizontal axis wind turbine operating in yawed flow conditions,” *Wind Energy*, Vol. 18, No. 11, 2015, pp. 1875–1891. doi:10.1002/we.1794.
- [121] Kulesh, V. P., Mosharov, V. E., Orlov, A. A., Ostroukhov, S. P., and Radchenko, V. N., “Application of pressure sensitive paint for determination of aerodynamic loads and moments on propeller blade,” *Optical Methods of Flow Investigation*, Vol. 6262, edited by Y. N. Dubnistchev and B. S. Rinkevichyus, International Society for Optics and Photonics, SPIE, 2006, p. 62620K. doi:10.1117/12.683025.
- [122] Wei, C., Jiao, L., Tong, F., Chen, Z., Liu, Y., and Peng, D., “Pressure field measurements on large-scale propeller blades using pressure-sensitive paint,” *Acta Mechanica Sinica*, Vol. 38, No. 2, 2022, p. 121366. doi:10.1007/s10409-021-09048-1.
- [123] Gregory, J., Asai, K., Kameda, M., Liu, T., and Sullivan, J., “A review of pressure-sensitive paint for high-speed and unsteady aerodynamics,” *Proceedings of the Institution of Mechanical Engineers, Part G: Journal of Aerospace Engineering*, Vol. 222, No. 2, 2008, pp. 249–290. doi:10.1243/09544100JAERO243.
- [124] Peng, D., and Liu, Y., “Fast pressure-sensitive paint for understanding complex flows: from regular to harsh environments,” *Experiments in Fluids*, Vol. 61, 2020, pp. 1–22. doi:10.1007/s00348-019-2839-6.
- [125] Haans, W., van Kuik, G., and van Bussel, G., “The Inverse Vortex Wake Model: A Measurement Analysis Tool,” *45th AIAA Aerospace Sciences Meeting and Exhibit*, AIAA Paper 2007-422, January 2007. doi:10.2514/6.2007-422.
- [126] Goyal, J., “Wake-informed Lifting Line Theory: Example Code,” *4TU.ResearchData.Software*, 2025. doi:10.4121/4bf0f63f-7ac2-48dc-a2b1-e3fb819b34c2.
- [127] Byrd, R. H., Gilbert, J. C., and Nocedal, J., “A trust region method based on interior point techniques for nonlinear programming,” *Mathematical programming*, Vol. 89, 2000, pp. 149–185. doi:10.1007/PL00011391.
- [128] Coleman, T. F., and Li, Y., “An Interior Trust Region Approach for Nonlinear Minimization Subject to Bounds,” *SIAM Journal on Optimization*, Vol. 6, No. 2, 1996, pp. 418–445. doi:10.1137/0806023.

ACKNOWLEDGMENTS

*Every time anyone accomplishes anything,
he or she achieves it with the help of a thousand silent heroes.*

Alex Dunphy
Modern Family

After years of emotional highs, existential lows, and technical crashes (both mental and computational), I present to you this dissertation, along with my sincerest thanks to the real MVPs who kept me going.

First of all, I would like to thank Tomas, who has been a true role model throughout this journey. Whether it was deep technical discussions or the inevitable existential crises about the PhD going nowhere, Tomas was always there as a mentor, showing me the path forward and reminding me that there *is* light at the end of the tunnel. His obsession with precision and detail has rubbed off on me so much that my lovely wife, Rashika, now often complains when I ask her to be more specific or technically correct in her sentences. Thank you for being the ~~most~~ perfect daily supervisor anyone could ask for.

Alongside Tomas was Francesco, always ready to guide me through aeroacoustics and PowerFLOW simulations. I've consistently been amazed by his responsiveness and ability to provide quick, thoughtful feedback, despite being involved with so many students. Even after moving to Italy, it never felt like he was far from Delft. His involvement remained constant, and for that I am incredibly grateful.

Then, I was fortunate to have Carlos as my promotor, someone who constantly challenged my choices and pushed me to think more critically. You helped me grow into a more independent researcher and reminded me to always keep the bigger picture in mind, especially when I found myself getting lost in technically interesting, but less relevant, rabbit holes. I hope you recover soon and that we'll meet again at the faculty.

Thank you, my wonderful supervisory team, for the opportunity to pursue this PhD and for giving me the chance to grow through such a rich and meaningful experience.

I would also like to thank Dani for generously stepping in as promotor for official purposes, despite having nothing to gain and only an increased workload, all while managing an already packed schedule. Beyond that, I'm deeply grateful to both you and Damiano for giving me the opportunity to continue doing research at the faculty as a part-time postdoctoral researcher. I'm learning a great deal from both of you and look forward to continuing our work together in the coming year, hopefully even beyond.

I would also like to thank Frits and Tercio for all the fun and technical conversations we've had, and will no doubt continue to have, as part of this new chapter. Frits, thank you especially for helping with the Dutch translations of the summary and propositions (bedankt!), and for enlightening me with the fact that underwater hockey and mermaid

swimming are both real activities. Tercio, thank you for your support with COMSOL, for always being approachable and ready to help, and for agreeing to co-supervise master's theses in collaboration with Suzlon.

I was also lucky to have some amazing colleagues who made the office environment light and fun, and were always ready for a trip to the coffee machine. Thank you for all the weird and wonderfully informative discussions we had over coffee, Robert, Ramon, Martijn, Fernanda, PJ, Daaman, Reynard, Nando, Hugo, Biagio, Aaron, Ankit, Kaushal, Rishikesh, Vaibhav, Debdutta, and many more. Ramon, thank you for helping me out with the Dutch translation of the summary. Bedankt!

Beyond the office, I was fortunate to have a strong support group that truly felt like a home away from home. The long cooking sessions, intense card games, PS4 battles, and crazy parties made for a golden time I will always remember and cherish. Whether it was Abhishek bringing his date (on their first meeting, now his better half) Rucha to the apartment, leading to wonderfully awkward conversations; or Sumit waging war to make the spiciest food; or Ashwin delivering passionate lectures on veganism, only to later start eating octopus; or Harjot trying to sleep through the late night parties while we knocked on his door, lifted him from his bed, and brought him to the living room; all the moments were incredibly fun and unforgettable. And of course, our almost flatmate Rahul, who was always ready to come over for every little occasion, and whose endless enthusiasm for food and life continues to be truly inspiring. Thank you all for giving me not just company, but a family and a sense of home far from home.

Now, if we are talking about the board and card game sessions, how could I forget the wonderful souls I shared them with: Raghul, Blonde Arvind & Mano, Normal Arvind, Karshima, Arun, Rohan, Kshitij, and Aman. From playing cricket to long conversations and endless laughter, the time spent with you all has been incredibly special. Thank you!

Of course, there are many people I have known since before my PhD, dear friends from long ago: Vipul, Neeraj, Harleen, Samhit, Mohit, and Mayank. Thank you for more than a decade full of memories. Then there were the years spent dreaming of launching our own startup with Chakshu and Shubham. Guys, let's make it a reality. Chakshu bhai, when is the next trip?

Above all, I owe everything to the support of my family. Thank you, Mom and Dad. I could not have done this without your love and encouragement. To my younger brother, Ravince, whom I have always enjoyed scolding but who continues to inspire me with his free spirit. To Maa, Bade Mumma, and Bade Papa, thank you for your unwavering support and belief in me. And of course, to my elder brother Novy, without whom I would not have made it to the Netherlands in the first place. I am also grateful to Anita Bhabhi for taking care of him and the whole family.

Last but not least, I want to thank my wife, my love, my friend, my partner in crime, and my constant support through all the ups and downs, the highs and the lows, the one and only Rashika. Thank you for bearing with me and all my tantrums, and for being my safe space when nothing seemed to be going right, but somehow everything still felt okay. I cannot thank you enough.

Jatinder Goyal
May 2025

CURRICULUM VITAE

Jatinder GOYAL

07-02-1996 Born in Mandi Kalan, Punjab, India.

RESEARCH & WORK EXPERIENCES

- 2024–Present **Aerodynamics Engineer**
Suzlon Energy Limited, Hengelo, the Netherlands
- 2024–Present **Postdoctoral Researcher**
Delft University of Technology, Delft, the Netherlands
- 2019–2020 **CFD Engineer**
VFA Solutions, Schiedam, the Netherlands
- 2018–2018 **Internship**
LM Wind Power, Heerhugowaard, the Netherlands

EDUCATION

- 2020–2025 **PhD in Propeller Aerodynamics and Aeroacoustics**
Delft University of Technology, Delft, the Netherlands
Thesis: Aerodynamics and Aeroacoustics of Propeller Operation at Negative Thrust: A Computational Study
Promoters: Prof. dr. ir. C. Simão Ferreira
 Dr. ir. T. Sinnige
 Prof. dr. F. Avallone
Project: FUTPRINT50
- 2017–2019 **MSc in Aerospace Engineering**
Delft University of Technology, Delft, the Netherlands
Thesis: Internal Flow Simulation of an ESP Air Purifier using RANS Flowfield and Lagrangian Tracking of Aerosols
Supervisor: Dr. ir. M. I. Gerritsma
Company: VFA Solutions, Schiedam, the Netherlands
- 2013–2017 **B.E. in Aerospace Engineering**
PEC University of Technology, Chandigarh, India

LIST OF PUBLICATIONS

JOURNAL PAPERS

5. **Goyal, J.**, Sinnige, T., Avallone, E., and Ferreira, C., “Estimation of Rotor Blade Loading Distribution From Slipstream Velocity Measurements,” *AIAA Journal*, 2025. doi:10.2514/1.J064736.
4. **Goyal, J.**, Sinnige, T., Ferreira, C., and Avallone, E., “Effect of Angle of Attack on Propeller Aeroacoustics at Positive and Negative Thrust,” *Journal of Aircraft*, 2025. doi:10.2514/1.C038073
3. Nederlof, R., **Goyal, J.**, Sinnige, T., Ragni, D., and Veldhuis, L. L. M., “Fast Numerical Modeling of Propeller-Wing Aerodynamic Interactions,” *AIAA Journal*, 2025. doi:10.2514/1.J064764.
2. **Goyal, J.**, Sinnige, T., Avallone, E., and Ferreira, C., “Benchmarking of Aerodynamic Models for Isolated Propellers Operating at Positive and Negative Thrust,” *AIAA Journal*, Vol. 62, No. 10, 2024, pp. 3758-3775. doi:10.2514/1.J064093.
1. **Goyal, J.**, Avallone, E., and Sinnige, T., “Isolated Propeller Aeroacoustics at Positive and Negative Thrust,” *Aerospace Science and Technology*, Vol. 147, 2024, p. 109021. doi:10.1016/j.ast.2024.109021.

CONFERENCE PAPERS

3. Wickersheim, R., **Goyal, J.**, Sinnige, T., and Keßler, M., “Computational Cross-Validation of Propeller Noise in Positive and Negative Thrust Conditions,” *AIAA Scitech 2025 Forum*, AIAA 2025-1046, January 2025. doi:10.2514/6.2025-1046.
2. **Goyal, J.**, Sinnige, T., Ferreira, C., and Avallone, E., “Aerodynamics and Far-field Noise Emissions of a Propeller in Positive and Negative Thrust Regimes at Non-zero Angles of Attack,” *AIAA Aviation 2023 Forum*, AIAA Paper 2023-3217, June 2023. doi:10.2514/6.2023-3217.
1. **Goyal, J.**, Sinnige, T., Avallone, E., and Ferreira, C., “Aerodynamic and Aeroacoustic Characteristics of an Isolated Propeller at Positive and Negative Thrust,” *AIAA Aviation 2021 Forum*, AIAA Paper 2021-2187, June 2021. doi:10.2514/6.2021-2187.

PUBLISHED CODES

3. **Goyal, J.**, “Wake-informed Lifting Line Theory: Example Code,” *4TU.ResearchData.Software*, 2025. doi:10.4121/4bf0f63f-7ac2-48dc-a2b1-e3fb819b34c2.
2. **Goyal, J.**, “Blade Element Momentum Theory for Positive and Negative Thrust Propellers,” *4TU.ResearchData.Software*, 2024. doi:10.4121/e748a68d-5f15-4757-b904-880bceec8217b.
1. **Goyal, J.**, “Hanson’s Model in Frequency Domain - Tonal Noise of Rotors in Uniform Inflow,” *4TU.ResearchData.Software*, 2024. doi:10.4121/7da5aa45-e44b-4fa3-9407-8bf61e835d99.

.... —*dary*

Barney Stinson
How I Met Your Mother

